Pseudorapidity Densities in p+p and Pb+Pb collisions at LHC measured with the ALICE experiment

Hans Hjersing Dalsgaard

January 4, 2012

SIGILLVM FACVLTATIS NATVRALIS VNIVERSITATIS HAFNIENSIS

Thesis
presented for the degree of
Doctor of Philosophy (PhD) in Physics

Supervisor: Jens Jørgen Gaardhøje, Niels Bohr Institute

Contents

Preface

I first started in heavy ion physics in 2004 when I did my bachelors project in the High Energy Heavy Ion (HEHI) group at the Niels Bohr Institute. The project concerned the high p_T suppression observed at the experiments at the Relativistic Heavy Ion Collider (RHIC), USA. Working with Signe Riemer-Sørensen and Casper Nygaard, we successfully measured the high p_T suppression in data from the BRAHMS experiment and our project was received very well. I decided that I was not done with heavy ion physics so Casper Nygaard and I collaborated to measure the stopping in Au+Au collisions at $\sqrt{s_{NN}} = 62.4$ GeV. This work was successful and was accepted by Physics Letters B in 2009 [1].

At the same time heavy ion physics was about to receive a major boost in Europe by the construction of the Large Hadron Collider, the largest machine ever built by man, in CERN, Geneva, Switzerland. This machine has the ability to increase the collision energies by a factor of ~ 25 compared to RHIC. *Twenty–five*! Luckily for me, the HEHI group was involved in the construction of the *Forward Multiplicity Detector* (FMD) as part of A Large Ion Collider Experiment (ALICE) at LHC. This meant that I could do my masters project on simulation studies of the performance and analysis of the FMD data. Following my masters degree in 2007 I was hired as a PhD student, and the culmination of almost 4 years of work on the FMD from it was stored in boxes at CERN prior to installation to now when it is taking data around the clock, is this thesis.

I did not do this work alone. Many people helped me with all kinds of things throughout my PhD studies. All deserve thanks and I will try to name some of the people who helped me along the way. First of all I would like to thank my supervisor, professor Jens Jørgen Gaardhøje for giving me the opportunity to pursue a PhD and for guiding me in this pursuit. A special thanks goes to Christian Holm Christensen, who apart from his invaluable help on physics, programming, and the shaping of this thesis also has been a key player in getting the FMD system up and running. Another key player in this process is Kristjan Gulbrandsen who also deserves many thanks. My fellow doctoral students, Casper Nygaard and Carsten Søgaard have made the route through the PhD studies enjoyable and have also contributed with countless useful comments and discussions. These thanks also goes to former master student in HEHI, recently a PhD student, Alexander Hansen who has developed his skills in the field of heavy ion physics impressively. I also thank the rest of HEHI, Ian Bearden, Hans Bøggild, and Børge Svane Nielsen for invaluable input, guidance, and advice as well as their effort in getting and keeping the FMD project on track. Also a special thanks to Jamie Nagle, who was a guest at NBI in 2011. At CERN and associated institutions in ALICE, many people have helped or inspired my work. Many thanks to Latchezar Betev, Cvetan Cheshkov, Andrei and Mihaela Gheata, Maxime Guilbaud, Peter Hristov, Andreas Morsch, Martin Poghosyan, Karel Safarik, Mario Sitta, Jurgen Schukraft, Jan–Fiete Grosse Oetringhaus, to name a few. If you read this and feel overlooked consider yourself thanked.

Finally I want to thank my family and friends for your love and support, in particular my wife Ditte–Marie. Without you I would not have been able to perform as I did nor get this project done in time. Finally there is my daughter Olivia. In some sense, it is all for her.

The field of heavy ion physics is evolving faster than ever and with the data from LHC a whole new realm of physics is opening up. To me, perhaps the most fascinating aspect of heavy ion physics is that it is possible to look back some 13 billion years in time to the origin of everything by colliding particles below Geneva. When things have been difficult or I have felt the weight of the project I have found some comfort and amusement in that thought. Happy reading.

Hans Hjersing Dalsgaard,
Copenhagen, October 2011

Use of results from this thesis. All results from this thesis and all plots deriving from ALICE detectors are the property of the ALICE collaboration and the University of Copenhagen. ALICE results are only official if published in a peer–reviewed journal. To use the contents of this thesis please contact either the author, supervisor, or the ALICE collaboration.

Contact information:

Address	Tom Kristensens Vej 22 3.th., 2300 Copenhagen S, Denmark
Phone	+45 21233854
E–mail	hansdalsgaard@gmail.com

Supervisor	Professor Dr. Jens Jørgen Gaardhøje, Niels Bohr Institute
E–mail	gardhoje@nbi.dk
Chair of Opponents	Professor Dr. Peter Hansen, Niels Bohr Institute
Opponent	Dr. Raju Venugopalan, Brookhaven National Laboratory, USA
Opponent	Professor Dr. Wolfgang Kühn, University of Giessen, Germany

Chapter 1

Heavy Ion Physics

Heavy Ion Physics is devoted to the study of matter under the extreme conditions as created in collisions of heavy ions at large energies. Experiments in Heavy Ion Physics are carried out using accelerator and collider facilities available at laboratories throughout the world notably the Relativistic Heavy Ion Collider (RHIC) at Brookhaven National Laboratory (BNL), USA and the Super Proton Synchrotron (SPS) and the Large Hadron Collider (LHC), CERN, Switzerland. This Chapter gives an overview of some basic concepts of Heavy Ion Physics. For a discussion of some of the kinematics and some basic concepts refer to appendix B. These include the *pseudorapidity* and the *centrality* that are crucial for the discussions in this work.

1.1 Matter

At all times one of the mysteries that has puzzled man is the composition of everything; what is at the heart of matter? Today the best answer lies in the Standard Model of particle physics which introduces the basic particles, forces, and the rules of their combinations and interactions. According to the Standard Model all matter consists of either leptons or quarks[1]. Table 1.1 summarizes the particles of the Standard Model. For a graphical overview of the interactions of these particles see Figure 1.1. All particles in the Standard Model have antiparticles with the same mass but with opposite electrical charge and color charge (see section 1.1.1 below). Antiparticles are denoted with a bar, so that an anti–up quark is labelled ū. Leptons have only been observed as free particles whereas quarks have not. In the present Universe the only quarks observed are the u and d quarks which are found in the neutrons (udd) and protons (uud). In general, composite particles built from quarks are called *hadrons*; hadrons containing two quarks are called *mesons* and hadrons composed of three quarks are called *baryons*. Thus, the neutron and the proton are baryons. The conservation of certain quantum numbers (electrical charge, spin, isospin etc.)

Quark	Mass	Charge	Lepton	Mass	Charge	Carrier	Force
up(u)	0.003	2/3	electron(e)	0.000511	-1	gluon(g)	strong
down(d)	0.006	$-1/3$	e-neutrino(ν)	$< 10^{-8}$	0	photon(γ)	electromagnetic
charm(c)	0.1	2/3	muon(μ)	0.106	-1	Z^0	weak
strange(s)	1.3	$-1/3$	μ-neutrino	< 0.0002	0	$W^{\pm}$	weak
top(t)	175	2/3	tau(τ)	1.7771	-1	H	weak
bottom(b)	4.3	$-1/3$	τ-neutrino	< 0.02	0	graviton ?	gravity

Table 1.1: The particles of the Standard Model. Masses are given in GeV and charges in multipla of the elemental charge, e.

---

[1] In older works, the term *partons* is sometimes used as a common name for quarks *and* gluons.

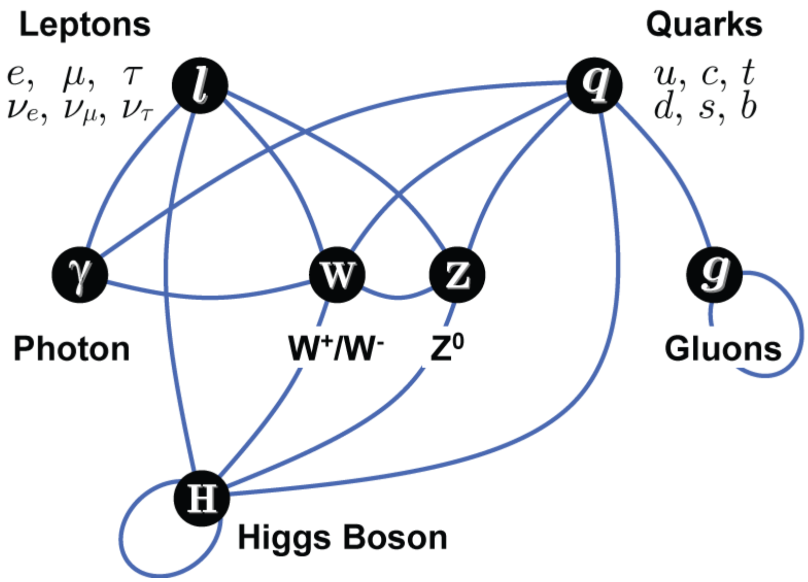

Figure 1.1: The interactions of the Standard Model. At the top are the quarks and leptons, in the middle the force carriers. At the bottom is the Higgs boson which is yet to be discovered. If the standard model Higgs boson exists it will be discovered at LHC. The allowed interactions are indicated by the lines.

determines the possible hadronic states. Examples of mesons are the pion, π^+ $(u\bar{d})$ and the kaon, K^+ $(u\bar{s})$[2].

1.1.1 Quantum Chromodynamics (QCD)

As can be seen in Figure 1.1 the Standard Model includes the basic interactions between particles. The electromagnetic forces and the weak nuclear interactions can be described within the framework of Quantum Electro–Weak Dynamics. Gravity is described by the General Theory of Relativity and cannot (so far) be described by any quantum theory. Finally, the strong nuclear interaction, responsible for binding hadrons together is described by QCD. Note that the nucleon–nucleon interaction has so far not been described by QCD even though attempts are being made [2].

In QCD a new quantum number, carried by quarks and gluons, is introduced. It is called color charge and particles carrying it interact strongly. This means that gluons mediate the strong force between quarks *and* they interact strongly themselves. This is not the case for e.g., photons that mediate the electromagnetic force without self-interactions. QCD is a non-Abelian gauge theory, which means that the strong interaction shows almost no resemblance to e.g., the electromagnetic interactions. To illustrate this the quark-quark potential calculated from QCD is shown in Figure 1.2. It is seen that the quark-quark potential rises with distance, indicating that it will require an infinite amount of energy to separate two quarks. This is the theoretical explanation of the phenomenon of *quark confinement* in hadrons. Figure 1.2 also reveals another important property of the strong interaction, namely that the qq-potential drops as the distance between the quarks becomes small, a concept known as *asymptotic freedom.* Confinement and asymptotic freedom are key concepts in the dynamics of heavy ion collisions. To further illustrate these concepts let us consider two scenarios, firstly: What happens if a quark is pulled (e.g., in scattering experiments) away from a the other quarks in a hadron? According to QCD the potential between the quark and the hadron will increase until there is enough energy to produce a new quark-antiquark pair, a phenomenon known as pair production. The new particles will then recombine to form hadronic states. In this way it becomes impossible to isolate a single quark because quark-antiquark pairs will be created to form new particles instead. The second scenario is: What if it was possible (e.g., in heavy ion collisions)

---

[2] And their antiparticles, π^- $(d\bar{u})$ and K^- $(s\bar{u})$.

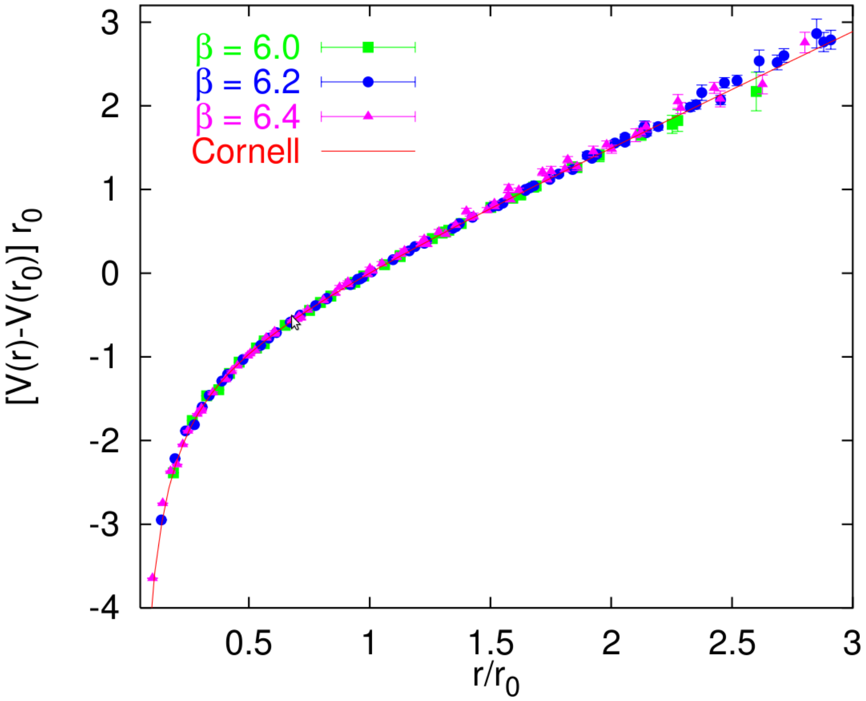

Figure 1.2: The quark–quark potential calculated from lQCD [3]. In the plot $r_0 = 0.5$ fm and $V(r_0) = 0$.

to create a high enough density of quarks in a nucleus (or a region of a compatible volume) for them to experience asymptotic freedom? The discoveries at RHIC supports the conjecture that this leads to the formation of a state of matter not observed since briefly ($t \leq 10^{-6}$ s) after the Big Bang. This state of matter is called a Quark Gluon Plasma (QGP), since it consists of 'free' (free to interact within a small volume, that is) quarks and gluons. The formation and study of the QGP is one of the primary challenges in Heavy Ion Physics.

Theoretically speaking the concept of quark confinement and its disappearance in the QGP phase is a feature of the socalled chiral symmetry restoration. The chiral condensate, defined as the vacuum expectation value of the quark condensate, $\langle\psi\bar{\psi}\rangle$ is non-zero in hadronic matter whereas it vanishes in the QGP phase, $\langle\psi\bar{\psi}\rangle \sim 0$ [4]. While a measurement of this quantity would bring immediate enlightenment on the formation of the QGP it is not possible to measure directly and therefore other experimental routes must be taken to study QGP formation.

For practical purposes there are two different QCD approaches: Lattice QCD (lQCD) where the calculations are done treating spacetime as discrete and pertubative QCD (pQCD) working from the Lagrangians of QCD in the high Q (momentum transfer) limit. The plot in Figure 1.2 was calculated using lQCD.

In recent years a new powerful, theoretical tool has been developed, the socalled AdS/CFT (Anti-de-Sitter / Conformal Field Theory) duality where it has been found that solving problems in the realm of general relativity can lead to easier paths to results in high energy physics [5]. This is a very promising new development that is already employed in many aspects of heavy ion physics, although still at a qualitative level.

1.1.2 Quark Gluon Plasma

The possible existence of a phase of highly compressed, asymptotically free partonic matter in the theoretical framework of the quark and gluon fields was proposed as early as 1975 [6]. Here it is speculated that such a state might have an density as high as $\rho = 6 \cdot 10^{16}$ g/cm^3. In 1974 it was proposed at the conference at Bear Mountain [7] that collisions of heavy ions could be used to probe this medium as well as the properties of the vacuum. This meeting is often mentioned[3] as the starting point of experimental heavy ion physics. Figure 1.3 shows a conceptual sketch of the creation of QGP by compression. As the compression increases the hadrons cease to exist individually which leads to the formation of a QGP. In heavy ion collisions this compression is of course extremely violent and the lifetime of the created state very short (of the order of 1 fm/c = 10^{-23} s or even shorter).

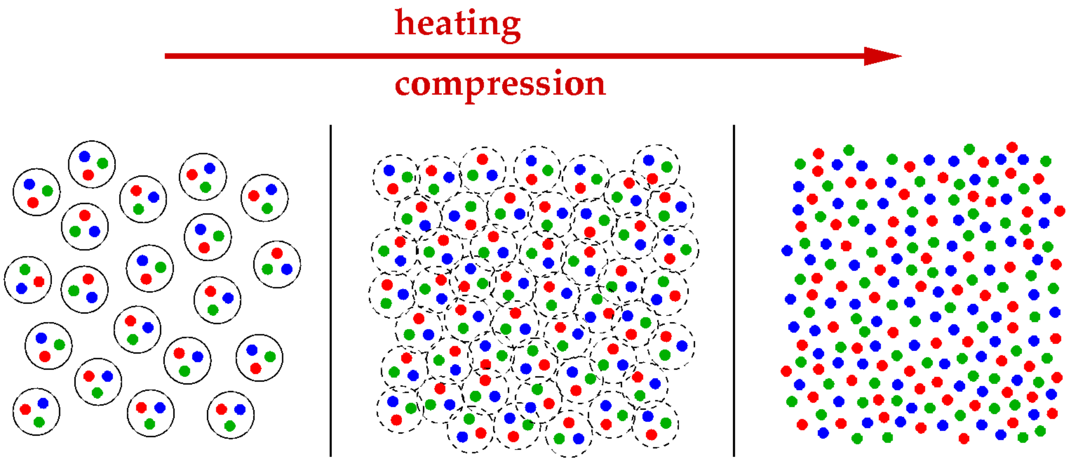

Figure 1.3: Compression and heating of matter leading to the formation of a QGP.

1.1.3 The Big Bang and the Early Universe

The general agreement in present cosmology is that the Universe was born in a violent, eruptive explosion, the Big Bang, the origin of which is a mathematical singularity in spacetime. All matter was present in a vanishingly small volume with correspondingly high energy density, temperature and pressure. However as the Universe expanded, it cooled and passed through several phases. At some point after the Big Bang, approximately at $t \sim 1$ μs, all matter in the Universe passed through a QGP phase before cooling further to “freeze out” to hadrons, leptons, and radiation. Some of this radiation is still visible in the Universe today as the Cosmic Microwave Background (CMB).

The discoveries at the Relativistic Heavy Ion Collider (RHIC) experiments have lead to two definitions of QGP: The sQGP (strongly interacting QGP) is believed to be formed in heavy ion collisions at least at RHIC energies whereas the ‘genuine’ QGP, the wQGP (weakly interacting QGP), is expected to be only weakly interacting like an ideal gas. The wQGP is the state of matter which is considered to have been in existence $\sim 10\mu$s after the Big Bang

The wQGP of the early Universe has existed in a time $t \sim 1$ns compared to the $t \sim 10^{-23}$ s lifetime the of the sQGP. Furthermore the baryon density of the early Universe was approximately $N_b/N \sim 10^{-10}$ compared to the $N_b/N \sim 0.1$ of a heavy ion collision[4][8]. This non negligible baryon density allows the QGP to interact strongly with the hadrons, an interaction not present in the early Universe[8]. Furthermore the relatively long lifetime of the QGP of the early Universe ensured that it must have been thermally equilibrated after some time. Whether the sQGP of heavy ion collisions can be considered to be in thermal equilibrium is still a topic of dispute although comparisons of measurements of the elliptic flow (see section 1.3.3) and hydrodynamical calculations suggest that this is in fact the case at RHIC and LHC.

---

[3] E.g., at the Quark Matter 2006 conference in Shanghai.

[4] Here N is to be understood as the total particles present, be they hadrons, leptons or radiation (photons).

1.1.4 Color Glass Condensate

Following the RHIC discoveries a conjecture has been put forward that beside the QGP there is also another new phase of matter in play in heavy ion collisions. Figure 1.4 shows HERA[5] data on the gluon distribution and a cartoon depicting the increased gluon density at high energy.

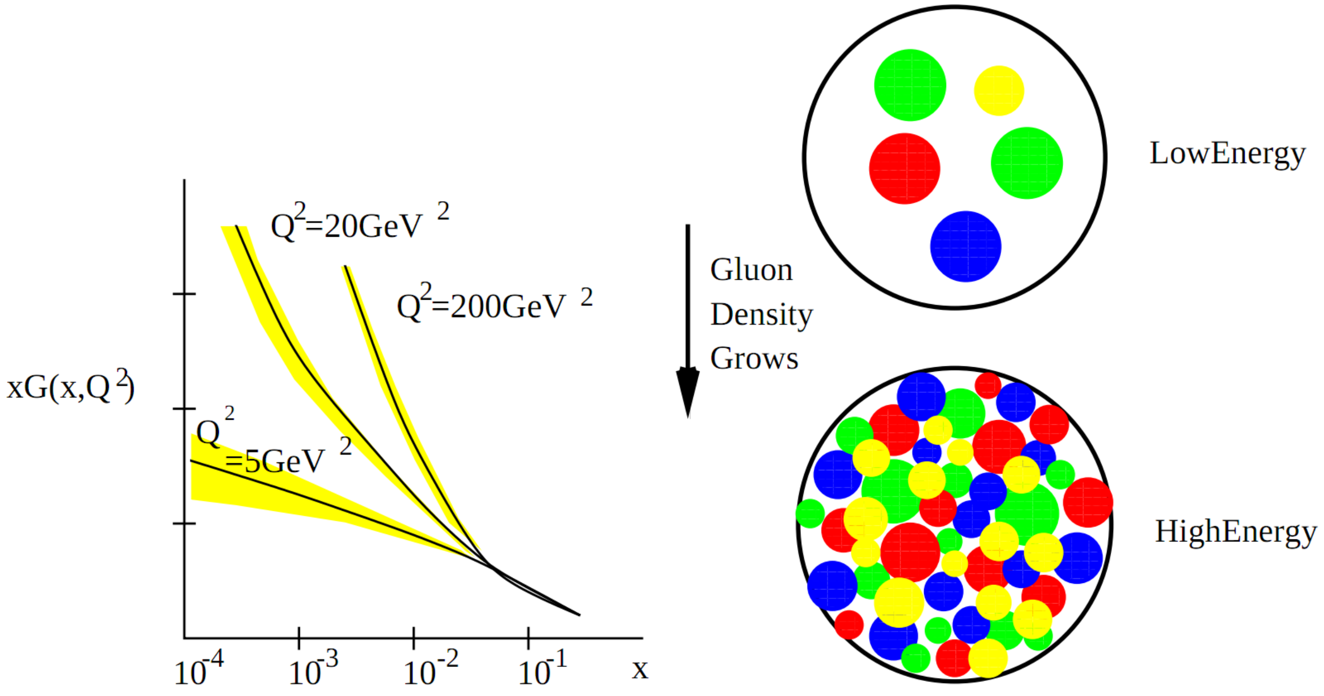

Figure 1.4: Left: The gluon density, $xG(x, Q^2)$ as function of x (and three values of Q^2) [9, 10]. Right: Sketch of the increase in gluon density with energy [9].

The HERA results mean that as the nuclei collide (and may form QGP at a later stage) the gluon density rises with the collision energy. The extra gluons are squeezed together within the longitudinally contracted nuclei and are affected by potentials similar to the qq potential (see Figure 1.2) so the strong interaction between the gluons should be absent. Hence the CGC should be weakly interacting unlike the sQGP. The term 'Color Glass Condensate' is derived from the following [9]:

- **Color** The gluons forming the CGC are colored.
- **Glass** The evolution of the additional gluons is Lorentz time dilated so it is slow compared to the 'natural' time scale of the collisions. A similar behavior is observed in glass over time.
- **Condensate** Due to the saturation of the phase space density of the gluons the quantum states of the system are highly populated. This bears some resemblance to Bose-Einstein condensates.

Figure 1.4 also illustrates the concept of the *saturation scale*, Q_s^2, a critical value of the momentum transfer. For momentum transfers above Q_s^2 the gluons exhibit saturation due to gluon shadowing [4]. This leads to an interpretation of the saturation scale as the border between two kinds of QCD scattering. For a fixed fraction of the longitudinal momentum, x, Q_s^2 can be defined as:

$$Q_s^2(x) = \alpha_s N_c \frac{1}{\pi R^2} \frac{dN}{dy} \tag{1.1}$$

---

[5] Hadron-Elektron-RingAnlage, Hadron-Electron Ring Accelerator, an experiment at the German DESY facility in Hamburg.

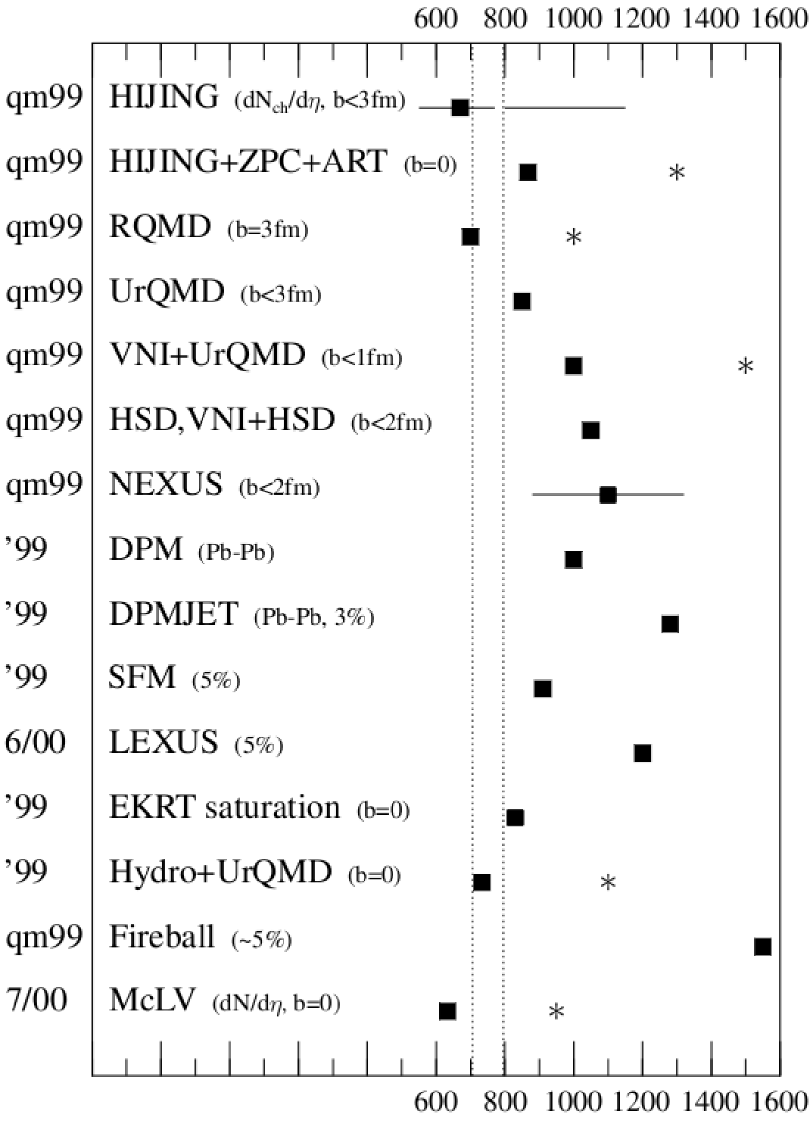

Figure 1.5: Predictions from various models for the dN/dy at $y = 0$. The CGC prediction is labeled 'McLV' [11]. The dotted vertical lines are the combined results from the RHIC experiments, 740 ± 50. The asterisks are the results for all particles and the squares are for the charged particles. The number of charged particles is derived from the total number by scaling with a factor 2/3. The lower than expected multiplicity observed at RHIC was a surprise to many in the community.

Here, πR^2 is the hadron area, $\alpha_s N_c$ is the color charge of a single gluon squared and $\frac{dN}{dy}$ is the x dependent gluon density.

While direct observations of the CGC are hard to make, models based on the CGC were able to predict the low multiplicities observed at RHIC. Figure 1.5 shows predictions of various models for the dN/dy at $y = 0$ compared to the combined results from the RHIC experiments. It is seen that the CGC based model does a good job while many models have problems and overestimate the multiplicity.

1.2 The Search for the QGP

1.2.1 QCD Predictions

QCD calculations predict the existence of a high density medium composed of deconfined quarks and gluons at high temperature [12, 4]. As early as 1951 a conjecture was put forward that the finite size of hadrons implied some critical compression above which matter could not exist in hadronic form [13]. To describe the QGP and the phase transition a statistical approach is often used. The QGP is assumed to be a thermally equilibrated fluid or gas of quarks and gluons. If the baryonic chemical potential is set to zero (ie. no net-baryons: $B = \bar{B}$, where B is the number of baryons) the partition functions for fermions and bosons in relativistic gases are [14]:

$$(T\ln Z)_f = \frac{g_f V}{12}\left(\frac{7\pi^2}{30}T^4 + \mu^2 T^2 + \frac{1}{2\pi^2}\mu^4\right) \quad \text{and} \quad (T\ln Z)_b = \frac{g_b V\pi^2}{90}T^4 \tag{1.2}$$

Here g_f and g_b are the degrees of freedom of fermions and bosons, respectively. Assuming that the equation of state is that of an ideal gas, $p = \epsilon/3$, and that the hadronic phase is composed only of pions, the following equations are obtained for the energy densities of the hadronic and QGP phases, respectively:

$$\epsilon_h/T^4 = \frac{\pi^2}{10} \quad \text{and} \quad \epsilon_{QGP}/T^4 = (32 + 21N_f)\frac{\pi^2}{60} \tag{1.3}$$

Evidently the QGP phase is characterised by a huge increase in the number of degrees of freedom caused by the asymptotically free quarks and gluons. No matter the value of the number of flavors, N_f, it is clear from Equation (1.3) that the energy density of the QGP phase is much higher compared to the hadronic phase. The case $N_f = 3$ (u,d,s) is known as the Stefan-Boltzmann limit.

It is possible to solve the QCD equations in lQCD to obtain the behaviour of the matter near the critical temperature of the phase transition, T_c. The value of T_c is believed to be $T_c \approx 170$ MeV[15]. The associated critical energy density is estimated to be around $\epsilon_c \approx 1$ GeV/fm^3. Figure 1.6 shows the result of a lQCD calcution for ϵ/T^4 around T_c. The increase in energy density discussed above for the ideal gas

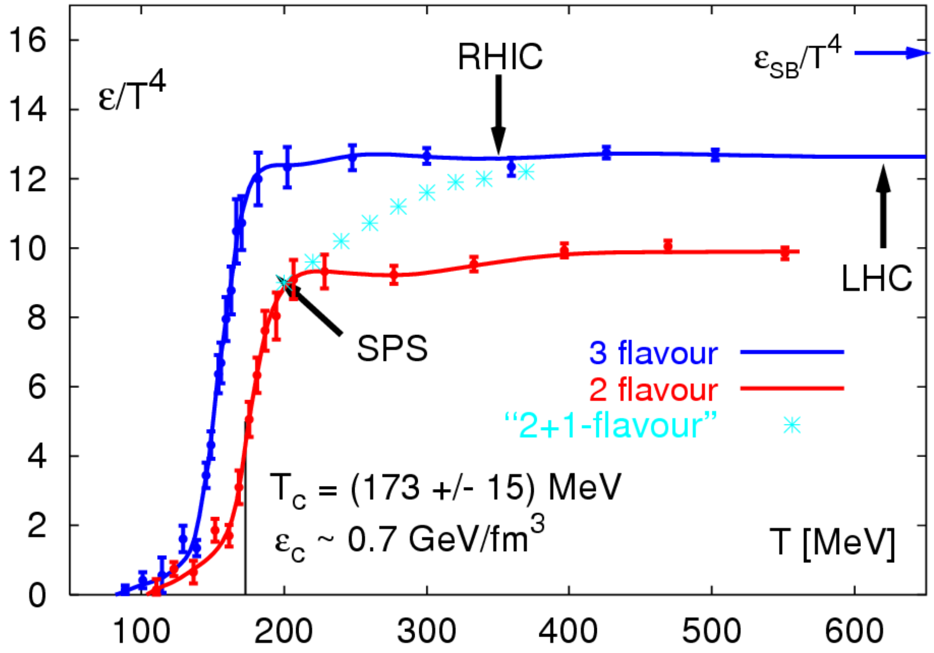

Figure 1.6: ϵ/T^4 from lQCD [15]. The calculations have been done for three choices of flavors as indicated in the Figure. The anticipated values of (ϵ, T) from SPS, RHIC and LHC are included.

case is evident from the figure. Also shown are the estimated (ϵ, T) of some of the heavy ion experiments in the field. The most realistic case shown in Figure 1.6 is the '2+1' case which has been calculated for 2 light quark flavors (u,d) and one heavy quark (s). The shape of the curve in Figure 1.6 is related to the nature of the phase transition.

A first order phase transition will be characterised by a discontinuity in the energy density around T_c whereas a second order transition will display a more smooth behaviour that does not necessarily involve a discontinuity. Finally there is the possibility that the transition takes place as a crossover where

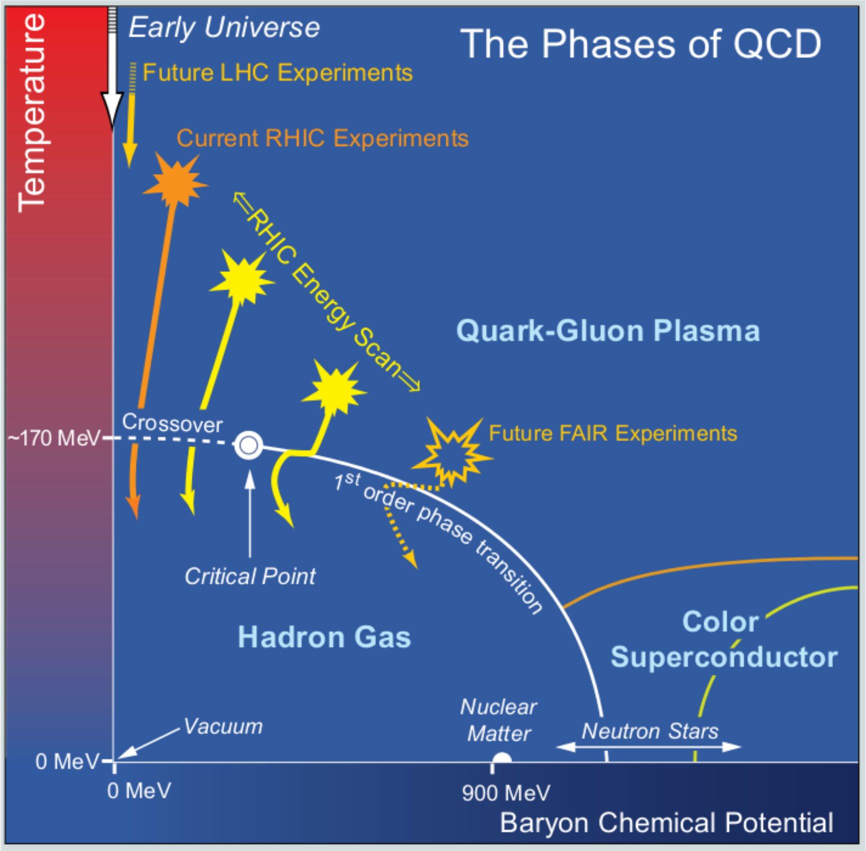

Figure 1.7: A sketch of the QCD phase diagram[19]. At the critical temperature, $T_c \sim 170$ MeV, the quarks and gluons form deconfined matter and beyond it, Quark Gluon Plasma. The 1st order line shows the prediction from QCD of the boundary between hadronic matter and quark–gluon matter ending in the critical point. The crossover transitions are shown as the dashed line at low baryon chemical potential. The diagram includes some of the capabilities of the accelerators available in heavy ion physics.

the hadronic and QGP phases coexist at some time during the transition. The '2+1' case in Figure 1.6 actually indicates such a crossover.

The nature of the phase transition (if it is there) in the data from SPS and RHIC is not entirely clear. It has been argued that the most probable form of phase transition is a crossover transition where the rise in the number of degrees of freedom and energy density are not discontinous [16]. This is certainly less dramatic than the discontinous and abrupt first order transition.

Using QCD, a phase diagram can be constructed in (ρ, T) space where ρ is the baryon density of the matter created. Figure 1.7 shows the QCD phase diagram, where ρ_n is the density of ordinary nuclear matter. The proposed path of some experiments to cross the phase boundary is indicated in the phase diagram as well as the suggested path of the Early Universe. As the collision energy increases the net-baryon content around $y = 0$ (midrapidity) drops[6] and so at LHC and RHIC the baryonic chemical potential, μ_b, vanishes. At LHC and RHIC the temperature is higher than at AGS or SPS as seen in the phase diagram. In general statistical and thermal models have been used with significant success to describe the bulk of the particle production in heavy ion collisions[4, 17, 18]. This leads to the distinction between the regime of the thermal models, the socalled 'soft' particle production which constitutes the bulk of the particles with transverse momenta $p_T < 2$ GeV and the 'hard' particle production that stems

---

[6] This means that the total baryon content is conserved (as it should be) as the baryons are transported away from midrapidity.

from direct QCD processes where the quarks and gluons interact directly to produce jets with $p_T > 2$ GeV.

1.2.2 Collision scenarios: The Landau Model

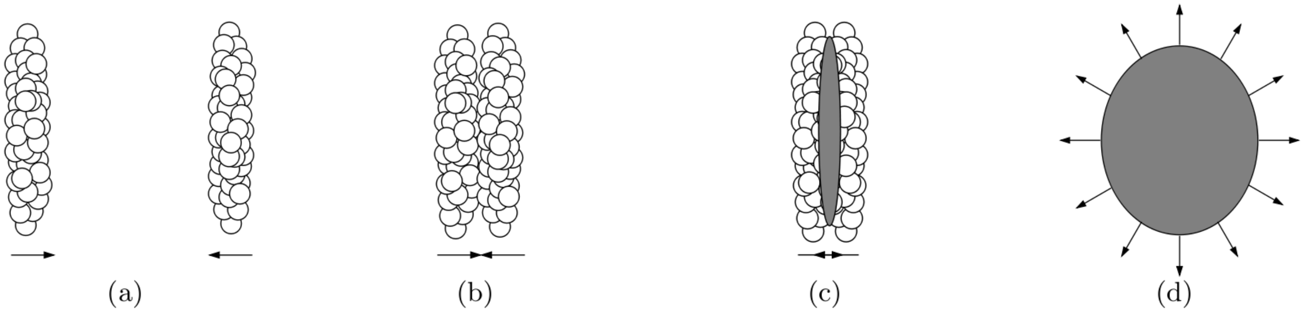

Figure 1.8: A heavy ion collision with full stopping (Landau picture).

Figure 1.8 shows a sketch of a heavy ion collision in the full stopping picture, introduced by Landau [20]. The following assumptions are made about the evolution of the collision:

1. Full Stopping. The nuclei are stopped completely as they hit each other and all their kinetic energy is deposited in the fireball.
2. Hydrodynamics. The particles have such a small mean free path that the state of the matter can be treated as an ideal fluid (ideal in the sense that it is non-viscous and non-heat-conducting).
3. Adiabatic expansion. The expansion of the fluid following the collision is adiabatic, ie. the entropy is constant.

In Landaus model the equation of state is set to the equation of state of an ideal relativistic gas: $p = \frac{\epsilon}{3}$, where p is the pressure and ϵ is the energy density[20]. As a consequence of this choice and the assumptions above the number of particles produced becomes directly proportional to the entropy, $N \propto S_0$, where S_0 is the initial entropy.

Relativistic hydrodynamics is calculated from the relations $\frac{\delta T^{ik}}{\delta x^k} = 0$ where T^{ik} is the energy-momentum tensor:

$$T^{ik} = pg^{ik} + (\epsilon + p)u^i u^k \tag{1.4}$$

Here, u^i is the four-velocity and $g^{00} = -1$, $g^{11} = g^{22} = g^{33} = 1$. For $i \neq k$, $g^{ik} = 0$. Solving the resulting equations of motion with the above assumptions, Landau demonstrated that the multiplicity distributions, $\frac{dN}{d\eta}$ must be expected to be Gaussian in η. This has been observed at RHIC energies for $\frac{dN}{dy}$ of pions and kaons by the BRAHMS experiment [21]. The similar LHC measurement is difficult due to the restricted y range with proper identification of particle type.

1.2.3 Collision scenarios: The Bjorken Picture

A different approach from the one applied by Landau has been suggested by Bjorken [22]. In this approach the nuclei are 'transparent' to each other so that in the collision, they interpenetrate losing a fraction of their energy in the process. Figure 1.9 shows a heavy ion collision with transparency. Bjorken makes the following assumptions about the evolution of heavy ion collisions:

1. Transparency. The collisions are transparent in the sense that the region around $y = 0$ is net-baryon free.

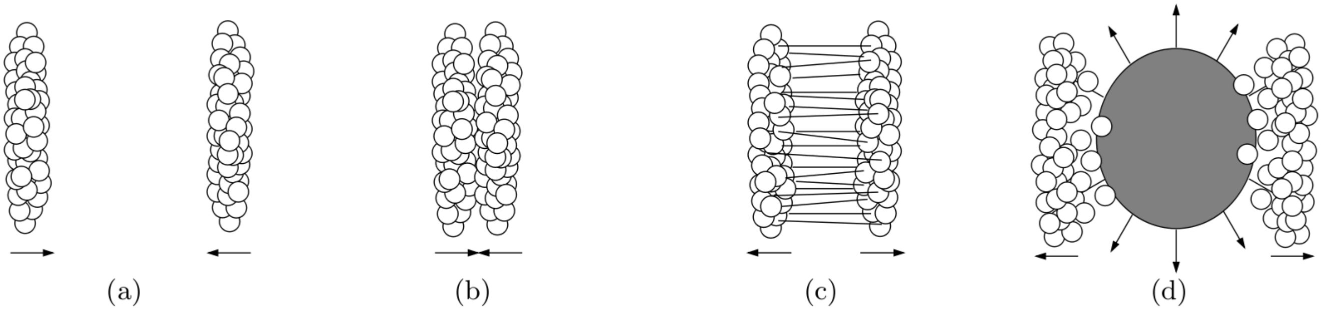

Figure 1.9: A heavy ion collision with transparency (Bjorken picture).

2. Boost invariance. The number of produced particles per unit rapidity, $\frac{dN}{dy}$, is assumed to be constant within a few units of rapidity around $y = 0$.
3. Hydrodynamics. At a time $t \sim 1$ fm/c the matter in the fireball is thermalized and relativistic hydrodynamics is applicable to describe the expanding fluid.
4. For central collisions transverse expansion can be ignored for a time comparable to the size of the nuclei divided by c. This reduces the problem of describing the collisions to a two-dimensional one in z and t.

From these assumptions two important results are derived: First of all assumption 2 implies homogeneity of the source. This means that there can be no longitudinal pressure gradient so all 'layers' of the fireball travel forward with $\beta = z/t$. The proper time of a layer is then $\tau = t/\gamma = t \cdot \sqrt{1-\beta^2} = \sqrt{t^2 - z^2}$. With these proper times the collisions can be visualized in a space-time diagram, where the $z - t$ curves are hyperbolas in space-time. Secondly the Bjorken collision scenario predicts the energy density in the fireball. Bjorken estimates $\epsilon = 1 - 10$ GeV/fm^3. This is high enough for a QGP to be created according to lQCD (Section 1.2.1).

1.2.4 Glauber Calculations in Heavy Ion Collisions

Regardless of the collision scenario considered it is possible to calculate geometrical properties of the collisions using socalled Glauber[7] Modeling. There are two variants of Glauber Modeling: The optical approach where quantum wave functions are used directly to calculate geometrical properties of heavy ion collisions and the Monte–Carlo Glauber approach where computer simulations are constructed based on Glaubers model. For both approaches two inputs are required from physics data [23]:

Nuclear Charge Densities Usually a Fermi distribution is used to describe the nuclear charge density, given by:

$$\rho(r) = \rho_0 \frac{1 + w(r/R)^2}{1 + \exp(\frac{r-R}{a})} \tag{1.5}$$

Here, ρ_0 is the density in the core of the nucleus, R is the nuclear radius, a is the 'skin depth' of the nucleus, and w measures the deviation from a spherical shape of the nucleus. w is usually very small. This holds at least for Au and Pb nuclei while U nuclei are known to be more elongated and have larger values of w.

Inelastic Nucleon–Nucleon Cross Section To simulate the individual nucleon–nucleon interactions in a heavy ion collision the corresponding experimental cross section, σ^{NN}_{Inel}, are needed for the calculation. These should be known from measurements of p+p collisions.

---

[7] After Nobel Laureate Roy J. Glauber who first considered using optical techniques for modeling of high energy subatomic reactions.

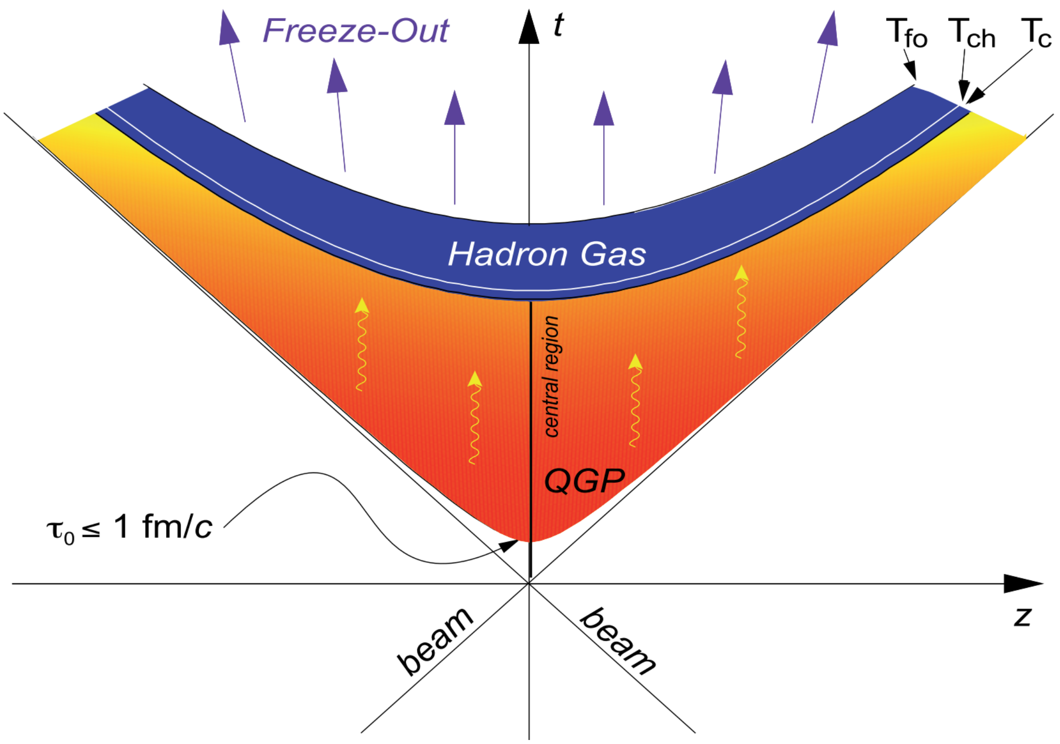

Figure 1.10: The Bjorken space-time diagram [4]. The (z, t) hyperbolas mark the boundaries between the different phases.

Figure 1.11 shows a geometrical sketch of a heavy ion collision and some fundamental quantities of the collision. The optical Glauber calculation is done in the so–called 'optical limit' where it is assumed that the nucleons of one nucleus see the other nucleus as a smooth entity. In these calculations, the number of collisions between individual nucleons in a A+B collision, N_{coll}, can be calculated as a function of the impact parameter (b):

$$N_{coll}(b) = \sum_{n=1}^{AB} nP(n,b) = AB\hat{T}_{AB}(b)\sigma_{inel}^{NN} \tag{1.6}$$

Here $\hat{T}_{AB}(b)$ is the thickness function of the overlap of A and B, satisfying: $\hat{T}_{AB}(\boldsymbol{b}) = \int \hat{T}_A(\boldsymbol{s})\hat{T}_B(\boldsymbol{s}-\boldsymbol{b})d^2s$. The *number of participants*, N_{part}, can also be determined. N_{part} is to be understood as the number of nucleons in the overlap region of the nuclei, ie. the nucleons that actually 'take part' in the collision. It is determined from optical Glauber calculations as [23]:

$$N_{part}(\boldsymbol{b}) = A\int \hat{T}_A(\boldsymbol{s})\left\{1-[1-\hat{T}_B(\boldsymbol{s}-\boldsymbol{b})\sigma_{inel}^{NN}]^B\right\}d^2s + B\int \hat{T}_B(\boldsymbol{s}-\boldsymbol{b})\left\{1-[1-\hat{T}_A(\boldsymbol{s})\sigma_{inel}^{NN}]^A\right\}d^2s \tag{1.7}$$

N_{part} and N_{coll} are important quantities for analysis of heavy ion collisions since they relate properties of the nuclei in collision to the centrality given by b. To get a more complete picture of this relation Monte–Carlo Glauber calculations can be performed. The concept is shown in Figure 1.12: Two groups of particles (nuclei) are collided in the simulation where each process concerning every nucleon is drawn randomly from the relevant probability distributions. In this way the collisions are evolved and properties like N_{part} and N_{coll} can be determined. Furthermore the approach allows calculation of the charged particle multiplicity and its relation to the centrality of the collisions. In this way the experimental centrality classes are related to the theoretical b.

Glauber calculations are incorporated into many modern event generators, including HIJING, VENUS, and RQMD [23]. In this work the main use of the Glauber model is to provide N_{part} and N_{coll} to study

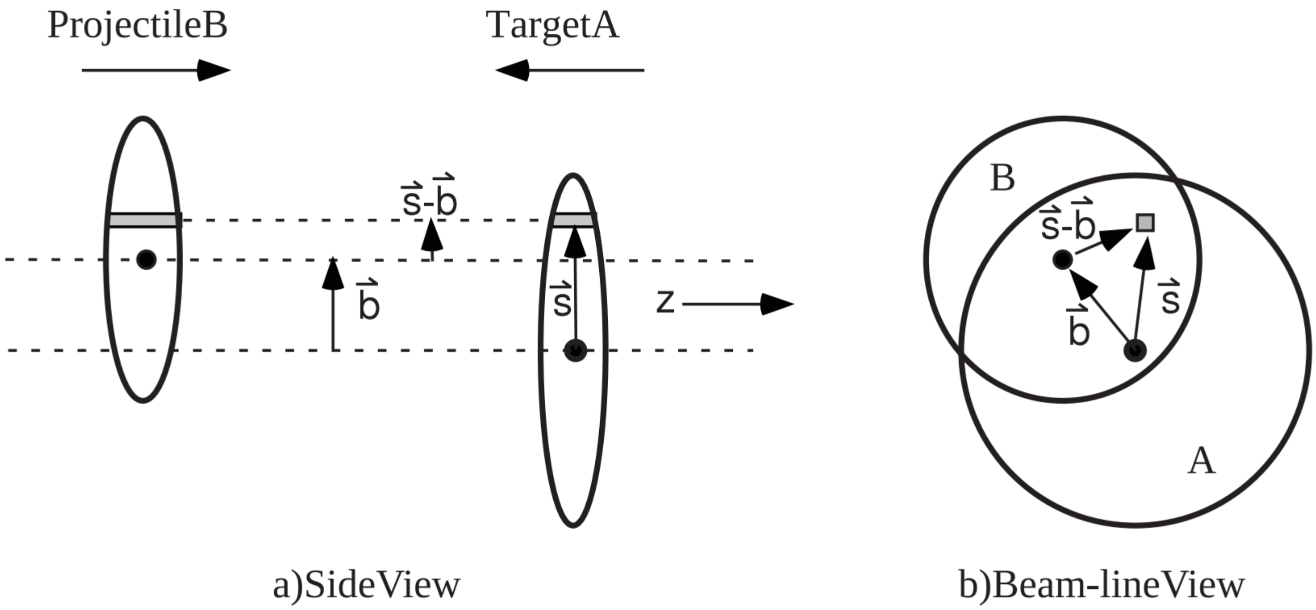

Figure 1.11: Sketch of heavy ion collision from the side (a) and along the beam direction (b) [23]. ***b*** is the impact parameter vector and ***s*** is the vector in the event plane to a slice of one of the nuclei.

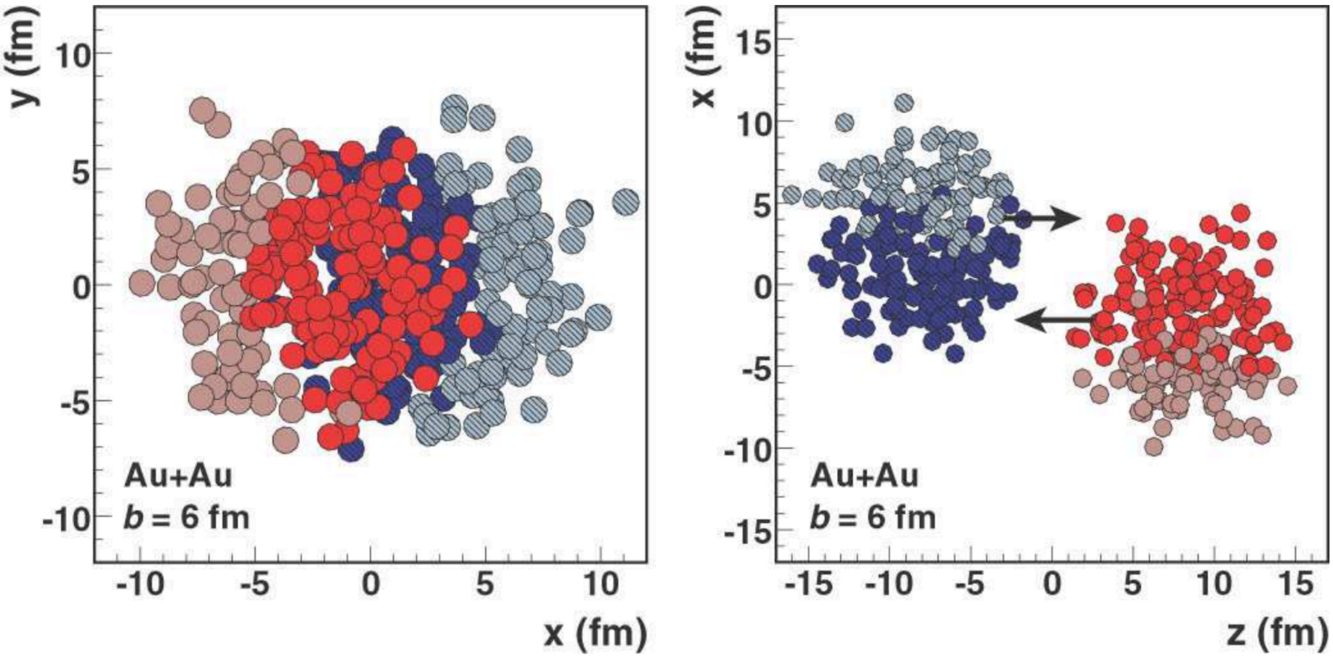

Figure 1.12: Schematic view of the Monte–Carlo Glauber concept of colliding groups of nucleons [23]. The red and blue nucleons are interacting as they are in the overlap region. The rest of the nucleons are spectators.

scaling in heavy ion collisions (see Chapter 7).

1.2.5 Stopping in Heavy Ion Collisions

The concept of stopping can be tested directly in heavy ion collisions through measurements of the net-baryon number. While a substantial part of the (anti-)baryons will be neutrons most experiments only detect the (anti-)protons since they carry electrical charge. Net-protons have been measured in experiments at AGS (E802, E877, and E917), SPS (NA49) and RHIC (BRAHMS) at various energies ranging from $\sqrt{s_{NN}} \sim 5$ GeV to 200 GeV. The combined net-proton measurements are shown in Figure 1.13. From the Figure it is evident that the net-proton yields depend on energy and that the midrapidity region at RHIC has very few net-protons compared to the AGS and SPS data. Note that the number of net-baryons is roughly twice the number of net-protons[1, 28]. This points to more Bjorken like conditions at RHIC whereas the AGS seems to agree with the Landau picture since the midrapidity region is very far from net-baryon free.

To get a measure of the stopping a quantity known as the rapidity loss is introduced. It is defined as:

$$\delta y = y_b - \frac{2}{N_{part}} \int_0^{y_b} y \frac{dN_{B-\bar{B}}}{dy} dy \tag{1.8}$$

Here N_{part} is the number of participants as described in section 1.2.4, $\frac{dN_{B-\bar{B}}}{dy}$ is the net–baryon distribution, and y_b is the beam rapidity. The rapidity loss can thus be calculated from the net-baryon distributions and this has been done for AGS, SPS and RHIC energies [1]. The results are shown in the right panel of Figure 1.13. For energies below the SPS energy ($\sqrt{s_{NN}} = 17$ GeV) the rapidity losses follow a linear trend (described in [29]) but for the RHIC energies it appears that the rapidity loss rises slower with energy. This could be consistent with a change from a Landau like collision evolution to a more Bjorken like scenario. It is worth noticing that the midrapidity net-proton yields at $\sqrt{s_{NN}} = 62.4$ GeV and $\sqrt{s_{NN}} = 200$ GeV are consistent with each other despite the jump in energy. The LHC results will reveal whether this holds at even higher energies or if the midrapidity region will be truly net-baryon free.

1.2.6 Hydrodynamics

Both the collision scenarios described involve hydrodynamical expansion of the medium created in heavy ion collisions. It is the common conjecture of heavy ion physics that the system undergoes such a phase after thermalization - at RHIC the medium created has been described as a ‘perfect liquid’ since it is found to have near vanishing viscosity [30]. The concept of hydrodynamics was presented in (1.4). Combined with the statistical picture of the created matter described in 1.2.1 and in particular the equation of state hydrodynamics governs the expansion of the thermalized QGP until freeze-out. At Quark Matter 2011 hydrodynamics was shown to be able to explain many of the new results from LHC in particular the results for transverse flow [31]. See sections 1.3.3 and 1.3.4.

1.3 QGP signatures

In this section we will review some of the possible signatures of a QGP that has been proposed or observed in experiments.

1.3.1 High p_T Suppression at RHIC

If the medium created in a heavy ion collision is truly strongly interacting it should affect jets propagating through it if these jets are able to interact strongly. Due to various low p_T collective effects such as color screening or Cronin enhancement this effect should be most pronounced at high p_T. To quantify this

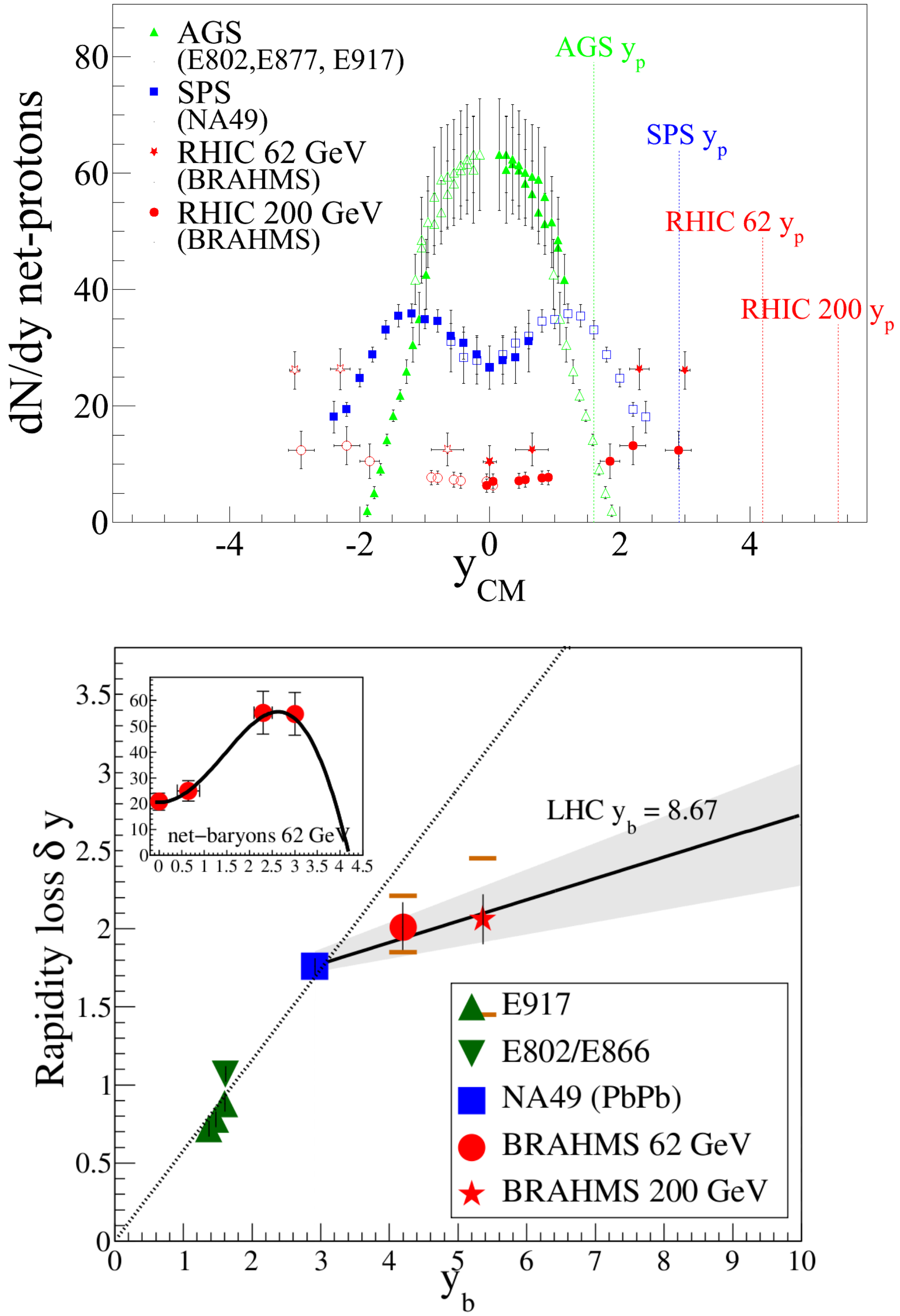

Figure 1.13: Top: $\frac{dN}{dy}$ of net-protons from AGS [24, 25, 26], SPS [27] and RHIC[1, 28]. The hollow points are reflected around midrapidity. Bottom: The rapidity losses from AGS, SPS and RHIC. There is clearly a change of trend with energies above the SPS energy.

effect the heavy ion yields are compared to the scaled yields of p+p collisions at the same energy. This is expressed through the nuclear modification factor, R_{AA} defined as:

$$R_{AA} \equiv \frac{2 \cdot d^2N/dp_T dy_{AA}}{N_{coll} \cdot d^2N/dp_T dy_{pp}} \tag{1.9}$$

R_{AA} is the transverse particle production of Au+Au collisions relative to p+p collisions scaled by the number of binary collisions, N_{coll} obtained using Monte Carlo Glauber simulations as described in section 1.2.4. If the physics of the underlying particle production in p+p collisions is the same as in heavy ion collisions, R_{AA} should approach unity at least for $p_T > 2$ GeV/c.

Figure 1.14 shows a measurement of the nuclear modification factor, R_{AA}, of direct photons[8], neutral pions and η particles in the PHENIX experiment at RHIC. It is seen that the particles composed of quarks and gluons (which interact strongly) are suppressed compared to the direct photons that do not interact strongly. This can be interpreted as an effect of the medium created in the collision. Thus, the medium is interacting strongly which supports that an sQGP state is formed. The suppression of hadrons in Au+Au collisions at RHIC has also been studied with the STAR experiment. The right panel of Figure 1.14 shows the yields on the away side of an observed jet[9]. There are very clear differences between the observations in Au+Au collisions p+p and d+Au collisions. This supports that the traversing hadrons are subject to effects of a strongly interacting medium.

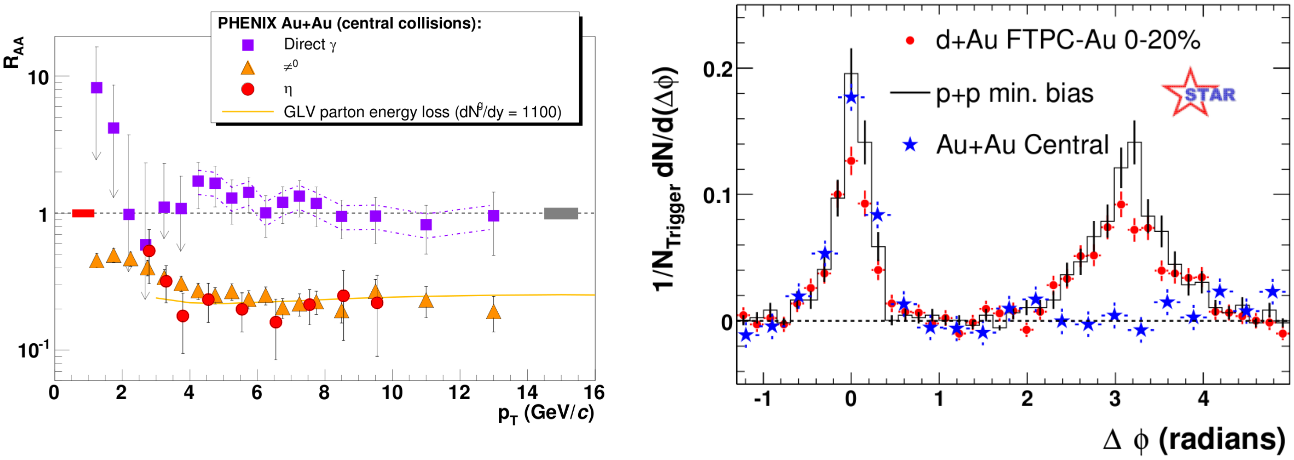

Figure 1.14: Left: R_{AA} of high p_T π^0 and η particles and direct photons [32]. The suppression of the strongly interacting particles compared to the photons is evident. Right: STAR measurement of the hadron yield at $\phi = \pi$ when triggering on a jet at $\phi = 0$ [30]. The effect of the medium is evident.

1.3.2 High p_T Suppression at LHC

Following the impact of the high p_T suppression results from RHIC measurements of R_{AA} are a top priority for the LHC experiments. At Quark Matter 2011 ALICE and CMS showed results on R_{AA} for charged particles for transverse momenta up to $p_T \sim 100$ GeV. These results are shown in Figure 1.15. The CMS results include R_{AA} of direct photons and similar to PHENIX there is no sign of suppression at any momenta while the charged particles exhibit suppression, however with R_{AA} rising as function of p_T. This suppression of the charged particles could point to a strongly interacting medium also being produced at LHC. The rise of R_{AA} with p_T most likely shows the distinction between the 'soft' region where particle production is dominated by thermal production of particles in the fireball and the 'hard'

---

[8] These are photons that come from the Interaction Point as opposed to photons created in various post-collision processes

[9] Technically speaking a cluster of high momentum particles.

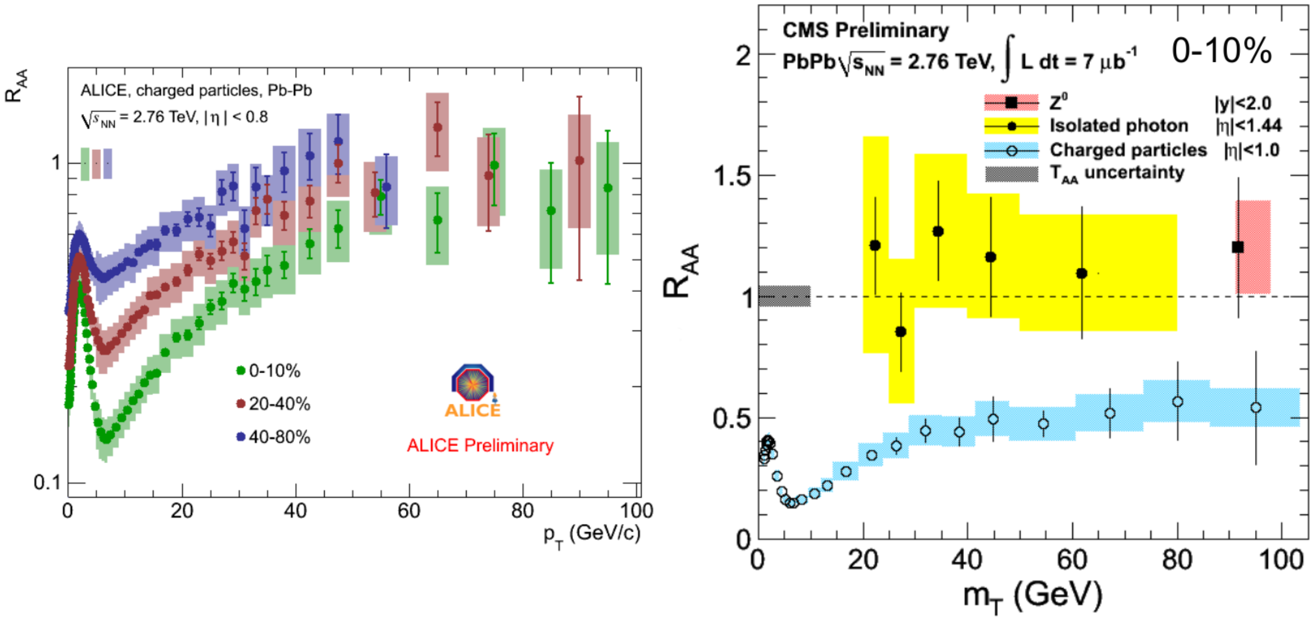

Figure 1.15: Left: R_{AA} of charged particles versus p_T from ALICE [33]. It is seen that at very high momenta the suppression seems to get less pronounced. Right: R_{AA} of charged particles, photons and Z^0 versus p_T from CMS [34]. Similar to PHENIX the CMS photon measurement shows no suppression at any momenta.

region where the production is due to high momentum qq interactions (which lead to formation of jets). It should be noted that the CMS and ALICE results differ for $p_T > 50$ GeV.

Studies of high p_T of the near- and awayside jets similar to that in Figure 1.14 are also performed at LHC. See Figure 1.20. Concerning studies of the near- and awayside jets one of the surprises at Quark Matter 2011 was that the jets are very similar even if they have different momenta. At RHIC the medium was thought to broaden the awayside jet but this was not found to be the case at LHC [35]. Instead the energy lost to in the medium by the awayside jet seems to be radiated in all directions.

1.3.3 Transverse Flow at RHIC

Compared to p+p collisions, heavy ion collisions reveal a large degree of collective dynamics that is not present in p+p collisions. One of these kinds of dynamics is anisotropic transverse flow which corresponds to a collective motion of the particles and must be expected especially for semi–peripheral collisions [36]. In the following only anisotropic transverse flow is considered, and for that a model independent method that can quantize the flow is needed. Several methods have been proposed but the one presented here is the one proposed in [37]. The idea is that the flow will reveal itself as an asymmetry in the azimuthal distributions of particles. This distribution, $r(\phi)$, can be written as a Fourier expansion [37]:

$$r(\phi) = \frac{a_0}{2\pi} + \frac{1}{\pi}\sum_{n=1}^{\infty}(x_n\cos(n\phi) + y_n\sin(n\phi)) \tag{1.10}$$

Here, a_0 is a constant ‘radius’ of the distribution and x_n and y_n are the components of the expansion corresponding to the X and Y axes, respectively. Figure 1.16 shows the distribution of particles in the XY plane, modified by anisotropic flow.

To quantize the flow, the components of the Fourier transformation [36] of the distribution of particles

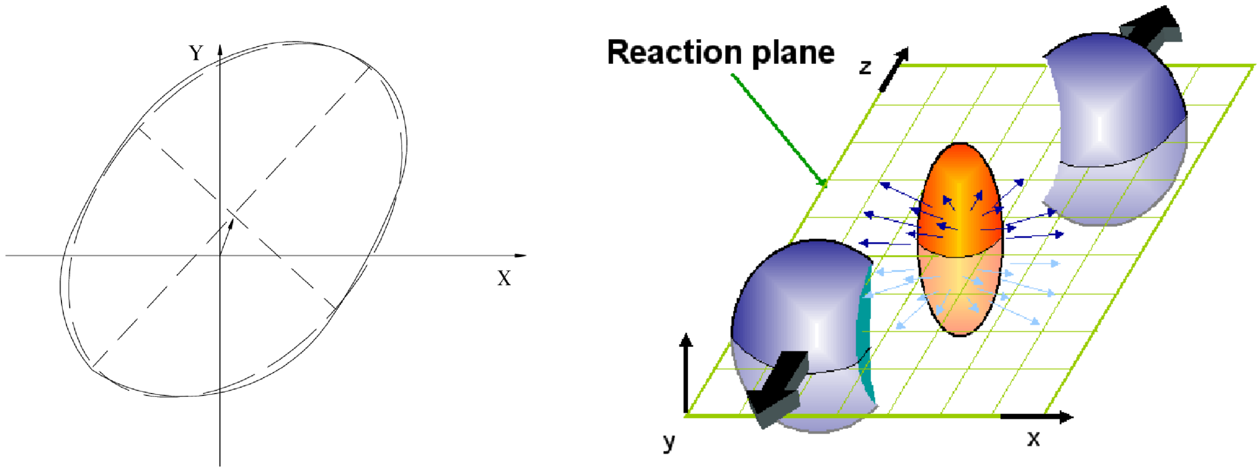

Figure 1.16: Left: The transverse distributions of particles [37]. The arrow indicates the shift of the distribution away from $(X, Y) = (0, 0)$ caused by direct flow. The dashed curve shows the modification of the distribution caused by elliptic flow. Right: Illustration of the Reaction Plane [38]. The spectator particles are seen as blue spheres, the fireball is the orange ellipsis with the flow marked as arrows. The reaction plane is the green grid with the impact parameter in the x direction.

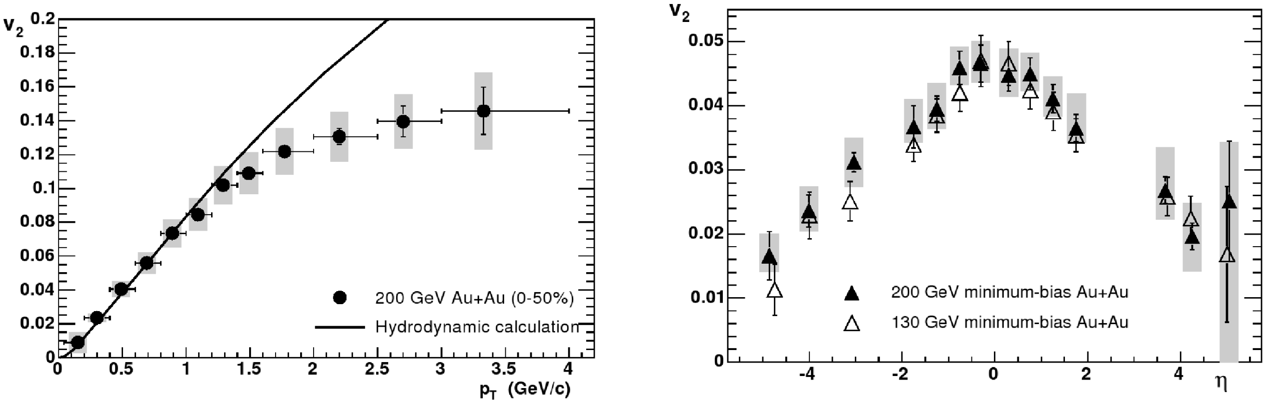

Figure 1.17: Left: The elliptic flow, v_2, as a function of p_T from PHOBOS [39]. Right: v_2 as a function of pseudorapidity.

are used . The transformation is:

$$E\frac{d^3N}{d^3p} = \frac{1}{2\pi}\frac{d^2N}{p_T dp_T dy}\left(1 + \sum_{n=1}^{\infty} 2v_n \cos(n(\phi - \Psi_r))\right) \tag{1.11}$$

Here, Ψ_r denotes the *reaction plane* angle, defined as the angle between the xz plane and the plane spanned by the impact parameter *vector* and the beam axis (z). For practical purposes this plane must be estimated using the azimuthal distributions. In this context the *event plane* is defined as the experimentally determined approximation to the reaction plane. Figure 1.16 shows an illustration of the reaction plane.

In (1.11) the coefficients v_n are the coefficients for the different kinds of flow also known as the harmonics of the flow. In particular v_1 is the *radial* (or direct) flow, v_2 is the *elliptic* flow. The significance of the higher order harmonics is discussed in section 1.3.4. They are determined by $v_n = \langle\cos(n(\phi - \Psi_r))\rangle$ where the average is taken over all particles in all events.

Figure 1.17 shows results on v_2 from PHOBOS at RHIC. The results clearly show that there is indeed

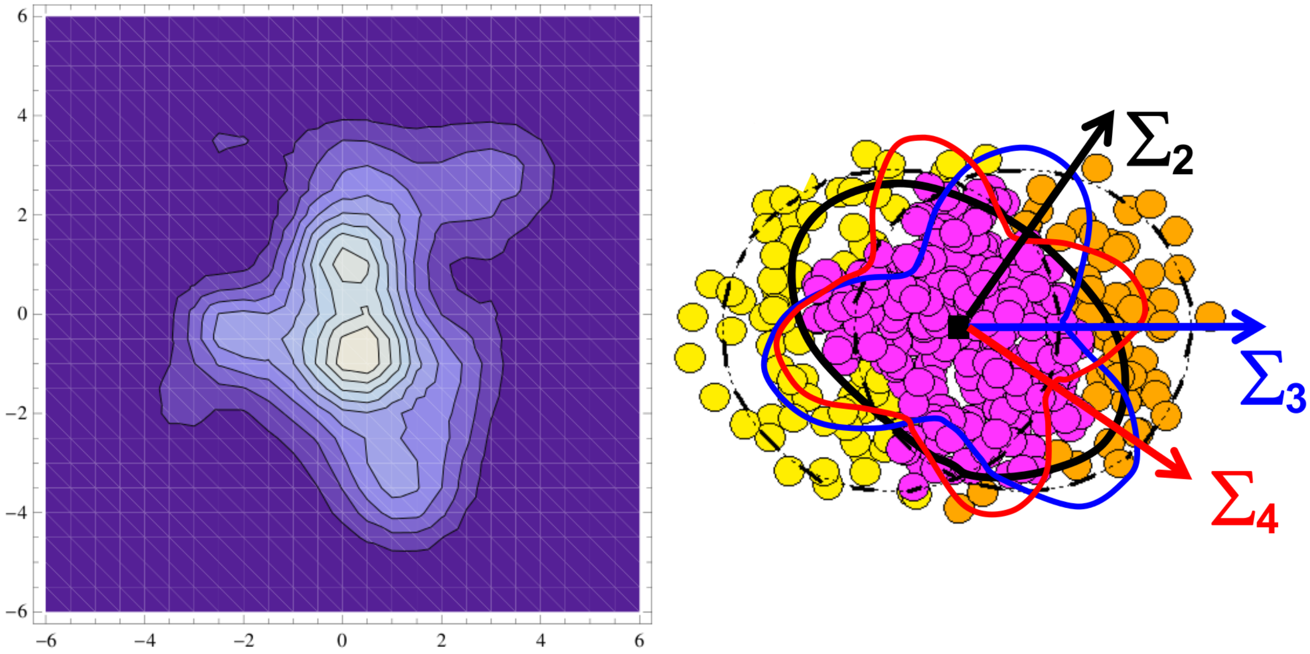

Figure 1.18: Left: The overlap region as seen from lQCD [40]. This is clearly a more complicated picture than that of an almond shaped overlap. Right: A more artistic impression showing the second, third and fourth component of the flow as well as Ψ_r more directly [41].

an elliptic flow component. This means that the fireball undergoes strong interactions after the collision since the elliptic flow represents a transformation from a spatial asymmetry to an asymmetry in the momenta of the particles. This transformation implies underlying dynamics from the strong interaction [9]. This tells us that if a QGP was formed at RHIC it will be strongly interacting, a 'sQGP' as discussed in section 1.1.3.

1.3.4 Higher orders harmonics of transverse Flow

The above discussion about direct and elliptic flow assumes the almond shaped overlap region shown in Figure 1.16. However, recent developments in lQCD suggests that this picture may not hold in reality. At the Quark Matter 2011 conference it was suggested that this should increase interest in the higher order components of the transverse flow, ie. the v_n in (1.11) for $n > 2$. Figure 1.18 shows the overlap region as it looks in lQCD calculations. It is clear from the figure that the overlap region is more complicated than the simple almond shape. This gives rise to higher orders of the flow since the initial spatial asymmetry now has components in all directions. This is also suggested in the right panel of Figure 1.18. At RHIC and LHC these components have been measured and were also presented at Quark Matter 2011. Results from and ALICE on v_n are shown in Figure 1.19 It is seen that while the elliptic flow, v_2, is still in general larger than the higher order harmonics, they are by no means negligible. This means they must be taken into account when describing the bulk properties of the collisions and they give additional constraints on theories and models.

An example of how this affects the interpretation of data can be taken from Quark Matter 2011. For central collisions a structure is observed in the away side jet as shown in Figure 1.20. The interpretation of this 'double hump' structure was for a long time that it was produced by the so–called Mach cone which was created by shock waves traversing the hot and dense medium. However, it seems that the presence of the higher order harmonics can explain the 'double hump' structure. Figure 1.20 includes fits to the data based on the observed components of the Fourier expansion of the particle spectra (the v_n in (1.11)). These fits reproduce very accurately the data which means the 'double hump' can be interpreted

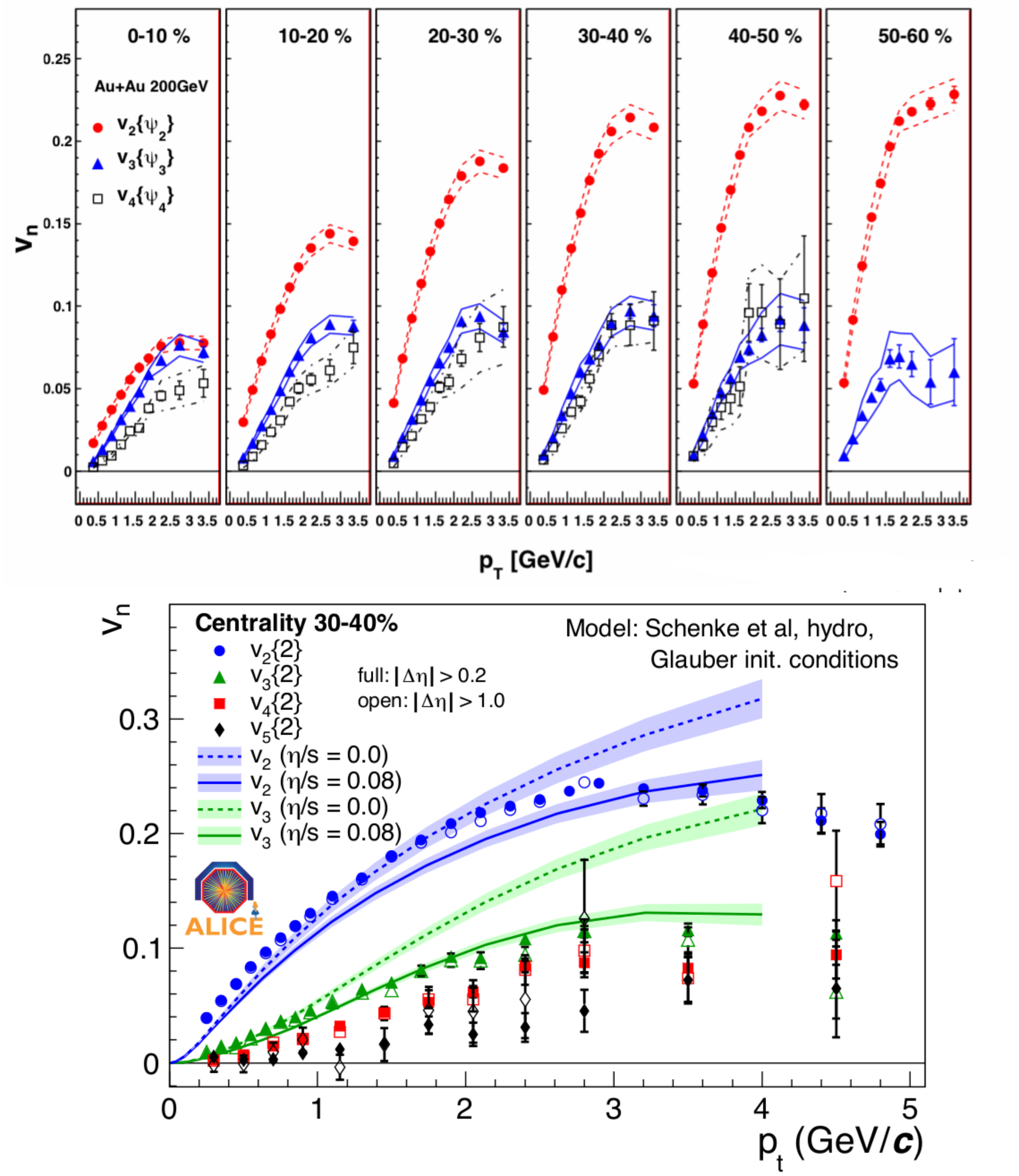

Figure 1.19: Higher order harmonics from Quark Matter 2011. Top: v_2, v_3, and v_4 as functions of p_T for 6 centrality classes in $\sqrt{s_{NN}} = 200$ GeV Au+Au collisions as measured by PHENIX at RHIC [42]. Bottom: The v_2, v_3, v_4, and v_5 as a function of p_T for $30-40\%$ centrality in $\sqrt{s_{NN}} = 2.76$ TeV Pb+Pb collisions measured by ALICE at LHC [43].

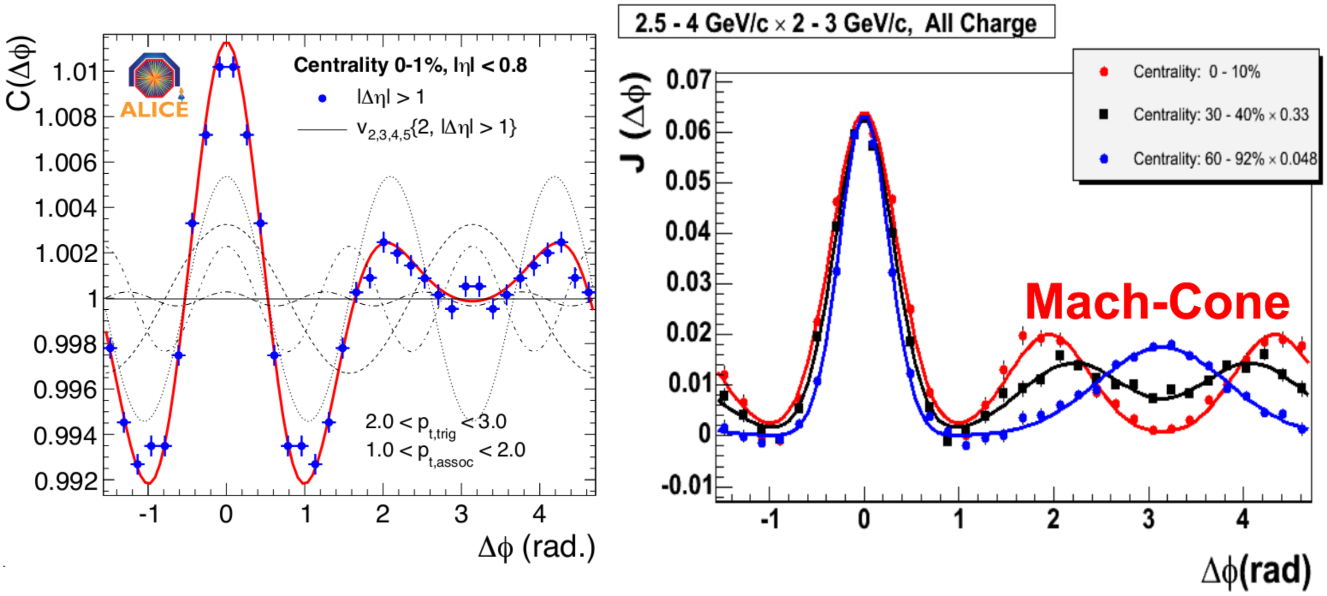

Figure 1.20: Left: The near and away side jets as measured by ALICE in $0-1\%$ central $\sqrt{s_{NN}} = 2.76$ TeV Pb+Pb collisions [43]. The ‘double’ hump structure is clearly visible but it is also evident that the fit to the higher order harmonics can reproduce the structure in the data. Right: The same plot from PHENIX for Au+Au collisions at $\sqrt{s_{NN}} = 200$ GeV where the location of the now explained ‘Mach Cone’ is also shown [42].

simply as a result of the modulation of the particle spectra by the higher order harmonics. This was one of the major findings of Quark Matter 2011.

1.4 p+p collisions as Baseline for Heavy Ion Physics

This work also contains p+p results. While interesting in their own right p+p collisions provide the perfect reference or baseline for heavy ion collisions. An example of this use of p+p is for example seen in (1.9) and the corresponding R_{AA} results from RHIC and LHC. Some features of p+p collisions collisions are:

- **Simpler System** A p+p collision has fewer components than a collision of two heavy ions. While the most central heavy ion collisions can involve up to ~ 1000 separate nucleon+nucleon collisions a p+p collision only ever involve 1.

- **No Collective Effects** p+p collisions have never been observed to exhibit the collective effects such as anisotropic transverse flow observed in heavy ion collisions. This means that properly scaled-up p+p collisions can serve as a model A+A system without collective effects. It has been speculated that collective effects (most prominently flow) would begin to appear in high multiplicity p+p collisions at LHC but this has yet to be observed. If one considers the energy density to be the crucial parameter this certainly could be a possibility if enough energy was carried by the protons.

- **Jet Studies** In heavy ion collisions the observed high-p_T suppression is often attributed to the interactions of the emitted jets with the hot and dense medium produced. Studies of p+p allow for detailed studies of jets in a more fundamental environment since the mechanism of jet production is believed to be similar namely hard q+q reactions.

While the system may be simpler studying p+p collisions is not necessarily simpler than measuring properties of heavy ion collisions. There are several reasons for this. Firstly all accelerator effects that

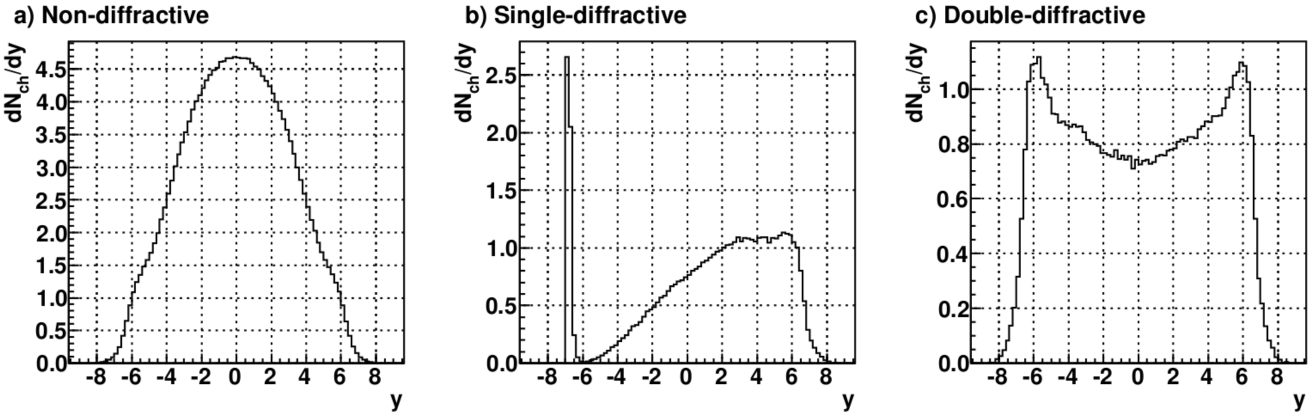

Figure 1.21: A simulated view dN_{ch}/dy per event of ND, SD, and DD p+p collisions generated with PYTHIA[46].

pollute the observations will affect the results in p+p collisions the most because the particle production is much smaller in p+p collisions. This makes it harder to distinguish signal and noise in p+p collisions compared to heavy ion collisions where the higher multiplicities will make the signal ‘cleaner’. Secondly there can be issues with the triggering of p+p collisions where again the low multiplicity makes it harder to detect the events. It requires accurate simulations to study and correct for the lower trigger efficiency. These points will be discussed further in Chapter 6.

1.4.1 Diffraction in p+p collisions

For the p+p collision we will consider two classes of events: Inelastic (INEL) and Non-Single Diffractive (NSD). In this section we will discuss their properties.

When two protons collide the collision can be either elastic (kinetic energy conservation) or inelastic (no kinetic energy conservation). In other words, the inelastic collisions are of little interest in nuclear and particle physics. Furthermore the elastic collisions are very hard to measure experimentally in any case. Hence, only INEL collisions will be considered in this work. For a definition of diffraction we can use [44, 45]:

“A reaction in which no quantum numbers are exchanged between the colliding particles is, at high energies, a diffractive reaction.“

Theoretically speaking diffraction is an interaction of the so–called pomeron, an intermediate QCD particle, between the protons.

If only one of the protons behave diffractively we call the collision single diffractive (SD) and if both protons exhibit diffractive behaviour the collision is called double diffractive (DD). As the name implies NSD collisions are then collisions which are INEL and **not** SD. Collisions that are INEL but neither SD or DD are labelled non diffractive (ND). The classes of collisions have quite different properties. Figure 1.21 shows a simulated view of the dN_{ch}/dy for ND, SD and DD collisions. From the distributions in the figure it is clear that the NSD $dN_{ch}/d\eta$ per event must be expected to be higher than that of INEL collisions because the INEL collisions include the SD collisions which have low multiplicity.

1.5 Quark Matter 2011: The outlook of Heavy Ion Physics

Many results from the Quark Matter 2011 conference have been presented here. The conference showed the massive progress in the field of heavy ion physics since the beginning of the LHC running. On the

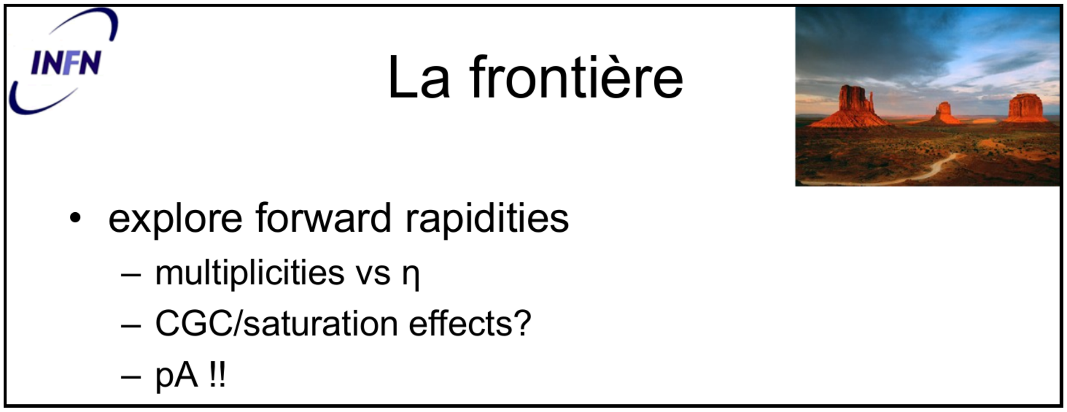

La frontière

- explore forward rapidities
  - multiplicities vs η
  - CGC/saturation effects?
  - pA !!

Figure 1.22: The message from Quark Matter 2011 [47].

final day of the conference a plenary summary talk was given by F. Antinori on the topic of “The High Energy Frontier of AA” [47]. Figure 1.22 shows the frontier of bulk production in heavy ion collisions as shown at Quark Matter 2011. It is seen that the key topics identified are:

Multiplicities versus η This is the main topic of this work. Results on $\frac{1}{N}\frac{dN_{\mathrm{ch}}}{d\eta}$ in a wide pseudorapidity coverage will be presented in Chapter 7.

Color Glass Condensate and Saturation Effects Results on $\frac{1}{N}\frac{dN_{\mathrm{ch}}}{d\eta}$ can shed more light on the understanding of CGC and saturation. Initial observations are made in Chapter 7.

p+Pb results Hopefully the LHC will deliver p+Pb data during the heavy ion run of 2011.

So for the exploration of forward rapidities? That is where we are going.

Chapter 2

Multiplicity and $dN_{ch}/d\eta$

This Chapter introduces the concept of the pseudorapidity density of charged particles, $dN_{ch}/d\eta$, in heavy ion physics as well as previous measurements. Model comparisons and various experimentally derived scaling properties are also included.

2.1 $dN_{ch}/d\eta$: A fundamental measurement

The multiplicity and in particular $dN_{ch}/d\eta$, the number of charged particles per unit pseudorapidity, plays an important role as a 'day-one' observable in heavy ion physics. Measurements of it are often among the first publications of a new experiment and it serves to immidiately fix a global property of the matter created in the collisions. This was also the case at LHC where ALICE published $dN_{ch}/d\eta_{|\eta|<0.5}$ for the most central Pb+Pb collisions at $\sqrt{s_{NN}} = 2.76$ TeV within a month of the time of the data were taken. The results are summarized in Figure 2.1. From a theoretical point of view, the problem with the charged particle multiplicity is that it is not possible to calculate from, say, a QCD Lagrangian. Estimates must be made using models, previous experiments or both. The multiplicity enters the calculations of many other quantities in heavy ion physics e.g., the energy density or the entropy.

There are some important differences between the theoretical notion of 'multiplicity' and the experimentally determined charged particle multiplicity. Most theoretical predictions or estimates will deal with the total multiplicity (including charged or neutral mesons, baryons or leptons) whereas the charged particles is the easiest measurement to perform in high energy experiments e.g., ALICE. The total multiplicity has been found to be approximately 1.5 times the charged particle multiplicity at high energies [49]. Theories will usually deal with dN/dy and not $dN/d\eta$ which will give differences, especially at midrapidity. In addition to this, theories may give the distributions at other times than at freeze-out, e.g., at the formation or equilibration time. This can be however be helped with the aid of models for decays and rescattering.

2.1.1 Energy Density

To give an example of a quantity that can be estimated from the $\frac{1}{N}\frac{dN_{\mathrm{ch}}}{d\eta}$ we will consider the energy density of the fireball. As the particle production in the fireball takes place primarily at midrapidity ($|\eta| < 1$) the energy density here is related to the charged particle multiplicity. As an example we will consider a calculation from PHOBOS where the $dN_{ch}/d\eta_{|\eta|<1}$ is used to estimate the energy density at midrapidity in Au+Au collisions at $\sqrt{s_{NN}} = 200$ GeV.

The following relation is used to calculate the total energy available at midrapidity [50]:

$$E_{tot} = 2E_{part}\frac{dN_{ch}}{d\eta}_{|\eta|<1} f_{neutral} f_{4\pi} \tag{2.1}$$

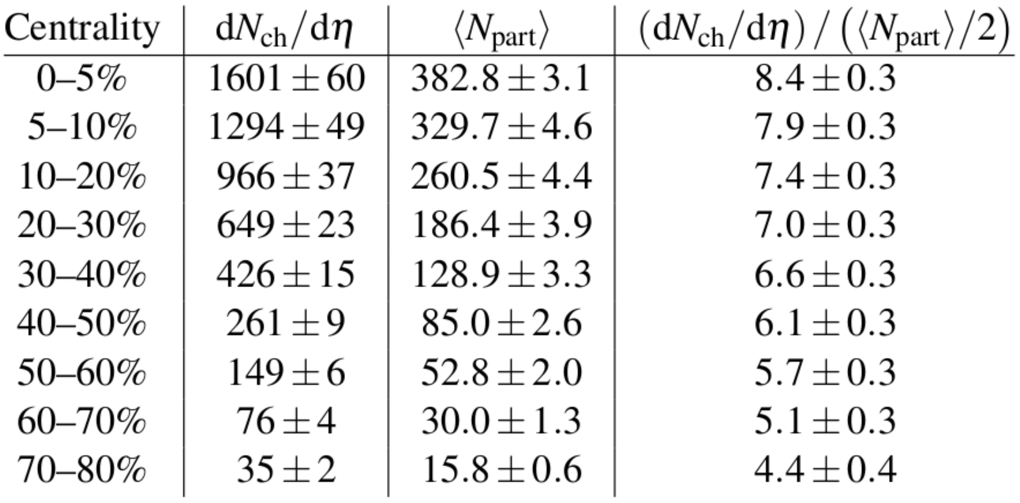

Centrality	$\mathrm{d}N_{\mathrm{ch}}/\mathrm{d}\eta$	$\langle N_{\mathrm{part}}\rangle$	$(\mathrm{d}N_{\mathrm{ch}}/\mathrm{d}\eta)\,/\,(\langle N_{\mathrm{part}}\rangle/2)$
0–5%	1601 ± 60	382.8 ± 3.1	8.4 ± 0.3
5–10%	1294 ± 49	329.7 ± 4.6	7.9 ± 0.3
10–20%	966 ± 37	260.5 ± 4.4	7.4 ± 0.3
20–30%	649 ± 23	186.4 ± 3.9	7.0 ± 0.3
30–40%	426 ± 15	128.9 ± 3.3	6.6 ± 0.3
40–50%	261 ± 9	85.0 ± 2.6	6.1 ± 0.3
50–60%	149 ± 6	52.8 ± 2.0	5.7 ± 0.3
60–70%	76 ± 4	30.0 ± 1.3	5.1 ± 0.3
70–80%	35 ± 2	15.8 ± 0.6	4.4 ± 0.4

Table 2.1: The $dN_{ch}/d\eta_{|\eta|<0.5}$ measured by ALICE in 9 centrality classes[48]. The table also includes the numbers of participant nucleons, N_{part}, calculated from the Glauber model (see section 1.2.4). Finally it includes $dN_{ch}/d\eta_{|\eta|<0.5}$ scaled by N_{part}.

Here E_{part} is the average energy carried by a charged particle, $f_{neutral} = 1.6$ is a factor to correct for neutral particles that are produced but not detected. $f_{4\pi}$ is a factor to correct for particles with similar momentum as the particles at midrapidity but not travelling in the transverse direction. The value is calculated from the solid angle coverage of $|\eta| < 1$ and is to be $f_{4\pi} = 1.3$[50]. For the PHOBOS measurements from RHIC the total available energy in 0-6 % central Au+Au collisions at $\sqrt{s_{NN}} = 200$ GeV is approximately 1600 GeV. To convert the total energy to an energy density an estimate for the volume of the fireball is required. Bjorken [22] uses a transverse size equal to that of the colliding nuclei and a longitudinal size of ~ 2 fm at $\tau \sim 1$ fm/c (the formation time). Using (2.1) and the total energy from PHOBOS the energy density becomes $\epsilon \approx 5$ GeV/fm^3. While higher that Bjorkens estimates of the energy density in the QGP it is in itself no proof that a QGP was actually created.

A calculation of E_{tot} at LHC will be attempted in Chapter 7 using $\frac{1}{N}\frac{dN_{\mathrm{ch}}}{d\eta}$.

2.2 Previous Measurements

In this section some of the results of experiments in heavy ion on $dN_{ch}/d\eta$ are presented to set the scene for the results presented in this work.

2.2.1 Heavy Ion Collisions

$dN_{ch}/d\eta$ has been measured in a huge variety of experiments and at many different energies so the results presented here are by no means complete but serve as a basis of comparison to the results presented in this work. Figure 2.1 shows $dN_{ch}/d\eta$ results from PHOBOS at three different energies namely $\sqrt{s_{NN}} = 19.6$ GeV, $\sqrt{s_{NN}} = 130$ GeV, and $\sqrt{s_{NN}} = 200$ GeV. The data are shown for 5 different centralities for $\sqrt{s_{NN}} = 19.6$ GeV and 6 centralities for the $\sqrt{s_{NN}} = 130$ GeV and $\sqrt{s_{NN}} = 200$ GeV data. PHOBOS was the detector at RHIC with the widest pseudorapidity coverage and this is clearly reflected in the data that shows $dN_{ch}/d\eta$ over more than 10 units of pseudorapidity.

From the Figure it is clear that distributions have similar properties in shape. While the midrapidity 'plateau' gets wider with energy the tails of the distributions seem to drop in the same manner. This point is expanded in section 2.2.3.

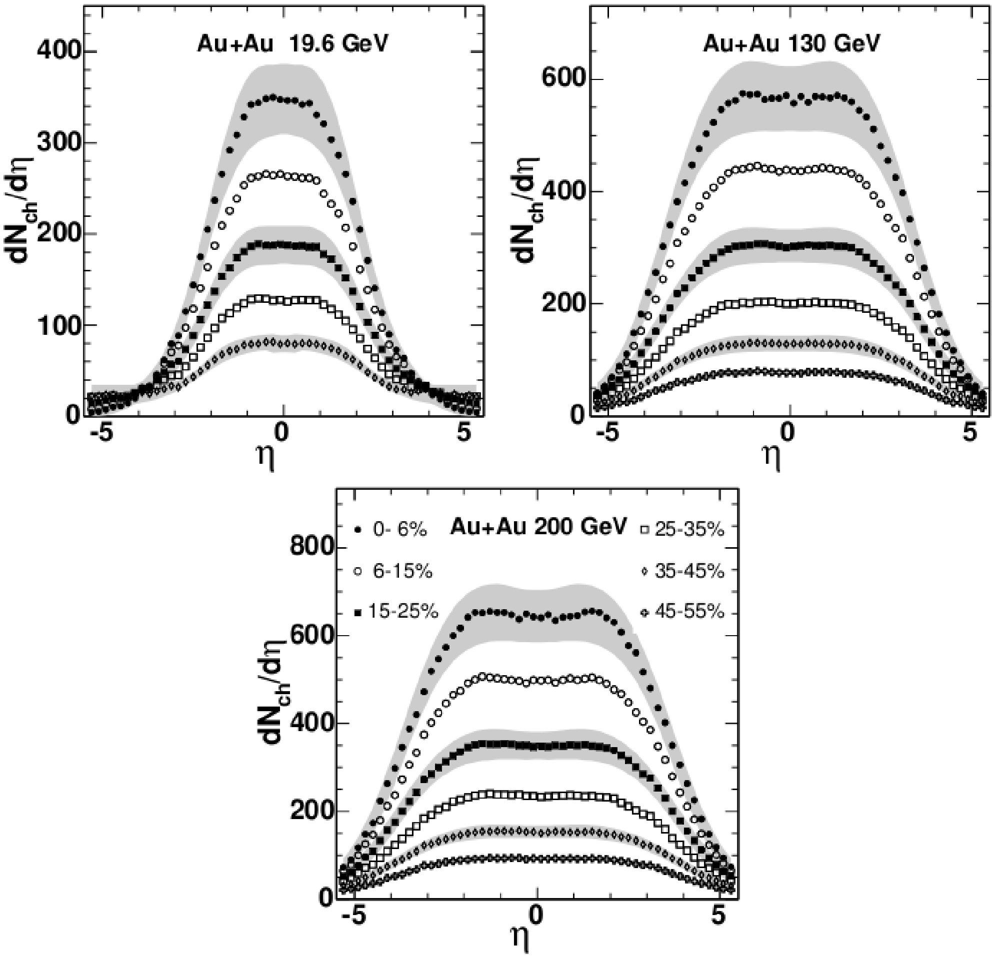

Figure 2.1: The figure shows $dN_{ch}/d\eta$ from PHOBOS for three energies ($\sqrt{s_{NN}} = 19.6$ GeV, $\sqrt{s_{NN}} = 130$ GeV, and $\sqrt{s_{NN}} = 200$ GeV) and various centrality classes with 0-6% being the most central [50]. The shapes of the distributions are very similar (though with a wider midrapidity 'plateau' with increasing energy) despite the jump in energy of a factor 10.

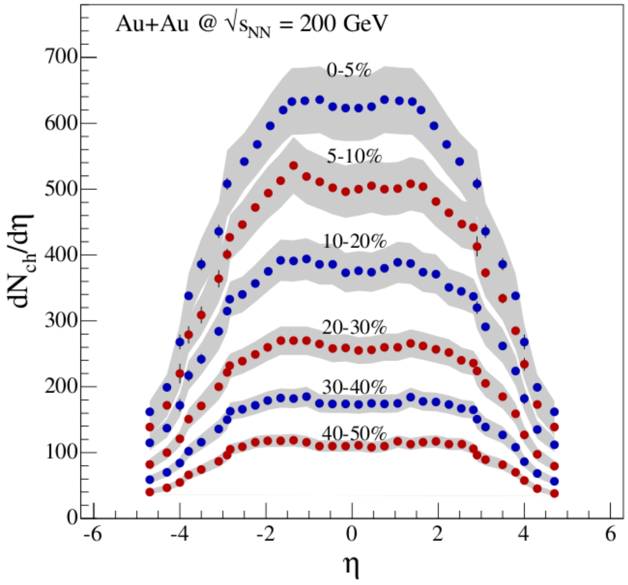

Centrality	$\eta = 0$	$\eta = 3.0$	$\eta = 4.5$	N_{ch}	$\langle N_{coll} \rangle$	$\langle N_{part} \rangle$
0-5	625±55	470±44	181 ±22	4630±370	1000±125	357±8
5-10	501±44	397±37	156±18	3810±300	785±115	306±11
10-20	377±33	309±28	125±14	2920±230	552±100	239±10
20-30	257±23	216±17	90 ±10	2020±160	335±58	168±9
30-40	174±16	149±14	64 ±7	1380±110	192±43	114±9
40-50	110±10	95±9	43 ±5	890±70	103±31	73±8

Figure 2.2: Left: $dN_{ch}/d\eta$ measured by BRAHMS in $\sqrt{s_{NN}}$ = 200 GeV Au+Au collisions shown in 6 centrality classes [51]. The centrality classes are identical to the classes used by ALICE. Right: A table summarising the results from BRAHMS including N_{part} [52].

In this work the centrality classes used by ALICE in section 2.1 will also be used so direct comparison to the PHOBOS measurements is difficult due to their choice of centrality classes. Therefore we include results from BRAHMS on $dN_{ch}/d\eta$ in Figure 2.2. The Figure shows $dN_{ch}/d\eta$ measured by BRAHMS in $\sqrt{s_{NN}}$ = 200 GeV Au+Au collisions in 6 centrality classes - the centrality classes are identical to the ALICE classes (see Figure 2.1) which makes comparison easier. However it is still necessary to take into account that the collision systems of BRAHMS and ALICE are different namely Au+Au at RHIC/BNL and Pb+Pb at LHC/CERN. To take this into account we will apply a scaling based on the numbers of participants in each type of collision when comparing $dN_{ch}/d\eta$. We will scale the BRAHMS $dN_{ch}/d\eta$ as:

$$\frac{dN_{ch(scaled)}}{d\eta} = \frac{N_{part,ALICE}}{N_{part,BRAHMS}} \frac{dN_{ch(BRAHMS)}}{d\eta} \tag{2.2}$$

This scaling will allow direct comparison between the BRAHMS and the ALICE data for purposes of particle production and scaling properties.

The first measurements of $dN_{ch}/d\eta$ from LHC were presented at Quark Matter 2011 by ALICE, ATLAS and CMS. For the ALICE results see appendix D and Chapter 7. Figure 2.3 shows the $dN_{ch}/d\eta/(0.5\times N_{part})$ presented by ATLAS and CMS at various centralities. The LHC results will be studied further in Chapter 7 where a comparison of ALICE $\frac{1}{N}\frac{dN_{\mathrm{ch}}}{d\eta}$ from this work will be compared to preliminary CMS and ATLAS results from Quark Matter 2011.

2.2.2 Proton-Proton Collisions

To set the scene for the p+p measurements presented in this work NSD (INEL for ISR) results from previous p+p(p̄) experiments are presented in Figure 2.4. A summary of the experiments is given below:

- **Intersecting Storage Rings (ISR)** was the first hadron collider in the world and was operating at CERN from 1971 to 1984. It had the record for luminosity until surpassed by the Tevatron in 2004. The measurement of $dN_{ch}/d\eta$ at $\sqrt{s}$ = 23.6 GeV is presented in [55].
- **Underground Area 5 experiment (UA5)** at the CERN Super Proton Synchrotron (SPS) operated from 1979 to 1989. It is the main p+p reference in this work since its measurements of $dN_{ch}/d\eta$ at

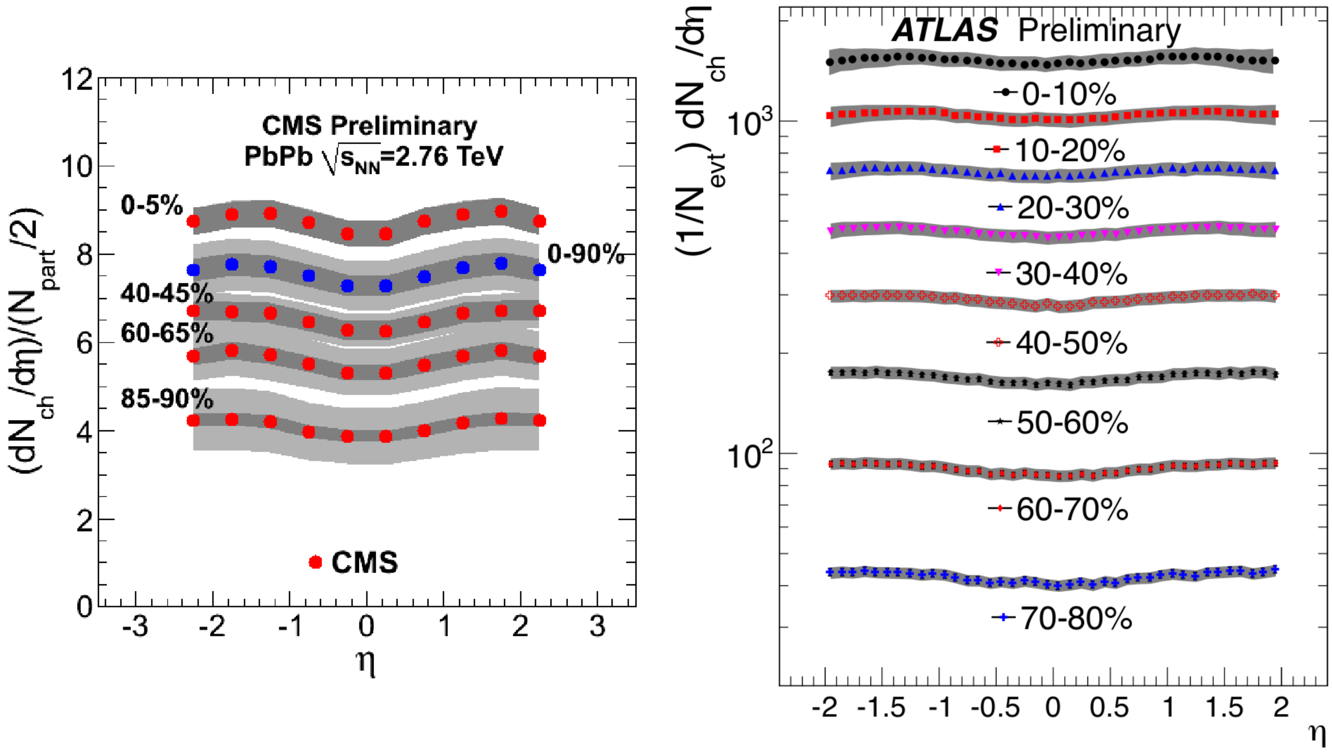

Figure 2.3: The figure shows $dN_{ch}/d\eta/(0.5 \times N_{part})$ in Pb+Pb collisions at $\sqrt{s_{NN}} = 2.76$ TeV. Left: The CMS measurement [53]. Right: The measurement from ATLAS [54]. Note the logarithmic axis.

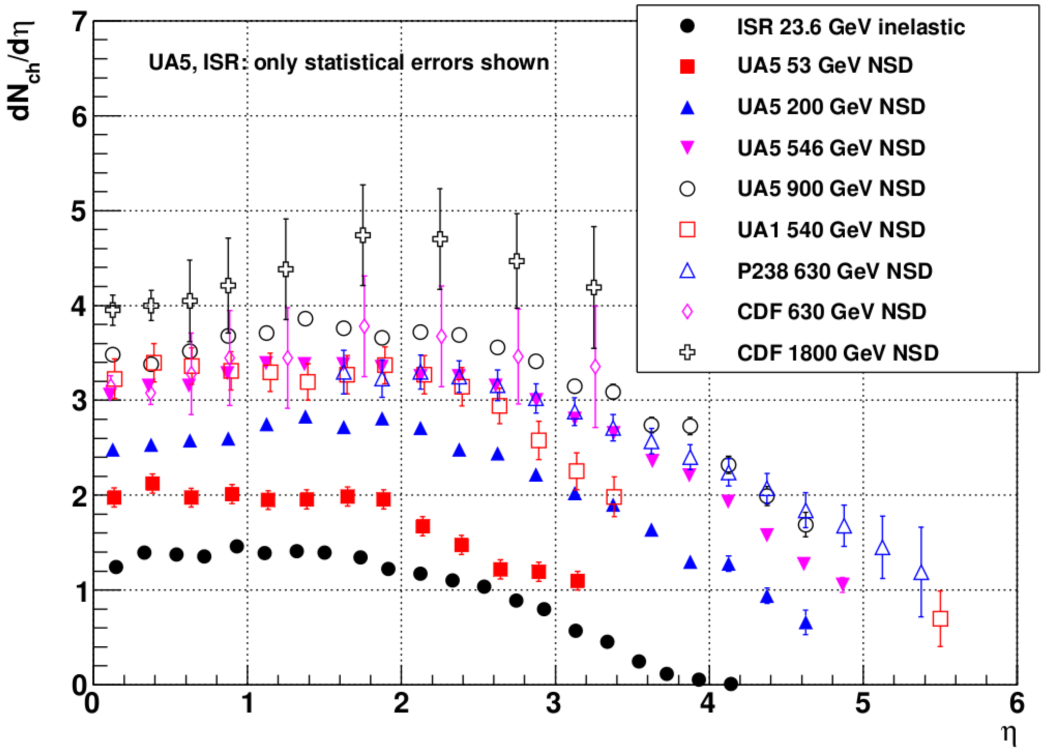

Figure 2.4: The $dN_{ch}/d\eta$ in NSD p+p($\bar{\text{p}}$) collisions measured by 5 pre-LHC experiments at several energies (see text for descriptions and references). Compilation taken from [46].

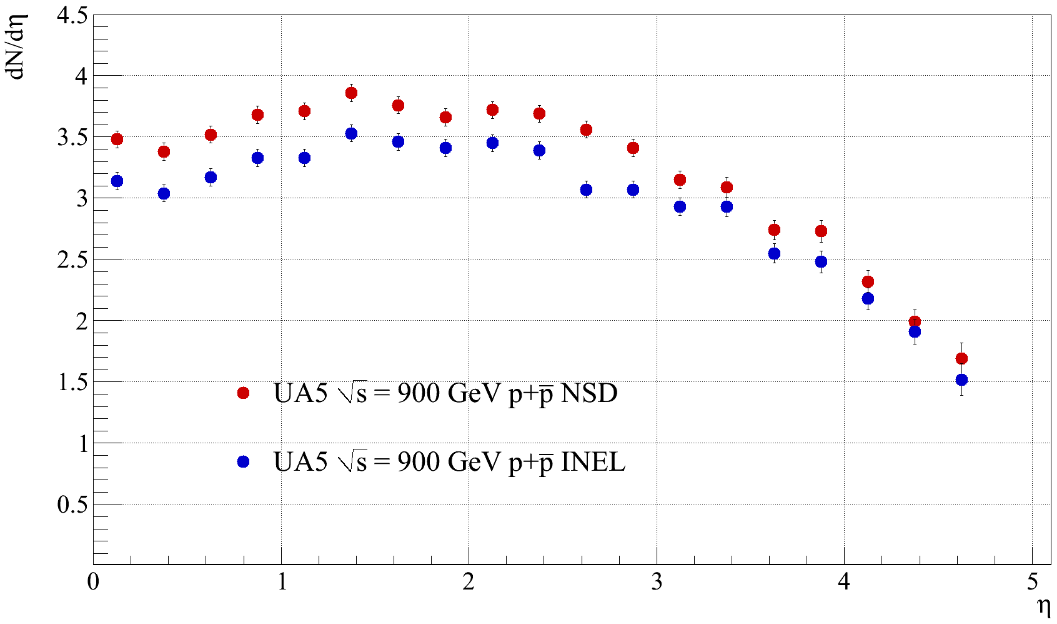

Figure 2.5: The INEL and NSD $dN_{ch}/d\eta$ in p+p(p̄) collisions at $\sqrt{s}$ = 900 GeV measured by the UA5 experiment [57]. These results will be used extensively for comparison in Chapter 7.

$\sqrt{s}$ = 900 GeV are directly compatible with the first LHC data (even if UA5 studied $\mathrm{p}+\bar{\mathrm{p}}$ collisions and LHC collides protons). The $dN_{ch}/d\eta$ measurements are found in [56, 57].

- **Underground Area 1 experiment (UA1)** at the CERN SPS ran from 1981 to 1993. The W and Z bosons were discovered at UA1 which also had the capability to measure $dN_{ch}/d\eta$ [58].
- **P238 Test Experiment** at the CERN SPS was a test setup for a microvertex detector and the experiment is considered a predecessor of the LHCb experiment at the LHC. The measurement of $dN_{ch}/d\eta$ at $\sqrt{s}$ = 630 GeV are from [59].
- **Collider Detector at Fermilab (CDF)** at the Fermilab Tevatron, the most powerful particle accelerator facility in the world before the opening of the LHC. CDF is a multipurpose detector, operational since 1985 with upgrades in 1989 and 2001. The main discovery at CDF is the discovery of the top quark in 1995. The $dN_{ch}/d\eta$ measurements are in [60].

For direct comparison to LHC p+p measurements only the UA5 data can be used. This is because the SPS is now used as injector for LHC so the energies of the UA5 data and the first LHC data are the same. This possibility of direct comparison is fortunate since it provides a testing ground for the analysis of LHC p+p data. Figure 2.5 shows the UA5 INEL and NSD results for $\mathrm{p}+\bar{\mathrm{p}}$ collisions at $\sqrt{s}$ = 900 GeV.

2.2.3 Extended Longitudinal Scaling

For p+p(p̄) it has been found that $dN_{ch}/d\eta$ exhibits a scaling behaviour known as extended longitudinal scaling. A common shape of $dN_{ch}/d\eta$ is found over various collision energies when the data are plotted as function of $y' = \eta - y_{beam}$ instead of η. The original ideas of searching for this scaling came from the “limiting fragmentation hypothesis”[61] where particle production was thought only to take place in the ‘fragmentation regions’ i.e., close to the beam rapidity. While this picture of the collisions failed to describe the observations at midrapidity the extended longitudinal scaling was observed and points to

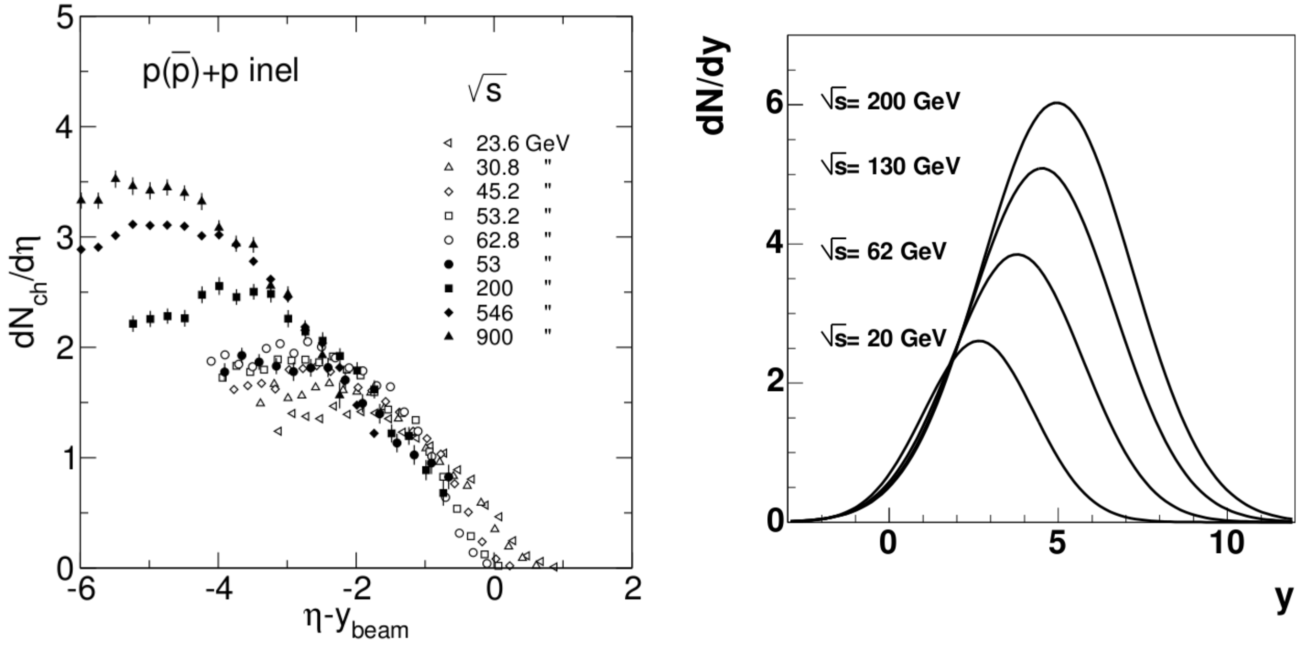

Figure 2.6: Left: Inelastic $dN_{ch}/d\eta$ as a function of $y' = \eta - y_{beam}$ for 9 different energies in p+p($\bar{p}$) collisions [50]. The data are from ISR, UA1, UA5, and CDF. Right: The predictions for longitudinal scaling from Landaus model [62].

the formation of two fragmentation regions. The positions of these fragmentation regions in y' seem to be independent of energy. In other words, the variable $y' = \eta - y_{beam}$ is simply a transformation to the rest frame of one of the colliding nuclei[1]. Figure 2.6 shows $dN_{ch}/d\eta$ as a function of y' in p+p collisions in a vast range of energies from many experiments. The extended longitudinal scaling is clearly visible for $y' > -2$. It was inferred [62] that the Landau collision picture (see section 1.2.2) actually predicts extended longitudinal scaling. The Landau expression for dN/dy is transformed to the rest frame of the 'target' ('projectile') and the following expression is obtained for the distribution:

$$\frac{dN}{dy'} \propto \frac{1}{\sqrt{L}} \exp(-\frac{y'^2}{2L} - y') \tag{2.3}$$

Here $L = (1/2)\ln(s/m_p^2)$. This expression varies little with L for $y' \sim 0$ where it reduces to:

$$\frac{dN}{dy'} \propto \frac{1}{\sqrt{L}} \exp(-y') \tag{2.4}$$

This would be the expected shape if longitudinal scaling was indeed present in the collisions. The right panel of Figure 2.6 shows this distribution for four values of $\sqrt{s}$ which have all been used in RHIC runs. It is clear from the overlap of the distributions in the fragmentation region that the longitudinal scaling is indeed present in the Landau collision scenario.

The uniquely wide pseudorapidity coverage of PHOBOS enabled detailed studies of extended longitudinal scaling in Au+Au collisions at RHIC. Figure 2.7 shows that extended longitudinal scaling is indeed also present in Au+Au collisions at RHIC energies.

2.2.4 Energy dependence

The evolution of $dN_{ch}/d\eta$ at midrapidity with $\sqrt{s_{NN}}$ has been studied extensively up to the startup of LHC. The left panel of Figure 2.8 shows measurements of $N_{ch}/(0.5 \times N_{part})$ against $\sqrt{s_{NN}}$ from RHIC,

---

[1] In the literature the two nuclei are often labeled 'target' and 'projectile' even if not truly applicable in collider experiments.

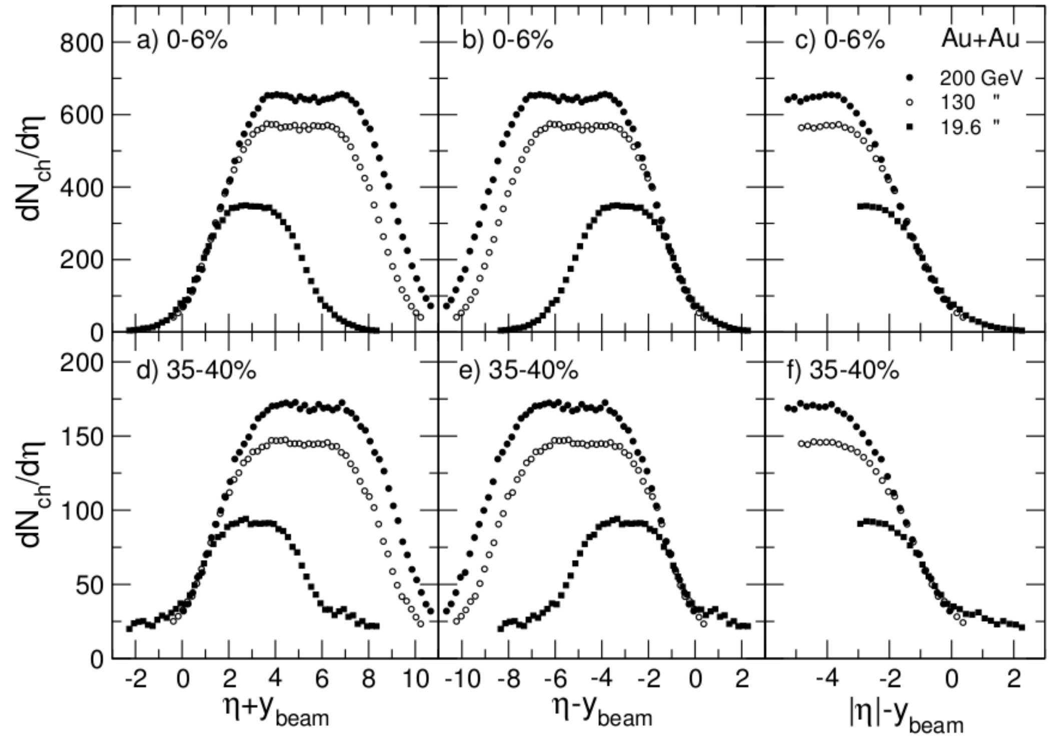

Figure 2.7: $dN_{ch}/d\eta$ as a function of $y' = \eta - y_{beam}$ for 3 different energies in 2 centrality classes in Au+Au collisions [50].

SPS and AGS for 0-5% centrality. Included in the Figure are p+p data as well as A+A data. The figure also includes four extrapolations of the data which were suggested to describe the data [49]:

1. **Saturation Model with power law** (long dashed) This curve is obtained from a saturation model using pQCD modelling [64]. The model assumes that all momentum transfers can be considered to be at the saturation scale, Q_s^2, and that multiplicities can be assessed directly from quarks and gluons in the calculations. N_{ch} is estimated to follow a power law as $N_{ch} = \frac{2}{3}A^{0.92}(\sqrt{s})^{0.4}$. Prediction for Pb+Pb ($A = 208$) collisions at $\sqrt{s_{NN}} = 2.76$ TeV: $N_{ch} = 2497$ or $N_{ch}/(0.5 \times N_{part}) = 13$.

2. **Quadratic** (dotted) A function of the form $N_{ch}/(0.5 \times N_{part}) = 0.7 + 0.028 \ln^2 s$ i.e., a quadratic function fit in the variable $\ln s$. Prediction for Pb+Pb collisions at $\sqrt{s_{NN}} = 2.76$ TeV: $N_{ch} = 1477$ or $N_{ch}/(0.5 \times N_{part}) = 7.7$.

3. **Linear** (short dashed) A function of the form $N_{ch}/(0.5 \times N_{part}) = 0.68 \ln(\sqrt{s}/0.68)$, ie. linear in $\sqrt{s}$. Prediction for Pb+Pb collisions at $\sqrt{s_{NN}} = 2.76$ TeV: $N_{ch} = 1080$ or $N_{ch}/(0.5 \times N_{part}) = 5.65$.

4. **Polynomial** (solid) The function $N_{ch}/(0.5 \times N_{part}) = 0.049 \ln^2 \sqrt{s} + 0.046 \ln \sqrt{s} + 0.96$ which is a second order polynomial in $\ln \sqrt{s}$. Prediction for p+p collisions at $\sqrt{s_{NN}} = 2.76$ TeV: $N_{ch} = 4.4 = N_{ch}/(0.5 \times N_{part})$ since for p+p $N_{part} = 2$.

These extrapolations are shown in the left panel of Figure 2.8. The first three fits have been used for the A+A data while the last fit was obtained from the p+p data. From Figure 2.1 it is seen that at LHC $\frac{1}{N}\frac{dN_{\mathrm{ch}}}{d\eta} \sim 1601 \pm 60$ so the the extrapolation that got closest to the LHC result was the quadratic extrapolation.

The right panel brings the story up to date with $N_{ch}/(0.5 \times N_{part})$ results from ALICE in p+p and Pb+Pb collisions as well as p+p results from CMS. Also included in the right panel are power law fits to the data. For the A+A results the expression $N_{ch}/(0.5 \times N_{part}) \propto \sqrt{s_{NN}}^{0.3}$ gives a good description

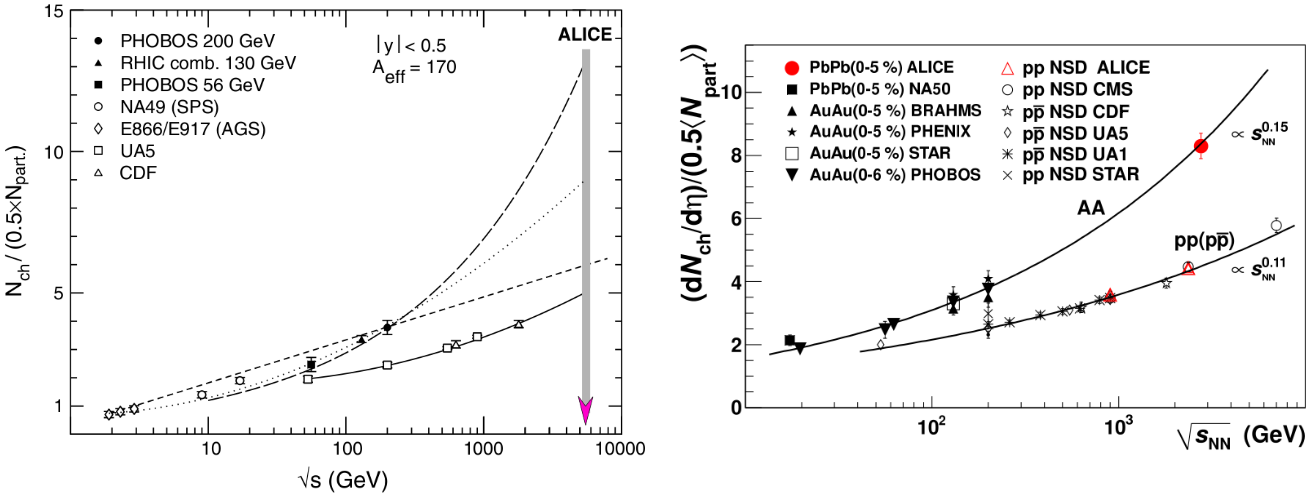

Figure 2.8: Left: Data from AGS, SPS and RHIC on $N_{ch}/(0.5 \times N_{part})$ against $\sqrt{s_{NN}}$ for 0-5% centrality [49]. The grey band marked 'ALICE' shows the future LHC top energy of $\sqrt{s_{NN}} = 5.5$ TeV. Four extrapolations based on data are included: Saturation Model (long dashed), Quadratic fit (dotted), Linear (short dashed), and Polynomial (solid), see text for details. Right: The first ALICE measurements from 0-5% central Pb+Pb collisions and p+p collisions [63]. Also included are power law fits to the data which are seen to describe the data well from RHIC to LHC. See text for discussion.

of the data while for p+p the expression $N_{ch}/(0.5 \times N_{part}) \propto \sqrt{s_{NN}}^{0.22}$ is used with success. It is worth noticing that for the saturation model fit used above the use of a power law was actually a reasonable choice even if the values used gave too high a result compared to the first LHC measurement.

2.2.5 System size dependence

Studies of the system size dependence of $dN_{ch}/d\eta$ may give additional information on the evolution of the collisions given that the particle production clearly depends on $\sqrt{s_{NN}}$ and N_{part}. To understand better the underlying dependence on N_{part} the trivial dependence is taken out in the quantity $(dN_{ch}/d\eta)/(N_{part}/2)$ by scaling with N_{part}. If the different centrality classes had the same properties, the distribution of $(dN_{ch}/d\eta)/(N_{part}/2)$ against N_{part} should be flat at approximately the level of p+p collisions. Figure 2.9 shows that this certainly not the case.

It is seen that $(dN_{ch}/d\eta)/(N_{part}/2)$ grows with N_{part} at both RHIC and LHC and at lower energies it approaches the level of p+p collisions. This means that there is higher particle production by a factor of ~ 2 in the most central A+A collisions compared to p+p collisions consistent with a thermalized volume of hot and dense matter being created in A+A collisions. It is worth noticing that the RHIC data scaled by a factor of $\frac{dN_{ch}(\text{LHC } \eta\sim 0)}{d\eta} / \frac{dN_{ch}(\text{RHIC } \eta\sim 0)}{d\eta} \sim 2.1$ (compared to the increase of a factor of ~ 13 in energy) agrees almost perfectly with the LHC results from ALICE. This seems to point to common dynamics playing a role at RHIC and LHC. Furthermore SPS data have been shown to follow the same scaling which may be even more surprising. This could point to this scaling being universal across many energies [47].

Figure 2.10 shows the data from Figure 2.9 overlaid with predictions from various models. There are in general two trends in the models: DPMjet[65] and the geometrical scaling model [67] fails to describe the shape of $N_{ch}/(0.5 \times N_{part})$ but for $N_{part} > 300$ at least DPMjet agrees well with the data. On the other hand, HIJING and the saturation models that use CGC initial conditions describe the shape of $N_{ch}/(0.5 \times N_{part})$ well and only one model agrees with both the level and the shape of the $N_{ch}/(0.5 \times N_{part})$ from ALICE.

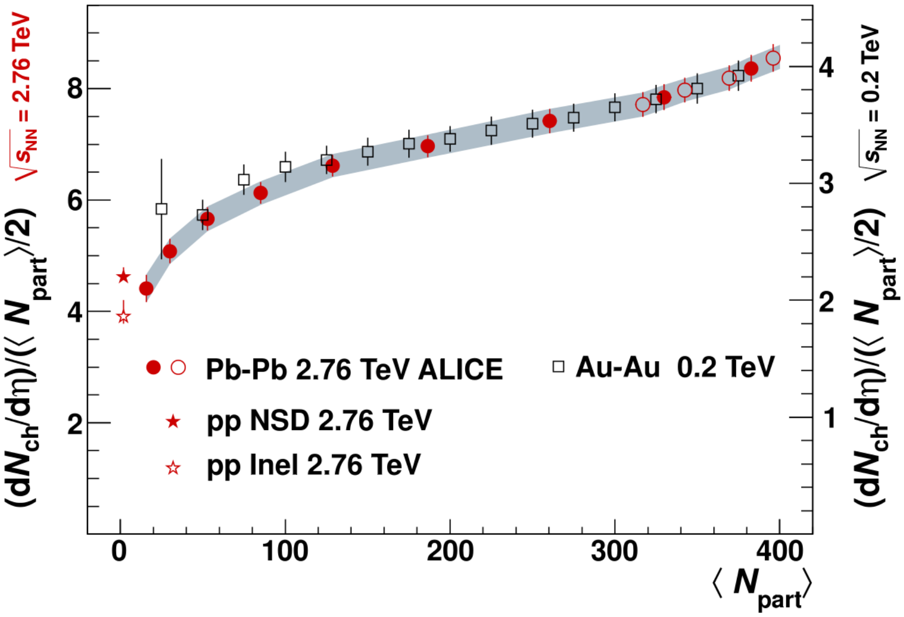

Figure 2.9: The $(dN_{ch}/d\eta)/(N_{part}/2)$ as a function of N_{part} and hence, centrality measured by ALICE in nine centrality bins [48]. Also shown are RHIC data scaled by a factor of 2.1 (axis for the RHIC data shown on the right). Furthermore the plot includes ALICE p+p data interpolated between $\sqrt{s} = 2.36$ TeV and $\sqrt{s} = 7$ TeV p+p data.

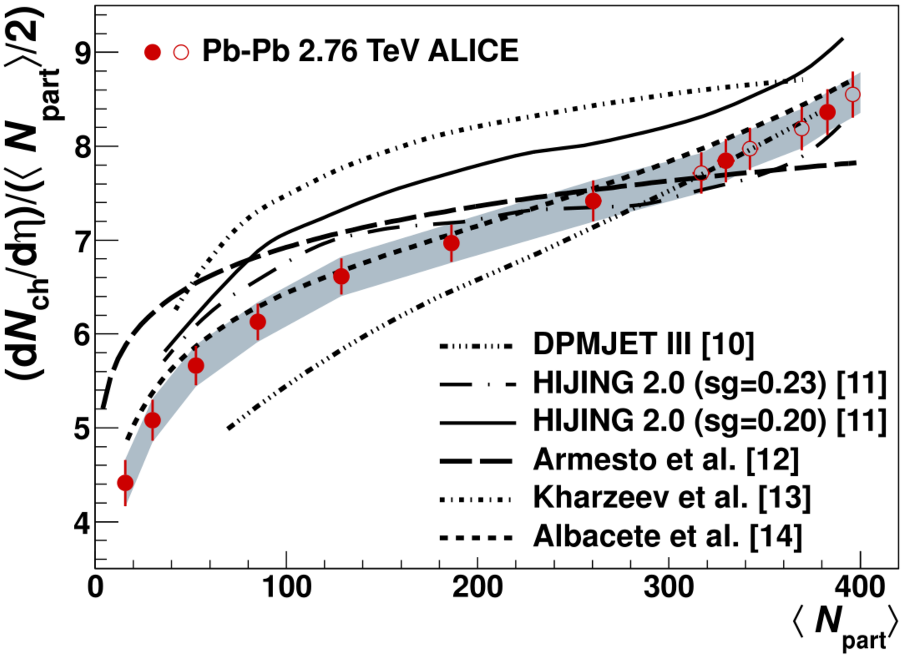

Figure 2.10: Model comparison to $N_{ch}/(0.5 \times N_{part})$ in $\sqrt{s_{NN}} = 2.76$ TeV Pb+Pb collisions [48] (References in the figure are from the paper). The dual parton model DPMJET [65] underestimates the $N_{ch}/(0.5 \times N_{part})$ except for the most central collisions. The two tunes of HIJING[66] have a reasonable estimate on the shape but they still overestimate $N_{ch}/(0.5 \times N_{part})$. A geometrical scaling approach (Armesto et al. [67]) has issues with the shape and the level of the distribution while saturation models with CGC initial conditions (Kharzeev et at. [68] and Albacete et al. [69]) reproduce the shape and the model by Albacete also reproduces the level of $N_{ch}/(0.5 \times N_{part})$ quite well.

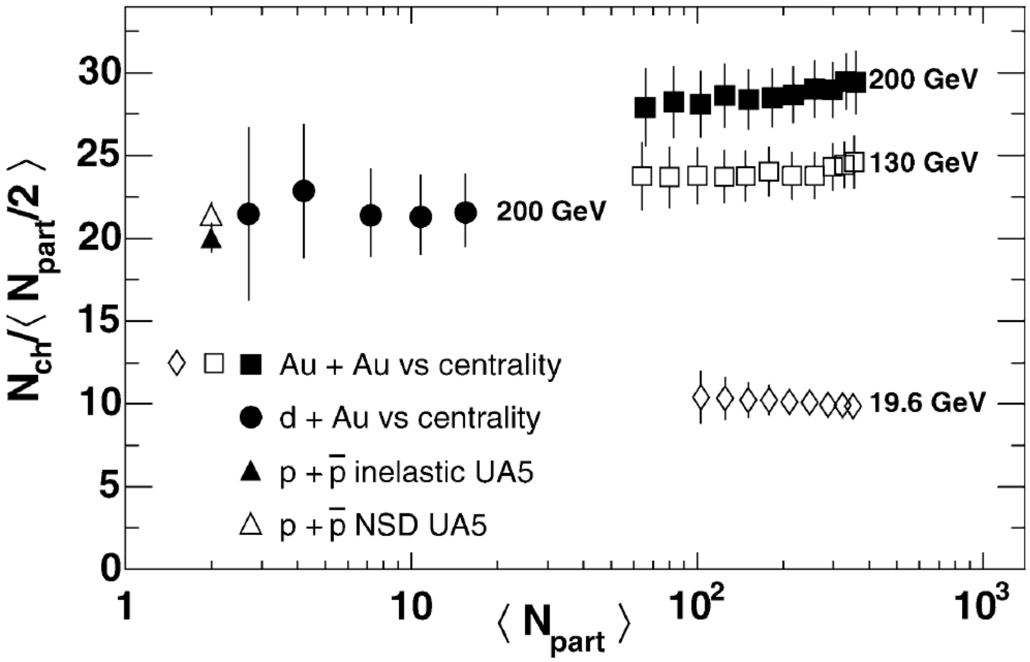

Figure 2.11: Total multiplicity dependence measured by PHOBOS in Au+Au collisions at 3 energies and d+Au collisions at $\sqrt{s_{NN}} = 200$ GeV [50] as well as p+p̄ collisions from UA5 [57].

2.2.6 Total Number of Charged Particles

PHOBOS has studied the dependence of the average total number of particles produced in Au+Au collisions, $N_{ch} = \int_{-y_{beam}}^{y_{beam}} \frac{1}{N}\frac{dN_{\mathrm{ch}}}{d\eta} d\eta$ as a function of N_{part}. Figure 2.11 shows $N_{ch}/(N_{part}/2)$ as a function of N_{part} for Au+Au collisions at $\sqrt{s_{NN}} = 19.6$ GeV, $\sqrt{s_{NN}} = 130$ GeV, and $\sqrt{s_{NN}} = 200$ GeV as well as d+Au collisions at $\sqrt{s_{NN}} = 200$ GeV and p+p̄ collisions from UA5. It is seen that the distributions are flat at all energies and systems even if a rising trend possibly appears in Au+Au collisions at $\sqrt{s_{NN}} = 200$ GeV. Whether this trend is enhanced at LHC or if $N_{ch}/(N_{part}/2)$ is constant there will be discussed in Chapter 7.

2.3 Models

In this section we will discuss and compare various models on the market in heavy ion physics. These models will serve two purposes in the following chapters; firstly they serve as input to the simulations used to correct the data in Chapter 6. This role as 'Event Generators' will be elaborated upon in Chapter 5. Secondly, they will be compared to the results in Chapter 7 to test their ability to describe the physics of heavy ion and p+p collisions.

2.3.1 HIJING

The first version of the Heavy Ion Jet INteraction Generator (HIJING) was released in 1991 [70]. It has been successfully used to describe heavy ion data and p+p data at lower energies and has been updated frequently to also include RHIC and LHC energies. The principle of operation for HIJING is based on a pQCD approach that is combined with multistring phenomenology at low p_T [70]. For multiple interactions in heavy ion collisions a Glauber approach is applied. As the name implies HIJING also models jets from $q - \bar{q}$ collisions as well as the modification of these jets by the hot and dense medium.

By design, HIJING does not contain anisotropic transverse flow except for what could be generated by the microscopic model.

2.3.2 AMPT

A Multi–Phase Transport (AMPT) is an extension of HIJING that uses HIJING for generation of initial conditions while changing the treatment of the resulting collision evolution [71]. The first version was published in 2005. In the AMPT setup the Zhang's Parton Cascade Model (ZPC) is then used for partonic (quarks and gluons) scatterings and A Relativistic Transport Model (ART) is used for the hadronic scatterings after the freezeout. The multi–phase design of AMPT makes it suited for studies of collective phenomena e.g., anisotropic transverse flow.

2.3.3 CGC based models

To supplement HIJING and AMPT we consider also the model by Albacete et al. [69] mentioned briefly in section 2.2.5. The model is based on a CGC initial condition and uses the so–called B-JIMWLK equations to evolve A+A systems to predict the multiplicity. The evolution is controlled by a parameter γ that distinguishes different initial conditions. While it is stated that proton–electron scattering data suggest a value of $\gamma \sim 1.119$[69] we will consider the original McLerran–Venugopalan CGC model which uses $\gamma \sim 1$. This choice is also used for the successful prediction from CGC shown in Figure 1.5. This choice was influenced by what was available from the author of this model[2].

2.3.4 PYTHIA

Similarly to HIJING PYTHIA is more than a decade old but still under continuing development [72]. PYTHIA is not an abbreviation but a name taken from the oracle in the ancient Greek city of Delphi. The heart of PYTHIA is the so–called 'Lund string model', first implemented in the JETSET routine in the eighties. Based on a string model, the fundamental reactions at the $\mathrm{q}-\bar{\mathrm{q}}$ level are modelled using color strings. Furthermore PYTHIA models the full event including fragmentation, hadronization, parton showers, photon physics and also optionally physics beyond the Standard Model. During its development, PYTHIA has been tuned to relevant data to provide good descriptions of collisions at p+p, p+$\bar{\mathrm{p}}$ and $\mathrm{e}^+ + \mathrm{e}^-$. Being a string model, PYTHIA is known to have issues with the description of diffractive processes[3]. The particular PYTHIA used throughout this thesis is the so–called Perugia0 tune of PYTHIA6 [73].

2.3.5 PHOJET

PHOJET was introduced in 1998 [74]. Being more recent than PYTHIA, PHOJET attempts to describe diffractive processes more thoroughly based on a two–component Dual Parton Model. It describes diffractive processes in terms of hadron–pomeron or pomeron–pomeron exchanges. It includes both soft (low–p_T) and hard $\mathrm{q}-\mathrm{q}$ and $\mathrm{q}-\bar{\mathrm{q}}$ processes.

---

[2] Javier Albacete, private communication.

[3] Peter Skands, private communication.

Chapter 3

The LHC and ALICE

In this chapter the main tools for discovery used in this work are presented: The giant particle accelerator, LHC, and the ALICE experiment are described setting the stage for the discussion of the specific detectors given in Chapter 4.

3.1 The Large Hadron Collider

The LHC[75] is constructed in the same tunnel as its predecessor, the Large Electron-Positron Collider (LEP). In 1984, the LHC was officially proposed as the next CERN project; it would take 25 years before it would be completed. The history of the LHC begins at the same time as that of LEP since for the construction of LEP in the eighties the tunnel was built wider than required to allow a hadron machine to be built later on. Following a very successful experimental program the LEP machine was shut down in 2000 to make room for the LHC.

The LHC is designed as a 27 km collider that can collide protons at energies up to $\sqrt{s} = 14$ TeV and Pb ions at $\sqrt{s_{NN}} = 5.5$ TeV. The machine was completed and began operations in the summer of 2008. During the commissioning phase, on September 19 2008 a massive magnet quench took place causing a violent helium leakage and extensive damage to parts of the LHC machine. Repairs and upgrades to prevent further incidents lasted almost a year so the LHC restart took place in the fall of 2009 resulting in the first p+p collisions at $\sqrt{s} = 900$ GeV being produced and observed in ALICE November 23 2009. Due to the restrictions imposed in the wake of the 'LHC incident' [1] and until a replacement of the magnet connectors scheduled for 2013 the maximum energies of the LHC is now $\sqrt{s} = 7$ TeV for p+p collisions and $\sqrt{s_{NN}} = 2.76$ TeV for Pb+Pb collisions. Table 3.1 summarizes the collisions recorded by ALICE until September 23, 2011 estimated from the ALICE run condition table.

Collision system	Energy	Events recorded
p+p	900 GeV	$9 \cdot 10^6$
p+p	2360 GeV	10^5
p+p	2760 GeV	$4 \cdot 10^7$
p+p	7 TeV	$1.6 \cdot 10^9$
Pb+Pb	2.76 TeV	$5 \cdot 10^7$

Table 3.1: ALICE datasets taken with the LHC.

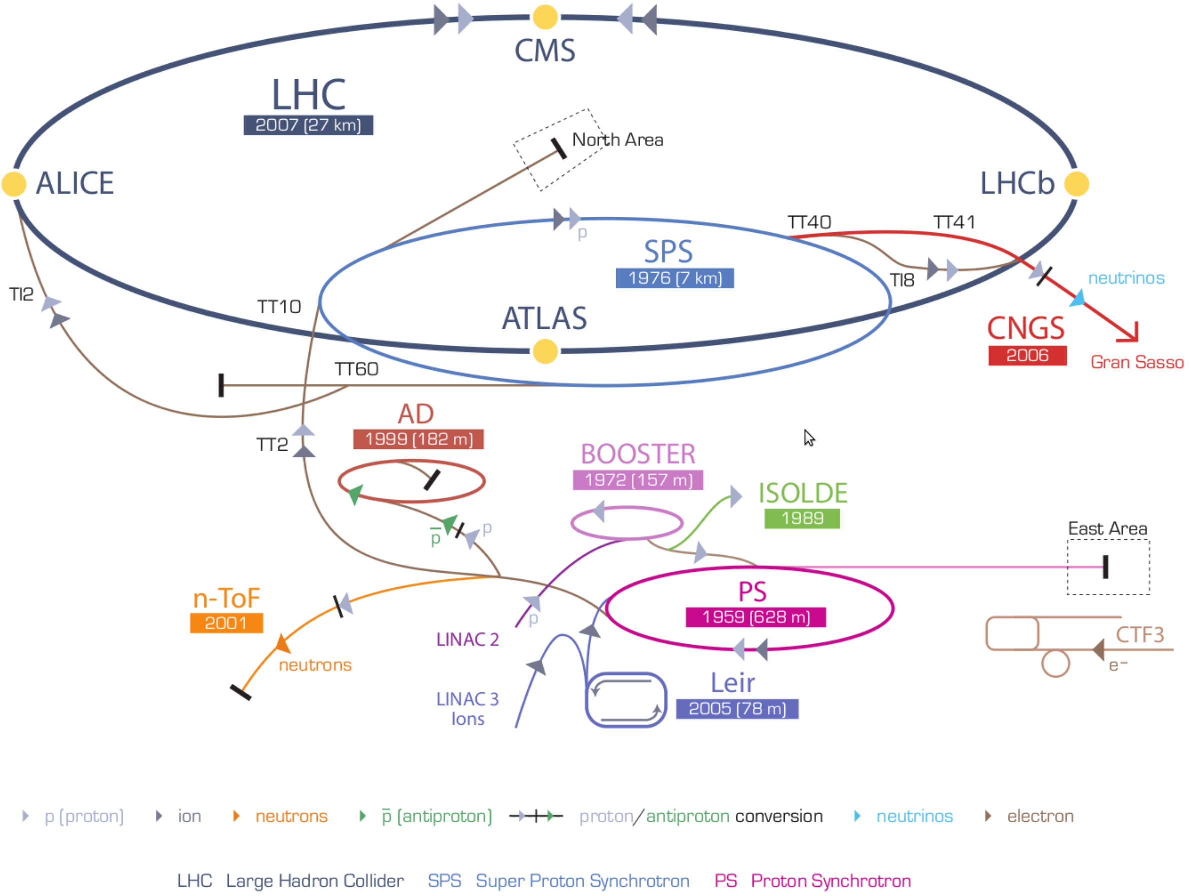

Figure 3.1: The CERN accelerator complex [76].

3.2 A Large Ion Collider Experiment (ALICE)

The ALICE experiment was approved in 1998 and has been designed to be housed in the former L3 LEP experimental cavern. This was quite a bargain because it included a 10.000 tonnes Russian built magnet inside which the main parts of ALICE was built. Figure 3.2 shows a schematic view of ALICE. An overview of the ALICE detectors and their roles will be given in the next section. Table 3.2 summarizes the capabilities of ALICE.

3.2.1 The Central Detectors

The main part of the ALICE experiment are the detectors covering the midrapidity region, also called the central region. The design goal of ALICE was to provide tracking and Particle Identification (PID) as detailed as possible in the central region. To illustrate the following detector descriptions Figure 3.3 shows a vertical section of ALICE.

Inner Tracking System (ITS)

The innermost detector in ALICE, the ITS [78] consists of three subsystems each with two concentric silicon layers, described here in order of proximity to the beam pipe [79]:

- **The Silicon Pixel Detector (SPD)** consists of two layers of silicon pixels with a staggering total of roughly 10 million channels. This allows the SPD to detect decays of exotic resonances very close

---

[1] This is the usual reference to what happened in the tunnel

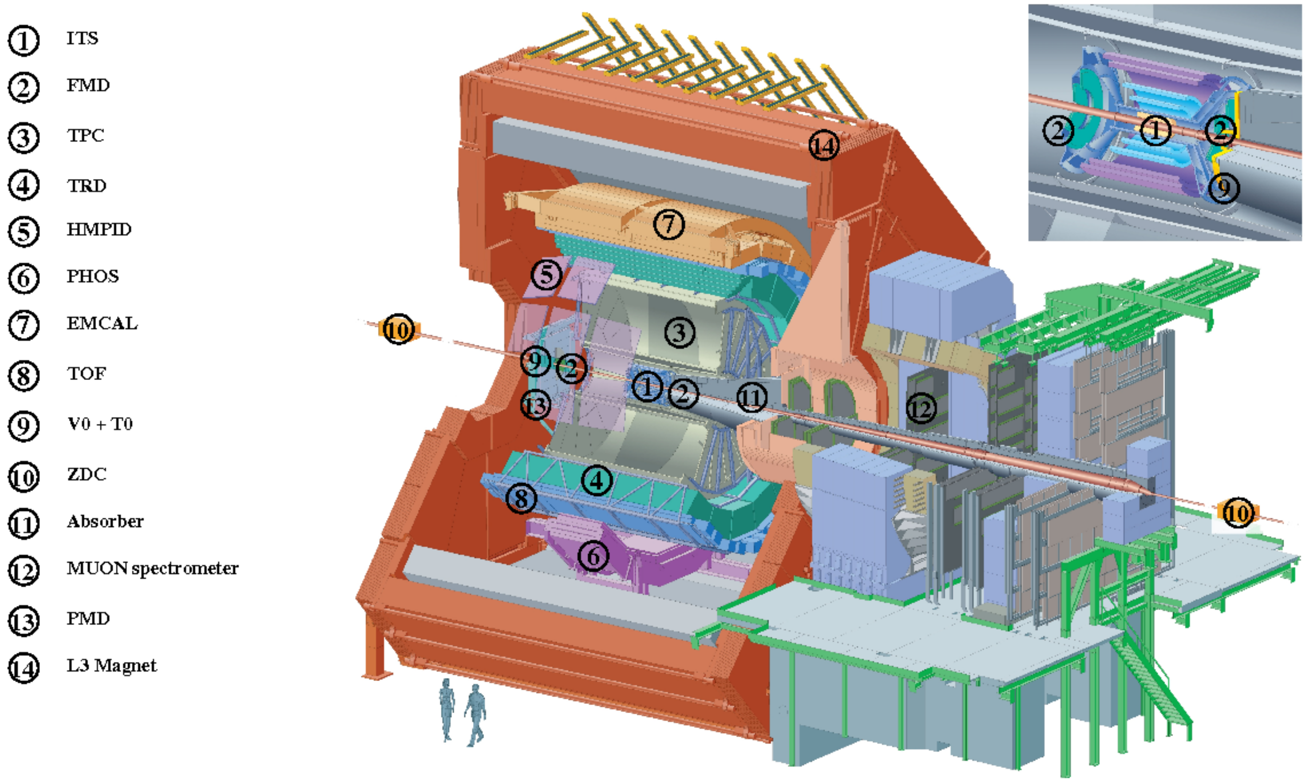

Figure 3.2: The ALICE experiment.

Detector	Detects	Tracking	Trigger detector
ITS	All Charged Particles	Full	Yes
TPC	All Charged Particles	Full	Yes
TOF	All Charged Particles	Adds PID	Yes
TRD	Electrons	Yes	No
HMPID	Hadrons	Adds PID	No
PHOS	Photons	Yes	No
EMCAL	All Charged Particles	Yes	Yes
MUON	Muons	Yes	Yes
FMD	All Charged Particles	No	No
PMD	Photons and Charged Particles	No	No
ZDC	Hadrons and Charged Particles	No	Yes
T0	All Charged Particles	No	Yes
V0	All Charged Particles	No	Yes

Table 3.2: Summary of the detection capabilities of the ALICE sub–detectors.

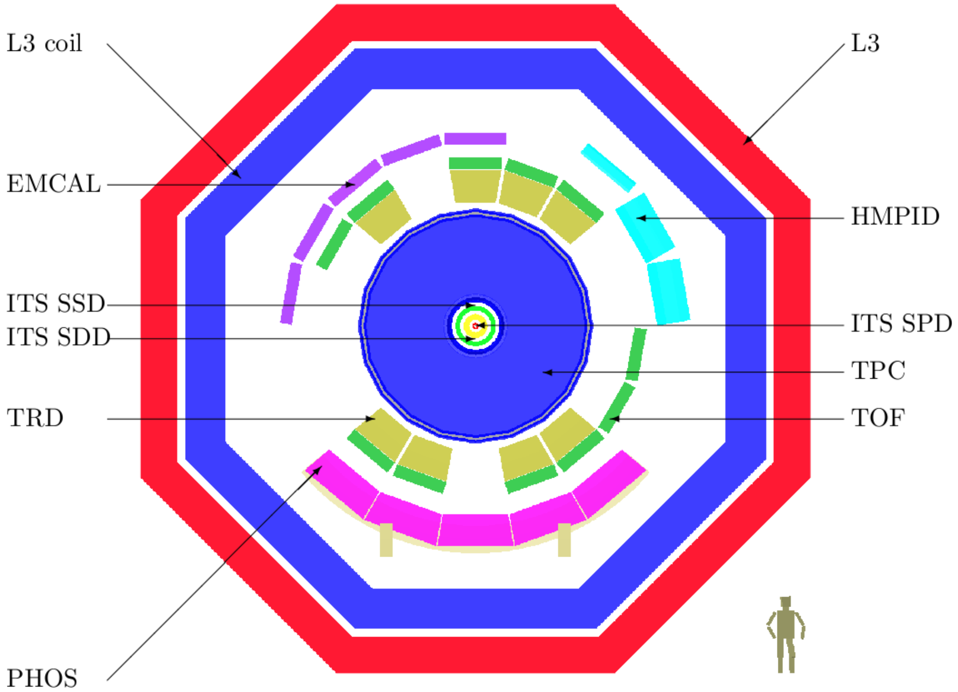

Figure 3.3: A cut through ALICE compared to the size of a standard physicist. Taken from [77].

to the Interaction Point. The SPD has an inner radius of 3.9 cm so there is just a thin layer of air between it and the beampipe. It plays a key role as a triggering detector since it has fast readout. Furthermore the SPD provides an accurate measurement of the collision vertex. Finally the two overlapping silicon layers enable the SPD to form tracklets i.e., basic particle trajectories consisting of the vertex and a point (cluster) in each layer.

- **The Silicon Drift Detector (SDD)** adds two layers of silicon to the ITS with the capability of tracking and providing dE/dx information for particle identification (PID) of low momentum particles. It has an inner radius of 15 cm.
- **The Silicon Strip Detector (SSD)** connects the ITS tracks to the tracks in the TPC. It also adds further dE/dx information. It has an inner radius of 38 cm. The ITS has an overall outer radius of 43.9 cm.

For multiplicity measurements the SPD covers $|\eta| < 1.98$ [49].

Time Projection Chamber (TPC)

The TPC is designed with the pre–RHIC predictions for the particle multiplicity in mind so it is designed to be able to handle 20000 particles in its acceptance with an event rate of 200 Hz. The TPC is huge: Its outer radius is 2.78 m and its inner radius is 0.86 m. The ALICE TPC is the most ambitious of its kind ever built and it has lived up to and exceeded the expectations so far.

It has been said that the TPC [80] is the heart of ALICE. The TPC performs the main part of the tracking in ALICE and provides dE/dx measurements for PID as well. It consists of a gaseous drift volume of 90 m^3 surrounded by a cylindrical field cage. The TPC anode plane sits in the center of the TPC and two cathode planes sit at each end of the TPC cylinder. As charged particles traverse the Ne/CO_2 gas in the TPC electrons are knocked free and start to drift in the electrical field. The electrons drift to the

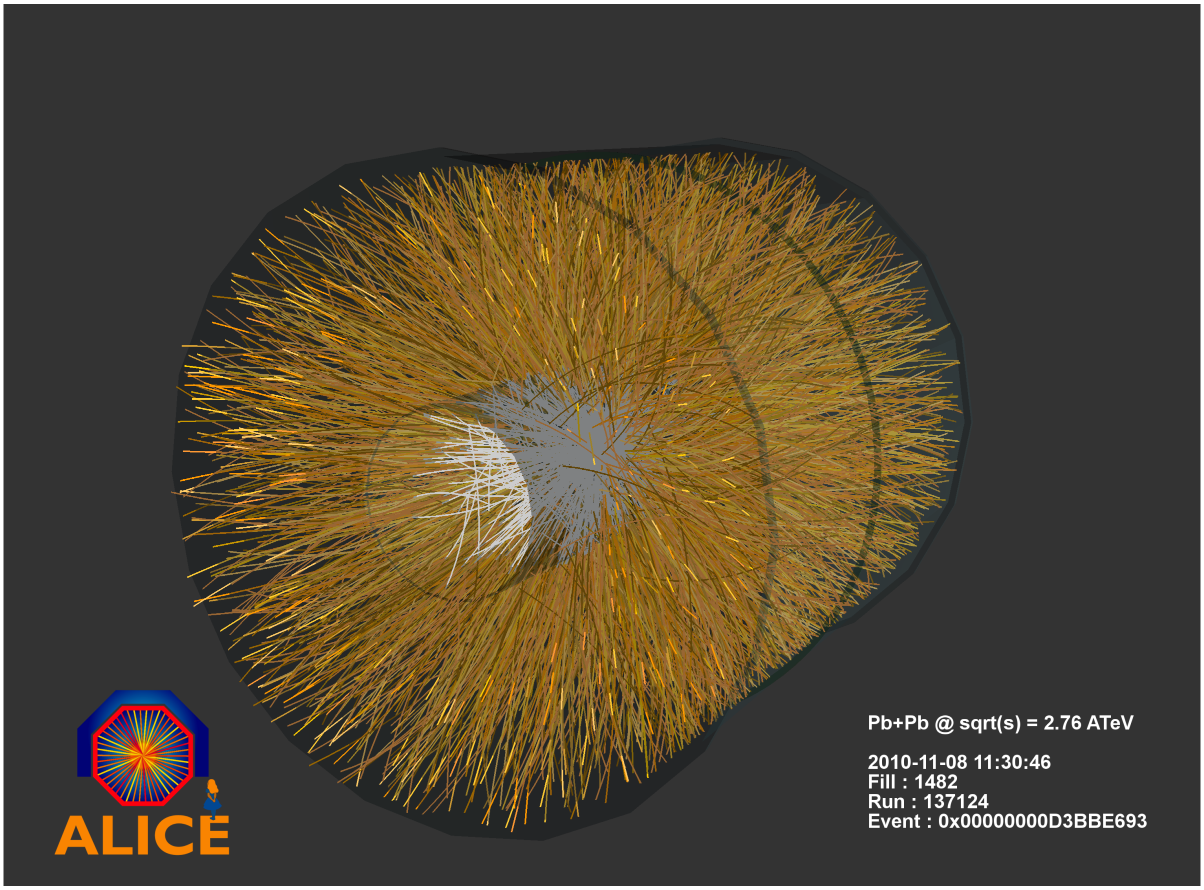

Figure 3.4: ALICE tracks. The white barrel is the ITS of ALICE. All the yellow tracks have been reconstructed using the ALICE ITS and TPC in a Pb+Pb event at $\sqrt{s_{NN}} = 2.76$ TeV.

anode plane and the ions drift to the cathode plane. The planes will then give the (x, y) projection of the tracks. The z coordinate can be found from the drift time along the z axis. The reconstructed (x, y, z) are fitted using a Kalman filter to form the tracks of the charged particles [81]. The ITS combined with the TPC provide full tracking in the region $|\eta| < 0.9$ [49].

To calibrate the TPC a laser system[2] provides perfectly straight tracks throughout the gaseous volume. This enables a crucial check of the tracking algorithms and calibration of the TPC electronics.

Figure 3.4 shows an example of a Pb+Pb event at $\sqrt{s_{NN}} = 2.76$ TeV as seen with ALICE tracks. It is seen that the ALICE tracking is indeed able to resolve thousands of charged particles traversing through the detector.

Time Of Flight (TOF)

The TOF [82] sits outside the TPC field cage within the acceptance of TPC tracking. Using an array of photomultipliers the time of flight from the Interaction Point is measured. Since the TOF sits outside the TPC and inside its acceptance the path and momentum of a given particle is known from its track. This allows determination of the mass of a particle starting from the definition of relativistic momentum:

$$|p| \equiv \gamma m \beta = \frac{m\beta}{\sqrt{1-\beta^2}} \quad \text{, thus} \quad m = |p|\sqrt{\frac{1}{\beta^2} - 1}$$

With the masses of most common particles known the TOF can be used to identify particles this way.

---

[2] This laser system was designed and built at the Niels Bohr Institute.

Transition Radiation Detector (TRD)

The purpose of the TRD[83] is to allow ALICE to identify electrons with momenta above 1 GeV/c [79]. It consists of a radiator (a 'sandwich' of carbon fibre laminated Rohacell/polypropylene) which causes electrons to emit transition radiation. Combined with the tracking properties of a multiwire proportional chamber attached to the radiating material the TRD can separate pions and electrons with momenta of above 1 GeV/c. The TRD is mounted just outside the TOF detector and has full azimuthal coverage in $|\eta| < 0.84$.

High Momentum Particle Identification (HMPID)

When a charged particle traverses a medium with higher speed than the speed of light in that medium $= c/n$ where n is the index of refraction of the medium, it will emit photons. This phenomenon is known as Cherenkov radiation [84] and it is employed by the HMPID[85] to identify particles with transverse momenta $p_T > 1$ GeV/c [79]. To identify a particle the angle of emission of the radiation must be measured. This is normally done by measuring the radius of the ring pattern created by the Cherenkov photons when they are detected. The relation between angle and the speed of the particle is then $\cos\theta = 1/\beta$. Combining this measurement with the TPC track associated with the particle it can be identified by calculating its mass. The HMPID is positioned outside and almost on top of the TRD; it does not have full azimuthal coverage but covers $1.2^\circ < \phi < 58.8^\circ$ in the TPC η acceptance.

Photon Spectrometer (PHOS)

Direct photons play a significant role as an observable since they are not affected by the strong interactions in the collision fireball. The PHOS[86] is an electromagnetic spectrometer specialized in measuring low p_T direct photons and π_0 decays through the primary decay channel: $\pi_0 \rightarrow \gamma + \gamma$. The detection of photons is done with lead-tungstate crystals coupled to photodiodes and preamplifiers. To identify photons a multiwire proportional chamber [84] is used as a charged particle discriminator [79]. The PHOS is mounted at the very bottom of ALICE. It covers $|\eta| < 0.12$ and $220^\circ < \phi < 320^\circ$.

Electromagnetic Calorimeter (EMCAL)

The final detector circumfering the TPC is the EMCAL[87]. Its construction began as late as 2008[3] and its full deployment was only complete in the spring of 2011. The motivation for the EMCAL is to enable ALICE to study jet physics in detail and in particular the quenching of jets in the medium created in heavy ion collisions. Combined with the tracking capabilities of the TPC and ITS the EMCAL allows jets to be reconstructed completely in p+p as well as Pb+Pb where the background is much larger [79]. Furthermore the EMCAL readout is fast enough that it can be used as a trigger for hard jets, photons and electrons. Since the LHC luminosity is so large this allows for a refinement of the data for jet studies at trigger level. The position of EMCAL is almost on top of the TRD and it covers $|\eta| < 0.7$ and $80^\circ < \phi < 180^\circ$.

3.2.2 The Muon Spectrometer (MUON)

Following the measurement of J/ψ suppression at SPS [88] there was considerable interest in the possible role of the J/ψ and other charmonia (ψ', Υ, Υ' and Υ") as signatures of the QGP. With this in mind the J/ψ were studied at RHIC and the Muon Spectrometer[89] was designed for ALICE. Several models suggested that there would be an enhancement of the J/ψ production in the QGP [8] or that the suppression would be reduced at RHIC and LHC due to medium effects. However measurements at RHIC revealed an increased suppression of the J/ψ [90] which reduces the potential of the J/ψ suppression or

---

[3] The EMCAL was not supposed to be part of the first run but the delay caused by the LHC incident changed this

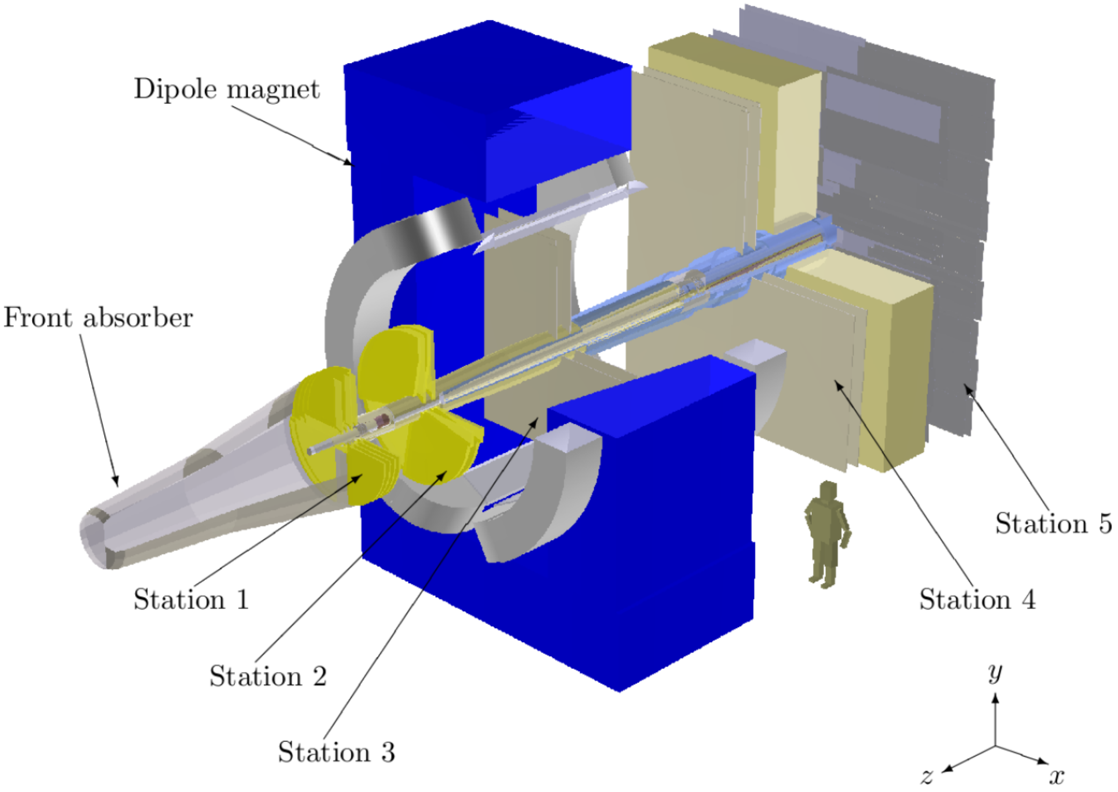

Figure 3.5: The MUON spectrometer with a standard physicist standing next to it. The dipole magnet yoke is shown in blue and the coil is shown in grey [77]. The particles pass through the front absorber to filter the muons that are detected in the tracking chambers past the dipole magnet.

enhancement as the 'smoking gun' of the QGP. Nevertheless the Muon Spectrometer will contribute to understanding of charmonium in the hot, dense medium created in Pb+Pb collisions at the LHC.

The MUON spectrometer completely dominates the C side of the ALICE experimental hall. A massive, conical iron absorber (shown in grey in Figure 3.5) filters the incoming particles so hadrons and photons cannot make it to the spectrometer[79]. The spectrometer itself consists of 10 tracking planes, the huge dipole magnet and four planes of trigger chambers. The trigger planes are shielded by a passive muon-filter wall to allow only muons to trigger the detector. There are four tracking planes on either side of the dipole magnet and two inside it. In total the tracking planes cover an area of 100 m^2. The trigger system provides six trigger signals to ALICE to allow the selection of only the events of interest to the charmonium studies.

The pseudorapidity coverage of the Muon Spectrometer is $-4.0 < \eta < -2.5$ with full azimuthal coverage [79].

3.2.3 The Forward Detectors

Studies of the forward regions at RHIC renewed the interest in forward physics. PHOBOS and BRAHMS successfully measured multiplicities, flow, and p_T spectra in the forward region to study the physics away midrapidity [51, 50]. With the BRAHMS and PHOBOS results in mind several forward detectors were included in ALICE. Since the budgets and space for these detectors were smaller the capabilities of the forward detectors are limited compared to the central region.

Forward Multiplicity Detector (FMD)

The main topic of this work is the FMD[91] and it will only be described briefly here for completeness. The FMD consists of five circular silicon planes (rings). It is equipped with 51200 channels for studies of multiplicity, number correlations, event plane, and flow. The combined FMD covers $-3.4 < \eta < -1.7$ and $1.7 < \eta < 5$ in pseudorapidity and has full azimuthal coverage. See Chapter 4 for more on the FMD.

Photon Multiplicity Detector (PMD)

The interest in studying photons is not limited to the central region. The PMD[92] adds photon detection capabilities to the forward region of ALICE. It covers $2.3 < \eta < 3.7$ and has full azimuthal coverage. The detector is composed of a gas proportional counter to detect charged particles as they enter the detector and veto them, a layer of iron and lead that absorbs charged particles and cause photons to create showers of electrons that are detected by a gas proportional counter [79]. The counters are highly granulated to allow the PMD to resolve all the distinct showers from different photons.

Zero Degree Calorimeters (ZDC)

When two nuclei collide the nucleons will form two groups: Participants that form the fireball and interact in the collision and spectators that continue down the beam line (see Chapter 1 and appendix B). The role of the ZDC[93] is to measure the spectator nucleons and hence provide estimates of the number of participants and the centrality of the collision. Assume all spectators are detected. Then the number of participants can be found from the energy deposit in the ZDC [79]:

$$E_{ZDC} = E_{beam} \times N_{spectators} \text{ and } N_{participants} = A - N_{spectators}$$

Here, E_{beam} is the energy of the beam; for the first LHC Pb+Pb run it is $E_{beam} = 2.76$ TeV/2 = 1.38 TeV. This relation is only valid for the more central collisions.

The ZDC has two subsystems: Two hadron calorimeters for detection of neutrons and protons from the colliding nuclei sitting on either side of the IP, 116 meters away. It also has two electromagnetic calorimeters (ZEM) on either side, 7 meters away from the IP. The purpose of the ZEM is to distinguish between peripheral events where the spectators are large enough (close to the Pb nuclei themselves) to escape the hadron calorimeters and continue in the beampipe and central events with very few spectators. The ZEM measure the energy of particles emitted at forward rapidities (in particular photons from π_0 decays). This energy increases with centrality so it can be used to distinguish between the two classes of events.

V0 and T0

The V0 and T0 detectors are the forward trigger detectors for ALICE[91]. The V0 is built from scintillating material connected to photomultipliers. When a charged particle traverses the scintillator it will cause emission of photons that are multiplied for detection. The V0 has a detector on each side of the IP, V0A on the A side covers $2.8 < \eta < 5.1$ and the V0C on the C side covers $-3.7 < \eta < -1.7$. Both systems are ring shaped and thus have full azimuthal coverage in their pseudorapidity coverage. While the main purpose of the V0 is to provide a trigger it is also used for centrality measurements.

The T0 has several purposes: It will provide a start time for the TOF system and measure the vertex with a precision of ±1.5cm. If it is able to find the vertex it can also provide a collision (L0) trigger. It operates two subdetectors, T0A on the A side and T0C on the C side, each equipped with 12 Cherenkov radiators connected to Photo Multiplier Tubes. The time is estimated via a mean timer as [79]:

$$t_{T0} = (t_{T0A} + t_{T0C})/2 + t_{delay}$$

where t_{delay} is the fixed offset in the analogue timer. T0A covers $4.61 < \eta < 4.92$ and the T0C covers $-3.28 < \eta < -2.97$ both with full azimuthal coverage.

3.2.4 Online Systems

Here a brief overview of the online systems in ALICE is given.

Data Aquisition (DAQ) The DAQ of ALICE has to handle data from all subdetectors at the same time as well as building final global events to be stored. Each detector is connected via Detector Data Links (DDL) to Local Data Concentrators (LDC) that handle the data blocks before they are transferred to the Global Data Concentrators (GDCs) that collect the final events.

Central Trigger Processor (CTP) The CTP handles the various low level trigger signals from the subdetectors. To ensure that only potentially interesting physics events are selected 3 steps are taken in the triggering process before an event is stored. The first level trigger, L0, must be processed at the CTP within 1.2 μs. The second level arrives after 6.5 μs while the third and final level, L2, arrives after 100 μs following the drift of particles in the TPC [46]. In section 6.1.1 the roles of the triggers in the analysis are presented.

High Level Trigger (HLT) The HLT is an online software trigger. The HLT reads directly from the data stream in the DDLs to supplement the CTP triggers. Using HLT a detailed online event display is also possible. An example is shown in Figure 3.6. The display shows an actual online reconstruction of the collision vertex.

Detector Control System (DCS) The DCS handles the actual running of the detectors as well as the full experiment (which is handled by the Experiment Control System, or ECS). It monitors all physical aspects of the running, from temperatures in the cavern to detector beam protection.

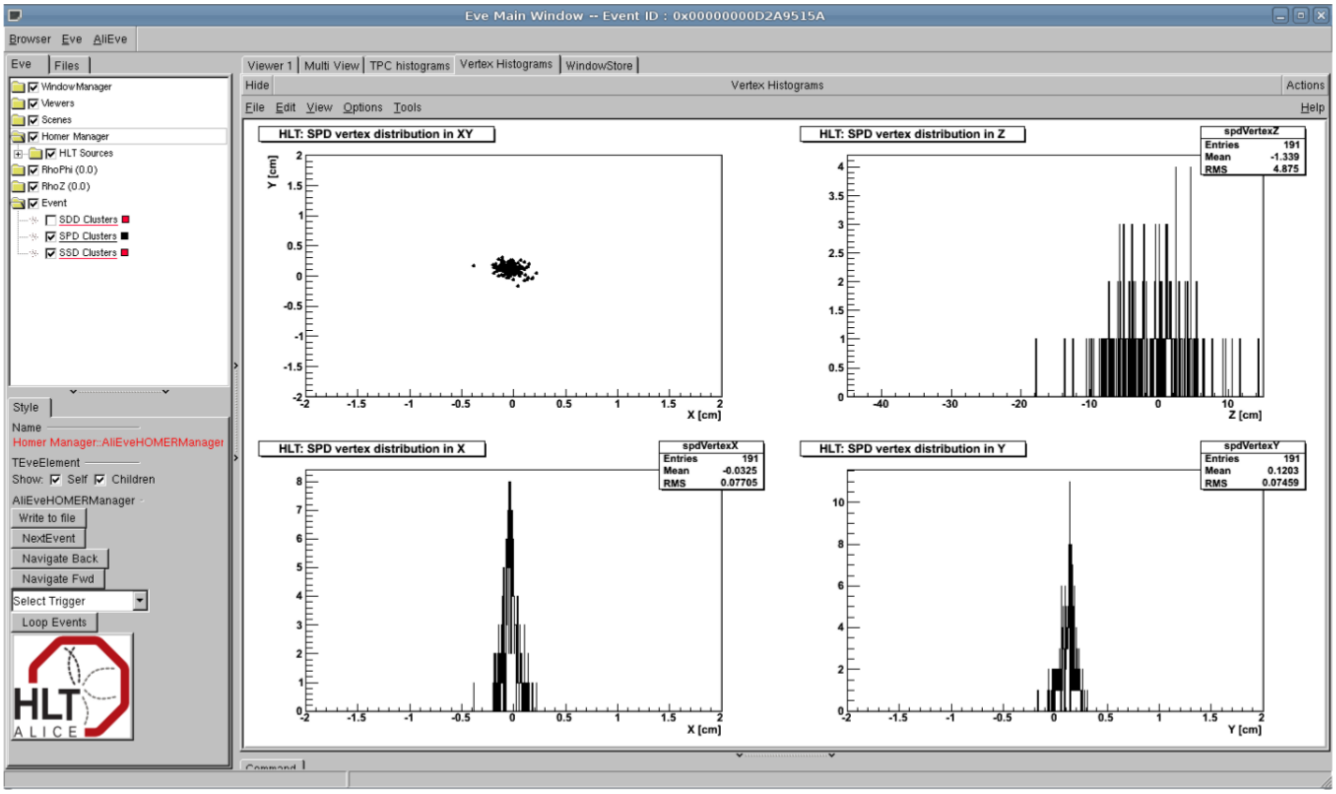

Figure 3.6: HLT event display from the ALICE control room [94]. The display shows the primary vertex distribution, reconstructed online.

Chapter 4

The FMD and SPD: A closer look

In this chapter the two ALICE detectors used for the actual measurements of charged particles, the FMD and the SPD, will be presented in more detail. We will introduce concepts on silicon detectors and describe the signals from the FMD and SPD which are the starting point for the data analysis. As an appetizer, Figure 4.1 shows images of FMD3 and the SPD as they were installed in the ALICE experimental hall.

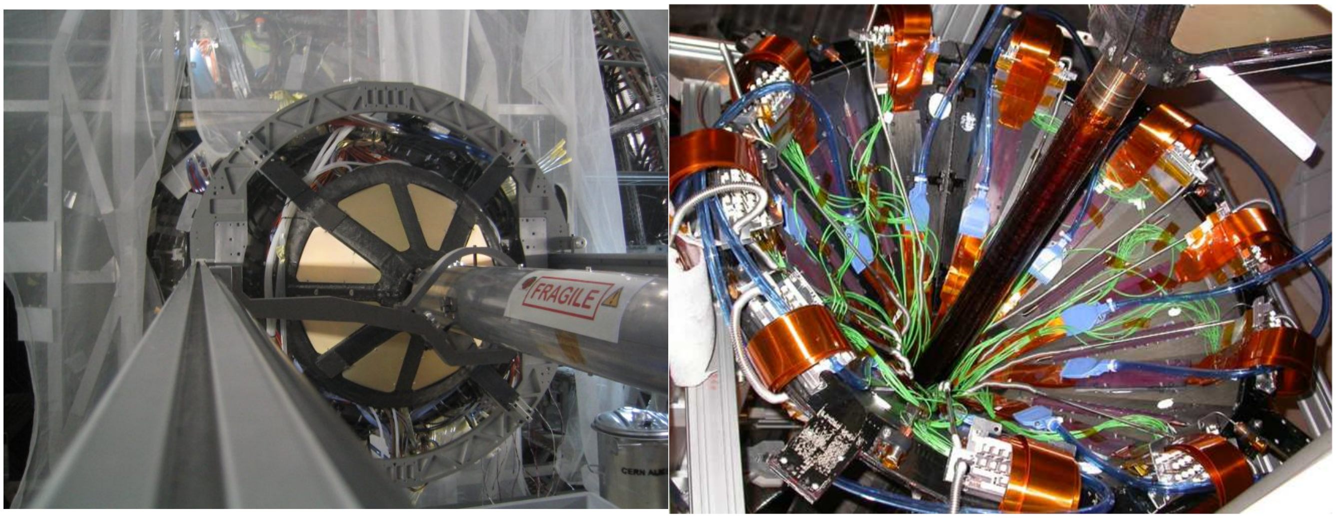

Figure 4.1: Left: FMD3 after installation in ALICE in 2007. Right: The SPD during installation in 2008. FMD3 is visible in the upper right corner.

4.1 Silicon Detectors

The FMD and SPD are silicon detectors so a review of the properties of silicon detectors is given here in preparation for the more detailed descriptions of these detectors. The concept of energy loss in absorbers is described using the theories of Bethe–Bloch and Landau.

4.1.1 Silicon as a Semiconductor

From solid state physics it is known that there are three types of solids: Conductors, insulators and semiconductors [95]. Sketches of their energy levels are shown in Figure 4.2. In the ground state the electrons of the material are located in the valence band from where they can be excited to the conduction band in the presence of a potential. Seen in Figure 4.2, the gap between the valence band and the conduction band is large for an insulator, small for a semiconductor and for a conductor the valence and

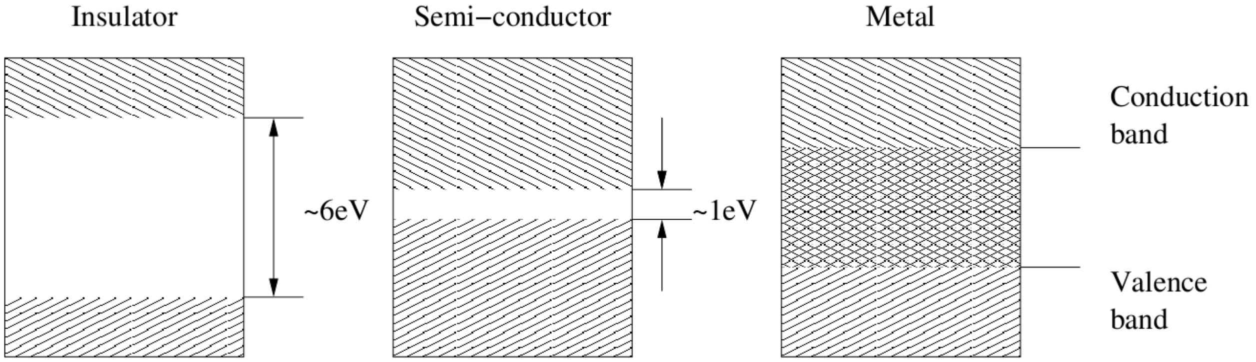

Figure 4.2: Conductor, insulator and semiconductor [77]. The boxes represent the allowed energy states and the gray areas are populations of these states. The valence band of an insulator is fully populated so ionisation requires a lot of energy. The conductor (metal) has many almost free electrons and the semiconductor has states available at the edges of the energy band.

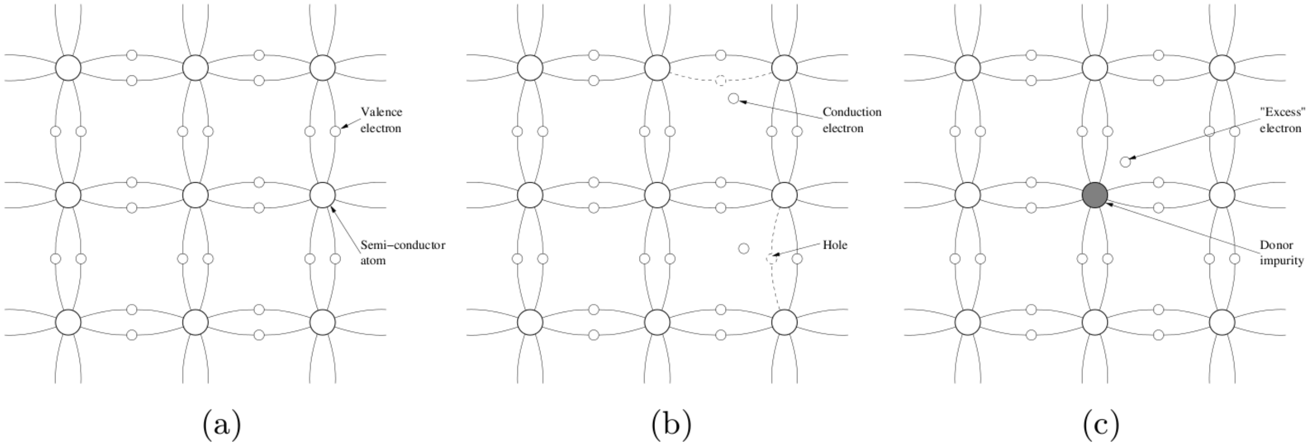

Figure 4.3: Doping [77]. Panel (a) shows semiconductor material without doping where the atoms are bound by valence electron bindings. Panel (b) illustrates the concept of a 'hole' left behind by a conduction electron. Finally, (c) shows doped semiconductor with the impurity atom inserted in the semiconductor lattice.

conduction band overlaps. This means that in the presence of a potential difference across either type of material the conductor will respond with a current while the semiconductor may respond with a current depending on if the potential is large enough to excite electrons from the valence band into the conduction band, and the insulator will in general not react with a current.

4.1.2 Doping and np–junctions

Semiconductor material can be 'doped' by inserting a small number of atoms with different numbers of valence electrons into it. Doping a semiconductor material makes it possible to create free charge in the material[1] by increasing or decreasing the number of conductive electrons. If a material is doped with material with a lower number of valence electrons than itself the resulting positive excess of charge is known as a 'hole'. By combining material doped with excess electrons (n-type material) with material

---

[1] The net charge of the material remains zero as the doping atoms will have the relevant number of positive charge in their nuclei corresponding to the free electrons.

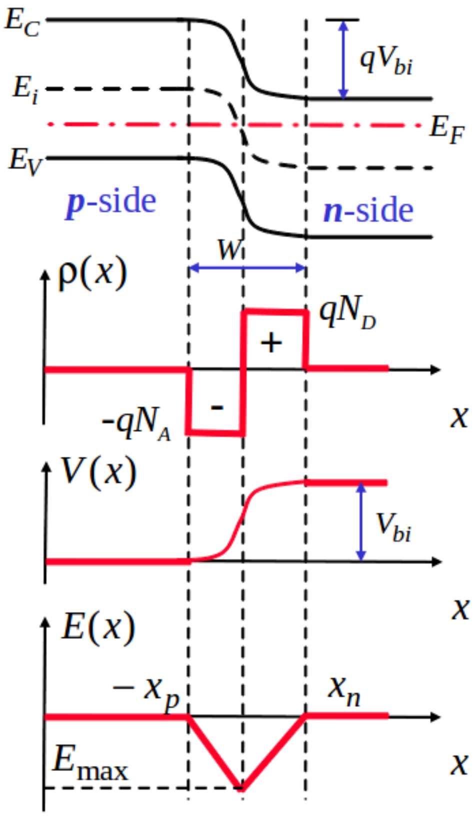

Figure 4.4: np-Junction [96]. a) The physical setup that creates the zone with zero net–charge. b) The electron energies around the Fermi level (no net charge and potential zero). c) The charge density. d) The electric field across the junction. When charge is deposited in the junction it is swept away by the field.

doped with excess holes (p-type material) an np–junction is created at the interface. Figure 4.4 illustrates the concept of an np–junction. Across the junction there is a potential difference created by the different doping of the materials. This creates the so–called depletion depth without any conduction electrons or holes as the potential changes sign across the interface. In this zone any charge induced by traversing particles interacting with the atoms will be swept away by the field. This charge can be collected and measured.

Reverse Bias Voltage To increase the depletion depth a so–called *reverse bias voltage* is applied to the n–p junction so that the depletion depth is increased.

Leakage Current In principle there should be no conduction in a n–p junction even under the influence of the reverse bias voltage. However in practical applications this does not necessarily hold. Several effects can cause a small current to flow over the junction, the most prominent being surface effects such as surface chemistry, contaminations, the surrounding atmosphere etc. [84]. Leakage Current effects will show up in data as increased noise.

4.1.3 Energy Loss in absorbers

The fundamental method of detection of charged particles in a silicon detector is through the measurement of the energy lost by the particle in the absorber. There are several mechanisms that cause charged particles to lose energy in an absorber. Examples are: Inelastic or elastic scatterings of atoms in the absorber, emission of Cherenkov radiation, or brehmsstrahlung [84]. These processes all contribute to the mean energy loss of charged particles traversing matter.

The mean energy loss through ionisation and atomic excitations per distance, $-\frac{dE}{dx}$, by charged particles traversing matter is described by the Bethe–Bloch equation [84]:

$$-\frac{dE}{dx} = 2\pi N_a r_e^2 m_e c^2 \rho \frac{Z}{A}\frac{z^2}{\beta^2}\left(\ln\left(\frac{2m_e\gamma^2 v^2 W_{max}}{I^2}\right) - 2\beta^2 - \delta - 2\frac{C}{Z}\right) \tag{4.1}$$

The quantities entering the equation are:

r_e:	classical electron radius	
ρ:	density of absorbing material	Si: 2330 kg/m^3
m_e:	electron mass	
z:	charge of incident particle in units of e	
N_a:	Avogadros Number	
β:	v/c	
I:	mean excitation potential	
δ:	density correction	
Z:	atomic number of absorbing material	Si: 14
C:	shell Correction	
A:	atomic weight of absorbing material	Si: 28.0855 u
W_{max}:	maximum energy transfer in a single reaction	

$-\frac{dE}{dx}$ is also known as the *stopping power* of the material. The term δ is a correction for density effects that take into account that the charged particles may polarize atoms in the absorber. The term $\frac{C}{Z}$ is a correction for the shell effects that arise from the assumption of Bethe–Bloch that the electrons in the atoms in the absorber are at rest.

The shell corrections are negligible for fast particles $\beta \sim c$ [84]. W_{max} is given as:

$$W_{max} = \frac{2m_e c^2\beta^2\gamma^2}{1 + 2\gamma m_e/M + (m_e/M)^2} \tag{4.2}$$

Where m_e is the electron mass and M is the mass of the traversing particle. In the Bethe–Bloch approach the particles lose energy through ionisation and atomic excitations for lower momenta. For high momenta radiation effects become increasingly important and there will be a rise in the energy loss due to this effect. Figure 4.5 shows the stopping power for μ^+ in copper where the rise in energy for high momenta is evident. For low energies the stopping power decreases with rising energies up to $3 < \beta\gamma < 3.5$ for $7 < Z < 100$. At this point the energy loss increases slightly with energy (or, $\beta\gamma$).

The minimum of the Bethe–Bloch curve for a particular particle species (p, π, K etc.) is known as the energy of a *Minimum Ionizing Particle* (MIP). So for each particle species there is an associated MIP energy for a given material. For the FMD, which is $\sim 320\mu$m thick the MIP energy for normal angle of incidence is calculated as:

$$E_{MIP} = \frac{dE}{dx}_{min} \cdot \rho_{Si} \cdot \Delta l_{Si} = 1.664\frac{\text{MeV}}{\text{g/cm}^2} \cdot 2330\ \text{kg/m}^3 \cdot 320 \cdot 10^{-6}\ \text{m} = 122\ \text{keV} \tag{4.3}$$

Here $\frac{dE}{dx}_{min}$ is the minimum of the tabulated stopping power [97].

4.1.4 Thin Absorbers

Thin absorbers are a special case when discussing energy loss especially because of the effects of delta electrons (‘knock–on electrons’) that can carry some of the energy lost by a charged particle out of the absorber. This will lead to a lower value of the expected energy loss.

The energy loss of a particular particle is a stochastic process which gives rise to a probability distribution. To distinguish different kinds of absorbers, the parameter $\kappa = \Delta/W_{max}$ is used. Here, Δ is the mean energy loss and W_{max} is the maximum energy transfer as in (4.1).

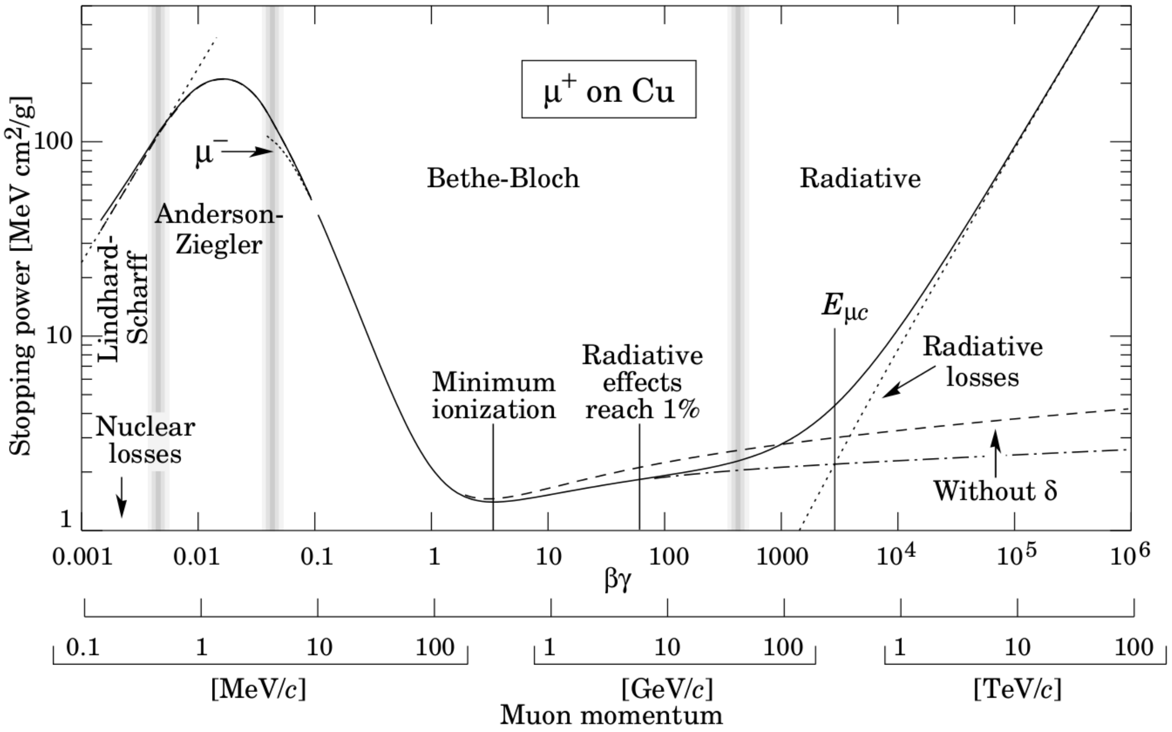

Figure 4.5: The stopping power for positive muons in copper [97]. The regime of the Bethe–Bloch approach is indicated by the vertical bars. The solid curve is the total stopping power. The radiative loss is also shown as well as the critical energy where the stopping power from ionisation and radiation are equal. Furthermore is shown the stopping power from ionisation with and without δ electrons.

For thick absorbers, $\kappa > 0.01$, the distribution of the energy deposits can be described by applying the central limit theorem, given that the number of collisions in the material is high enough. In the case of the FMD and SPD the layers of silicon are very thin ($\sim 300\ \mu$m) so the number of collisions will not be high enough for the central limit theorem to apply. One of the first theoretical treatments of the case of thin absorbers ($\kappa \leqq 0.01$) was given by Landau [98] and the following assumptions are made:

1. The maximum energy in each collision, W_{max} in Equation (4.1), goes to infinity.
2. The energy transfers are sufficiently large to treat the electrons in the absorber as free.
3. The particles passing through the absorber move at constant velocities, i.e., few interactions with low Δ.

Under these assumptions, Landau computed the relative probability for different energy losses in a very thin absorber. While later progress in the understanding of thin absorbers introduced more accurate descriptions the Landau distribution remains the safe first order approximation to the energy distributions in thin absorbers. The formal definition of the Landau distribution is [99]:

$$L(x, \Delta) = \frac{\frac{1}{\pi}\int_0^\infty \exp(-u \ln u - u\lambda)\sin(\pi u)du}{\xi} \quad \text{with} \quad \lambda = \frac{1}{\xi}(\Delta - \xi(\ln \xi - \ln \varepsilon + 1 - C)) \tag{4.4}$$

Here Δ is the energy loss, C is Euler's constant and

$$\xi = 2\pi N_a r_e^2 m_e c^2 \rho \frac{Z}{A}(\frac{z}{\beta})^2 x \quad \text{and}$$

$$\ln \varepsilon = \ln \frac{(1-\beta^2)I^2}{2mc^2\beta^2} + \beta^2 \quad .$$

I is the mean excitation potential and m is the particle mass. The *Most Probable Value (MPV)*, Δ_p corresponds to the maximum of the Landau distribution and is in general different from the mean of the distribution[2]. The left panel of Figure 4.6 shows the Landau distribution and also points out the Δ_p and the mean. It is discussed in [99] that the Landau 'peak' approaches a Gaussian in λ and that the Δ_p and ξ can be interpreted similarly as the mean and standard deviation of a Gaussian, respectively (below the Δ_p).

Landaus theory was improved by Vavilov and Shulek [100, 101] to get a better description of the energy loss in a thin absorber. It is found that a convolution of the Landau with a Gaussian should be included to account for shell effects. The case of several hits in a single sensor is also discussed. Here it is found that the energy loss distributions of multiple particles can be described as a convolution of Landau distributions (convoluted with Gaussians). A detailed derivation can be found in [102]. This means that the full functional form of the energy loss of up to N particles can be written as:

$$F_N(x; C, \Delta_p, \xi, \sigma, \mathbf{a}) = C\sum_{i=1}^{N} a_i F(x; \Delta_{i,p}, \xi_i, \sigma_i) \tag{4.5}$$

Here, $F(x; \Delta_p, \xi, \sigma)$ is the Landau function convoluted with a Gaussian for a single particle:

$$F(x; \Delta_p, \xi, \sigma) = \frac{1}{\sigma\sqrt{2\pi}}\int_{-\infty}^{+\infty} d\Delta' f_L(x; \Delta', \xi)\exp -\frac{(\Delta_p - \Delta')^2}{2\sigma^2} \quad , \tag{4.6}$$

In general $F_N(x; C, \Delta_{mp}, \xi, \sigma, \mathbf{a})$ has $N+2$ free parameters: Δ_p, ξ, the standard deviation of the Gaussians, and a_i (where a_1 can be fixed to unity). In this work we will use $N = 3$ and hence $F_N(x; C, \Delta_{mp}, \xi, \sigma, \mathbf{a})$ will have 5 free parameters.

---

[2] Formally the mean of the Landau distribution is infinite but it can be calculated if the range of Δ is limited by a cut–off.

When fitting to several Landau functions, only Δ_p and ξ of the first Landau function are free as it is shown in [102] that Δ_p and ξ of the i'th Landau distribution are:

$$\Delta_{p,i} = i\Delta_p + \xi i \ln i \tag{4.7}$$

$$\xi_i = i\xi \tag{4.8}$$

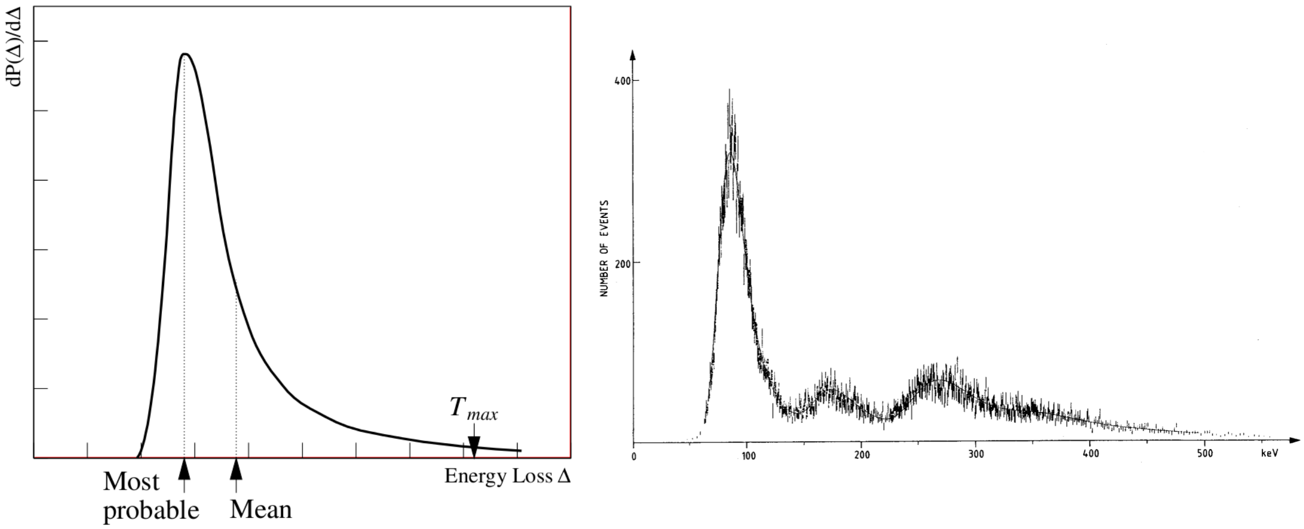

Figure 4.6: Left: The Landau distribution with the Most Probable Value (Δ_p) and the mean (calculated for $\Delta < T_{max}$) pointed out [77]. Right: Results from multiparticle fits to data with several particles impinging on a detector [100].

4.1.5 The Theories of Landau and Bethe–Bloch

The Bethe–Bloch equation describes the mean energy loss of particles in matter. Now consider ionizing particles with energies, W, of $W < W_{cut} < W_{max}$ where W_{cut} is a cut–off. The term containing W_{max} in the Bethe–Bloch equation gives the (relativistic) rise of the curve following minimum ionisation as seen in Figure 4.5. When W_{max} is replaced by W_{cut} in the Bethe–Bloch equation for the restricted energy losses the curve approaches a constant value for momenta above the momentum of a MIP. This constant value is known as a Fermi plateau [97]. The most probable energy loss of the theory of Landau reaches a Fermi plateau [97]. Figure 4.7 shows examples of the Fermi plateaus for different values of W_{cut} and for different thicknesses of silicon in the theory of Landau.

It is evident that the most probable energy loss of Landaus theory is lower than the MIP energy of the Bethe–Bloch theory. This is due to effects of δ electrons carrying energy out of the absorber and the stochastic process of energy loss in a thin absorber.

4.2 Layout of the FMD

Figure 4.8 shows a sketch of the FMD. The FMD consists of five separate rings as shown in the figure. There are two outer rings (FMD2O and FMD3O) and three inner rings (FMD1I, FMD2I, and FMD3I) in the FMD. FMD2 and FMD3 measure essentially the same region of pseudorapidity on either side of the IP even though the inner rings are positioned differently. FMD1 is located the longest distance from the IP which means that it covers the most forward region in pseudorapidity. The FMD silicon sensors are built from wafers of silicon with a thickness of ≈ 320 μm [91]. The sensors are mounted on thin ceramic

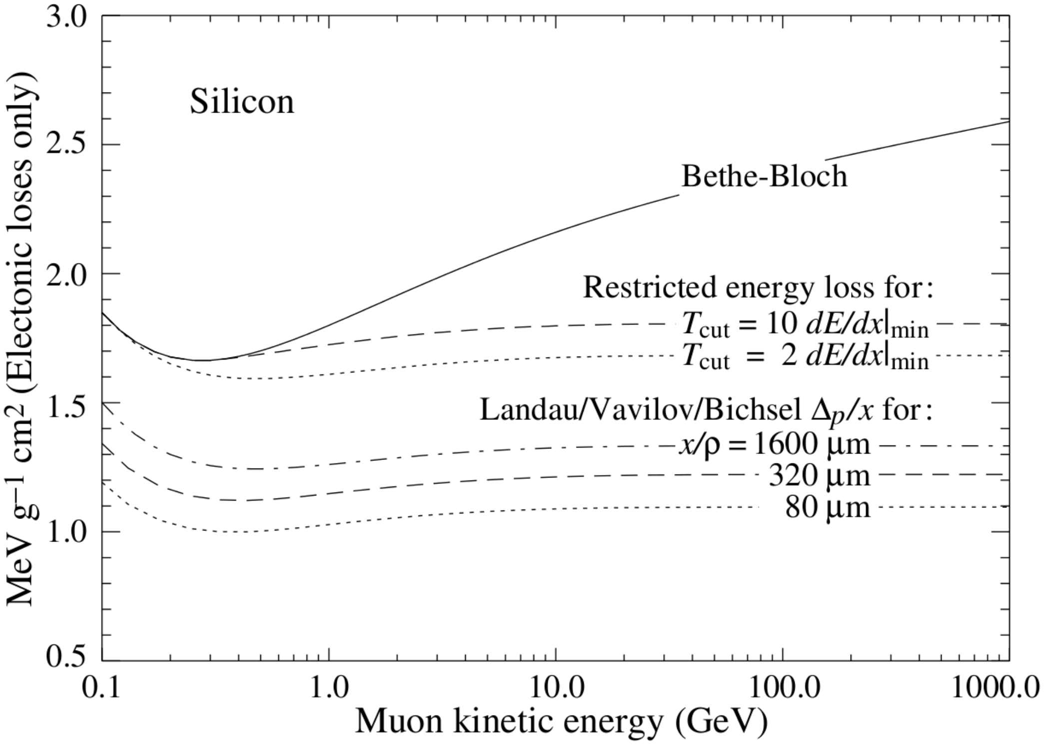

Figure 4.7: Comparison of the Bethe–Bloch curve for different values of W_{cut} and the stopping power in the theory of Landau for different thicknesses of silicon [97]. It is seen that for 320μm the Fermi plateaus in the theory of Landau are lower than for Bethe–Bloch. Again $\frac{dE}{dx}_{min} = 1.664$.

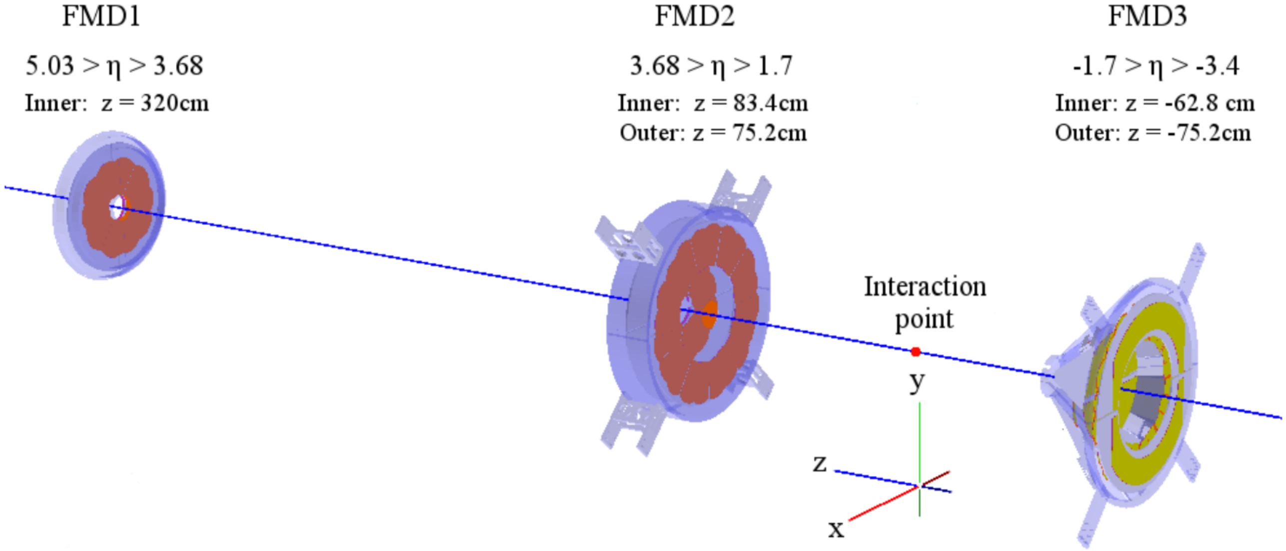

Figure 4.8: The Forward Multiplicity Detector. FMD2 and FMD3 surround the IP and FMD1 provides forward pseudorapidity coverage.

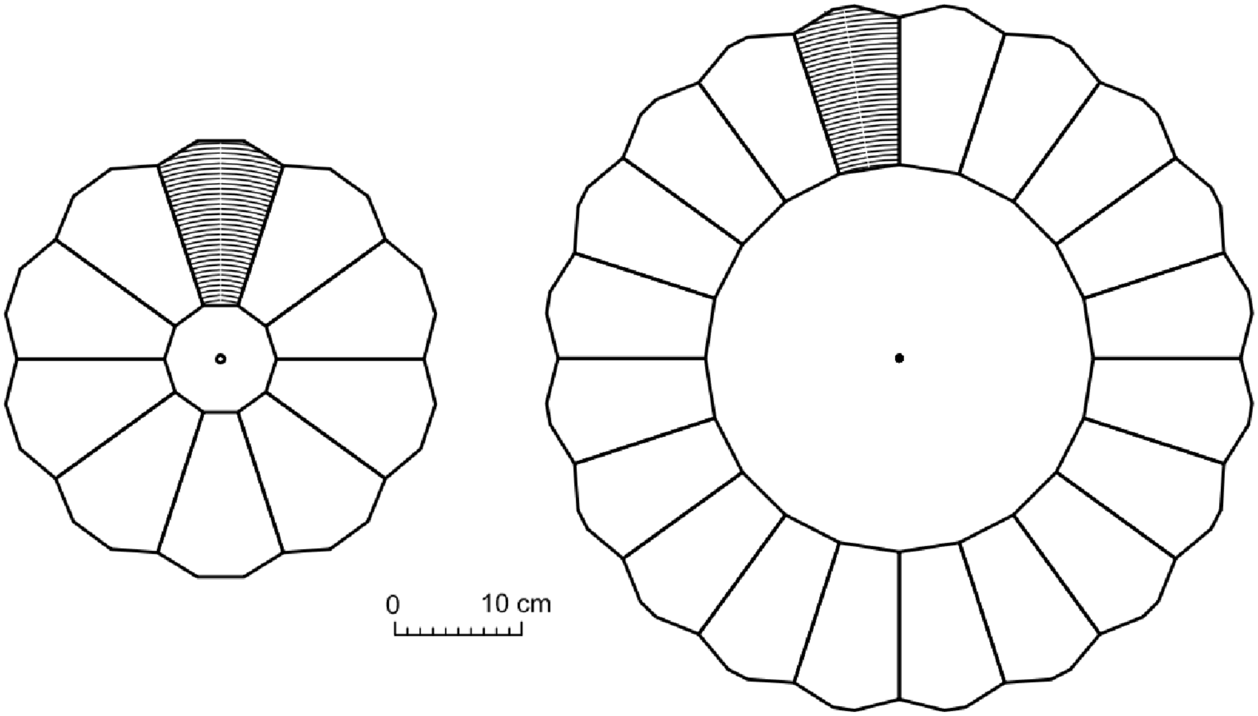

Figure 4.9: An inner ring (left) with 20 azimuthal sectors containing 512 strips and an outer ring (right) with 40 sectors of 256 strips.

	Radial Coverage (cm)	# of Azimuthal Sectors	# of radial Strips
FMD1I	4.2-17.2	20	512
FMD2I	4.2-17.2	20	512
FMD2O	15.4-28.4	40	256
FMD3I	4.2-17.2	20	512
FMD3O	15.4-28.4	40	256

Table 4.1: FMD segmentation and radial coverage [91].

spacers which are glued onto the hybrid cards containing preamplifier electronics (see Section 4.3). A sensor and a hybrid card forms a silicon module. The silicon modules are mounted on a honeycomb support structure to form the FMD rings.

Each FMD ring is segmented into 10240 separate strips. In the inner rings there are 20 azimuthal sectors with 512 radial strips each and the outer rings have 40 azimuthal sectors with 256 radial strips each. Figure 4.9 shows a close–up view of an inner and an outer ring. The segmentation and the radial coverage of each ring is shown in Table 4.1. Note that there is a radial overlap between the inner and the outer rings which transforms into an overlap in pseudorapidity. This provides a consistency check between the rings as well as to ensure a smooth distribution of measured quantities across the rings. The positions of the FMD rings as well as the pseudorapidity coverage for each ring are listed in Table 4.2. Note that the pseudorapidity overlap is much larger for FMD3 than for FMD2 due to the different relative positions of the inner and outer rings.

Ring	z(cm)	η coverage
FMD1I	320 cm	$3.68 < \eta < 5.03$
FMD2I	83.4 cm	$2.28 < \eta < 3.68$
FMD2O	75.2 cm	$1.70 < \eta < 2.29$
FMD3I	-62.8 cm	$-3.40 < \eta < -2.01$
FMD3O	-75.2 cm	$-2.29 < \eta < -1.70$

Table 4.2: FMD ring positions and pseudorapidity coverage [91].

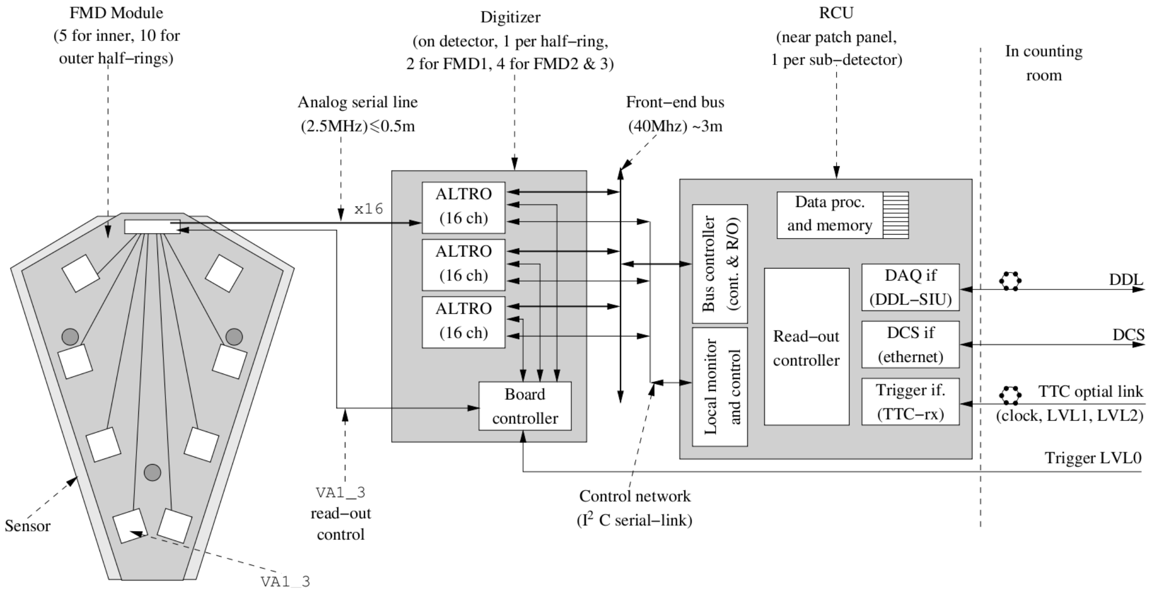

Figure 4.10: Electronics of the FMD [77]. The silicon modules are connected to the digitizer boards that send the data to the Readout Control Unit, RCU, for Data Acquisition (DAQ).

4.3 Analog and Digital Electronics of the FMD

Figure 4.10 shows a sketch of the FMD electronics. Directly attached to the FMD silicon modules are the preamplifiers that enhance the relatively weak signal from the silicon strips and shapes the signal with an exponential shape with a typical peak time of $\sim 1.5 - 2$ μs. This signal is then sent to the Analog-to-Digital Converter (ADC), ALTRO, that transforms the analog signal from the sensors into a digital signal. From here the *ADC counts* are sent to the Readout Control Unit (RCU) where subevents are assembled and sent to the DAQ for readout and storage.

4.4 Layout of the SPD

In this section we will describe the layout and workings of the SPD. Figure 4.11 shows the position of the SPD inside the ITS. The SPD consists of two cylindrical layers of silicon concentrical around the beam pipe. The basic module in the SPD is the sensor ladder consisting of $256 \times 160 = 40960$ silicon diodes. Two sensor ladders and readout electronics form a so–called halfstave The halfstaves are visible in the section shown in Figure 5.6. There are 60 full staves in the SPD, 20 in the inner layer and 40 in the outer. Due to its central position in ALICE and fast electronics the SPD generates a lot of heat. Thus, while the SDD and SSD are able to dissipate most of their heat in the endcaps the SPD dissipates most into the barrel ($\sim$ 1350 W [79]). This makes effective cooling crucial for the operation of the SPD. During the

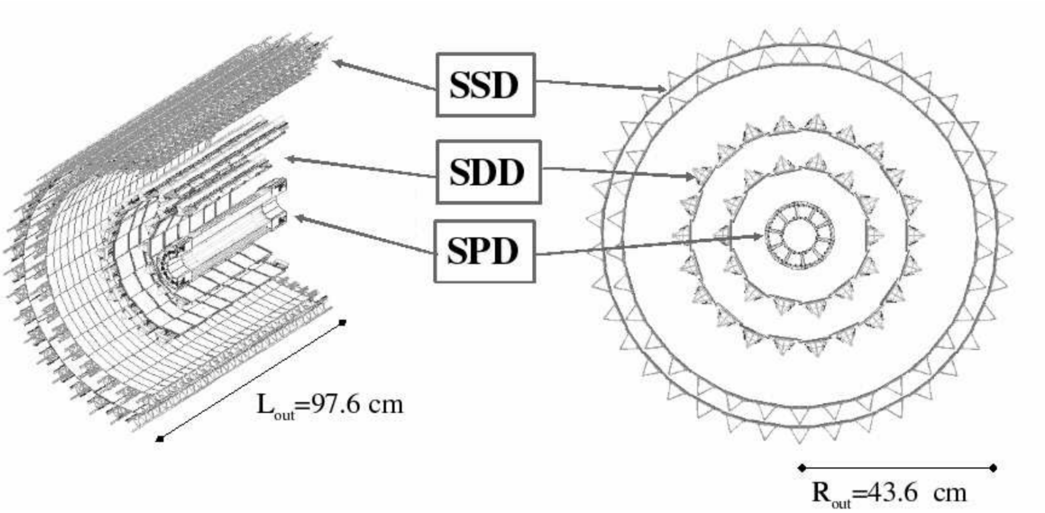

Figure 4.11: An overview of the ITS system, showing the position of the SPD [79].

Layer	Radius (cm)	$\pm z$(cm)	Area (m^2)	Channels
1	3.9	14.1	0.07	3276800
2	7.6	14.1	0.14	6553600

Table 4.3: Propertiels of the SPD layers [79].

runs of 2010 and 2011 the cooling was not sufficient so the SPD had to run without all of its halfstaves active. This is clearly visible in the data (Chapter 6).

Table 4.3 summarizes the basic properties of the two SPD layers. One immidiate observation is that the number of channels is much higher than in the FMD. As it is a pixel detector the SPD works differently from the FMD because it does not reconstruct the energy for each pixel seperately. Instead it records only hit pixels with signals above some threshold which are sent to the DAQ for storage.

Contrary to the FMD the SPD has fast readout on the frontend electronics so it can be used as a triggering system to provide L0 triggering for ALICE. The SPD provides the FAST ‘OR’ trigger that is sent to the CTP and processed with other trigger detectors.

Chapter 5

Prerequisites for Data Analysis

This Chapter sets the stage for the discussion on the data analysis itself. Simulations, analysis software and data structure will be discussed and finally the data sets for analysis are described.

5.1 ROOT

ROOT's Object Oriented Tools [103], or ROOT, is a general analysis framework developed primarily at CERN. As the name implies, it is written in the object oriented programming language, C++, and contains classes for just about any task in analysis: Data storage, data management, visualization of data as well as several mathematical and statistical tools. The ROOT project started in 1994 and has now obtained status as an independent project at CERN. ROOT is primarily used in high-energy physics but has been used in several other fields, including economics and finance.

5.2 AliROOT

The ALICE collaboration has developed AliROOT, a specific framework based on ROOT with a full representation of the ALICE detector geometry and a full simulation environment. AliROOT has been under development by the ALICE offline project since 1998. AliROOT also contains reconstruction and analysis code.

The flow of the simulation, data taking and reconstruction is shown in Figure 5.1. The important thing to note is that at the bottom of the figure the output of the simulations has the same format as the data stream coming from the DAQ. This gives the most realistic simulations and hence, the best test of the reconstruction. The purpose of the simulations is to use the best possible virtual model of the experiment to create simulated data that resemble the physics data as closely as possible. For a discussion of the simulations (the left branch in the figure) see section 5.3. The task of the reconstruction is to reconstruct the events in terms of physical observables from the raw data so that the reconstructed data contain all necessary information for analysis. Furthermore the goal is to reduce the size of the data volume so that the strain on storage becomes smaller. With Figure 5.1 as reference, Table 5.1 summarizes the steps in the reconstruction for the FMD and SPD. From the table it is seen that the reconstruction for the FMD is somewhat simpler than for the SPD. In sections 5.2.1 and 5.2.2 we will discuss the FMD and SPD reconstruction relevant for the analysis in Chapter 6.

5.2.1 From ADC counts to Energy in the FMD

The ADC counts contain all the information necessary for reconstruction of the events. However before they can be used for analysis the counts must be converted to energy deposits in the strips. To do the conversion, the counts must have the *pedestals* subtracted and be *gain calibrated*:

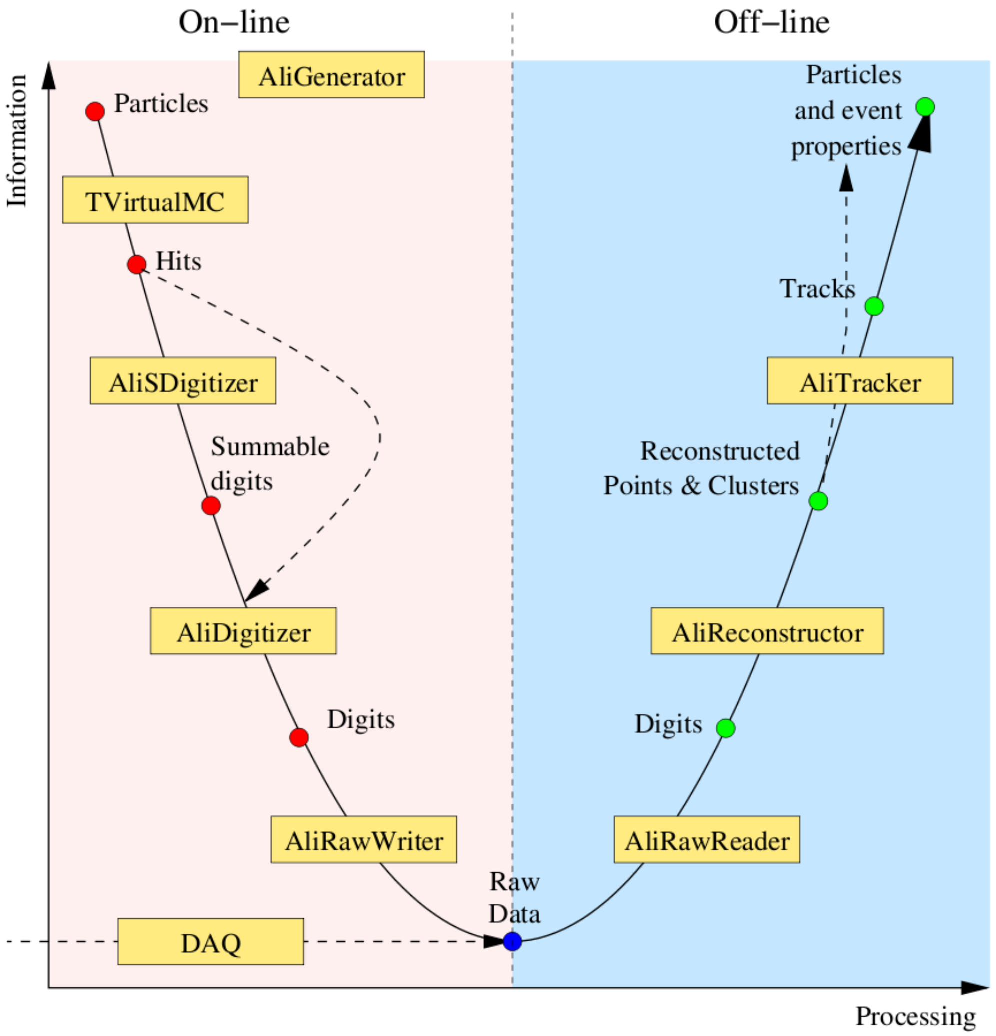

Figure 5.1: ALICE simulation and reconstruction chain [77]. As shown, there are two possible inputs for the reconstruction (right–hand branch): The physics data (DAQ) and the output of the simulations (left branch). In the simulations the primary particles are generated by an Event Generator before being transported through the detectors and support material. The signals left by the particles are then digitized and transformed into the raw data format.

Detector	Signal	Tracking	Vertex Finder
FMD	Deposited Energies, E_{dep}/E_{MIP}	None	None
SPD	Clusters Tracklets	Tracklets formed from clusters Tracklets are matched to rest of ITS for ITS tracks	Reconstruction of v_z or full vertex
	ALICE tracks	ITS tracks are matched to TPC and TRD tracks	

Table 5.1: Reconstruction Steps for FMD and SPD. Read from top to bottom the signals for the SPD become more advanced as the reconstruction progresses.

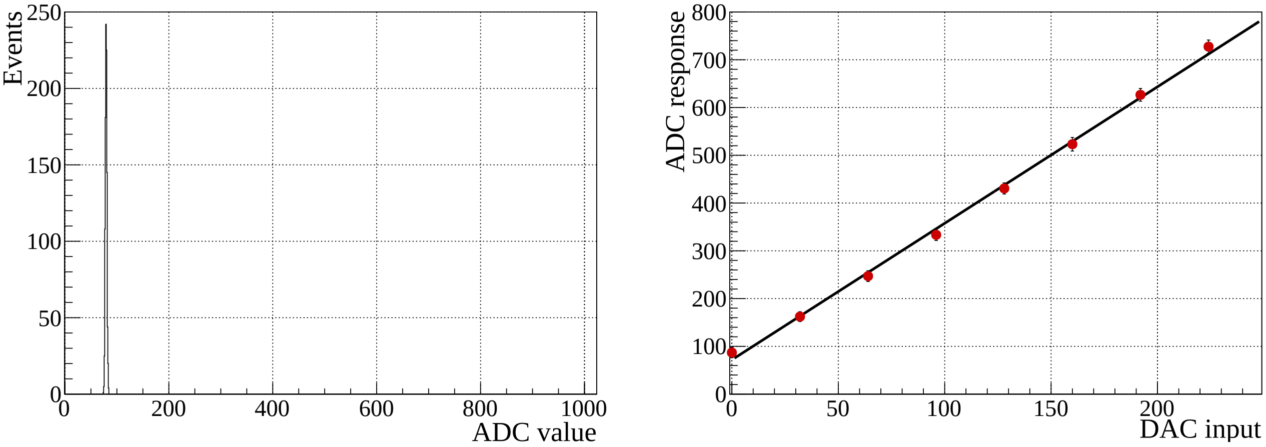

Figure 5.2: Left: The pedestal from FMD2I, sector 8, strip 3 taken in a calibration run. The pedestal is mean of the distribution and the noise is the standard deviation. Right: The gain calibration in FMD2I, sector 8, strip 3. The abcissa is the input from the pulser given as the output of the DAC (Digital–to–Analogue–Converter) of the pulser. Each point is the mean response measured in 100 events. The slope of the straight line fit is the gain calibration.

Pedestal Subtraction Pedestals correspond to base–line signals in the absence of an impinging particle. Their primary origin is the constant voltage kept over all the strips to maintain the field necessary for the detection of particles but also effects from electronic noise contribute. The pedestal must be subtracted from the signal before the conversion to energy is done. Pedestals are collected in special calibration runs for the FMD. Roughly 1000 events are taken with no beam in LHC and all channels are read out. The left panel of Figure 5.2 shows a typical pedestal from 1000 events. It is seen that the pedestal distribution is Gaussian which should be expected if the pedestals are distributed randomly.

Gain Calibration As the FMD detector system is mounted on several digitizer boards the output must be calibrated to the preamplification of each strip. This is done by using a pulser (DAC) that injects a known amount of charge into the FMD and comparing this input charge to the output data. The relation between the input charge and the output signal gives the relative gain calibration. A special calibration run is used to obtain the gain calibration. The 128 strips on the 400 VA chips are calibrated sequentially so the calibration iterates through the 128 strips on all chips at the same time. For each input value 100 events are taken to estimate the response of the strip. In total 8 different inputs are used which means at least $128 \times 8 \times 100 = 102400$ events are needed to calibrate the gain. After obtaining the 8 responses per strip they are fitted to a straight line. The slope of this line is the gain of the particular strip. The right panel of Figure 5.2 shows an example of this procedure for one strip.

The *noise* is the width of the pedestal and the signal is the Δ_p of the Landau distributed energy deposits. This defines the *signal–to–noise* ratio as the signal divided by the noise. For the FMD the signal to noise ratio has been measured to 25:1 for the outer rings and as high as 45:1 for the inner rings. Figures 5.3, 5.4, and 5.5 show pedestals, noise and pulse gain values valid for run 138225. It is seen that the pedestals, p, have values of $p \sim 100$ ADC counts, the measured noise, n, is $n \sim 2$ ADC counts in the inner rings and ~ 2.5 ADC counts in the outer rings. The gain calibration values, g, are $g \sim 3$ ADC counts per DAC input.

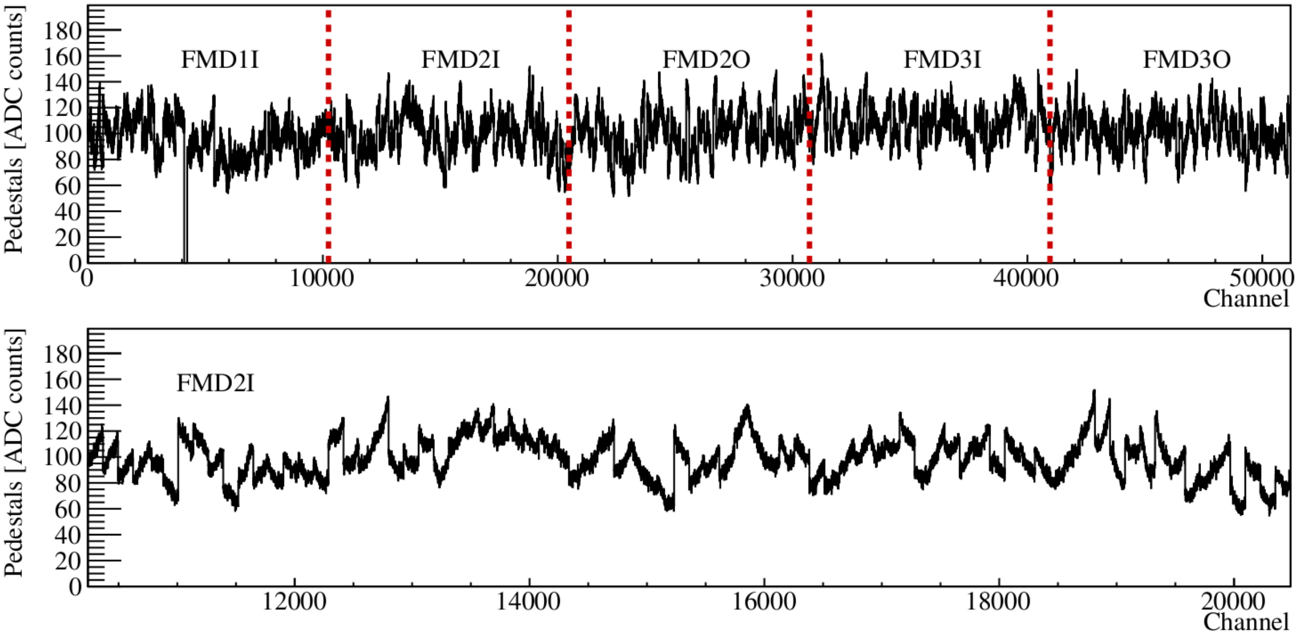

Figure 5.3: The pedestals valid for run 138225 shown for all channels in the FMD.

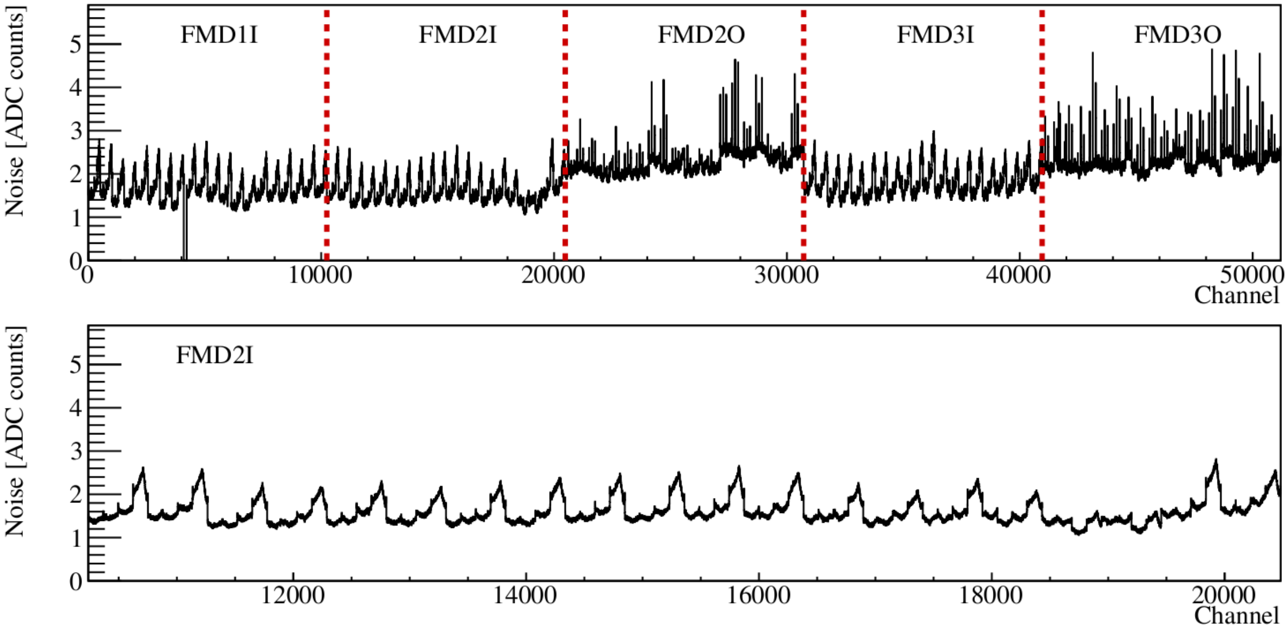

Figure 5.4: The measured noise valid for run 138225 shown for all channels in the FMD.

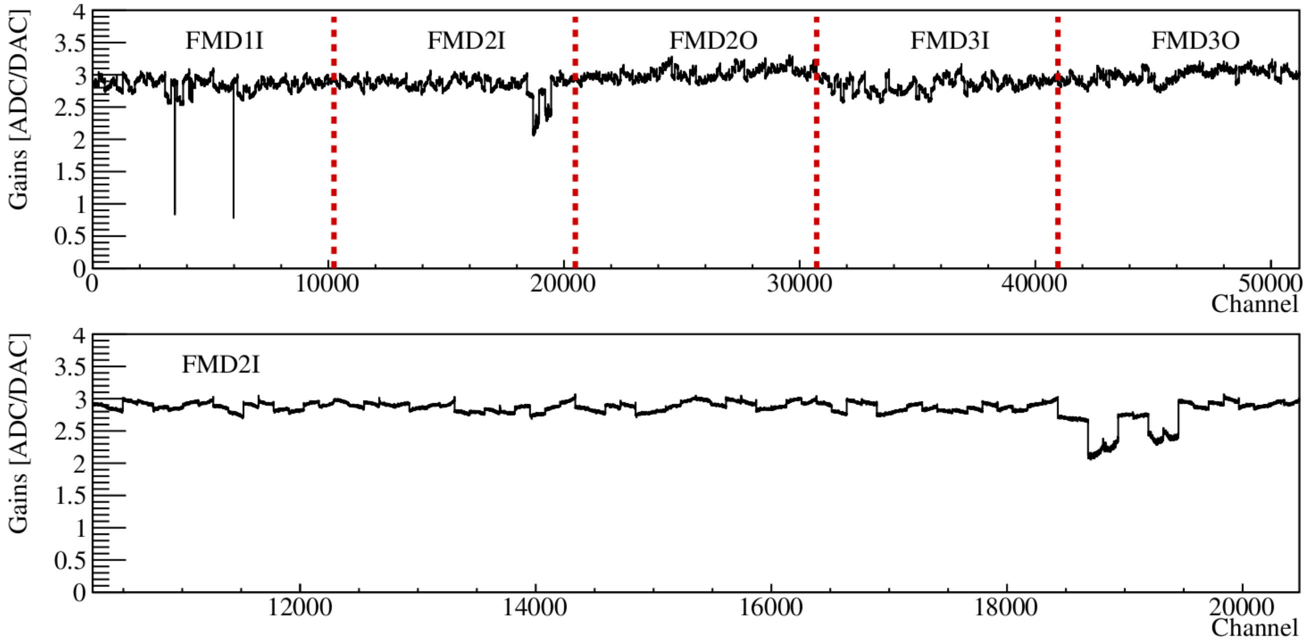

Figure 5.5: The gains valid for run 138225 shown for all channels in the FMD.

Following the pedestal subtraction and the gain calibration the ADC counts must be converted into units of energy comparable to the MIP energy. The conversion is done as:

$$E_{dep} = \frac{c_{ADC} - c_{pedestal}}{g \cdot f_{DAC-per-MIP}} \cdot E_{MIP} \tag{5.1}$$

Here, c_{ADC} is the readout ADC value, $c_{pedestal}$ is the pedestal, g is the gain of the strip. The global constant $f_{DAC-per-MIP} = 29.67$ is the proportionality factor between charge and energy in the sensors. $E_{MIP} = 122$ keV is the average energy deposit in $320\mu m$ silicon. Note that we will use E_{dep} for the measured energy loss where Δ in section 4.1.4 is understood as the theoretical energy loss.

In this work we will work with the signal in multipla of the MIP energy so that the conversion from the measured ADC counts to energy is:

$$\frac{E_{dep}}{E_{MIP}} = \frac{c_{ADC} - c_{pedestal}}{g \cdot f_{DAC-per-MIP}} \tag{5.2}$$

Most particles will hit the FMD in a not normal angle which means that they will have a longer path in the silicon than particles that hit the FMD in a normal angle. This means that the particles with longer paths will deposit more energy on average as the energy deposition depends on path length. To be able to compare all particles equally this has to be corrected for. This is done as:

$$\Delta E_{corr} = E_{dep} \cdot \cos(\theta) \tag{5.3}$$

Where θ is defined in Figure B.2 in Appendix B. In a sense this angle correction picks up the ‘normal component’ of the energy loss.

Zero Suppression

During data taking many channels of the FMD will be empty and only the pedestals would be read out. If these channels are included in the raw data the data size will be so large that the possible rate of events

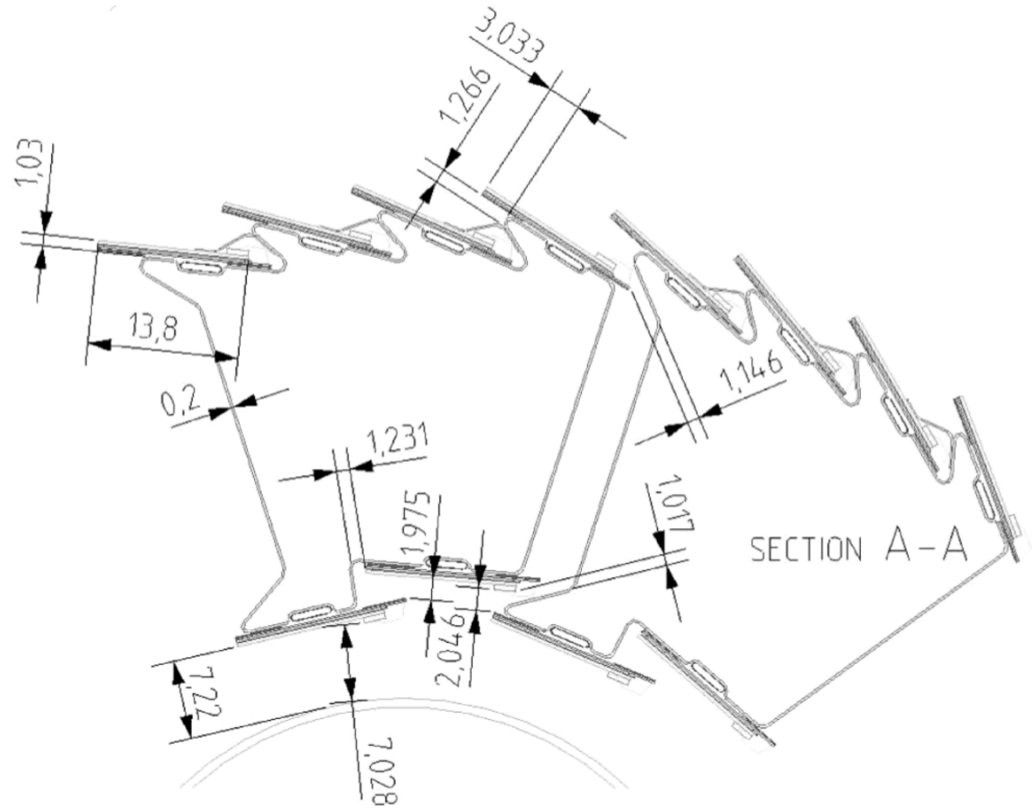

Figure 5.6: A cut through the SPD showing the positions of the Si-pixel (half)staves [79]. The beampipe is visible at the bottom. Note that the gap between the SPD and the beampipe is only ~ 7 mm so the SPD almost literally sits on top of the beampipe.

drops. To avoid this the FMD electronics perform *zero–suppression* where the pedestal subtraction is done directly in the electronics instead of offline subtraction based on calibrations. Thus, only signals satisfying $s > p + 3n$ (here s is a signal, p is the pedestal, and n is the noise) will be readout and stored – all other signals will be set to zero and compressed away. Since the pedestals are found to be distributed as a Gaussian (see Figure 5.2) this should remove 99.85% of the empty channels. For practical purposes the readout signals become $s = c_{ADC} - c_{pedestal} - 3n$. In the reconstruction the $3n$ will be added back into the signals.

5.2.2 Cluster and Vertex Reconstruction in the SPD

By design of the detector charged particles can deposit energy in several neighbouring pixels while crossing the SPD layers. This means that particles can be reconstructed by counting 'clusters' ie. groups of hit pixels. Using the clusters in the two layers socalled 'tracklets' can be found by combining the clusters of the two layers and the primary vertex. This is a very powerful method for analysis since it immidiately selects only primary particles with very high efficiency [46]. In this work we will focus on using the clusters of the inner layer as the basic input of the analysis.

The summary of a study of the SPD clusterizer in test–beam data and in simulations is shown in Figure 5.7. It shows that the various possible found clusters are well understood and that the majority of the clusters consist of 1 or 2 pixels fired.

Furthermore as mentioned in section 3.2.1 the SPD can measure the primary vertex position. The procedure is summarized in Figure 5.8. The point of intersection between the most of the tracklets is taken to be the vertex.

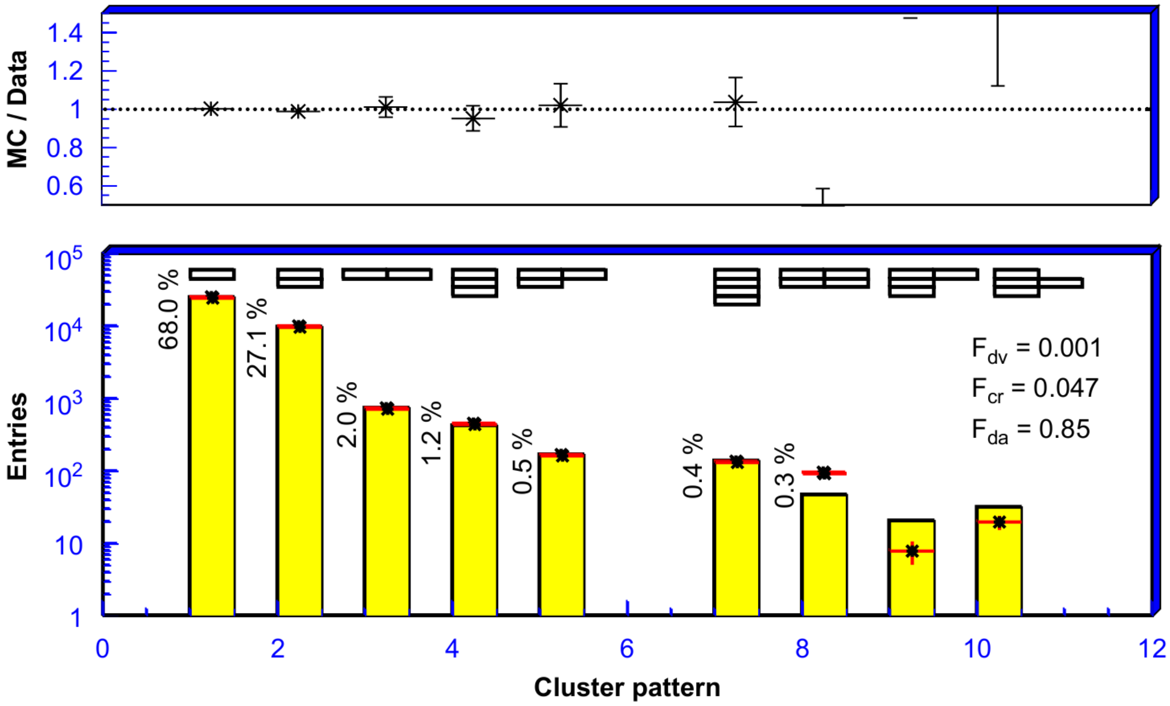

Figure 5.7: The figure shows a summary of a study of the SPD clusterizer in test–beam data and in simulation [104]. Bottom panel: The obtained results for different cases of clusters. The points are from the data and the red bars are from simulation. The fractions indicate the relative contributions of the cluster patterns. Top panel: The ratios of the results from the bottom panel. It is seen that there is very good agreement between data and simulations.

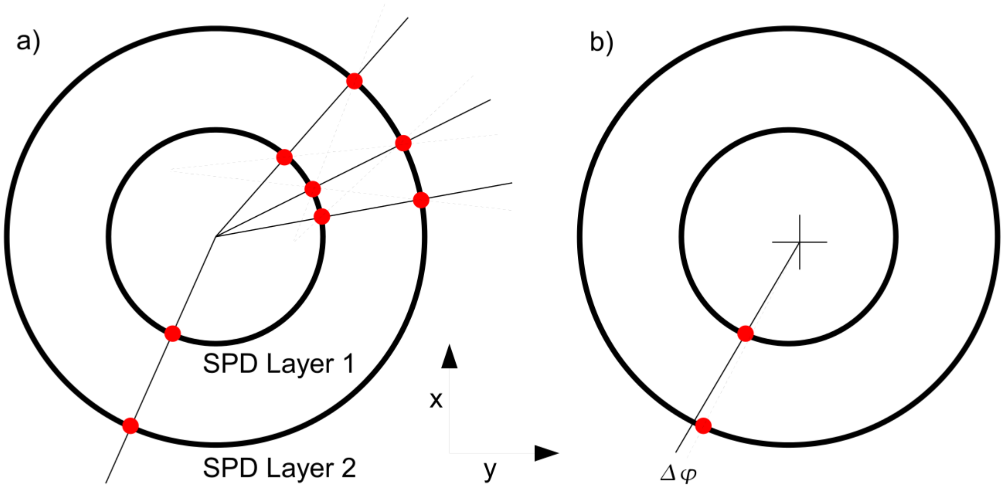

Figure 5.8: The SPD vertex determination [46]. Left: Tracklets are found from the clusters in the SPD layers and the vertex position is determined as the intersection between most of them. Right: The tracklets have to satisfy a requirement not to curve too much in ϕ.

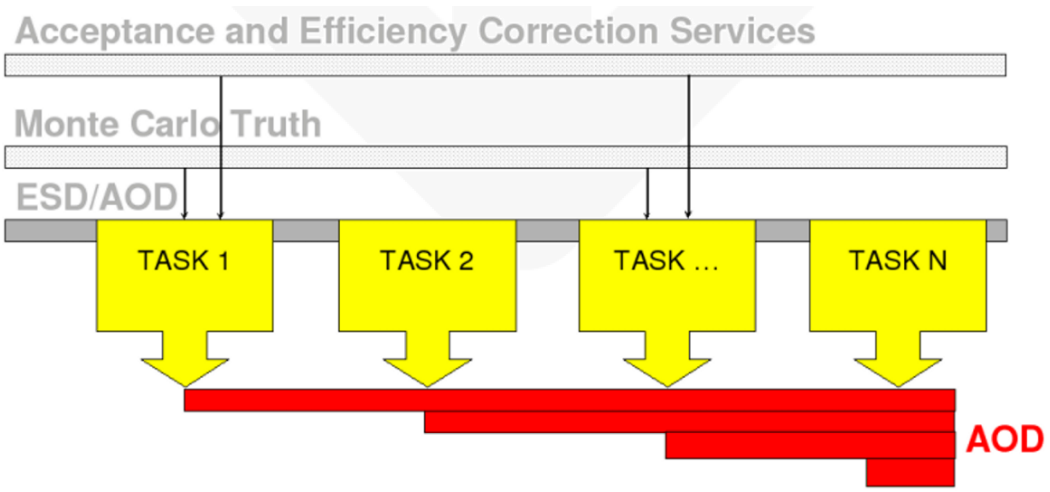

Figure 5.9: Illustration of the analysis train [105]. The analysis manager loops over the ESD or AOD input and the simulation output if applicable and managers input/output. The tasks are limited to their own part of the analysis and are independently adding results to the output AOD. Tasks can also connect to each other so that one task takes the output of another task as input during analysis.

5.2.3 Event Summary Data (ESD)

Following the reconstruction the data are stored in the ESD format. The idea of the ESDs is to have available all data to be used for *any* analysis. This includes trigger information, vertices from several detectors, tracks, PID etc. The ESDs are the fundamental starting point for all analysis in ALICE.

5.2.4 Analysis Object Data (AOD)

While the ESDs contain everything the concept of AODs is to have available all data needed for some specific analysis. This makes the AODs more flexible since an analysis can take AOD objects as input to produce AOD files with more refined analysis, different cuts etc. It is possible to reduce the amount of data enough that analysis on AODs can be performed on a workstation or laptop. Local analysis of larger data samples at the ESD level is in general quite demanding for even a high–end desktop computer. Special tools are required to create AODs from ESDs accurately, efficiently, and on reasonable time–scales, see section 5.4.

5.2.5 The ANALYSIS framework

The AliRoot component dedicated to the analysis of physics (and simulated) data is the ANALYSIS framework. The framework handles the creation of AODs from ESDs and is versatile to allow very different analysis to run in the same framework without limiting some to the requirements of others. To analyze data so–called 'analysis trains' are run over the data. Figure 5.9 shows the concept of the analysis train and illustrates the train analogy. In this analogy the 'engine' of the train is the *analysis manager* class, that handles input/output for all the 'cars' attached to the train and performs the actual loop over the data. Here, the cars are the *analysis tasks*, pieces of user code that performs the actual analysis. Each analysis task handles one kind of analysis and in this way the tasks are independent of the environment or actual data sets which are handled by the analysis manager. The analysis presented in Chapter 6 makes full use of this framework.

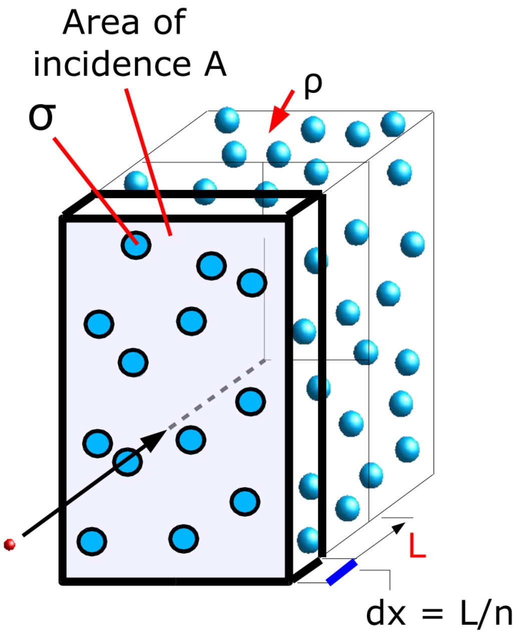

Figure 5.10: Interaction of a charged particle with matter. A charged particle (left corner) traversing a block of material with density ρ, length L, divided into n slabs of thickness $dx = L/n$.

5.3 Monte Carlo Simulations in AliROOT

One of the most important components of AliROOT, the simulations[1], are used extensively for the analysis presented in this work. The simulations represent the best understanding of the experiment and are used for corrections, comparisons and for the study of detector effects. For an illustration of the different steps in the simulations see the branch to the left in Figure 5.1.

5.3.1 Event Generators

The first thing required for simulation of a physics event in ALICE is obviously a physics event. The decision of the composition and interactions of the physics events is made in a so–called event generator, a program that has a number of possible physics processes available with a probability given by the theoretical knowledge of that process. Alternatively the probabilities of specific types of events can be altered to increase the number of such events generated.

The event generators used for the simulations used in this work have been presented in section 2.3. We use HIJING for generation of heavy ion events, and PYTHIA and PHOJET for generation of p+p events. For the p+p events PYTHIA is used only for the data at $\sqrt{s} = 2.76$ TeV due to a lack of proper ALICE simulations with PHOJET at that energy. We prefer PHOJET since it is known to give a better description of diffractive processes than PYTHIA[2]. The output of the event generator is in essence the 4–momentum vectors of the primary particles, possibly amended by additional per–particle or global properties.

5.3.2 Transport code and GEANT

Following the event generation the generated primary particles must be propagated through the virtual model of ALICE to simulate the effect of the interaction of the particles with the detector material. These interactions are handled by the software library, GEometry And Tracking, GEANT, developed at CERN [106]. ALICE uses GEANT3 for the simulations while a newer version, GEANT4, is being evaluated.

---

[1] The simulations relies on drawing of random numbers and Monte–Carlo techniques so in daily language the simulations are often referred to as ‘Monte–Carlo simulations’ or just ‘MC simulations’.

[2] Peter Skands, private communication.

GEANT handles interactions of charged particles in an effective way. To give an example of such an approach consider the sketch in Figure 5.10 (inspired by [107]). Here, a charged particle traverses a block of material with density ρ, length L, divided into n slabs of thickness $dx = L/n$. Inside the material are 'obstacles' (atoms) with transverse area σ and the total transverse area is A. What is the probability of an interaction of the charged particle with one of the obstacles? Each block contains N_0 obstacles, calculated as:

$$N_0 = \rho A dx = \frac{\rho A L}{n} \tag{5.4}$$

With the area of the obstacles, $A_{obstacles}$ given by $A_{obstacles} = N_0\sigma$ the probability of hitting an obstacle is:

$$P_{hit} = \frac{A_{obstacles}}{A} = \frac{N_0\sigma}{A} = \frac{\rho L\sigma}{n} \tag{5.5}$$

$$P_{no-hit} = 1 - \frac{\rho L\sigma}{n} \tag{5.6}$$

Here P_{no-hit} is the probability of not hitting any obstacle in the slice. Now, the probability of no interaction in the n slices of the block becomes:

$$P_n(L) = P^n_{no-hit} = (1 - \frac{\rho L\sigma}{n})^n P(L) = \lim_{n\to\infty}(1 - \frac{\rho L\sigma}{n})^n = \exp(-\rho L\sigma) \tag{5.7}$$

Thus, the probability to have an interaction after distance x becomes:

$$p_{interaction} = 1 - P(x) = 1 - \exp(-\rho x\sigma) \tag{5.8}$$

The flow of an effective method is then:

1. In step n
2. Get values of ρ and σ for current material
3. Propagate the particle in steps of Δx until interaction with probability $p_{interaction}$ (probabilistic). The length of the step for each iteration depends on the possible interactions, the material traversed etc.
4. Simulate interaction (probabilistic)
5. If new particles are created put them on stack and resume
6. If particle survives the interaction repeat the process or start over with the next particle on the stack

This is of course a simplified model but it serves as illustration of the processes that take place millions of times during an ALICE simulation. During the transport of particles through ALICE GEANT maintains a the so–called 'stack' of particles and each time a new particle is created it is put onto the stack for later processing. The transport of particles continue until no particles are left on the stack.

GEANT is interfaced by a virtual base class defined in ROOT shown in Figure 5.1. The advantages of such an implementation is that it is possible to replace GEANT3 of ALICE with another transport code on the market, such as for example FLUKA or GEANT4 without having to make changes to the simulations themselves.

After the GEANT propagation the simulated data contains 4–vectors of all particles that were produced during the simulation as well as other information such as e.g. hits in the detectors, including information about position and energy loss.

5.3.3 Simulating detector response

The final parts of the left hand side of Figure 5.1 are concerned with the transformation of the deposited signals from the transport code into the format of the physics data. For the FMD this takes place by reversing (5.1). The transport code leaves behind deposited energies, $\Delta E_{deposit}$, in the FMD silicon which must be converted into ADC counts (digits). This is done as follows:

$$\begin{aligned} \Delta E_{deposit} &= \frac{c_{ADC} - c_{pedestal}}{g \cdot f_{DAC-per-MIP}} \cdot E_{MIP} \rightarrow \\ c_{ADC} - c_{pedestal} &= \frac{\Delta E_{deposit}}{E_{MIP}} \times (g \cdot f_{DAC-per-MIP}) \end{aligned} \tag{5.9}$$

To simulate the measured detector noise $c_{pedestal}$ is replaced with a random number $f_{pedestal}$ selected from a Gaussian function $\exp -\frac{(c-\mu)^2}{2\sigma^2}$ with $\mu =$ pedestal and $\sigma =$ noise. This means that the final simulated ADC value becomes:

$$c_{ADC} = \frac{\Delta E_{deposit}}{E_{MIP}} \times (g \cdot f_{DAC-per-MIP}) + f_{pedestal} \tag{5.10}$$

Returning to Figure 5.1 the term ‘Digits’ correspond to the ADC value in (5.10) while the summable digits, ‘SDigits’, are created using the measured pedestal with no noise smearing. Summable digits are needed for studies of embedding and event mixing. As indicated in the Figure the creation of summable digits is not essential for the simulation of digits so it can be skipped.

Following the creation of digits the transformation to raw data is mechanical. The digits are written in the standard FMD raw data format and can now be processed completely like the physics data.

5.4 The GRID and AliEn

One of the big challenges in the running of the LHC experiments is the sheer data volume and the computing power required to actually process it. For previous high–energy physics experiments it has been possible for a single University or Laboratory to provide sufficient computing power and storage. This is almost impossible with the coming of LHC. The annual production of data from LHC has been estimated to take up 1 PB (Peta–Byte[3]) of storage. Considering that the storage requirements must include backup and space for users and derived data this is too high for any single standard computing facility to handle. Furthermore the processing of this amount of data is impossible as a single job in a single computing center. The answer to these challenges are *parallelization* and *GRID computing*. The ALICE implementation of these concepts is called the ALICE Grid Environment, or *AliEn*.

Parallelization Parallel computing allows the computation of complex tasks over large quantities of data by running parts of the computation in parallel splitting the load over many CPUs. The user specifies the requirements for the job and provides scripts and programs as needed. The job is then executed as a number of sub–jobs running in parallel[4]. The advantage of such an approach is that the basic unit of a computing center can be ordinary computers with regular CPUs and hardware. This reduces the cost of these facilities compared to the costs of supercomputers and the like. Parallel computing is possible at many computing centres around the world.

GRID The key concept behind the World Wide Web (WWW) was the sharing of information across the world quickly. The user requests a webpage or file from some homepage and does not care where the information or file exists in the physical world. The idea behind GRID computing is to expand this

---

[3] 1 PB = 1024 × 1024 GB

[4] This could be considered a different kind of parallelization than ‘classical’ parallelization where a shared memory is often required between the jobs.

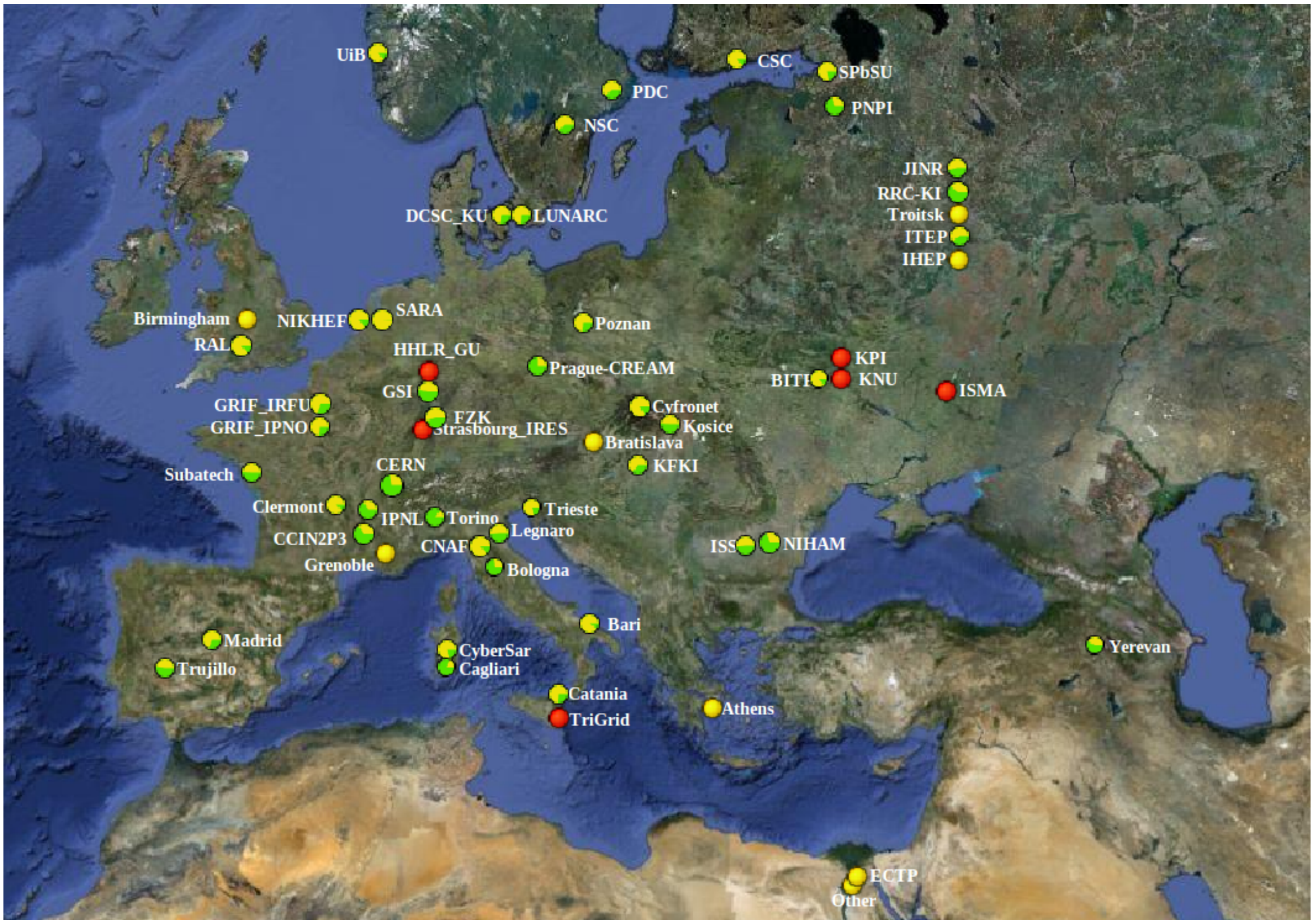

Figure 5.11: The figure shows an overview of the AliEn operations in Europe August 2 2011 around noon [108]. The circles show the activities at the various computing centers. Red circles show no job execution while the yellow and green circles show job execution with some but not full efficiency.

Collision System	$\sqrt{s_{NN}}$	Run Numbers	Number of events
p+p	900 GeV	118506, 118507, 118518, 118556, 118560	4.7M
p+p	2.76 TeV	146805, 146806, 146817	11M
p+p	7 TeV	119159, 119161, 119841, 119862	9.3M
Pb+Pb	2.76 TeV	138190, 138192, 138197, 138201, 138225	1.8M

Table 5.2: Data sets for analysis.

concept to include computing power as well as information (data). So in a GRID system the user does not care where the data or computing resources are located. Similarly to the WWW the user specifies the data to be analysed and the specifics of the analysis and leaves the details to the GRID system. The GRID system then looks up the data and books the computing power in computing centres around the world before distributing the jobs. The job output ends up in some storage element where the user can pick it up, merge it[5] or analyse it further. GRID systems put high demands on network connections between the involved centres since a user present in Copenhagen may request data stored in Japan which will be analysed in Germany while the output ends up in Hungary. From the user perspective this is of no importance since the overall virtual filesystem allows access to the output from all over the world.

AliEn The ALICE implementation of a GRID system is called AliEn (ALICE Environment) and is based on web services and standard protocols. The advantage of this approach is that ALICE could deploy a working prototype fast and begin exploring the possibilities in GRID computing. Thus, in 2004 the first 400.000 analysis and production jobs had been run in AliEn [109]. AliEn implements a virtual filesystem so that the users always have access to their jobs and data as well as a package manager for preinstalled software and a ressource broker to divide the jobs and distribute the computing power between the users. The 3 main tasks of AliEn are the reconstruction of physics data, the simulation of physics events in ALICE and the analysis of data all of which are ideally suited to parallel computing. The ANALYSIS framework is completely integrated with AliEn to allow optimal performance for analysis. All results presented here are obtained using the ANALYSIS framework in AliEn. AliEn also implements monitoring of its services using MonALISA (Monitoring A Large InfraStructure Architecture). An example of this monitoring is found in Figure 5.11 which shows all the European AliEn centres and their status[6].

5.5 The Data Sets

The data sets that will be analysed in this work are shown in Table 5.2. The sets have been selected so that for each setting there will be more than sufficient statistics for a proper measurement of $dN_{ch}/d\eta$. The p+p data at $\sqrt{s}$ = 900 GeV and $\sqrt{s}$ = 7 TeV as well as the Pb+Pb data were taken during 2010 while the p+p data at $\sqrt{s}$ = 2.76 TeV were collected after the winter shutdown in 2011. To support the selected data sets Table 5.3 shows the selected simulations from official ALICE simulation productions. The selected productions are all using settings identical to the data runs selected. In this way the simulated data are ‘anchored’ to the physics data; thus productions run in this way are known in ALICE as ‘anchor runs’.

---

[5] due to the parallel computing, there will be many output files with similar content that must be merged

[6] Outside the map there are also centres in the USA, South Africa, Egypt, China, Korea, Japan, India, and Pakistan.

Collision System	$\sqrt{s_{NN}}$	MC production	Generator	Number of events
p+p	900 GeV	LHC11c1	PHOJET	2M
p+p	2.76 TeV	LHC11b10a	PYTHIA	5M
p+p	7 TeV	LHC11b6	PHOJET	5M
Pb+Pb	2.76 TeV	LHC10h8	HIJING	100k

Table 5.3: Simulation Productions for analysis.

Chapter 6

Data Analysis

In this Chapter the data analysis of 2010 and 2011 LHC data will be presented. Due to the volume of this chapter it begins with an overview:

Event Selection is discussed in section 6.1 and includes trigger, vertex, and centrality selection of events. This is the starting point of the analysis as only selected events contribute to the final $\frac{1}{N}\frac{dN_{\text{ch}}}{d\eta}$.

Counting Particles in the FMD is described in section 6.2 which covers the conversion of the deposited energies into N_{ch}. This process involves hit merging and a correction for high occupancy.

Counting Particles in the SPD is covered in section 6.3. Here, the counting of clusters to get N_{ch} is discussed. The SPD analysis works from the clusters in the ESDs.

Correcting for Secondaries is a crucial step in the analysis and it is discussed in section 6.4. The correction includes effects of secondary particles from the detector material and decays of short lived particles.

The Calculation of $\frac{1}{N}\frac{dN_{\text{ch}}}{d\eta}$ is described in section 6.5. This includes a discussion on the calculation of the number of events. Furthermore the subtraction of beam–gas and beam–halo events is discussed.

Final Corrections from Simulations are described in section 6.6. These include corrections for trigger and vertex bias in p+p collisions and a correction for enhanced production of secondary particles with strangeness measured by ALICE.

Systematic Errors are covered in section 6.7. Systematic errors from all of the above are described and evaluated.

An overview of the programs and C++/AliROOT code used for this analysis is found in Appendix C. Some Figures have been included for completeness in Appendix F.

6.1 Event Selection

In this section the details of the event selection will be discussed. This includes trigger conditions with rejection of beam background (beam-halo events), vertex selection, and for the analysis of Pb+Pb data, the centrality of the collisions.

6.1.1 Trigger Selection

The first step of the analysis is the trigger selection. The selection of Minimum Bias events is made in the ANALYSIS framework (see Section 5.2.5) and the framework automatically deals with the varying settings of the trigger detectors run by run.

Data set	Basic Trigger Condition	Main MB trigger mask
p+p @ $\sqrt{s} = 900$ GeV	V0A or V0C or SPD	CINT1B-ABCE-NOPF-ALL
p+p @ $\sqrt{s} = 2.76$ TeV	V0A or V0C or SPD	CINT1-B-NOPF-ALLNOTRD
p+p @ $\sqrt{s} = 7$ TeV	V0A or V0C or SPD	CINT1B-ABCE-NOPF-ALL
Pb+Pb @ $\sqrt{s_{NN}} = 2.76$ TeV	2 of the following: SPD hits in outer layer > 2 V0A V0C	CMBACS2-B-NOPF-ALL
NSD @ p+p	(V0A and V0C) or SPD hits > 5	N/A

Table 6.1: The trigger conditions for this analysis. The right column consists of the 'trigger words' that summarize the conditions of the trigger separated by dashes. The first part is the condition for MB from the second column ('Basic Trigger Condition') plus the information from LHC that there was a bunch crossing ('B'), the second part is a flag for which partitions were active. 'NOPF' is short for 'No Past–Future Protection', and finally the last part tells which trigger detectors were active in the particular trigger mask.

In this analysis we are interested in the inelastic and NSD event samples for p+p collisions and the Minimum Bias (MB) event sample for Pb+Pb collisions. The inelastic and MB samples are the collision candidates with the least strict selection criteria in order to get a sample with the least possible bias. For p+p data the NSD selection takes place on inelastic events that satifies the NSD conditions given in Table 6.1 The trigger selection takes place twice as described in the following. First, during data–taking the trigger detectors are formed into so–called trigger words that will give an online signal when the trigger detectors fire in accordance with the trigger mask. These online signals are stored along with the event data. Secondly, during event selection the trigger conditions are recreated using the reconstructed signals from the trigger detectors. Events that fulfill this off–line trigger condition and the proper trigger mask are selected for analysis. Table 6.1 summarizes the trigger conditions used here.

Trigger Efficiencies

The fundamental trigger efficiency of a trigger class, C, is defined as:

$$\epsilon_C = \frac{N^C_{detected}}{N^C_{true}} \qquad C = \text{INEL,NSD,...} \tag{6.1}$$

Here $N^C_{detected}$ is the number of events found to fulfill the trigger condition of C in reconstructed simulated ESD data and N^C_{true} is the actual number of events generated with that trigger class.

For this analysis the only trigger classes considered are INEL and NSD for p+p collisions and MB (INEL) for Pb+Pb collisions. While (6.1) is simple to evaluate in simulations the actual trigger efficiency of the physics data is harder to calculate correctly due to discrepancies between the data and the simulations concerning the event definitions and ratios between events in the different event classes. For p+p collisions the Single–Diffractive events are notoriously hard to describe in simulations. Therefore for the efficiencies used in the analysis of physics data are taken from ALICE calculations while the efficiencies used for analysis of simulated data are calculated from the simulation productions in Table 5.3 using (6.1). For the NSD efficiencies no detailed ALICE calculations are complete at the time of this work[1]. Therefore the values calculated directly from the simulations have been used instead. Table 6.2 summarizes the trigger efficiencies used in this analysis.

---

[1] Martin Poghosyan, private communication.

Data set	Data ϵ_{INEL}	Simulated ϵ_{INEL}	Data ϵ_{NSD}	Simulated ϵ_{NSD}
p+p @ $\sqrt{s} = 900$ GeV	$91.6 \pm 1.3\%$	97.1%	108.8%	108.8%
p+p @ $\sqrt{s} = 2.76$ TeV	$88.3 \pm 3\%$	92.9%	103.4%	103.4%
p+p @ $\sqrt{s} = 7$ TeV	$85.2 \pm 2.4\%$	96.4%	105.7%	105.7%
Pb+Pb @ $\sqrt{s_{NN}} = 2.76$ TeV for centralities $< 80\%$	100%	100%	N/A	N/A

Table 6.2: The trigger efficiencies for this analysis. The values from simulations are calculated from the simulation productions in Table 5.3 while the inelastic p+p data values are taken from [110]. The full efficiency in Pb+Pb data values is a result from [48]. For the NSD values, the ALICE calculations are not complete at the time of this work. As a consequence the trigger efficiencies for NSD are equal to the simulated ϵ_{NSD}.

6.1.2 Background Event Rejection

Even if the vacuum of the LHC is more perfect than that of outer space there are still atmospheric gas molecules lurking inside the beampipe such as O_2 or N_2, and the beam particles will inevitably collide with these. Since many particles can be produced in such collisions they are likely to fire the online triggers in ALICE. Furthermore particles from such *beam–gas* interactions can flow downstream along with the beam so they can disturb the signals from the real collisions.

Another consideration is that during data–taking and running the bunches of particles in LHC will dilute and prolong to reduce the probability of physics interactions over time. At the same time the continuing collisions may create a gas of charged particles, the so–called *halo*, that travel with the beam. The *beam–halo* can interact with the beam particles in the same way as the gas molecules. This phenomenon is known as *beam–halo* interactions.

Despite their different origins the signatures of beam–halo and beam–gas are similar namely triggered events without coincidence between the two sides as is required for a physics interaction. To study the beam–halo and beam–gas interactions ALICE records special triggers that fire in accordance with the definitions in Table 6.1 when a bunch is crossing from one side while the bunch from the other side is empty. These triggers are known as *control triggers*. The events with control triggers will be read out in all detectors so that the beam–empty background during data–taking can be assessed.

The sample of physics triggers is cleaned for beam–empty triggers by demanding coincidence between the signals of V0A and V0C in physics events. Events that do not fulfill this requirement are not considered for analysis. Figure 6.1 summarizes this procedure. The cut values are determined from analysis of dedicated beam–background triggers. Despite the cleaning by V0 beam–gas and beam–halo events may be included in the final sample of physics events. The treatment of such events is discussed in section 6.5.4.

Pile–up in p+p collisions

When a p+p event is triggered and data recording is either in progress or is about to begin it can happen that another collision takes place close to or in the IP. The SPD has the ability to reconstruct the vertices left behind by such collisions leading to an identification of the so–called *pile–up* events. These events should not be considered for physics analysis because the FMD and SPD inner layer cannot distinguish particles from the proper collision and the particles from the pile–up vertex. We apply the condition for rejection that the second pile–up vertex must have at least 3 contributing tracklets and be at least 0.8 cm away from the primary vertex. Pile–up events are being studied intently as well as the efficiency of the removal of pile–up events.

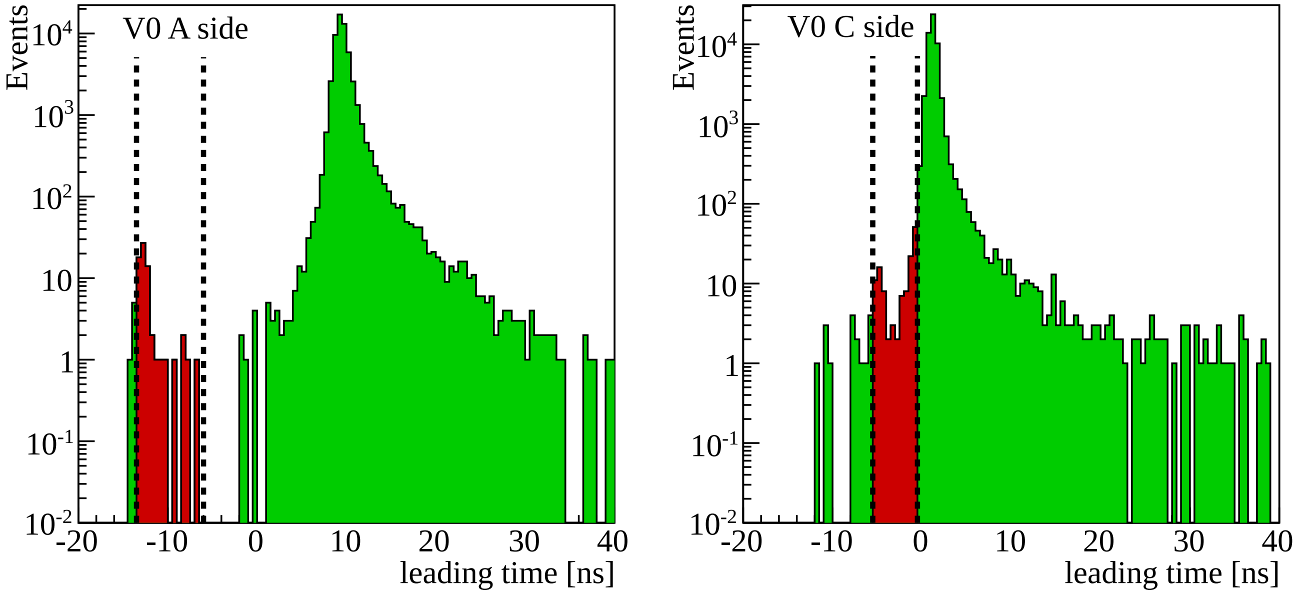

Figure 6.1: Rejection of beam background with the V0 detector in p+p collisions at $\sqrt{s} = 900$ GeV. The lines show the windows that are considered for beam–halo interactions. Events outside the window (marked in green) are considered for analysis.

6.1.3 Vertex Selection

The vertex selection is performed using the vertex measured by the SPD as outlined in Section 4.4. Only events that have a reconstructed vertex are considered for analysis. We impose a requirement on the vertices that the maximum allowed error on the z component, δv_z is ± 0.2 cm. Figure 6.2 shows the distributions of v_z in Pb+Pb collisions at $\sqrt{s_{NN}} = 2.76$ TeV and p+p collisions at $\sqrt{s} = 900$ GeV, $\sqrt{s} = 2.76$ TeV, and $\sqrt{s} = 7$ TeV.

To reduce the possibility of selecting beam–halo or beam–gas events we require that $-10 < v_z < 10$ cm. Only events in this range are considered for analysis. Figure 6.2 illustrates the effects of these cuts on the sample of events. In the analysis the data are divided into 10 vertex intervals, 2 cm wide. The main motivation for these ‘vertex–bins’ is that the pseudorapidity measured with the FMD depends on v_z so all corrections dependent on pseudorapidity should be applied to a region where the variation in v_z is small. The analysis is done separately in these vertex–bins until all η dependent corrections have been applied.

In events with higher multiplicity it is possible to measure v_x and v_y as well as v_z. Examples are shown in Figure 6.2. These measurements show that the average vertex position is shifted in y (and to a lesser extent, also x). This means that the beams are not perfectly aligned at $(0, 0, 0)$ in the ALICE IP. However, the shift is incorporated into the simulations so it should be handled properly for purposes of corrections and comparison to simulations. Furthermore, the effect of the (x, y) shift is considered negligible for the pseudorapidity of the signals in the FMD.

6.1.4 Centrality Selection

For the analysis of Pb+Pb collisions we need to divide the data into centrality classes to study dependence on the impact parameter, b. Several means of centrality determination are possible in ALICE. For this analysis the centrality is determined using the V0 detector. This choice is motivated in Figure 6.4 where it is clear that this method has the best resolution.

To determine the centrality with the V0 detector the signal of the V0 is histogrammed as shown in

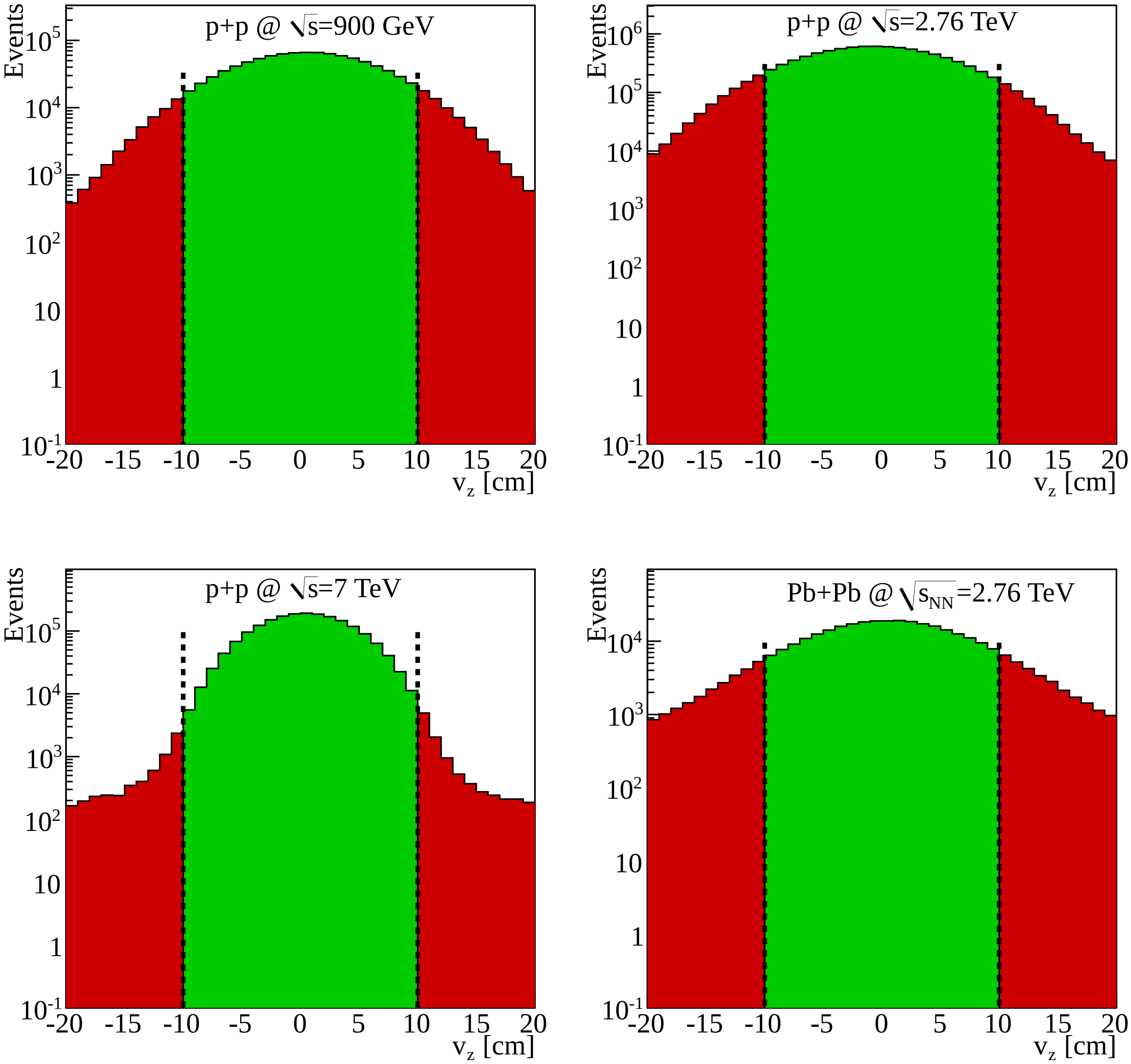

Figure 6.2: The four panels show distributions of z of the vertex measured with the SPD. The cuts of $-10 < v_z < 10$ cm are indicated by the vertical dashed lines and the selected distribution is shown in green.

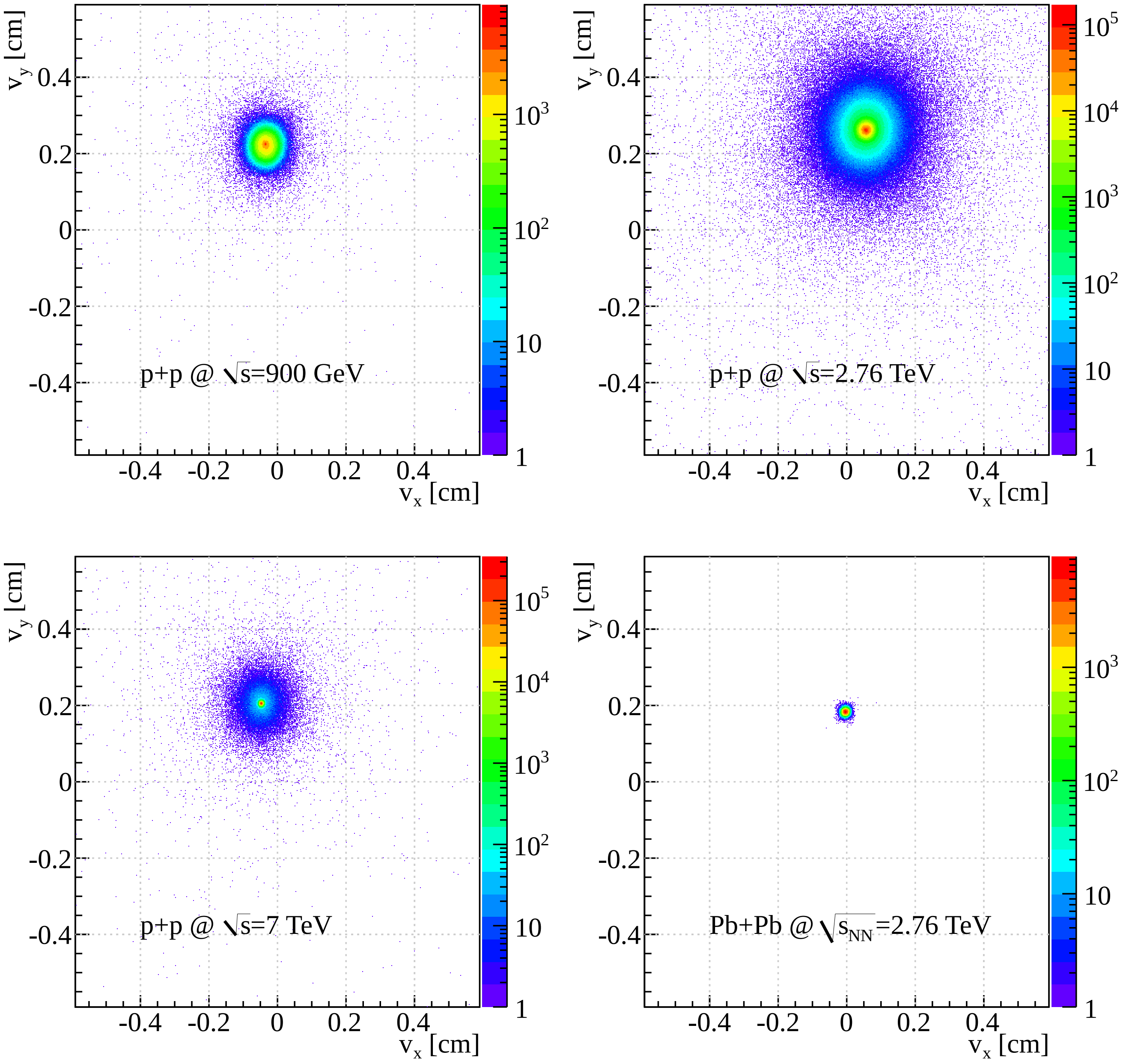

Figure 6.3: The four panels show distributions of (x, y) of the vertex measured with the SPD. The displacement of the beam from $(x, y) = (0, 0)$ is clearly present at all energies and for p+p as well as Pb+Pb collisions.

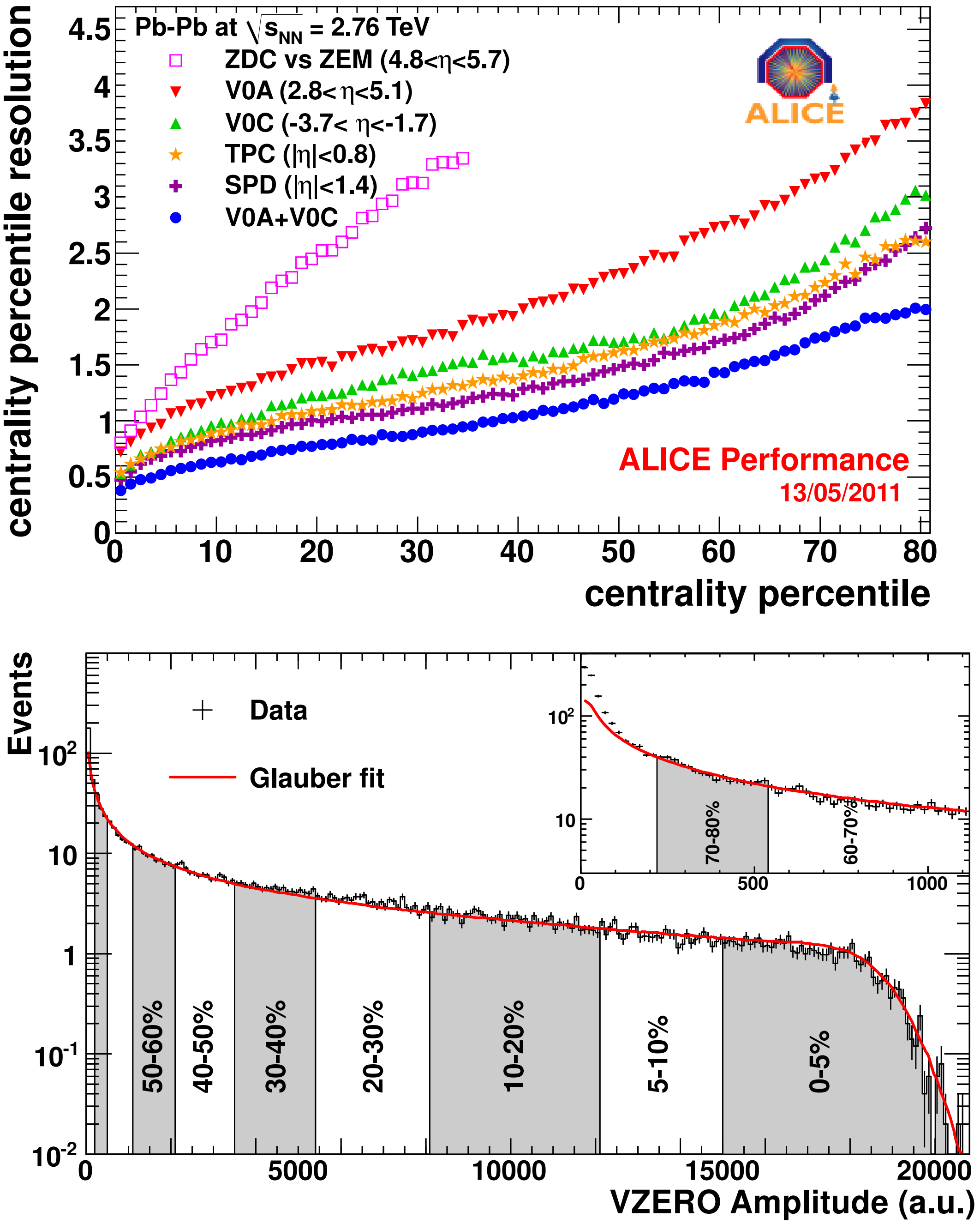

Figure 6.4: Top: The Figure shows a comparison of the resolution of the centrality percentile for various methods of determining centrality in ALICE [111]. The resolution is calculated using an iterative procedure where the centrality of one method is compared to the mean of the centralities of the other methods. From the figure using V0A+V0C for centrality determination is the proper choice because it has the lowest percentile resolution. Bottom: The selection of the centrality classes with the V0 detector. The figure shows the integrated signal from the V0 and the centrality classes from integration of the distribution. The figure also includes a fit with a two–component Glauber model [112] which is seen to give a very good description of the data.

Centrality class	b range	$\langle N_{part} \rangle$	$\langle N_{coll} \rangle$
0-5%	$0 - 3.5$ fm	382.8 ± 3.1	1686.87 ± 197.7
5-10%	$3.5 - 4.95$ fm	329.7 ± 4.6	1319.89 ± 153.7
10-20%	$4.95 - 6.98$ fm	260.5 ± 4.4	923.26 ± 99.6
20-30%	$6.98 - 8.55$ fm	186.4 ± 3.9	558.68 ± 56.4
30-40%	$8.55 - 9.88$ fm	128.9 ± 3.3	321.20 ± 31.0
40-50%	$9.88 - 11.04$ fm	85.0 ± 2.6	171.67 ± 15.2
50-60%	$11.04 - 12.09$ fm	52.8 ± 2.0	85.13 ± 8.0
60-70%	$12.09 - 13.06$ fm	30.0 ± 1.3	38.51 ± 3.8
70-80%	$13.06 - 13.97$ fm	15.8 ± 0.6	15.78 ± 1.3

Table 6.3: The centrality classes used in this analysis. The table includes the corresponding impact parameter ranges, number of participants, and number of binary nucleon–nucleon collisions found from simulations [48].

Figure 6.4. The distribution is fitted with a two–component model where the number of particle producing sources is assumed to be $f \times N_{part} + (1 - f) \times N_{coll}$. Here N_{part} is the number of participants and N_{coll} is the number of binary nucleon–nucleon collisions. The parameter f controls their relative contributions [48]. Each source is fitted with a negative binomial and the combinations of these is the function indicated by the solid red curve in Figure 6.4.

The centrality is determined by integrating the fitted distribution and dividing into fractions of the full integral. (6.2) relates the integral of the cross section to the impact parameter of the collisions or in other words, what values of the impact parameters corresponds to a given centrality class.

$$c = \frac{\int_0^{b_c} \frac{d\sigma_{in}(b')}{db'} db'}{\sigma_{in}} \tag{6.2}$$

Here σ_{in}, $\frac{d\sigma_{in}(b')}{db'}$ and b_c are the total inelastic nuclear reaction cross section, the differential cross section and a cut-off in the impact parameter, respectively. Using HIJING the impact parameter and the number of participants can be calculated as discussed in section 1.2.4. Table 6.3 summarizes the centrality classes used here, the impact parameter values and N_{part} values as well as the number of binary collisions, N_{coll}. This is the number of nucleon–nucleon interactions in a given centrality class.

6.2 Counting Particles in the FMD

In this section the procedure for counting the particles in the FMD will be discussed.

6.2.1 FMD Energy Distributions

As the starting point the distributions of deposited energy from the FMD will be discussed. Figure 6.5 and 6.6 show a summaries of energy distributions from FMD2I in Pb+Pb collisions at $\sqrt{s_{NN}} = 2.76$ TeV and p+p collisions at $\sqrt{s} = 900$ GeV, $\sqrt{s} = 2.76$ TeV, and $\sqrt{s} = 7$ TeV for physics data and simulated data, respectively. The shapes of the energy distributions are as expected from the discussion in section 4.1.4: For $E_{dep}/E_{MIP} \sim 0$ some of the pedestal above the zero suppression cut remains. For E_{dep}/E_{MIP} between the pedestal remnant and the MIP peak (seen at $\sim 0.6 E_{dep}/E_{MIP}$ in physics data and $\sim 0.7 E_{dep}/E_{MIP}$ in simulated data) we see a flat region which is interpreted as signals that share energy between neighboring strips with a lower deposit than the MIP energy in each (see section 6.2.3). Beyond the shared region the expected Landau–like shape of the signal is observed with the characteristic long tail. The overall trends of the simulated energy distributions are similar to those of the physics data but two main differences are noted: Firstly the second MIP peak in Pb+Pb collisions is more pronounced

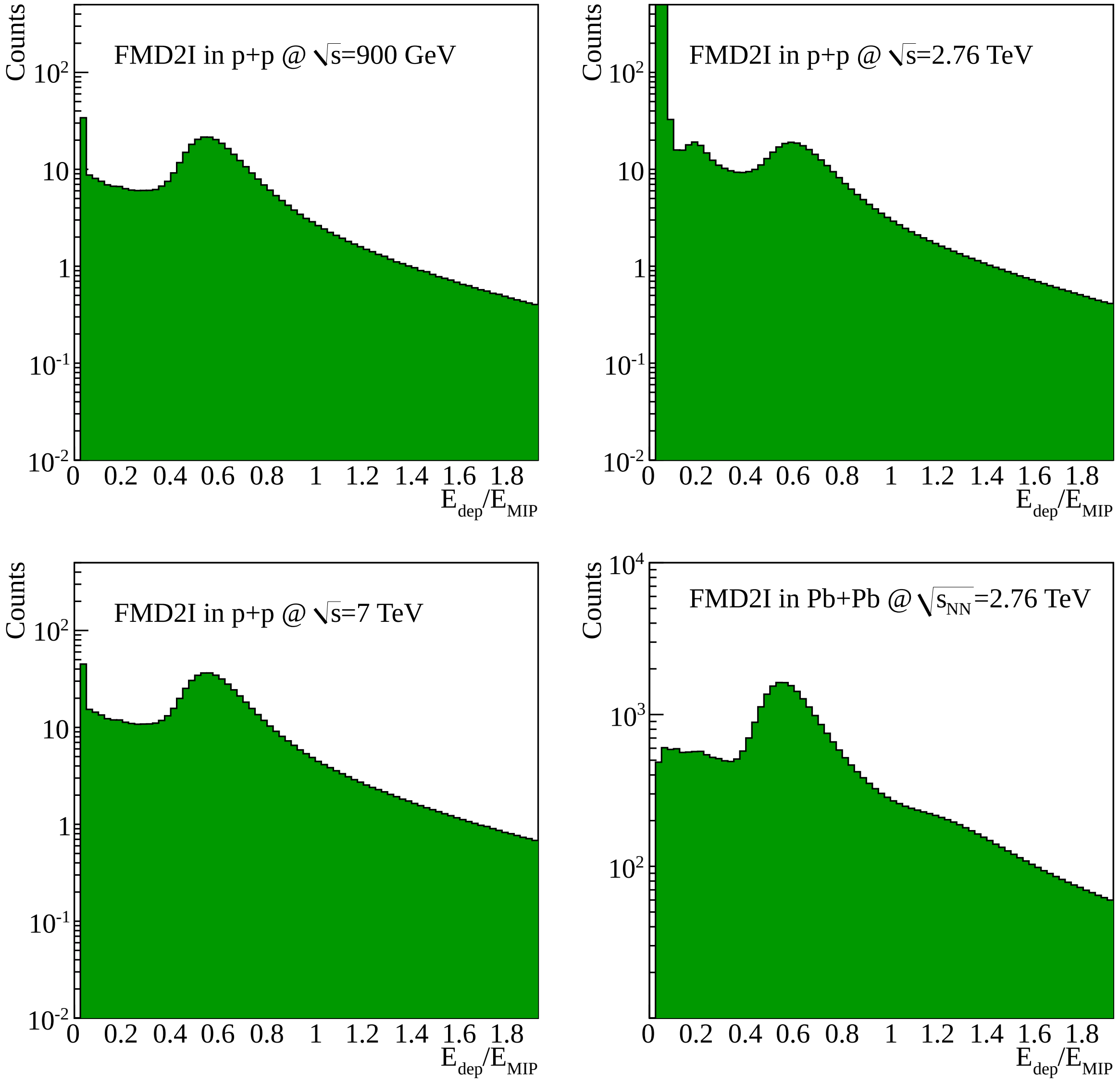

Figure 6.5: Energy distributions from FMD2I in Pb+Pb collisions at $\sqrt{s_{NN}} = 2.76$ TeV and p+p collisions at $\sqrt{s} = 900$ GeV, $\sqrt{s} = 2.76$ TeV, and $\sqrt{s} = 7$ TeV. As expected the levels are much higher in Pb+Pb collisions than in p+p collisions.

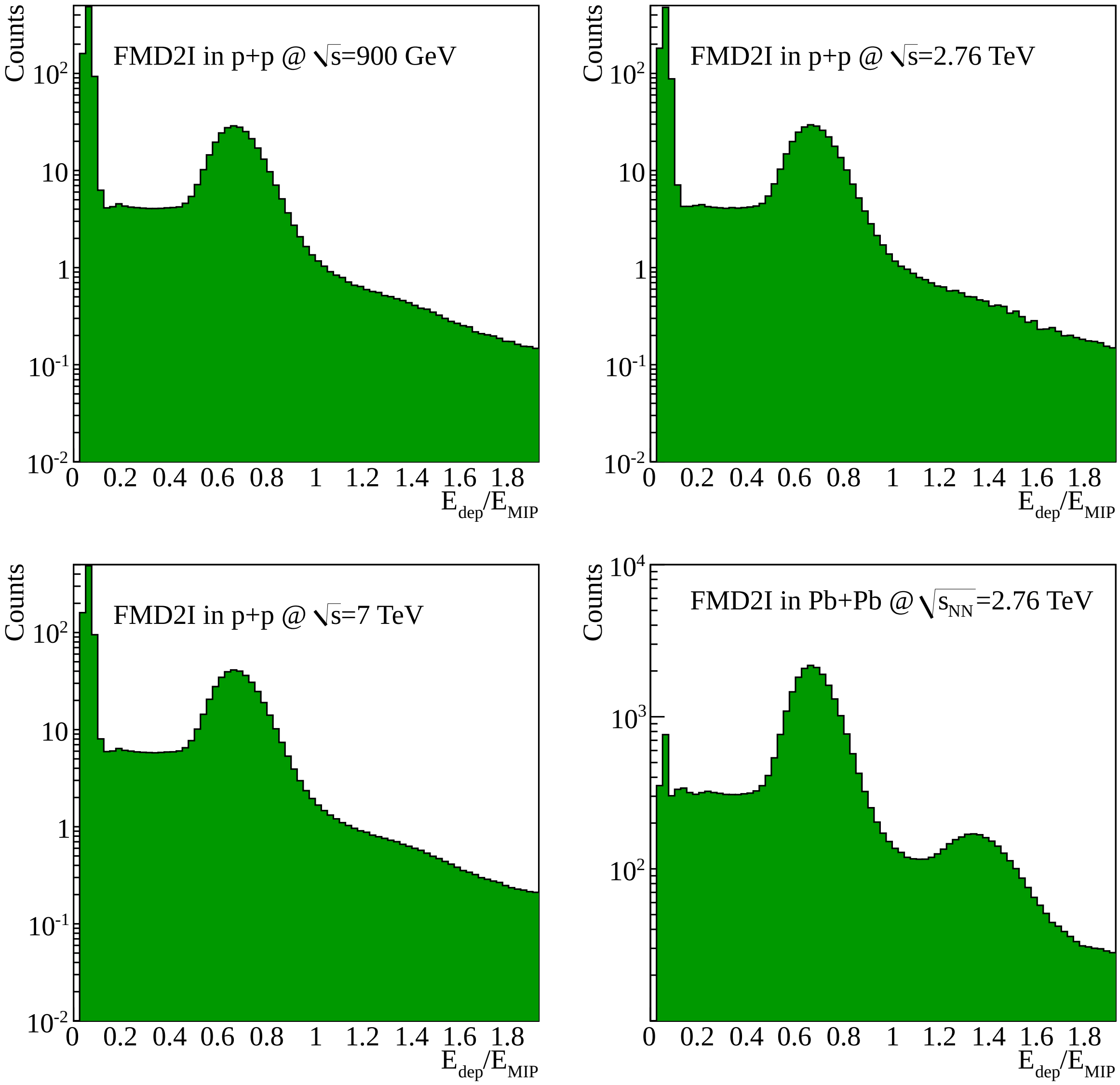

Figure 6.6: Energy distributions from simulated data for FMD2I in Pb+Pb collisions at $\sqrt{s_{NN}} = 2.76$ TeV and p+p collisions at $\sqrt{s} = 900$ GeV, $\sqrt{s} = 2.76$ TeV, and $\sqrt{s} = 7$ TeV.

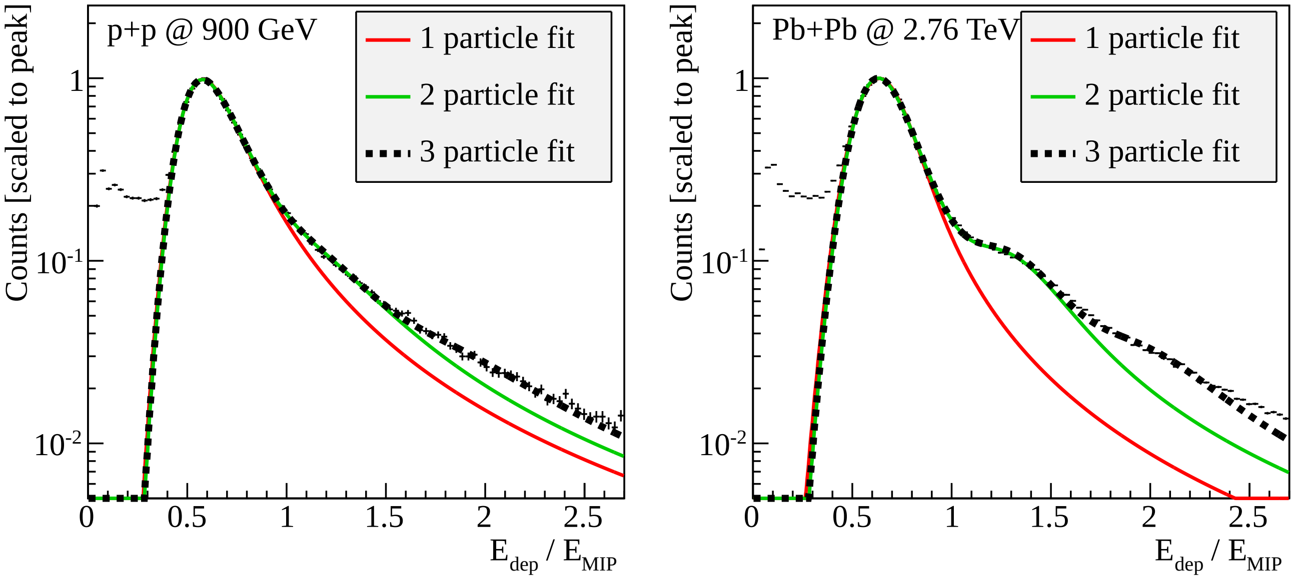

Figure 6.7: The energy distributions of FMD2O for $1.95 < \eta < 2$ in p+p collisions at $\sqrt{s} = 900$ GeV and Pb+Pb collisions at $\sqrt{s_{NN}} = 2.76$ TeV fitted with the function in (4.5). The fits are seen to give a good description of the data over several orders of magnitude.

in the simulations. Secondly the position of the MIP peak is shifted slightly up in the simulated data relative to the physics data. The latter is understood to be a scaling factor since (5.1) is calculated slightly differently for simulations and data. The broadening of the second MIP in physics data compared to simulations is on the other hand not understood. For a more elaborate discussion of these issues see section 7.5.3.

6.2.2 Fits to the energy distributions

To quantify the information of the energy distributions the data are fitted with the function described in section 4.1.4. In summary this function assigns a Landau function convoluted with a Gaussian to each MIP peak. The fits are carried out in η intervals to be able to take into account the variations in the particle production with η. Figure 6.7 shows examples of fits to the data of FMD2O in p+p collisions at $\sqrt{s} = 900$ GeV and Pb+Pb collisions at $\sqrt{s_{NN}} = 2.76$ TeV. In general we find the functions to describe the data well. This also holds for the fits to the simulated energy distributions even if the shapes are slightly different with the more pronounced higher order MIP peaks. The fits are carried out prior to data analysis so that the fit parameters are available during analysis.

6.2.3 Sharing and Hit Merging

As discussed briefly above we expect some particles to deposit energy in more than one strip because the particles hit the detector in a shallow angle. Figure 6.8 shows the principle of *hit sharing* where a particle physically hits two or more adjacent strips. In principle it could also be possible for a signal in one strip to leak into the adjacent strips, a phenomenon known as *energy sharing* but this is very unlikely in the FMD due to the high voltage over the strips. In any case the two kinds of sharing would be indistinguishable in the data as the signature would be the same.

To correct for the effects of the shared signals we will develop an algorithm to decide which signals are shared and how they should be merged. From a simple geometrical argument it is unlikely that a primary particle from the IP or a secondary particle retaining the direction of a primary (mother) particle will

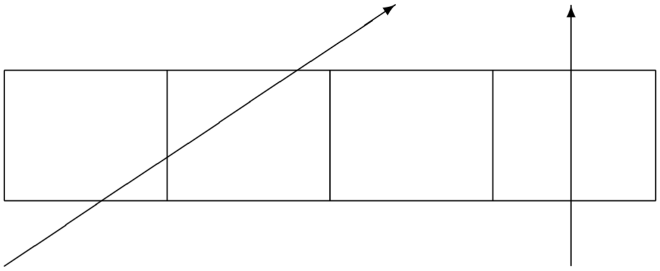

Figure 6.8: Illustration of hit sharing. The particle on the right hits only one strip, depositing energy there while the particle on the right will leave a signal in both strips traversed.

ever traverse more than two strips. However, it is found in simulation studies that particles scatter or backscatter into the detector to share energy in 3 or even more strips[2]. For this reason we will allow up to three signals to be merged into one strip.

Another consideration before presenting the algorithm is where to place the merged signal. There are two cases with sharing across three strips:

- In case of sharing across two strips the final signal is assigned to the strip with the largest initial signal.
- In case of sharing across three strips the final signal is placed in the middle strip even if it does not contain the largest single signal. No matter the choice here the change to the value of η would be negligible.

The algorithm incorporating the choices made here is shown in Figure 6.9. To put the algorithm to work the thresholds, E_{low} and E_{high} must be determined.

Determination of E_{low}: To determine the lowest acceptable component of a shared signal a cut slightly above 3 times the noise is made. Thus, $E_{low} \sim 3\sigma_{noise}$. From Figure 5.4 and (5.2) we see that this corresponds to values of $E_{low} \sim \frac{3 \cdot 2.5}{3 \cdot 29.67} \times E_{MIP} \sim 0.084 \times E_{MIP}$ in the inner FMD rings and $E_{low} \sim \frac{3 \cdot 3.5}{3 \times 29.67} \times E_{MIP} \sim 0.12 \times E_{MIP}$ in the outer FMD rings. To stay completely clear of the pedestal the cuts are set to $E_{low} = 0.1 \times E_{MIP}$ in the inner rings and $E_{low} = 0.15 \times E_{MIP}$ in the outer rings.

Determination of E_{high}: The high limit for the sharing algorithm is set using an argument from simulations where it is possible to follow a track and analyze the deposited energy signals directly. The results of such an analysis are shown in Figure 6.11. It is seen that a value $E_{high} = 0.7\Delta_p$ is a reasonable choice because above this value the probability that adjacent energies are in fact separate signals rises. Above E_{high} signals cannot be considered a shared component of another signal above the cut.

Figure 6.10 shows some examples of the sharing algorithm in action for some specific examples. Table 6.4 shows the fractions of single signals, and merged signals from two signals ('doubles'), and merged signals from three signals ('triples'). It is seen that singles and doubles constitute $> 98\%$ of the final energy distributions. The corresponding results for analysis of simulated data is shown in Table 6.5.

The discrepancies between the fractions in simulated data and physics data are not understood at the moment and should be subject to further study and possible tuning of the simulations. This is discussed further in section 7.5.3. For now, the discrepancies are accepted 'as is' and no attempts are made to correct for them.

It is also observed that the merged signal from triple signals appears to be at the position of the second MIP peak. This would indicate that the triple signals are in fact 2 hits next to each other rather than single particles depositing energy in 3 adjacent strips. It could be argued that it would be more correct to disable sharing across 3 strips or unfold them into 2 hits. However, due to the design of the algorithm

---

[2] Sharing across more than 3 strips is extremely rare so it will not be included in the algorithm developed here

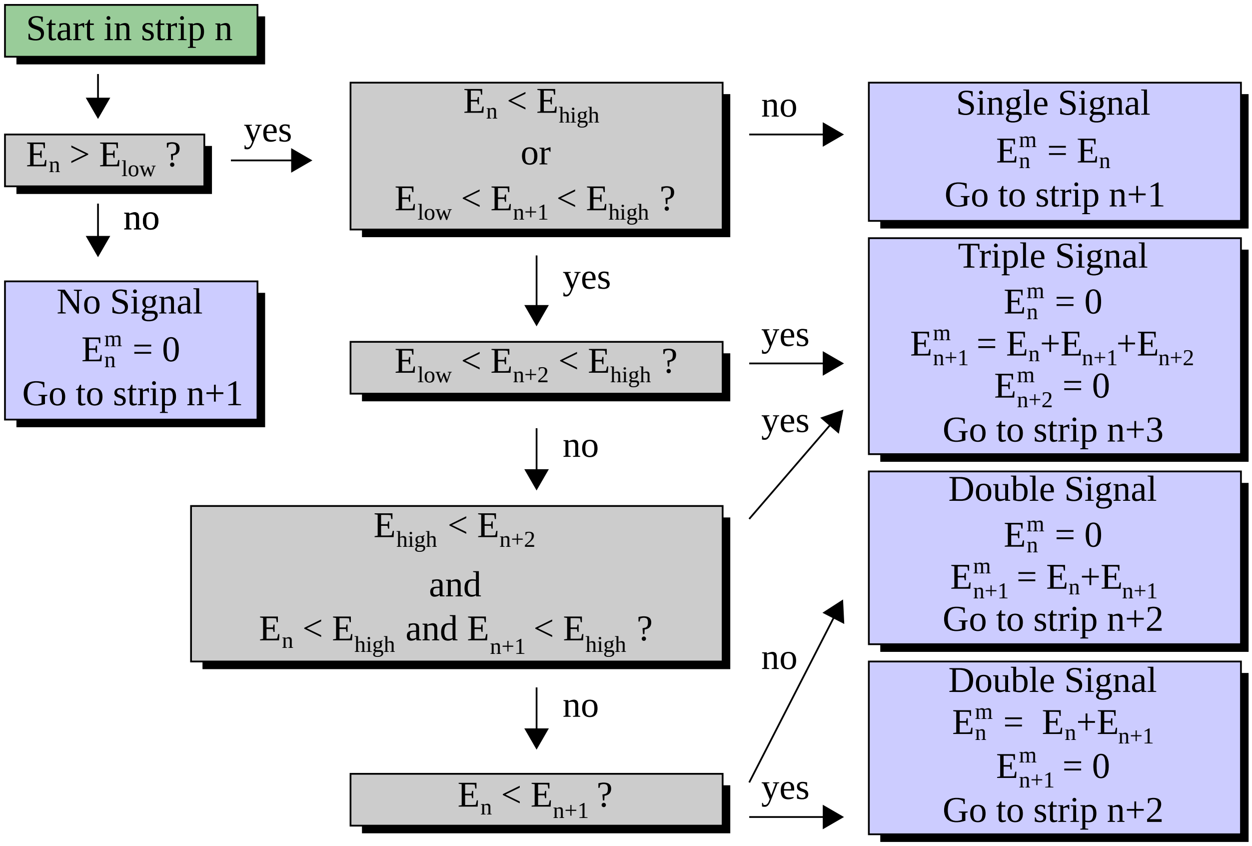

Figure 6.9: The figure shows the flow diagram of the hit merging algorithm used in this analysis. It depends on two thresholds, E_{low} and E_{high} which are described in the text. The merged signals is marked with a superscript ‘m’ so that the merged signal in strip n becomes E_n^m.

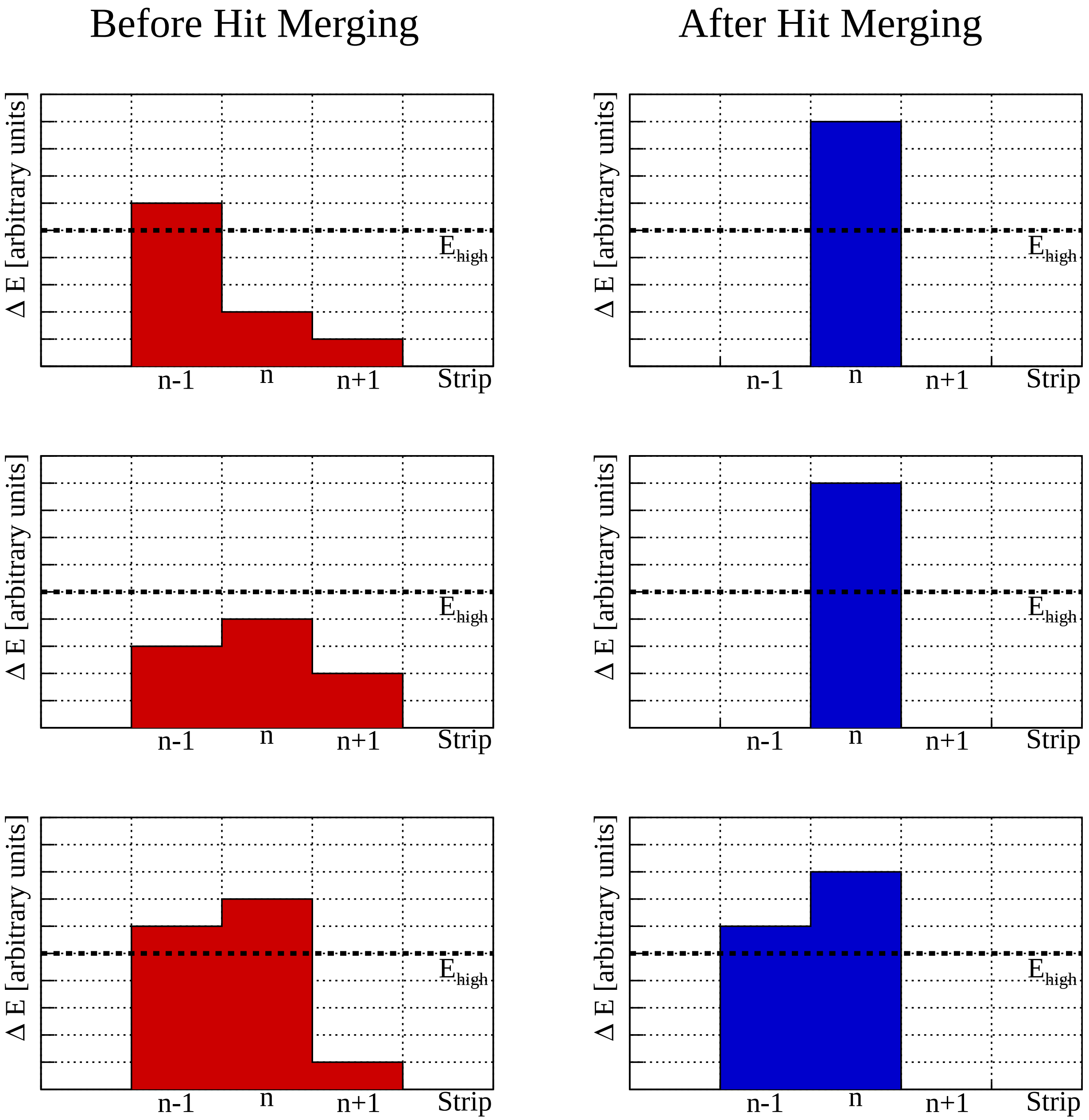

Figure 6.10: Examples of hit merging. In these three cases the algorithm in Figure 6.9 is used. The abscissa shows a strip, n, with its neighbors, $n-1$, and $n+1$. The signals are shown are shown as the red and blue areas. All signals are assumed to be above E_{low} and the dotted line in the plots show E_{high}.

System	Ring	Single signals	Double signals	Triple signals
p+p @ $\sqrt{s} = 900$ GeV				
	FMD1	86.99 %	12.71 %	0.30 %
	FMD2I	87.07 %	12.67 %	0.26 %
	FMD2O	92.26 %	7.64 %	0.10 %
	FMD3I	85.65 %	13.99 %	0.36 %
	FMD3O	91.96 %	7.86 %	0.18 %
Pb+Pb @ $\sqrt{s_{NN}} = 2.76$ TeV				
	FMD1	88.95 %	9.67 %	1.38 %
	FMD2I	88.48 %	9.95 %	1.58 %
	FMD2O	91.22 %	7.91 %	0.87 %
	FMD3I	88.24 %	10.17 %	1.59 %
	FMD3O	91.79 %	7.37 %	0.84 %

Table 6.4: The fractions of single, double, and triple merged signals after the sharing algorithm. It is seen that the fraction of triple merged signals is without significance.

System	Ring	Single signals	Double signals	Triple signals
p+p @ $\sqrt{s} = 900$ GeV				
	FMD1	90.75 %	8.95 %	0.31 %
	FMD2I	86.77 %	12.93 %	0.30 %
	FMD2O	88.37 %	11.53 %	0.10 %
	FMD3I	83.92 %	15.65 %	0.43 %
	FMD3O	87.61 %	12.22 %	0.17 %
Pb+Pb @ $\sqrt{s_{NN}} = 2.76$ TeV				
	FMD1	90.72 %	8.26 %	1.03 %
	FMD2I	87.41 %	10.88 %	1.70 %
	FMD2O	88.34 %	10.50 %	1.16 %
	FMD3I	85.20 %	12.67 %	2.13 %
	FMD3O	87.73 %	10.98 %	1.29 %

Table 6.5: The fractions of single, double, and triple merged signals in simulated data after the sharing algorithm.

in Figure 6.9 and the choice of E_{Hit} (=E_{High}) discussed next in this section the extra single signals would be cut away anyway so we have chosen to keep the triple signals. Furthermore it could be speculated the particles are slow secondary particles since from a geometrical point of view particles traversing 3 strips will be secondary. Slow particles deposit more energy than E_{MIP}, see Figure 4.5), per hit strip so if the triple signals indeed came from a single particle these particles could be slow secondaries.

Determination of E_{hit} To select hits in the FMD, E_{hit}, the threshold above which a merged signal is considered a hit for analysis or not, must be determined. In principle and in case of a flawless detector any merged signal above E_{low} could be considered a hit but in the following we will discuss the choice of $E_{hit} = 0.7\Delta_p$ made here. Consider first Figures 6.12 and 6.13 that shows the distributions of singles, doubles, and triples after hit merging in p+p and Pb+Pb data. It is clear that the remaining 'low energy tail' between the pedestal remnant and the MIP peak is completely dominated by single signals that are not merged. In other words, the low energy tail is not simple noise merged into double or triple signals.

A special mention should go to distributions of singles, doubles, and triples in the p+p data at $\sqrt{s} = 2.76$ TeV shown in Figure 6.14. It is seen that the double signals exhibit a different behaviour

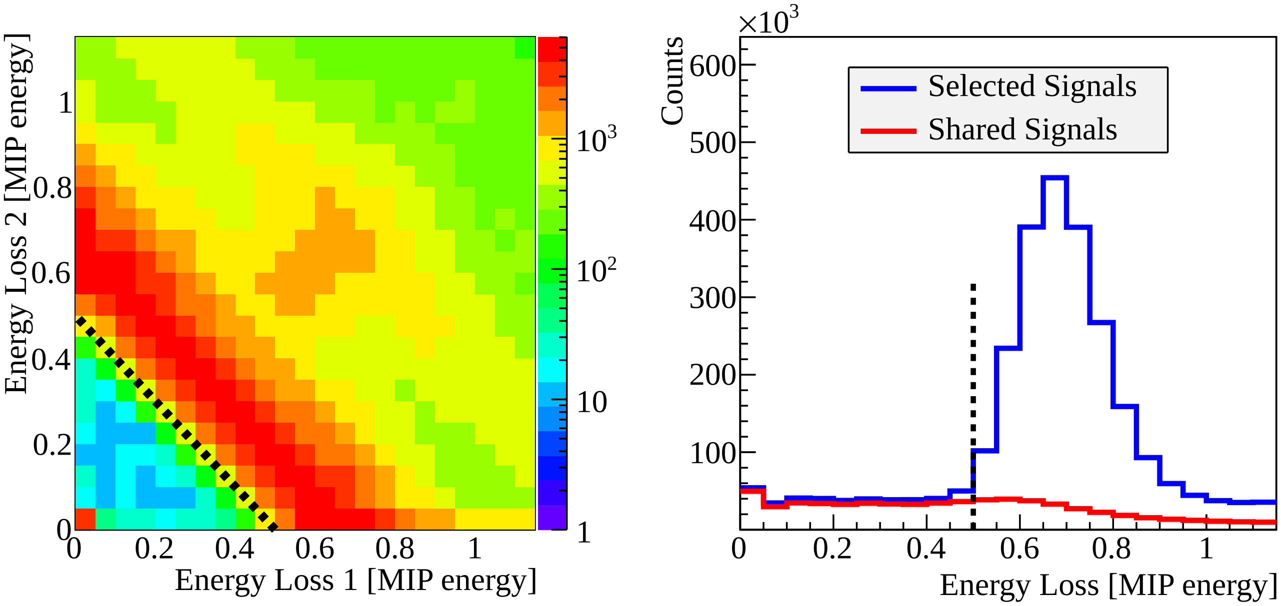

Figure 6.11: Left panel: The plot is made with the knowledge from simulations of the actual shared signals. It shows the correlation between adjacent strips with shared signals in the FMD. The line shows the approximate position of $E_{high} = 0.7\Delta_p$ which is seen to contain the vast majority of the shared signals well. Right panel: The energy distributions of the selected hits (blue) and the possible shared components (red). Note that the selected hits contain the single hits so that all signals in the red distribution have an associated 'partner' in the blue distribution while the opposite is in general not true. The dashed line again shows the selected value of $E_{high} = 0.7\Delta_p$.

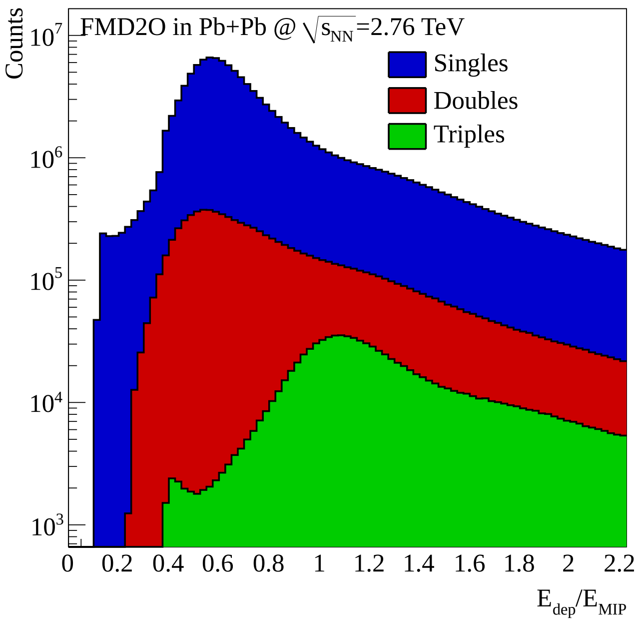

Figure 6.12: The figure shows the distributions of single, double, and triple signals after hit merging in the FMD in Pb+Pb collisions. Left panel shows physics data and the right panel is from simulations. At low energies the single signals dominate.

than expected from $\sqrt{s} = 900$ GeV data or simulations. This is interpreted as a consequence of the very broad pedestal remnant observed in the energy distributions shown in Figure 6.5. The observed pedestal broadening is not understood but could be present in all 2011 FMD data. The study of it should be a priority before the 2011 LHC Pb+Pb run. In this work no further attempt is made to correct for it.

It is suspected that the low energy tail is a non–understood noise component that should be cut away. Consider Figure 6.15 that shows the energy distributions per strip as a function of E_{dep}/E_{MIP} drawn as a contour plot in Pb+Pb data (physics and simulated). As expected for geometrical reasons the particle production is highest for the strips closest to strip zero[3] both in the MIP peak and the high energy tail. For a close–up view consider also Figure 6.16.

A structure is observed in the low energy signals for physics data which does not appear in the simulated data. This is clear from Figure 6.15 where it is also seen that there are more remaining low energy signals in data than in the simulations. While the excess of low energy signals in data is not a clear indication that these signals should be cut away, the structures are certainly suspicious. With these considerations the value of E_{hit} is set to $E_{hit} = 0.7\Delta_p$ for Pb+Pb collisions as well. The structures at low energies after hit merging are a feature in the data that is not understood and should be studied further but this will not be pursued more in this work.

Sharing and hit selection summary

Figures 6.17 and 6.18 show the results of the hit merging algorithm for p+p collisions at $\sqrt{s} = 900$ GeV and Pb+Pb collisions at $\sqrt{s_{NN}} = 2.76$ TeV, respectively. Figure 6.19 shows an example of neighboring strips in FMD1I in p+p collisions at $\sqrt{s} = 900$ GeV. It is seen that the hit merging algorithm reduces the low energy tail by roughly an order of magnitude. As discussed already, the origin of the remaining

---

[3] The strips are numbered radially outward so strip zero sits at the lowest angle where the particle production is highest.

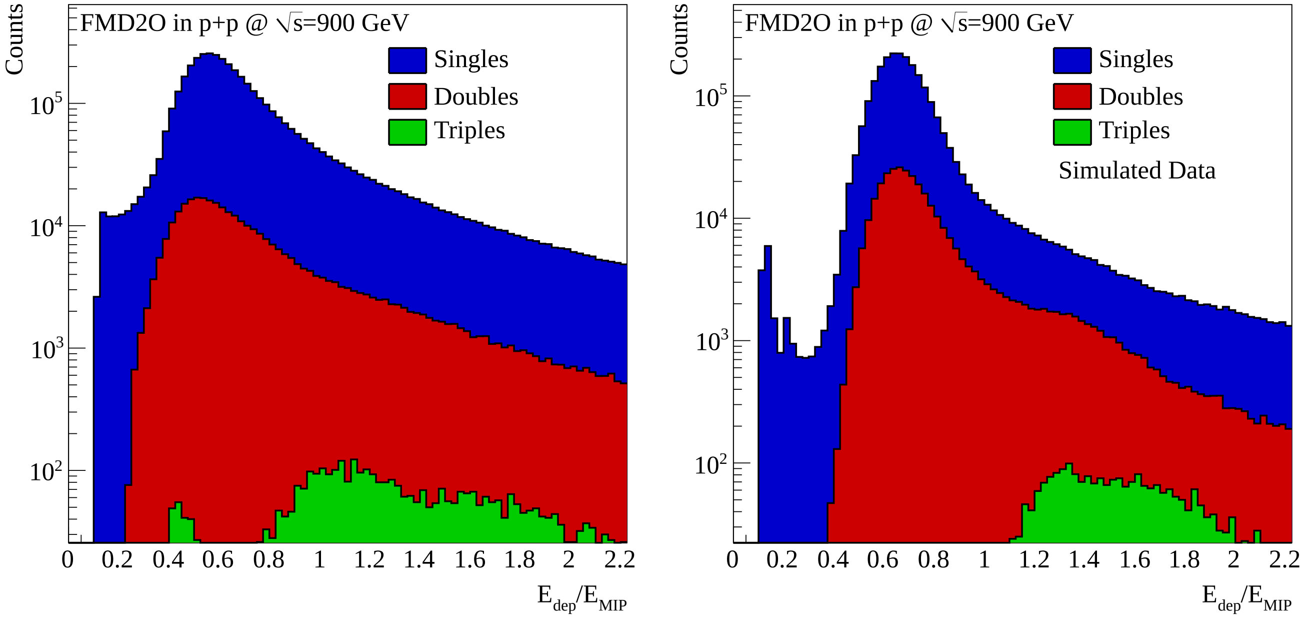

Figure 6.13: The figure shows the distributions of single, double, and triple signals after hit merging in the FMD in p+p collisions at $\sqrt{s} = 900$ GeV. Left Panel: Physics Data. Right Panel: Simulated data. At low energies the single signals dominate.

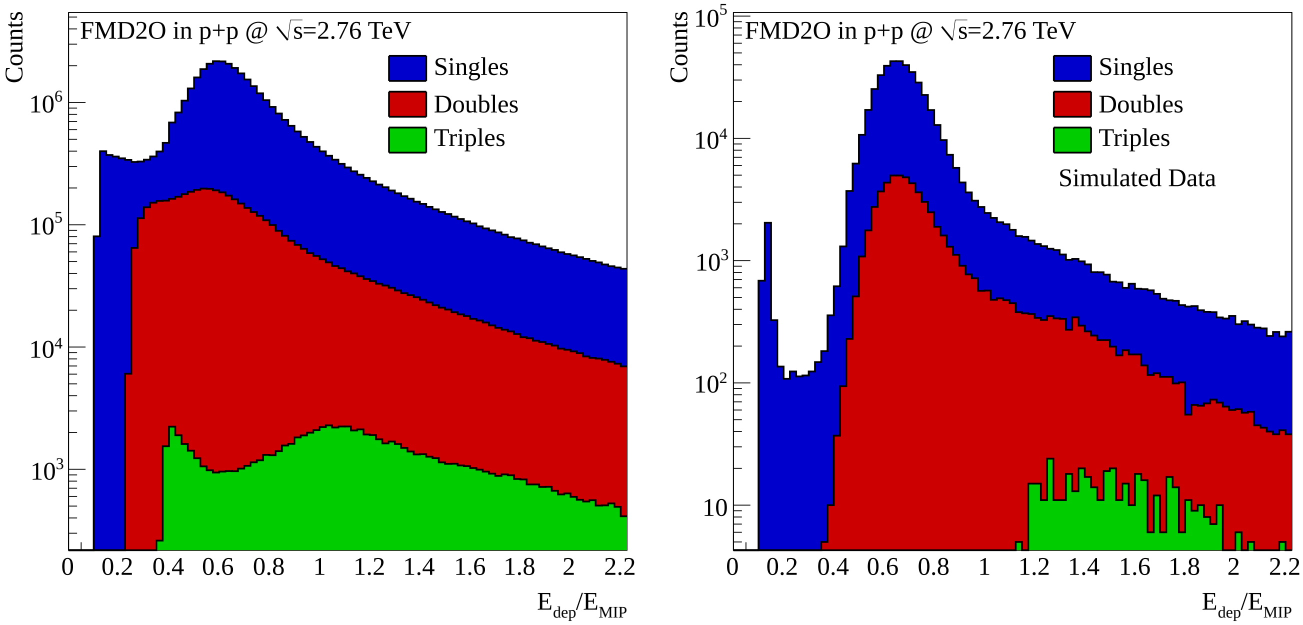

Figure 6.14: The figure shows the distributions of single, double, and triple signals after hit merging in the FMD in p+p collisions at $\sqrt{s} = 2.76$ TeV. Left Panel: Physics Data. Right Panel: Simulated data. At low energies the single signals dominate. It is seen that the distributions of doubles in physics data is broader than expected.

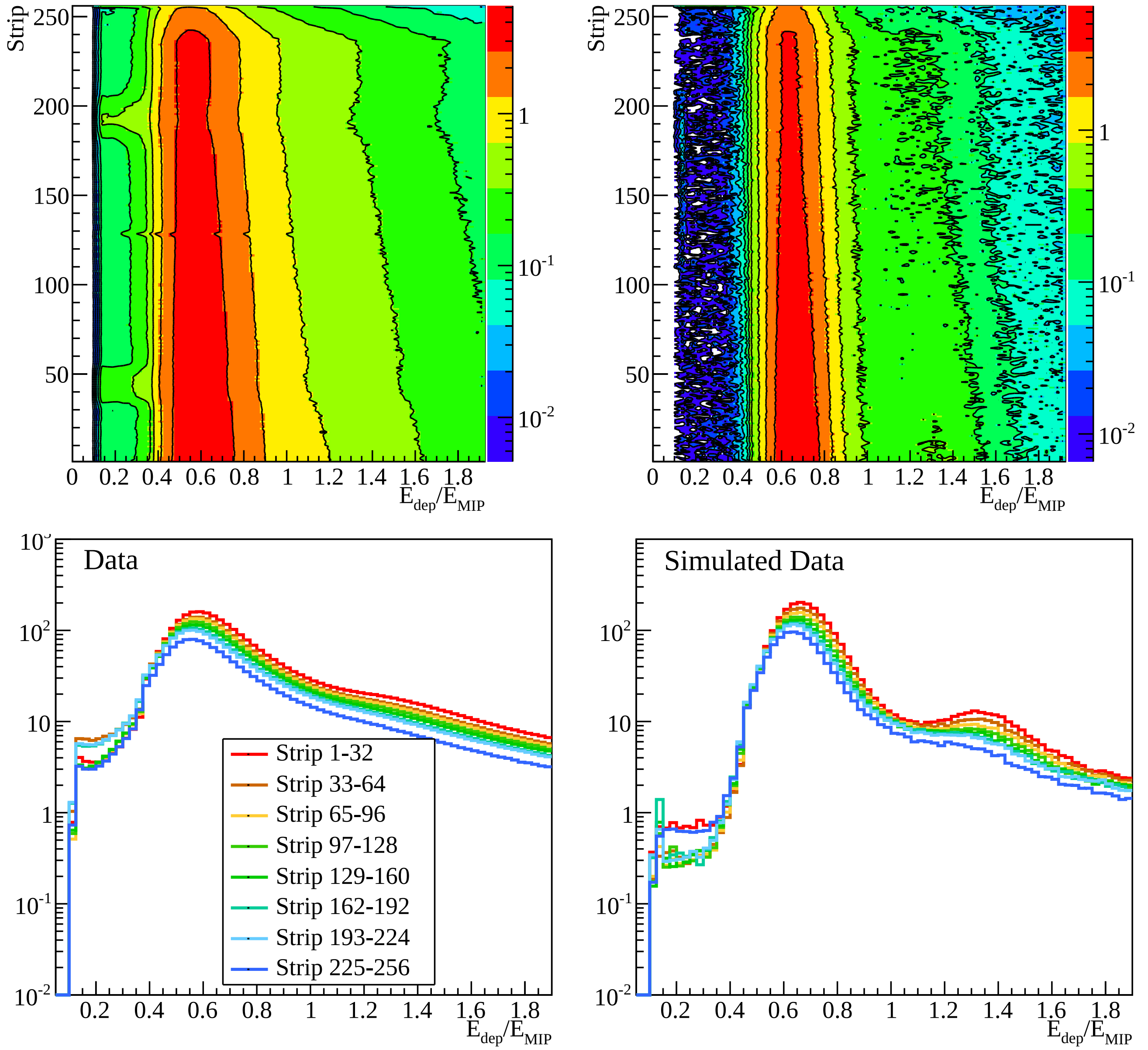

Figure 6.15: The top panels show the single strip energy signals versus strip in FMD2O in $\sqrt{s_{NN}} = 2.76$ TeV Pb+Pb physics data (left) and simulated data (right). While the general features are similar a structure at low energies ($E_{dep}/E_{MIP} \sim 0.2$) is observed in physics data which is not present in the simulated data. This is also evident from the lower panels which show the projections of groups of 32 strips. Apart from the observed structure it is clearly seen that the low energy tail is much more pronounced in physics data than in simulated data. This behavior is not understood so the threshold for a hit strip is set to $E_{hit} = 0.7\Delta_p$ ($\sim 0.35 \times E_{dep}/E_{MIP}$ in physics data and $\sim 0.4 \times E_{dep}/E_{MIP}$ in simulated data).

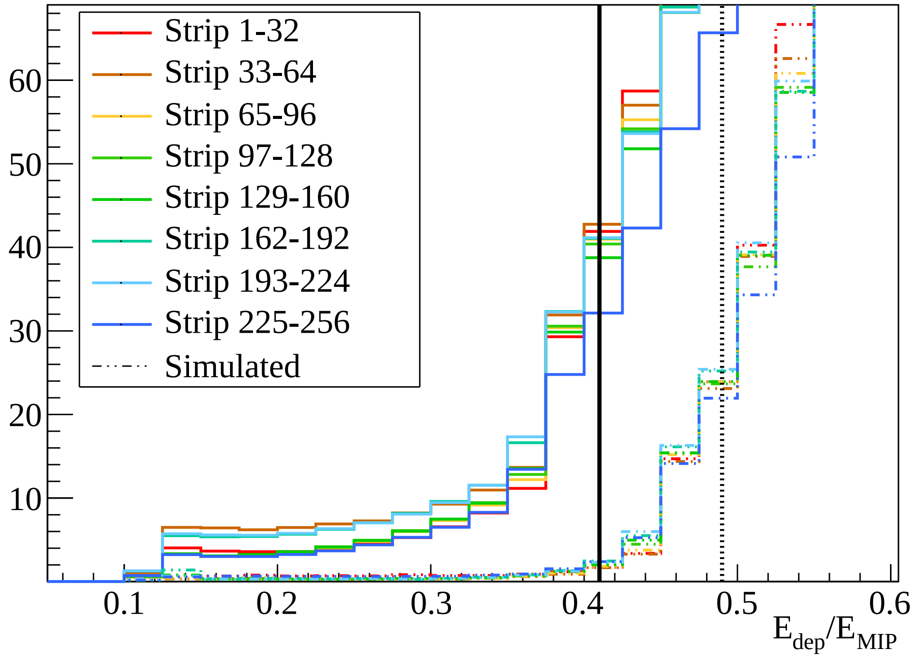

Figure 6.16: A zoom of Figure 6.15 with a comparison of the low energy region between data and simulations in Pb+Pb collisions at $\sqrt{s_{NN}} = 2.76$ TeV. The solid vertical line indicates the approximate position of E_{hit} for data while the dotted vertical line indicates E_{hit} for the simulated data.

low energy signal tail that comes from single signals is not completely known. The selected energy distributions are included in the Figures.

6.2.4 Calculating N_{ch}

Following the hit merging and hit selection high occupancy must be taken into account. The hit merging concerned the case where the same particle hit several adjacent strips in the FMD. It is also possible that several particles deposit energy in the same strip. This has already been discussed briefly as this is what gives rise to the second and higher order MIP peaks in the energy distributions discussed in section 6.2.1. Since we cannot distinguish multiple hits from slow particles with high energy deposit a correction is applied to get the number of charged particles, N_{ch}, per channel from the hits in the strips. Two methods have been implemented, a method based on Poisson statistics and one based on the fits to the energy distributions. For the results presented in Chapter 7 the correction based on Poisson statistics is used exclusively.

For a region of the FMD containing N_{strips} strips we can define the true occupancy as:

$$\mu = N_{\text{ch}}/N_{strips}$$

Here, N_{ch} is the number of charged particles in the region. The measured occupancy in the same region in an event becomes:

$$\mu_{meas} = N_{hits}/N_{strips}$$

Here N_{hits} is the number of strips with a signal above E_{Hit}. Note that $N_{hits} \leq N_{strips}$. Since each FMD strip recorded as a hit can be hit by several charged particles, in general $N_{\text{ch}} \neq N_{hits}$. For a detector with infinitely many channels, it would be expected that $N_{\text{ch}} = N_{hits}$. This is for example the case in the SPD which has a very high number of channels so the occupancy will be low enough to have $N_{\text{ch}} = N_{hits}$.

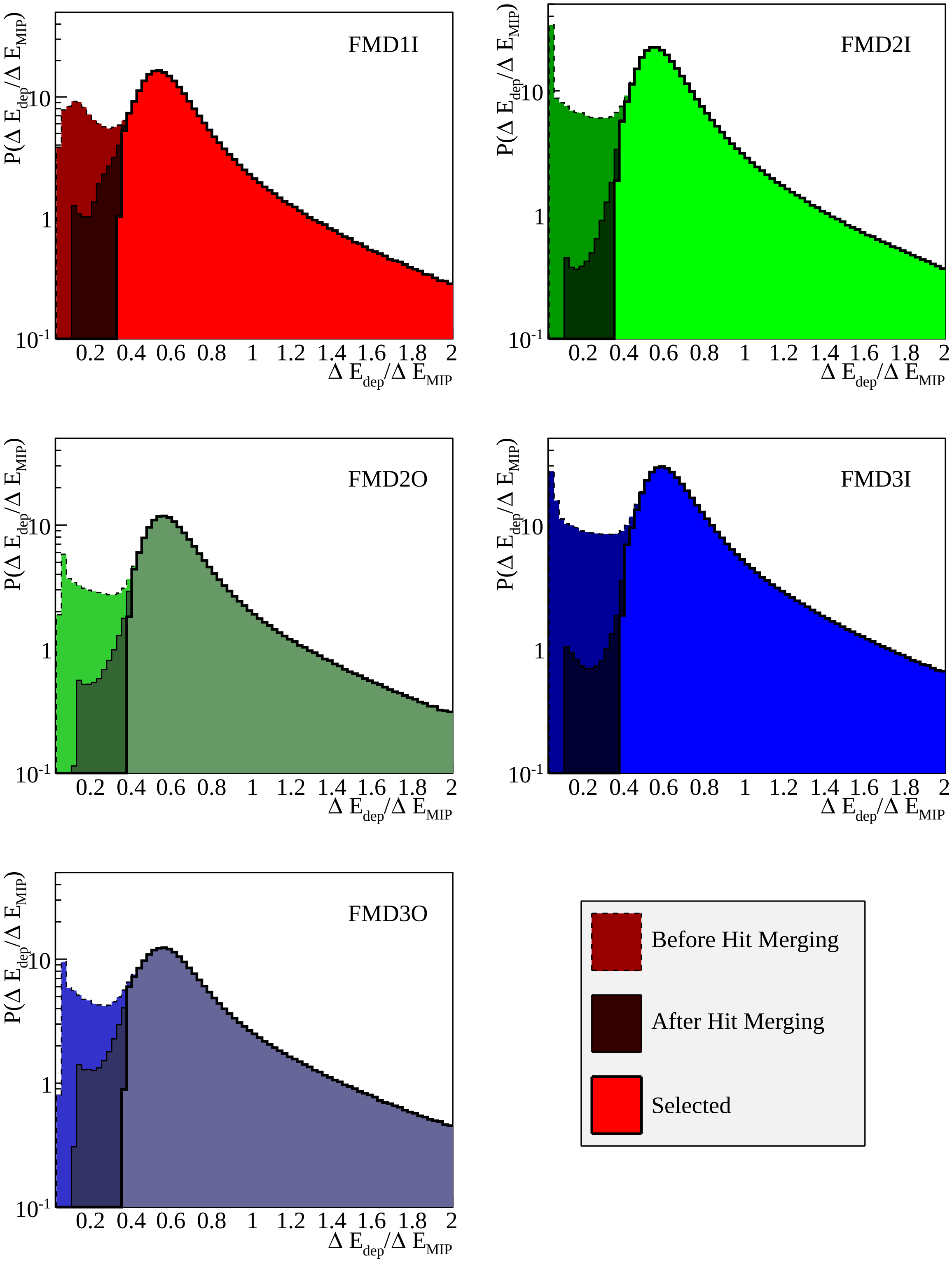

Figure 6.17: Hit merging results in the energy distributions for p+p collisions at $\sqrt{s_{NN}} = 900$ GeV. The figure includes the orignal distribution, the result of hit merging, and the final selected distribution.

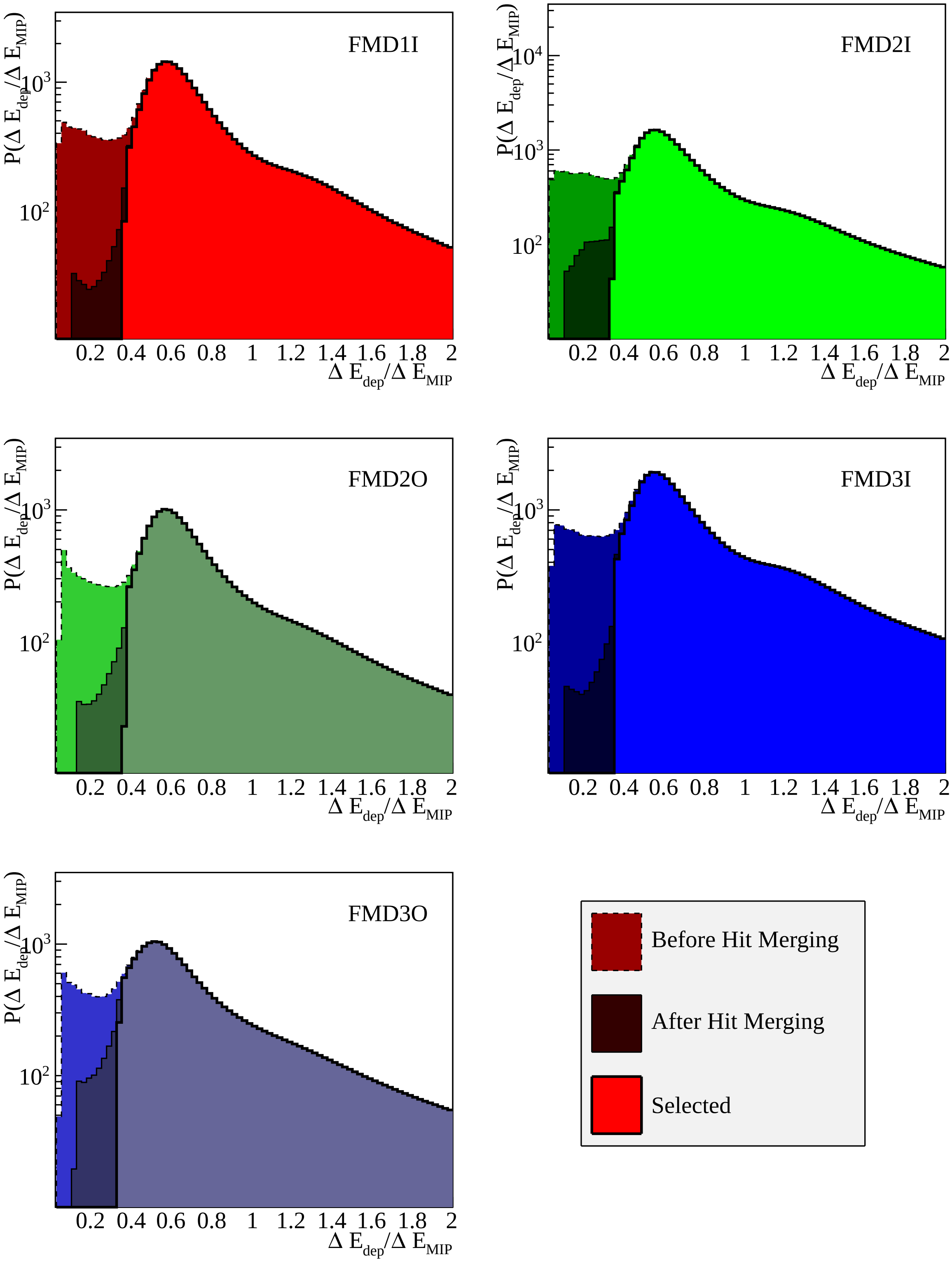

Figure 6.18: Hit merging results in the energy distributions for Pb+Pb collisions at $\sqrt{s_{NN}} = 2.76$ TeV. The figure includes the orignal distribution, the result of hit merging, and the final selected distribution.

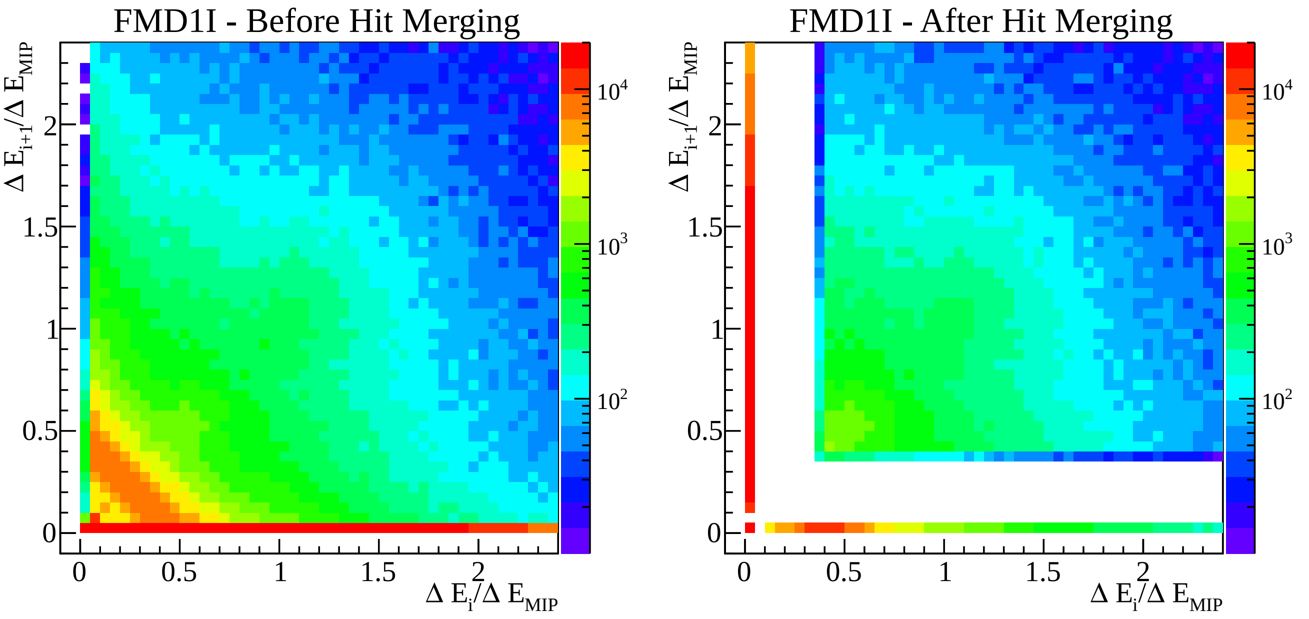

Figure 6.19: Hit merging results for neighboring strips in FMD1I in p+p collisions at $\sqrt{s} = 900$ GeV before and after hit merging and selection.

Figure 6.20 shows the mean occupancy in FMD2I Pb+Pb collisions at $\sqrt{s_{NN}} = 2.76$ TeV and p+p collisions at $\sqrt{s} = 900$ GeV, $\sqrt{s} = 2.76$ TeV, and $\sqrt{s} = 7$ TeV. The calculation is done in regions of 256 strips. It is seen that the maximum occupancy in the most central Pb+Pb collisions reaches $\sim 90\%$ in some regions.

Poisson Method

We assume that in a region of the FMD N_{ch} is distributed according to a Poisson distribution. This means that the probability of $N_{\text{ch}} = n$ becomes:

$$P(n) = \frac{\mu^n e^{-\mu}}{n!} \tag{6.3}$$

In particular the measured occupancy, μ_{meas}, is the probability of any number of hits, thus using (6.3) :

$$\mu_{meas} = 1 - P(0) = 1 - e^{-\mu} \tag{6.4}$$

which implies:

$$\mu = \ln(1 - \mu_{meas})^{-1} \tag{6.5}$$

The mean number of particles in a hit strip becomes:

$$\begin{aligned} C &= \frac{\sum_{n>0} nP(n>0)}{\sum_{n>0} P(n>0)} \\ &= \frac{e^{-\mu}}{1-e^{-\mu}}\mu \sum \frac{\mu^n}{n!} \\ &= \frac{e^{-\mu}}{1-e^{-\mu}}\mu e^{\mu} \\ &= \frac{\mu}{1-e^{-\mu}} \end{aligned} \tag{6.6}$$

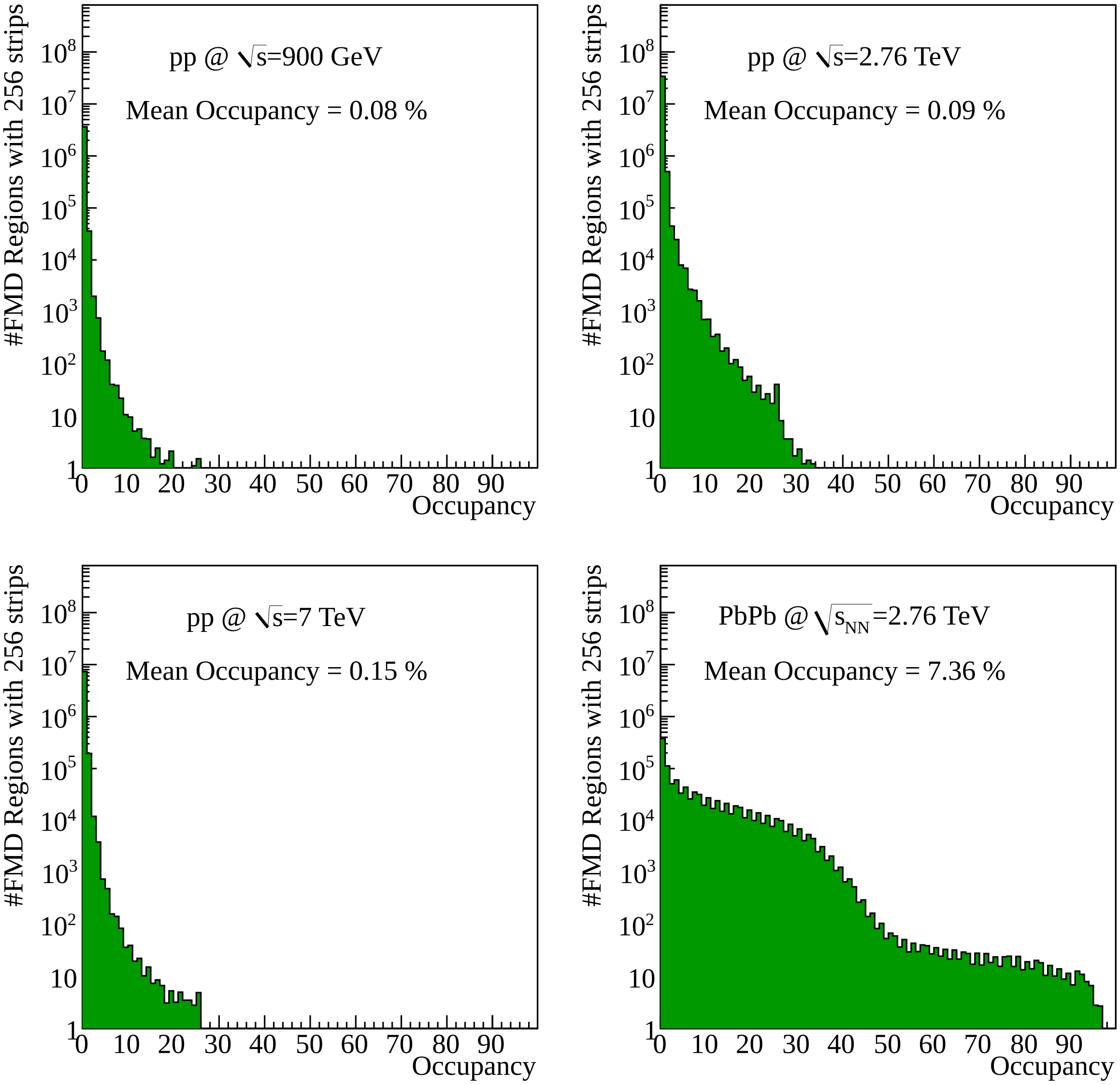

Figure 6.20: Mean occupancies in FMD2I in Pb+Pb collisions at $\sqrt{s_{NN}} = 2.76$ TeV and p+p collisions at $\sqrt{s} = 900$ GeV, $\sqrt{s} = 2.76$ TeV, and $\sqrt{s} = 7$ TeV. The calculation is done in groups of 256 strips.

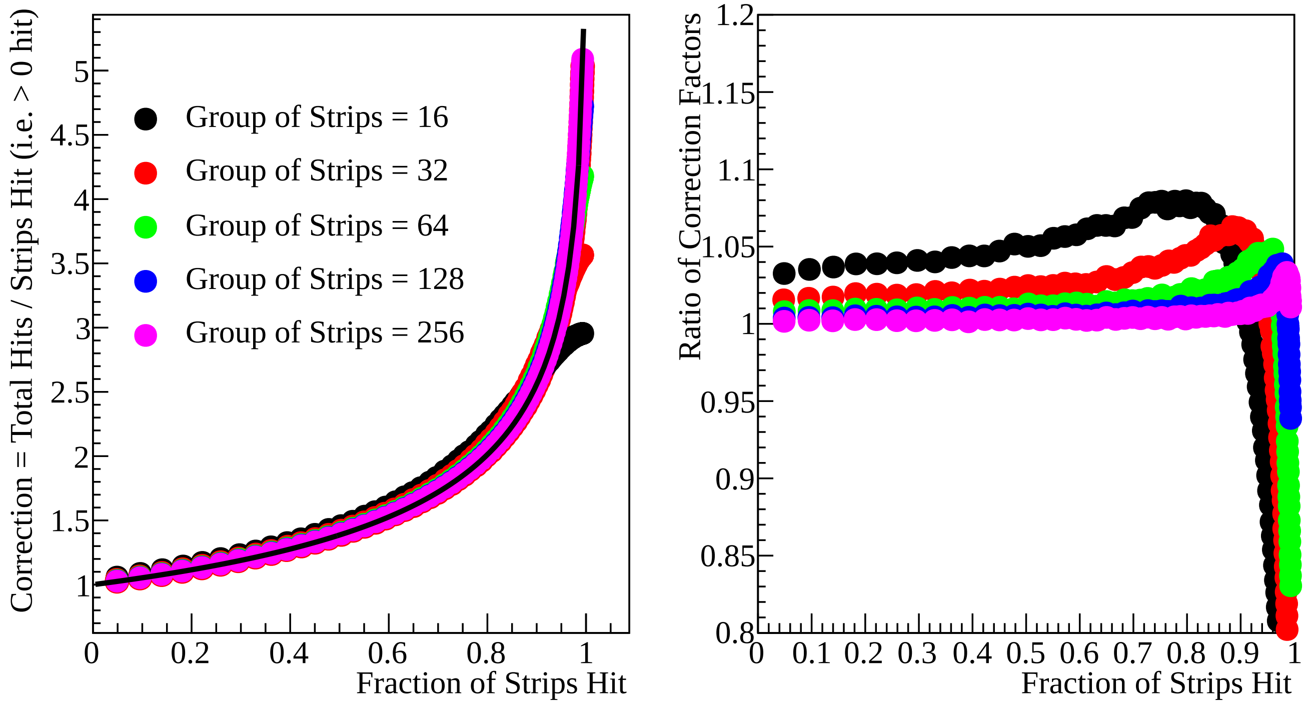

Figure 6.21: Left panel: The correction factors, $C(\mu_{meas}^{region})$ for various numbers of strips in the region obtained from a simulation compared to the Poisson calculation shown as the black curve. Right Panel: Ratios of $C(\mu_{meas}^{region})$ and the analytical calculation.

With μ defined in (6.5) this calculation is carried out per event in regions of the FMD each containing 256 strips. In such a region, N_{ch} for a hit strip ($N_{hits} \equiv 1$) in that region becomes:

$$N_{\text{ch}} = N_{hits} \times C = 1 \times C = C \tag{6.7}$$

Where C is calculated using μ_{meas}^{region}. Another approach to this calculation is to calculate μ_{meas} as an average over all events and then apply C as a final correction [102]. Technically this is the most correct approach as the obtained corrections could vary from event to event especially if the number of strips in a region is small. To take into account such variations, Figure 6.21 shows a comparison between the average calculation of C and $C(\mu_{meas}^{region})$ for different numbers of strips in the selected regions obtained using simulations. In the most central Pb+Pb collisions where the highest occupancies are reached the mean occupancy in some regions is up to $\sim$ 90%. Considering Figure 6.21, it is seen that with the choice of 256 strips per region there would only be a difference between the results of the calculations for occupancies $>$ 80%. It is evident from Figure 6.20 that the difference between the methods is negligible due to the very low number of regions with so high occupancies.

Energy Fit Method

An alternative way to correct for the high occupancy in the FMD is to use the fits to the energy loss distributions discussed in section 6.2.2. As described in section 4.1.4 the fits give the relative weights of the higher order MIP peaks, a_i. Using the energy deposit of strip t, Δ_t, we can construct N_{ch} as:

$$N_{\text{ch},t} = \frac{\sum_i^{N_{max}} i\, a_i\, F(\Delta_t; \Delta_{i,p}, \xi_i, \sigma_i)}{\sum_i^{N_{max}} a_i\, F(\Delta_t; \Delta_{i,p}, \xi_i, \sigma_i)} \quad , \tag{6.8}$$

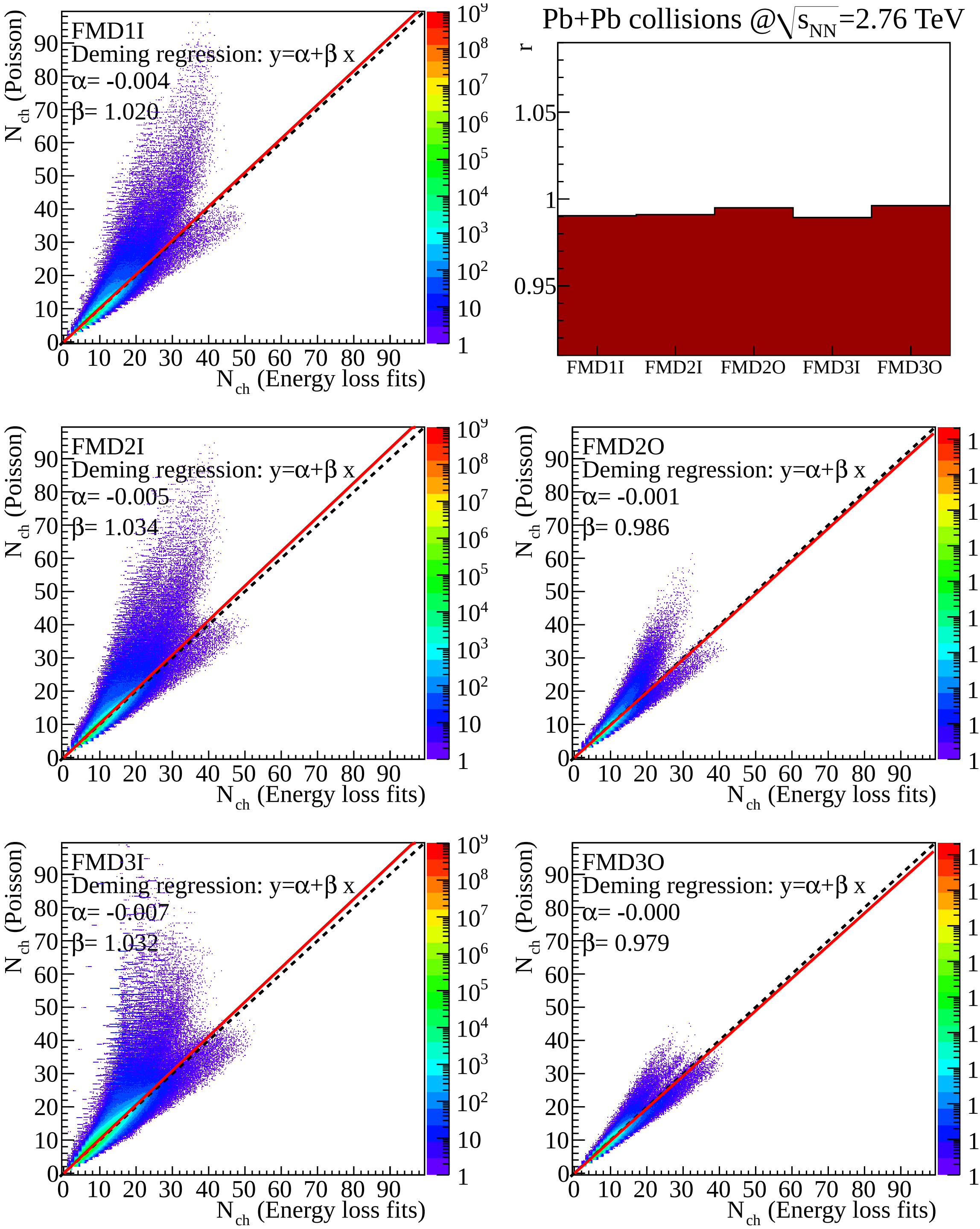

Figure 6.22: Poisson and Energy fit high occupancy correction comparison in Pb+Pb collisions at $\sqrt{s_{NN}} =$ 2.76 TeV. It is seen that there is reasonable correspondance between the two methods as the red line is a fit to the data and the black line is $N_{\mathrm{ch}}(\mathrm{Poisson}) = N_{\mathrm{ch}}(\mathrm{Energy\ Loss\ Fits})$. The upper right corner shows the correlation coefficients of the fits to the data. At high multiplcities we observe a wide spread in the correlations. This is not completely understood but could be consequence of the lack of centrality dependence in the energy fit method.

Here, the function $F(\Delta_t; \Delta_{i,m}, \xi_i, \sigma_i)$ was discussed in section 4.1.4 and $N_{max} = 3$ for this analysis.

Figure 6.22 shows the correlation between N_{ch} calculated with the Poisson and Energy fit methods in the regions of 256 strips in analysis of Pb+Pb collisions. It is seen that there is reasonable correlation between the two calculations to within $\sim 3\%$ in all rings in the Pb+Pb analysis. We find agreement in p+p analysis within $\sim 4\%$. The agreement seems to be better in the inner rings than in the outer rings.

We use the Poisson method because it is the simplest of the two methods. Furthermore we have found reasonable agreement between the Poisson method and the energy fit method. A better understanding of the small discrepancies would be desirable but here we instead include a contribution in the systematic error.

Following the hit merging and high occupancy correction the FMD analysis is contained in the following sum:

$$\left.\frac{d^2N_{\text{ch}}}{d\eta d\varphi}\right|_{incl,r,v,i(\eta,\varphi)} = \sum_{t}^{t\in(\eta,\varphi)} N_{ch,t} \tag{6.9}$$

For practical purposes each $\frac{d^2N_{\text{ch}}}{d\eta d\varphi}$ is a separate object in the program.

6.2.5 Acceptance

The limits in the FMD acceptance can be divided into three categories:

1. **Pseudorapidity Acceptance** Figure 6.23 shows the pseudorapidity acceptance of the FMD as a function of the vertex z component v_z. It is clear that full coverage is only achieved by combining the full vertex range.

   Cuts are applied in η to avoid edge effects. These edge effects arise from the fact that within an FMD ring there are displacements in the z position of the hybrids. Therefore the edge bins in η will have different acceptance. Furthermore the limits of the η bins are not set exactly on the edge of the sensors so the first ‘proper’ bin may have issues in the corrections since the limited coverage can cause numerical instabilities which are completely dependent on the precision of the simulations. To remove the edge effects for each vertex–bin we cut away the first and last η bin (over all φ) as well as all bins where the correction for secondaries is below 0.5 corresponding to a cut of no more than $\Delta\eta = 0.1$. With these cuts the pseudorapidity coverage of the FMD for this analysis becomes $-3.5 < \eta < -1.75$ and $1.75 < \eta < 5$.

2. **Azimuthal (geometrical) Acceptance** The FMD was intended for maximal azimuthal coverage. However, it is obvious from Figure 4.9 that the missing corners of the silicon sensors will affect the azimuthal acceptance of the FMD. Since $dN_{\text{ch}}/d\eta$ involves an implicit integral over φ the missing corners must be corrected for. This correction is included in the correction for secondary particles (see section 6.4). Since the correction is purely geometrical it can also be calculated from knowledge of the FMD geometry. The correction in strip i becomes:

   $$C_{acceptance,i} = \frac{l_{strip,i}}{l_{nominal,i}} \tag{6.10}$$

   where l_{strip} and $l_{nominal,i}$ are the lengths of a strip taking into account the missing corners and the length assuming the corners are still there, respectively. The result of this calculation is shown in Figure 6.24 where it is seen that for the shortest strips the correction is quite large.

3. **Dead strips** The FMD is designed to be very radiation tolerant. However, over time some strips will malfunction or become unresponsive due to electronics issues. These ‘dead’ strips must be taken into account in the analysis. In the FMD the criteria for a channel to be alive are the following:

   $$0.5 < g < 5 \text{ and } 0 < n < 10$$

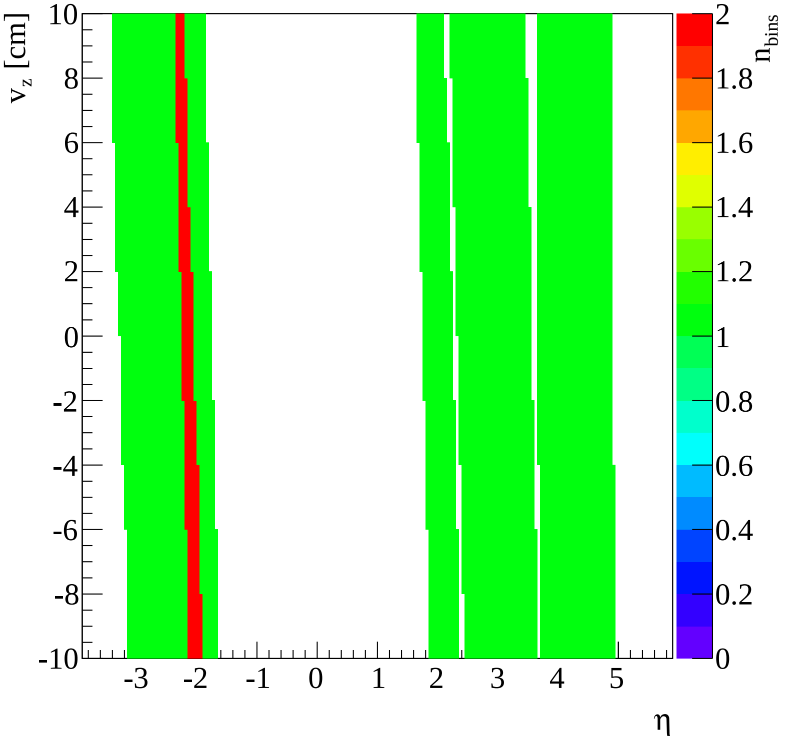

Figure 6.23: FMD pseudorapidity acceptance as a function of the vertex. It is seen that the full coverage requires merging of overlapping η bins. The red band in negative η is the overlap in FMD3 which is larger than the overlaps between FMD1 and FMD2.

where g is the gain of the strip and n is the noise. With this definition 0.93% of the strips in the p+p data at $\sqrt{s} = 900$ GeV are marked as dead while in the later runs a better implementation of the software on the front–end electronics reduced this to 0.25% which holds for p+p collisions at $\sqrt{s} = 2.76$ TeV and $\sqrt{s} = 7$ TeV and Pb+Pb collisions at $\sqrt{s_{NN}} = 2.76$. The 0.25% comes from a single VA chip of FMD1 which is found to be dead. The correction for dead strips, $C^{\eta}_{\mathrm{dead},v,n}$ in strip n is carried out as:

$$C^{\eta}_{\mathrm{dead},v,n}(\eta,\varphi) = \frac{\sum_t^{t\in(\eta,\varphi)} \begin{cases} 1 & \text{if not dead} \\ 0 & \text{otherwise} \end{cases}}{\sum_t^{t\in(\eta,\varphi)} 1}, \tag{6.11}$$

It is possible that the criteria for a strip to be dead are too loose. No systematic study has been done to sharpen the criteria. However, issues have been been identified in FMD2I that must be taken into account.

FMD2I Issues

In Figure 6.18 it is seen that there is a ‘bump’ at lower energies (around $E_{dep}/E_{MIP} \sim 0.2$) for FMD2I which is not observed in the other rings. A closer look at the pre–amplification chip (VA) level reveals that this structure comes from 4 VA chips in FMD2I as shown in Figure 6.25. While sectors 16 and 17 are included in Figure 6.18 the corresponding (η, φ) bins are removed from the final $\frac{d^2N_{\mathrm{ch}}}{d\eta\, d\varphi}$ before projection of the data and their absence is corrected for. The exact origin or nature of these issues is not understood but should be made a priority for future studies of FMD performance. This behaviour could explain the substantial low energy ‘tail’ observed after hit merging if it happened in isolated strips or during running (eg. spontanously in a few events). This has not been confirmed so instead a low cut–off was applied as discussed in section 6.2.3. In the data in this analysis the pattern has not been observed anywhere else than FMD2I. The two removed sectors correspond to 10% of FMD2I.

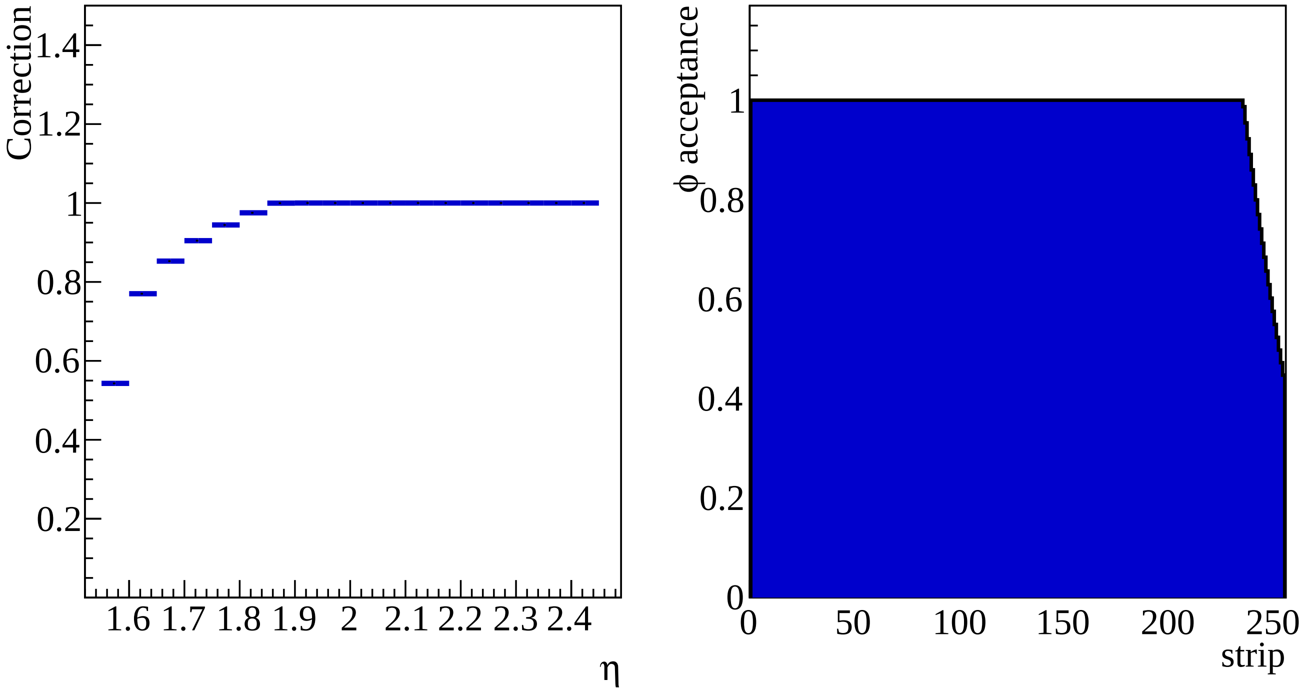

Figure 6.24: FMD geometrical acceptance as calculated in FMD2O using (6.10). As expected the acceptance is unity for most of the coverage however the effect of the missing corners is significant and must be corrected for. This correction is included in the correction for secondaries.

6.2.6 Detector Efficiency

The detector efficiency of the FMD modules was measured using a test beam at the ASTRID facility in 2007 [113]. The efficiency of the modules was found to be better than 99.7% and as good as 99.9% in FMD3[4].

6.3 Counting Particles in the SPD

In this section the counting procedure for charged particles in the SPD inner layer will be discussed. The clusterizer has been discussed in section 4.4 and the clusters it produces are the basic input of this analysis. Similarly to the FMD procedure the analysis performed in vertex–bins to take into account that the pseudorapidity depends on the vertex. Using the cluster input the following histograms are constructed:

$$\left.\frac{d^2N_{\mathrm{ch}}}{d\eta d\varphi}\right|_{incl,v,i(\eta,\varphi)} = \sum_{t}^{t\in(\eta,\varphi)} N_{ch,t} \tag{6.12}$$

6.3.1 Acceptance

Similarly to the FMD the limits of the SPD acceptance can be divided into three categories:

1. **Pseudorapidity Acceptance** Figure 6.26 shows the pseudorapidity acceptance of the SPD as a function of the z vertex component v_z. It is clear that full coverage is only achieved by combining the full vertex range.

---

[4] Of the five FMD rings, FMD3 was constructed first so after testing all the sensors the best were picked for FMD3.

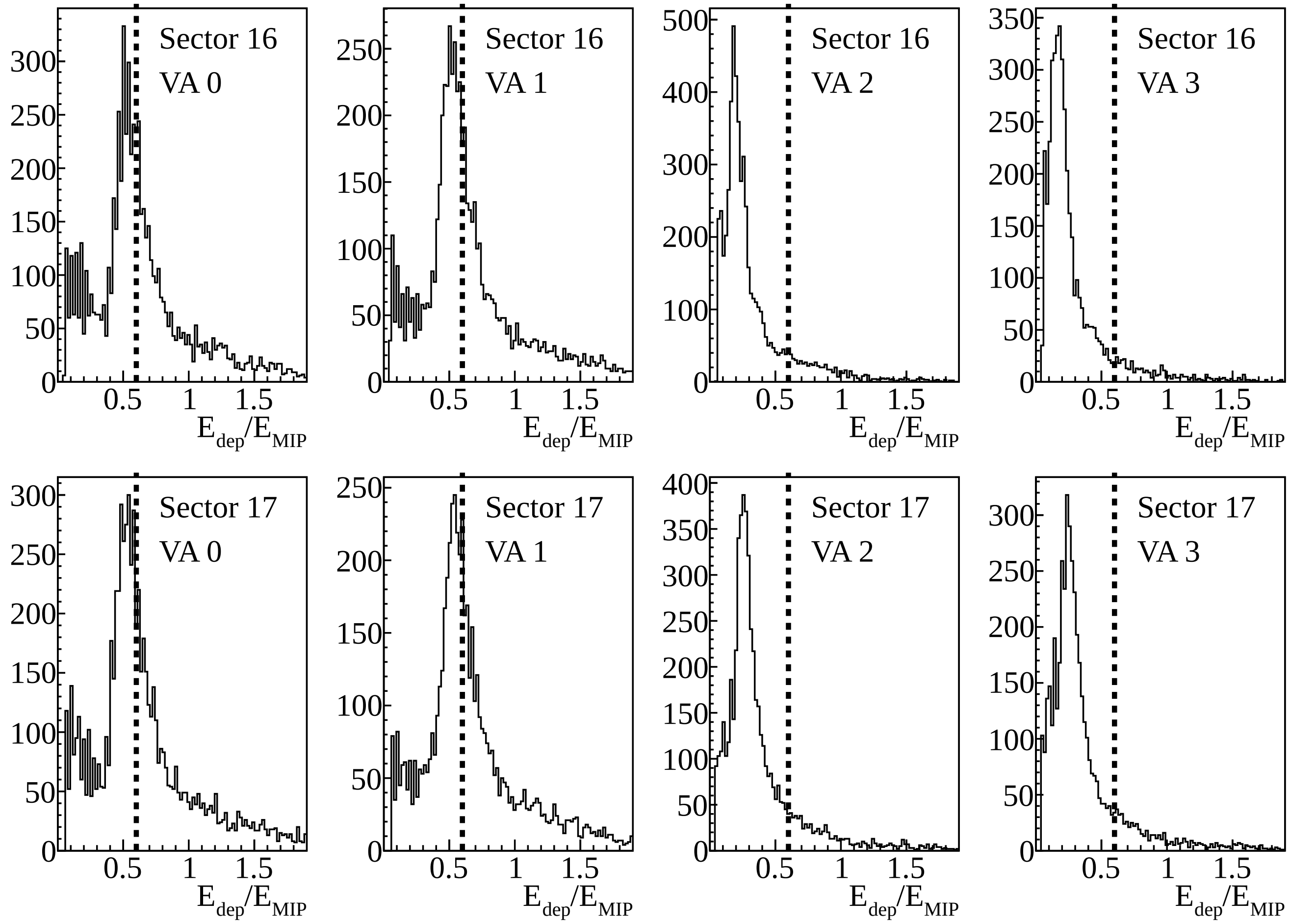

Figure 6.25: FMD2I energy distributions per VA chip in sectors 16 and 17 from run 138225. Each plot shows the energy loss distribution of 128 strips of a single VA chip. It is seen that there are clear issues. It appears that the MIP peak is shifted down in 4 out of 8 VA chips which will affect the analysis. The dashed lines mark $E_{dep}/E_{MIP} = 0.6$ to guide the eye when comparing the plots.

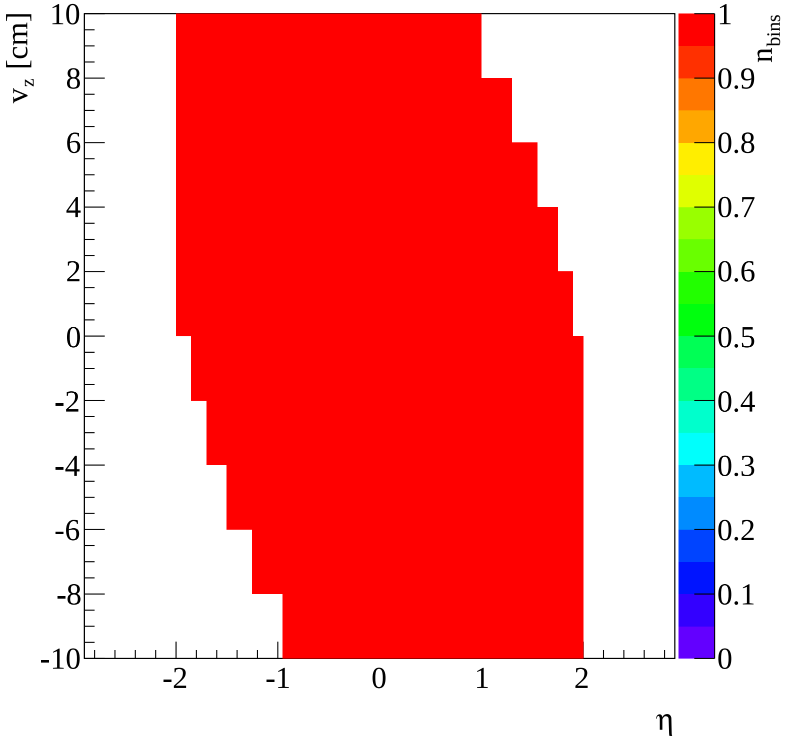

Figure 6.26: SPD pseudorapidity acceptance as a function of vertex. It is seen that there is more variation of the coverage as function of the vertex than observed in the FMD. This is due to the low pseudorapidity values. The truncation at $|\eta| = 2$ is due to application of 'fiducial' cuts in the analysis.

The SPD data are cut similarly to the FMD to avoid edge effects. With these cuts the pseudorapidity coverage of the SPD for this analysis becomes $-2 < \eta < 2$.

2. **Azimuthal (geometrical) Acceptance** The SPD is designed for full azimuthal coverage. So in principle there is no need to apply a correction for geometrical acceptance.

3. **Dead channels** While by design the SPD has no issues with azimuthal acceptance it suffers from the cooling issues touched upon in section 4.4. From the calculation of the secondary correction in section 6.4 it is seen that the SPD maps are full of holes in the azimuthal acceptance. These holes come from half–staves being turned off because of the cooling issues. On top of this there will be channels that are 'proper dead' but this is a negligible fraction compared to the fraction turned off to avoid overheating. This means that the correction for dead channels (or 'dead channels acceptance') will be large. The correction in channel t is constructed as:

$$C^{\eta}_{v,i}(\eta) = \frac{\sum_t^{t\in(\eta)} \begin{cases} 1 & \text{if active} \\ 0 & \text{otherwise} \end{cases}}{\sum_t^{t\in(\eta)} 1}, \qquad (6.13)$$

Whether a channel is active or not is deduced from the secondary maps. We mark (η, φ) bins with a correction factor > 0.9 to be active; all other bins are taken to be dead in this context.

Figure 6.27 shows this correction for 3 vertex–bins of the SPD. It is seen that this is a significant correction and is even of a larger magnitude than the correction for secondaries as discussed in section 6.4.

6.3.2 Detector Efficiency

When the eliminated half–staves are taken into account the physical performance of the SPD pixels is very good. The efficiency has been measured to be $> 99\%$ [104]. The few proper dead channels are included in the correction discussed above.

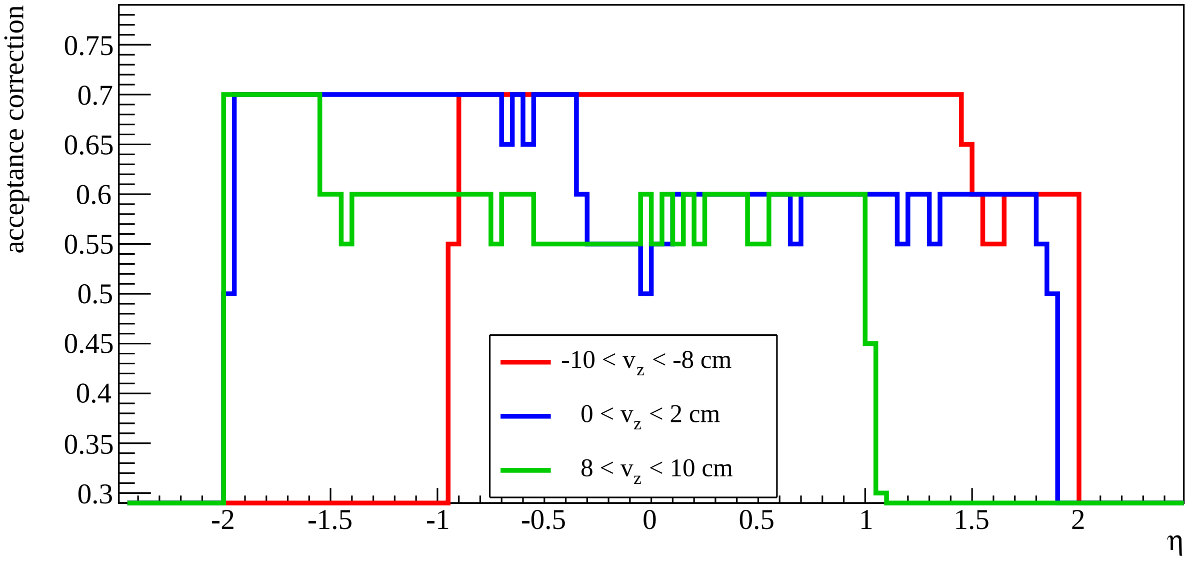

Figure 6.27: The Figure shows the SPD acceptance correction applied to the data after correcting for secondaries. The magnitude of the correction is caused by the high number of dead (or turned–off) channels in the SPD (see text).

6.4 Correction for Secondaries

After the counting the inclusive N_{ch} a correction for the secondary particles produced in the experiment must be applied to the data. The sources of the secondary particles are twofold:

1. **Interactions with material** The main part of the secondary particles comes from interactions of particles (primary or secondary) with the material in the experiment. In the simulations these interactions are handled by GEANT as described in section 5.3.2. Note that these particles can come from anywhere since multiple scatterings are possible during transport of the particles through ALICE. While many steps have been taken to reduce the material budget in front of the ALICE detectors it remains *the* main issue for the forward detectors.

2. **Decays of short lived resonances (weak decays)** While the main component of the background comes from material interactions weak decays play an important role as well. An example of such a decay is for example:

$$\Lambda \rightarrow p + \pi^-$$

   where the electrically neutral Λ particle decays into a proton and a charged pion. The property to change neutral particles into charged ones makes an accurate description of the decays in the simulations very important. ALICE uses PYTHIA to decay short lived particles for p+p and Pb+Pb collisions.

Figure 6.28 shows the comprehensive simulated $dN_{\text{ch}}/d\eta$ from the various sources for the FMD and the SPD inner layer. It is clear that the FMD is hit by a very large background of secondary particles and that the correction for it will be of a large magnitude. The SPD, on the other hand, is located just outside of the beryllium[5] beampipe so it will almost only see the few secondary particles produced there. While the background in FMD3 is indeed high the particularly high peak in Figure 6.28 is due

---

[5] Besides being toxic, expensive and difficult to work with, Beryllium is the number 1 choice for beampipe material through the LHC experiments since it produces very little background compared to other metals. From the discussion here it is clear that this is a key property for beampipe material. The nuclear interaction length of beryllium is $\sim$ 42 cm compared to $\sim$ 17 cm for steel, the material most of the LHC beampipe is made from.

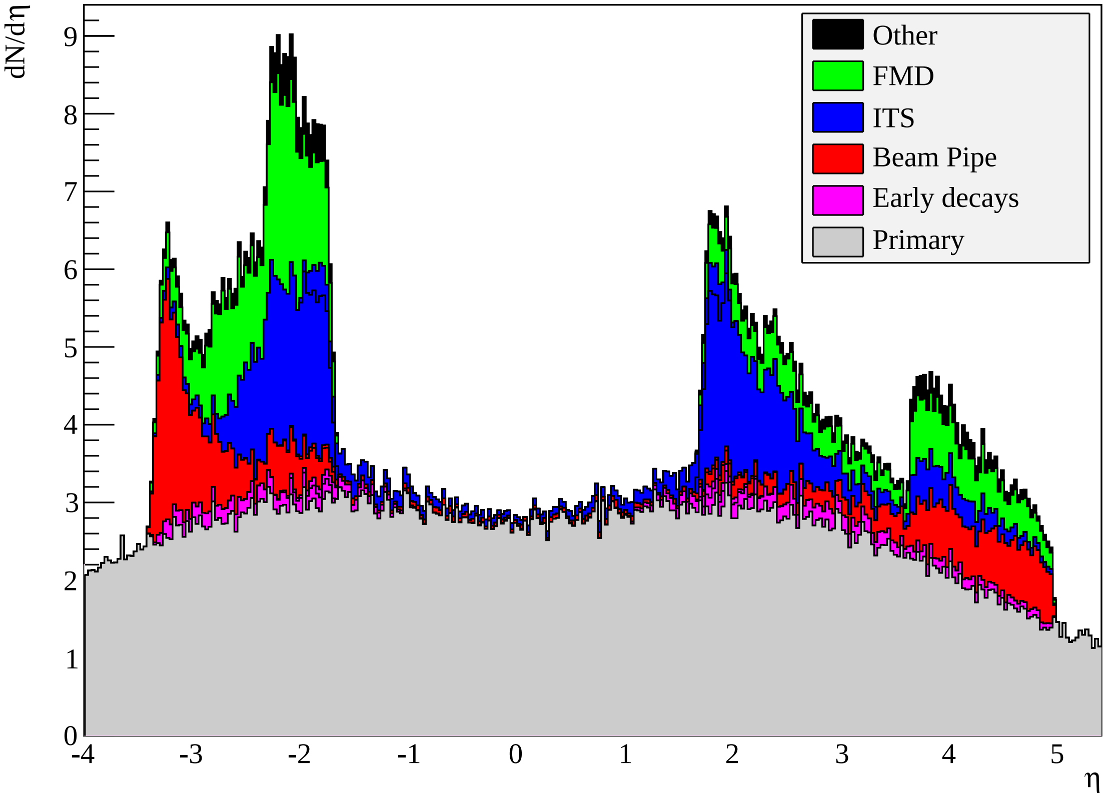

Figure 6.28: Summary of the origin of the particles detected by the FMD and SPD from simulations. It is clearly seen that the FMD is hit by many more secondary particles than the SPD due to their different positions in ALICE. Furthermore it is seen that the FMD itself contributes significantly to the secondaries. The 'spike' at $\eta \sim -2$ is caused by the large FMD3 η overlap (between FMD3I and FMD3O). The rising contribution from the beampipe in FMD3 around $\eta \sim -3$ comes from a steel bellow at the end of the Be beampipe where it is connected to the LHC steel pipe.

to the overlap between FMD3I and FMD3O. Plots for each FMD ring and the SPD are shown in Figure 6.29. The two figures confirm that the main part of the background of secondary particles is indeed from material interactions. For the FMD the contribution from the beampipe is larger than for the SPD due to the smaller angle of the particles and hence longer path through the beampipe.

Note that for both the FMD and SPD a high fraction of the secondaries comes from the detectors themselves. To correct for the background of secondary particles it is important to keep in mind that the FMD and the inner SPD layer will detect any charged particle that is thrown at it. Furthermore there is no way to detect the direction of a charged particle which makes the direct distinction between primary and secondary particles impossible. Therefore the definition of the correction for secondary particles becomes the following simple fraction, calculated from simulations:

$$C_{secondary} = \frac{\sum_i^{N_{t,v}} N^i_{ch,\text{ primary}}(\eta,\varphi)}{\sum_i^{N_{t,v}} N^i_{ch,\text{ secondary + primary}}(\eta,\varphi)} \tag{6.14}$$

where $N_{t,v}$ is the number of events with a valid trigger and a vertex in bin v, and $N^i_{ch,\text{ secondary + primary}}$ is the total number of charged particles that hit the FMD in event i in the specified (η,φ) bin and $N^i_{ch,\text{ primary}}$ is the number of primary charged particles in event i within the specified (η,φ) bin. As discussed in section 6.2.5 the correction for secondaries by construction contains the correction for geometrical acceptance for

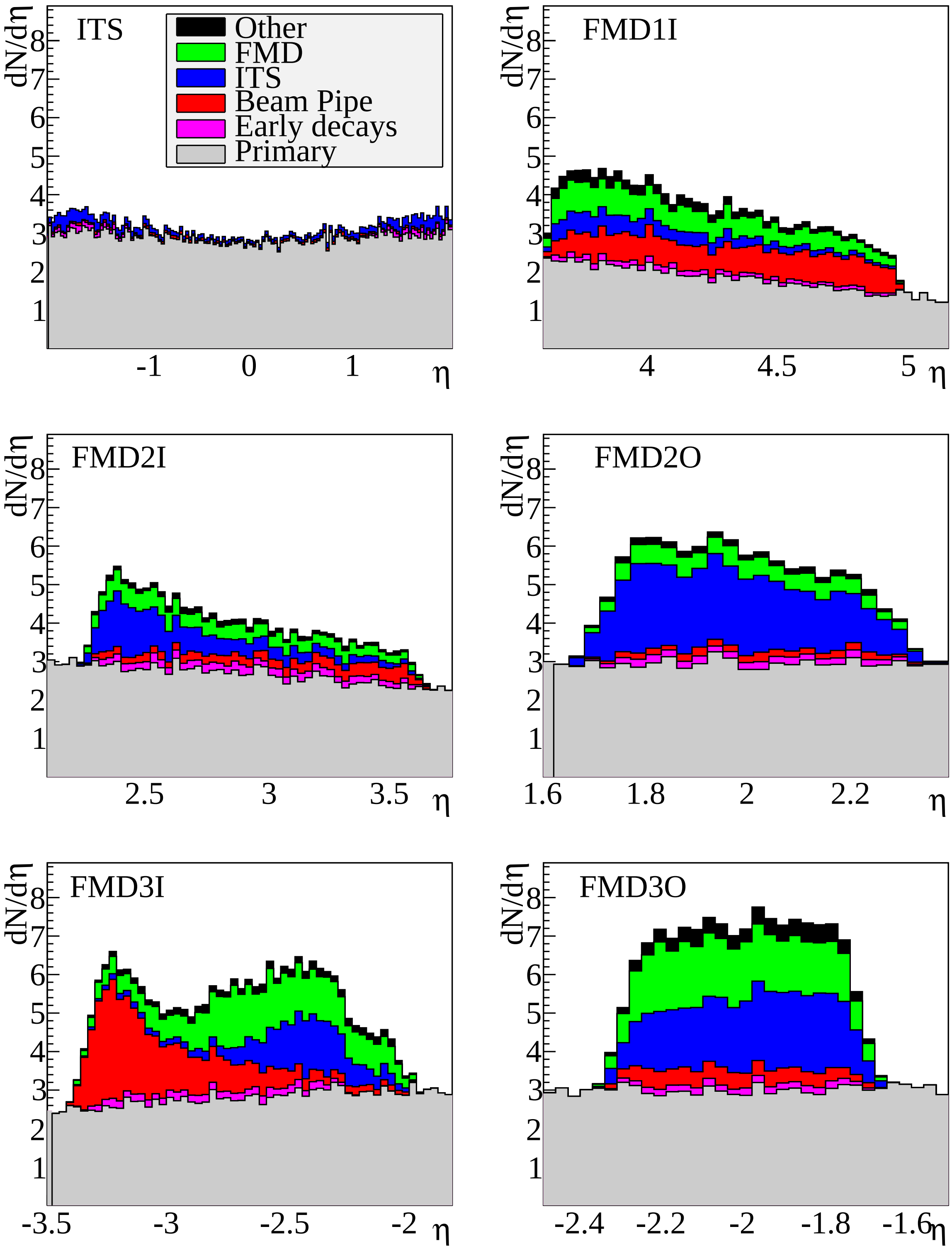

Figure 6.29: Detailed view of the secondary contributions from Figure 6.28. It is clear from the Figure that the correction for secondaries is crucial for any meaningful physics results to come out of this analysis.

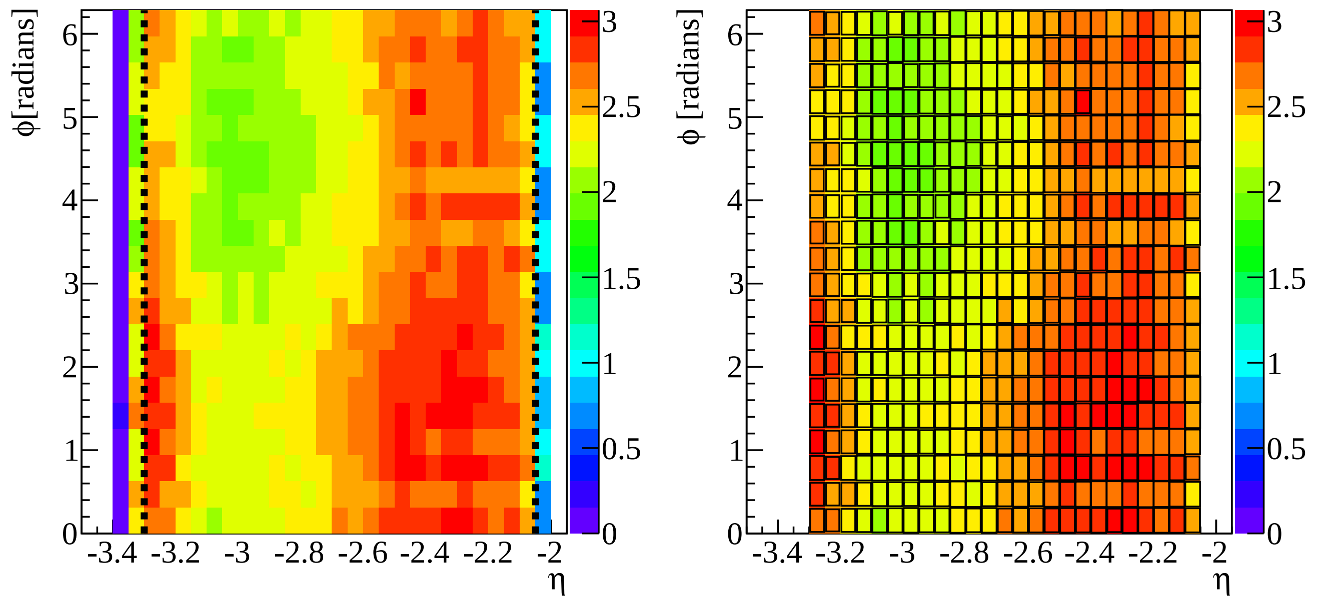

Figure 6.30: Left Panel: The secondary correction in FMD3I for Pb+Pb collisions at $\sqrt{s_{NN}} = 2.76$ TeV for $v_z \in [0, 2]$. The lines mark the 'fiducial' cuts described in the text. It is seen that the correction is indeed large, up to $C \sim 3$. Right Panel: The same secondary map after cuts, overlaid with the data drawn as a box plot. These plots are the basic result of this analysis from which $\frac{1}{N}\frac{dN_{\mathrm{ch}}}{d\eta}$ is derived.

the FMD. This is because the nominator in (6.14) includes all primary particles. Therefore the corners are only missing in the denominator because it includes only FMD hits.

The correction is applied per (η, φ) 'bin'. Figures 6.30 and 6.31 shows the correction map for a vertex–bin overlaid with the data in the same bin for the FMD and the SPD. To first order it is a good sanity check of the simulations that the data actually matches the secondary maps derived from simulations. The figures also illustrate the 'fiducial cuts' described in section 6.2.5.

6.5 Building $dN_{\mathrm{ch}}/d\eta$

In this section the process of summing, projecting, and normalizing the data to extract $dN_{\mathrm{ch}}/d\eta$ will be discussed.

6.5.1 Summing the Data

Following the corrections for secondaries and acceptance the data are collected into one object (a 2–dimensional histogram) per event for the FMD and the SPD. There is one histogram for the FMD and one for the SPD and they are constructed as follows:

$$\left.\frac{d^2N_{\mathrm{ch}}}{d\eta\, d\varphi}\right|_{v,i(\eta,\varphi)} = \frac{1}{N_{r\in(\eta,\varphi)}} \sum_{r}^{r\in(\eta,\varphi)} \left.\frac{d^2N_{\mathrm{ch}}}{d\eta\, d\varphi}\right|_{r,v,i(\eta,\varphi)} \left.\frac{1}{C}\right|_{r,v,i(\eta,\varphi)} \tag{6.15}$$

$$\delta\left[\left.\frac{d^2N_{\mathrm{ch}}}{d\eta\, d\varphi}\right|_{v,i(\eta,\varphi)}\right] = \frac{1}{N_{r\in(\eta,\varphi)}} \sqrt{\sum_{r}^{r\in(\eta,\varphi)} \delta\left[\left.\frac{d^2N_{\mathrm{ch}}}{d\eta\, d\varphi}\right|_{r,v,i(\eta,\varphi)}\right]^2 \left.\frac{1}{C}\right|_{r,v,i(\eta,\varphi)}} \quad , \tag{6.16}$$

Here, C is the total correction factor, obtained as: $C = C_{secondary} \times C^{\eta}_{v,i}$ from (6.14), (6.11), and (6.13). $N_{r\in(\eta,\varphi)}$ is the number of overlapping histograms in (6.15).

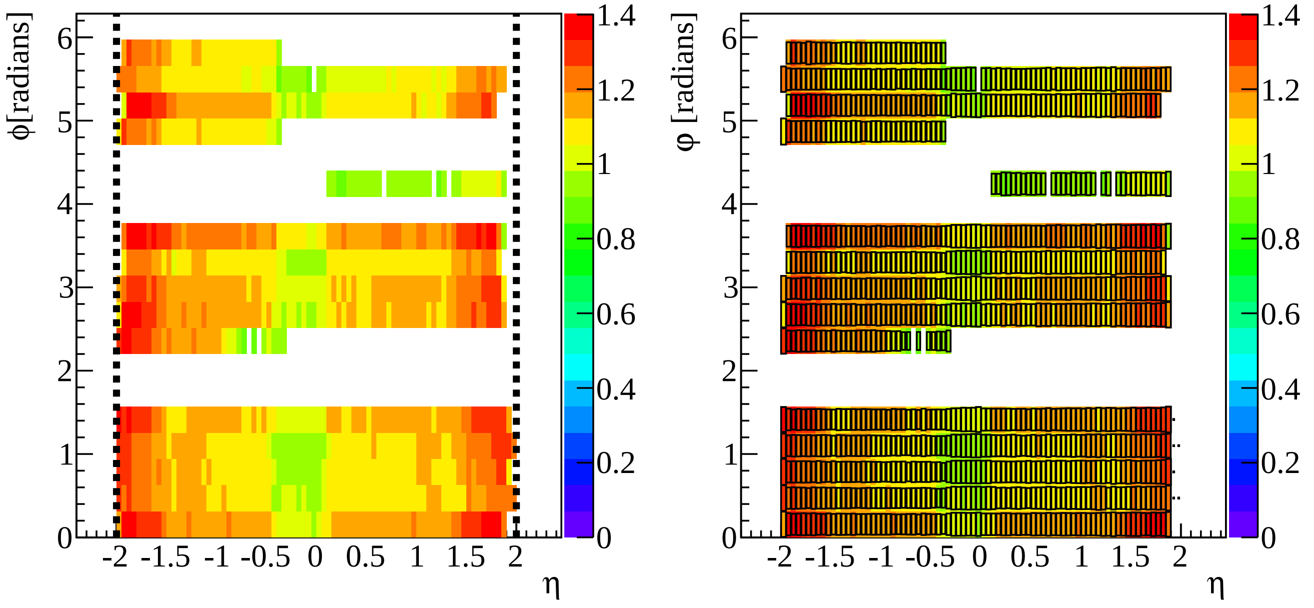

Figure 6.31: Left Panel: Secondary correction for the SPD in Pb+Pb collisions at $\sqrt{s_{NN}} = 2.76$ for $v_z \in [0, 2]$. It seen that the correction is significantly smaller than in the FMD. The lines mark the 'fiducial' cuts at $|\eta| = 2$. Right Panel: The secondary map after cuts overlaid with the data.

These histograms constitute the AOD objects for the FMD and SPD analysis as discussed in Chapter 5. For the SPD the sum over the rings is obviously not applicable.

6.5.2 Normalization

To obtain the number of events in a trigger class (INEL or NSD), N_X, it is calculated as:

$$\begin{aligned} N_X &= \frac{1}{\epsilon_X}\left[N_{\mathrm{A}} + \alpha(N_{\bar{\mathrm{V}}}-\beta)\right] && (6.17)\\ &= \frac{1}{\epsilon_X}\left[N_{\mathrm{A}} + \frac{N_{\mathrm{A}}}{N_{\mathrm{V}}}(N_{\mathrm{T}} - N_{\mathrm{V}} - \beta)\right] \\ &= \frac{1}{\epsilon_X}N_{\mathrm{A}}\left[1 + \frac{1}{\epsilon_V} - 1 - \frac{\beta}{N_{\mathrm{V}}}\right] \\ &= \frac{1}{\epsilon_X}\frac{1}{\epsilon_V}N_{\mathrm{A}}\left(1 - \frac{\beta}{N_{\mathrm{T}}}\right) && (6.18)\end{aligned}$$

where

ϵ_X is the trigger efficiency for type $X \in [\mathrm{INEL}, \mathrm{NSD}, ...]$ discussed in section 6.1

$\epsilon_V = \frac{N_{\mathsf{V}}}{N_{\mathsf{T}}}$ is the vertex efficiency evaluated over the data.

N_{A} is the number of events with a trigger *and* a valid vertex in the selected range

N_{V} is the number of events with a trigger *and* a valid vertex.

N_{T} is the number of events with a trigger.

$N_{\bar{\mathsf{V}}} = N_{\mathsf{T}} - N_{\mathsf{V}}$ is the number of events with a trigger *but no* valid vertex

$\alpha = \frac{N_{\mathsf{A}}}{N_{\mathsf{V}}}$ is the fraction of accepted events of the total number of events with a trigger and valid vertex.

$\beta = N_a + N_b - N_e$ is the number of background events *with* a valid off-line trigger.

The two terms in the brackets in (6.17) refers to the observed number of event N_{A}, and the events missed because of no vertex reconstruction. The rationale behind the expression is that we try to recover the number of events with a given trigger class assuming that $N_{\not\mathrm{V}}$ has a similar vertex distribution to N_{A}. Thus, we add to N_{A} the assumed fraction of the number of events out of $N_{\not\mathrm{V}}$ within the vertex range. However, some of $N_{\not\mathrm{V}}$ will come from beam–halo events that are included in the event sample by mistake. The subtraction of β takes this contamination into account. See 6.5.4 for a discussion of beam–halo contamination.

Note, for $\beta \ll N_{\mathrm{T}}$ (6.17) reduces to the simpler expression

$$N_X = \frac{1}{\epsilon_X}\frac{1}{\epsilon_V} N_{\mathrm{A}}$$

Since beam–halo events are not simulated in the simulations, $\beta = 0$ there.

6.5.3 Projection of the Data

The data are summed over N_{A} events with a valid trigger and a valid vertex satisfying $-10 < v_z < 10$ cm as described in section 6.1. Due to the different acceptance, the number of events in each η bin may vary. This is handled by keeping track of the number of events per η bin in the analysis. For a vertex–bin v the number of events per η bin can be calculated as an acceptance factor, $I(\eta)$:

$$I_{v,i}(\eta) = \frac{1}{N_{r\in(\eta)}} \sum_{r}^{r\in(\eta)} \left\{ \begin{array}{ll} 0 & \eta \text{ bin not selected} \\ 1 & \eta \text{ bin selected} \end{array} \right. \quad , \tag{6.19}$$

To build the $\frac{d^2N_{\mathrm{ch}}}{d\eta\, d\varphi}$ distribution it is enough to sum (6.15) and (6.19) over all N_{A} events and correct for the acceptance $I(\eta)$

$$\left.\frac{d^2N_{\mathrm{ch}}}{d\eta\, d\varphi}\right|_{(\eta,\varphi)} = \sum_{i}^{N_{\mathrm{A}}} \left.\frac{d^2N_{\mathrm{ch}}}{d\eta\, d\varphi}\right|_{i,v(\eta,\varphi)} \tag{6.20}$$

$$I(\eta) = \sum_{i}^{N_{\mathrm{A}}} I_{i,v}(\eta) \quad . \tag{6.21}$$

Note, that by construction $I(\eta) \leq N_{\mathrm{A}}$. Here (6.20) will be the $\frac{d^2N_{\mathrm{ch}}}{d\eta\, d\varphi}$ per event in the selected event sample N_{A}. We need to divide with the number of events in the event class of interest from (6.18) to obtain the $\frac{d^2N_{\mathrm{ch}}}{d\eta\, d\varphi}$ of a specific trigger class.

The final event–normalised charged particle density becomes:

$$\frac{1}{N}\frac{dN_{\mathrm{ch}}}{d\eta} = \frac{1}{N_X}\int_0^{2\pi} d\varphi \frac{\left.\frac{d^2N_{\mathrm{ch}}}{d\eta\, d\varphi}\right|_{(\eta,\varphi)}}{I(\eta)} \tag{6.22}$$

6.5.4 Beam–halo effects and β

To study the beam–halo effects in the data the control triggers discussed in section 6.5.4 must be used. The specific beam–halo events taken are exposed to the same event selection as the proper physics triggers discussed in section 6.1. From this study the value of β in (6.17) can be assessed. A value of $\beta \sim 0.001 \times N_{\mathrm{T}}$ is obtained in p+p collisions at $\sqrt{s} = 900$ GeV, $\sqrt{s} = 2.76$ TeV, and $\sqrt{s} = 7$ TeV.

While β describes the effect of beam–halo contamination on the *event level* the effect at the *hit level* must also be considered. In other words: What is the measured signal from the beam–halo events that will be included in $dN_{\mathrm{ch}}/d\eta$? This question can be answered through $dN_{\mathrm{ch}}/d\eta$ analysis of the β events. The results of such an analysis is shown in Figure 6.32. It is seen that the particle production per event in beam–halo events is actually quite high compared to p+p collisions (see Figure 2.4 or peek at Figure 7.3 in Chapter 7 to see results on particle production in p+p events). This is not so hard to understand as the beam–halo events include p+O_2 or p+N_2 collisions which must be expected to have a higher particle production. Along the same lines the lower observed values in the SPD are also understandable as the particle production in beam–halo would be expected to be higher at forward rapidities. To subtract the beam–halo contribution to $\frac{1}{N}\frac{dN_{\mathrm{ch}}}{d\eta}$ it must be scaled by β/N_{A} which makes the magnitude of the correction $< 1\%$ in p+p collisions at all three energies.

6.6 Simulated Analysis Correction and final $dN_{\mathrm{ch}}/d\eta$

In this analysis the choice is made to 'isolate' the effects of the secondaries to the correction for secondaries and then run the full analysis on the simulated data along with that of physics data. In this way we can assess the accuracy of the method separately from the correction of secondaries as well as estimate a correction for detector effects etc. Thus, the strategy is to run the full analysis of physics data and simulated data, calculating $\frac{1}{N}\frac{dN_{\mathrm{ch}}}{d\eta}$ for both using (6.22). A correction can then be applied from the analysis of simulated data to ensure that the correspondence between the simulation analysis and the simulated input $\frac{1}{N}\frac{dN_{\mathrm{ch}}}{d\eta}$ is one-to-one. Thus we construct the final $\frac{1}{N}\frac{dN_{\mathrm{ch}}}{d\eta}$ as:

$$\left.\frac{1}{N}\frac{dN_{\mathrm{ch}}}{d\eta}\right|_{\mathrm{final}} = \left.\frac{1}{N}\frac{dN_{\mathrm{ch}}}{d\eta}\right|_{\mathrm{analysis}} \frac{\left.\frac{1}{N}\frac{dN_{\mathrm{ch}}}{d\eta}\right|_{\mathrm{simulation\ truth}}}{\left.\frac{1}{N}\frac{dN_{\mathrm{ch}}}{d\eta}\right|_{\mathrm{simulated\ analysis}}} \tag{6.23}$$

The magnitude of this final simulation–based correction is up to 10% in p+p analysis and 5% in Pb+Pb analysis. For p+p analysis the correction by design includes the vertex and trigger bias correction discussed in section 6.6.1.

Examples of the correction in p+p collisions at $\sqrt{s} = 900$ GeV and in Pb+Pb collisions at $\sqrt{s_{NN}} = 2.76$ TeV are shown in Figure 6.33. As a sanity check of the method, Figure 6.34 shows the analysis of simulated data for p+p collisions at $\sqrt{s} = 900$ GeV before and after the correction. Is it seen that the correction works as anticipated.

Apart from the final correction based on analysis of simulated data two additional corrections must be applied as well. These are described in the following sections.

6.6.1 Correction for Trigger and Vertex Bias

For p+p collisions a correction is needed because of the fact that the trigger or the vertex reconstruction may bias the data. This can be understood from the trigger definitions in Table 6.1 considering also that the SPD is used for vertex determination. Thus, the trigger selection covers almost 10 units of pseudorapidity while the vertex selection covers only 4. This means that the sample of events not selected for analysis because of a missing vertex can have a different $\frac{1}{N}\frac{dN_{\mathrm{ch}}}{d\eta}$ distribution than the events analyzed. To see this effect from simulations consider Figure 6.35 which shows the $\frac{1}{N}\frac{dN_{\mathrm{ch}}}{d\eta}$ from simulated primary particles of the selected events (normalized using (6.17)) compared to the simulated 'truth' (the $\frac{1}{N}\frac{dN_{\mathrm{ch}}}{d\eta}$ from all generated events (Inelastic or NSD)). The difference is clear and its η dependence reveals that the effect is larger at more forward rapidities. Fortunately, Figure 6.35 also gives the correction for this effect, namely the ratio of the two distributions.

For Pb+Pb collisions no trigger or vertex bias is found and the trigger efficiency is found to be 100% and all events with centrality $< 80\%$ get a vertex due to the high multiplicities.

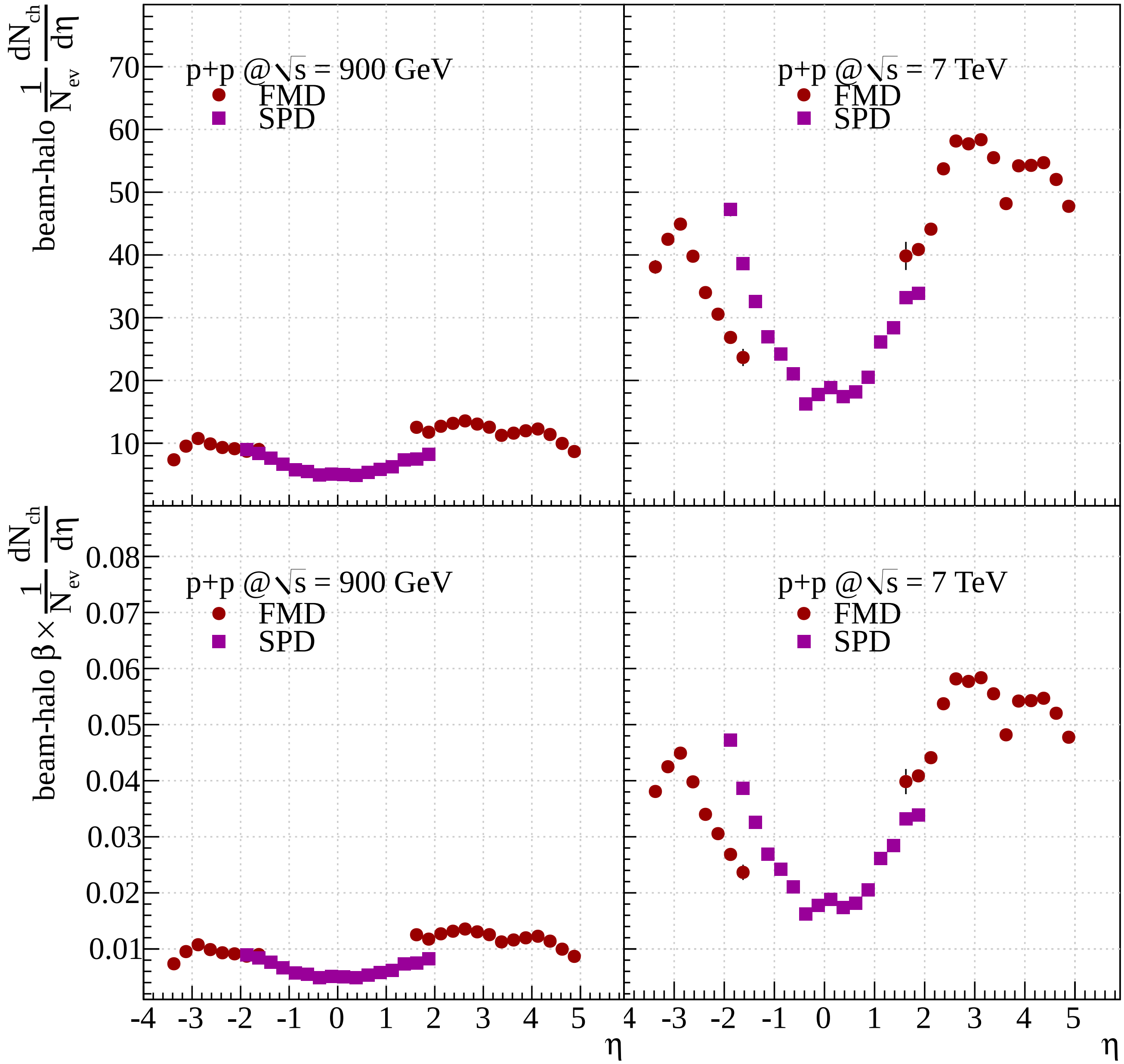

Figure 6.32: Analysis of beam–halo triggers in p+p analysis at $\sqrt{s} = 900$ GeV and $\sqrt{s} = 7$ TeV.

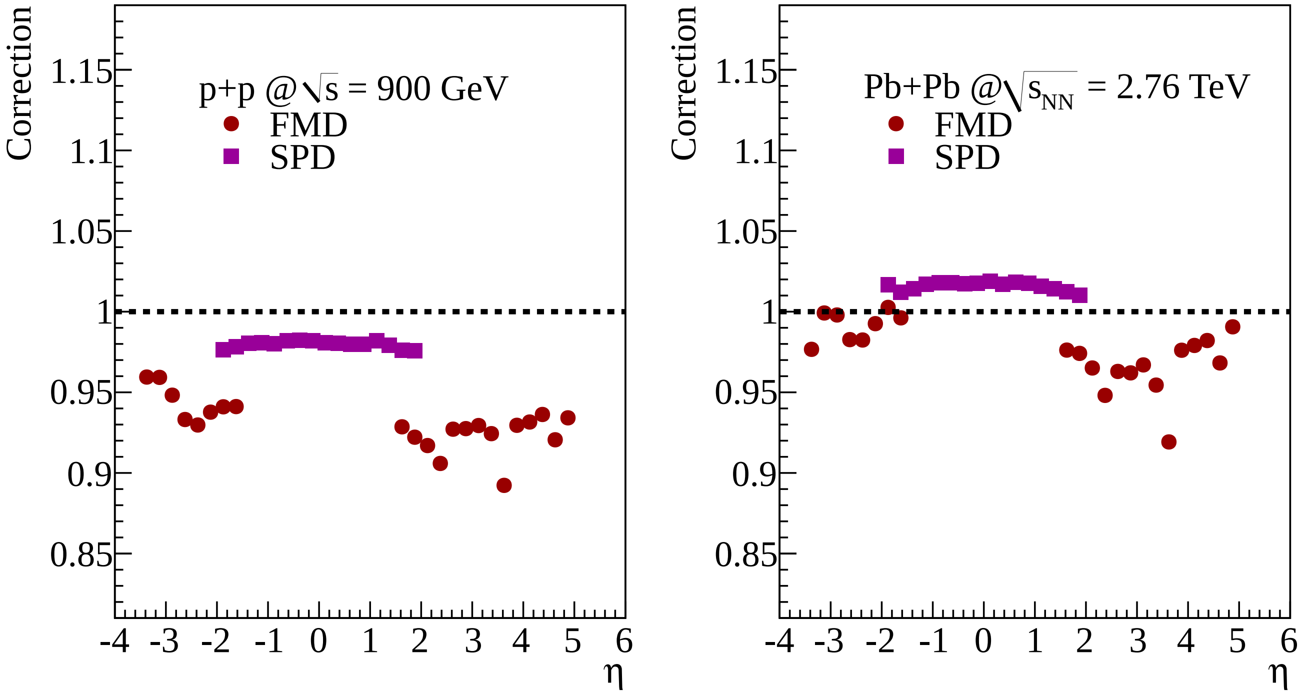

Figure 6.33: Final correction from analysis of simulated data in p+p collisions at $\sqrt{s} = 900$ GeV and in Pb+Pb collisions at $\sqrt{s_{NN}} = 2.76$ TeV.

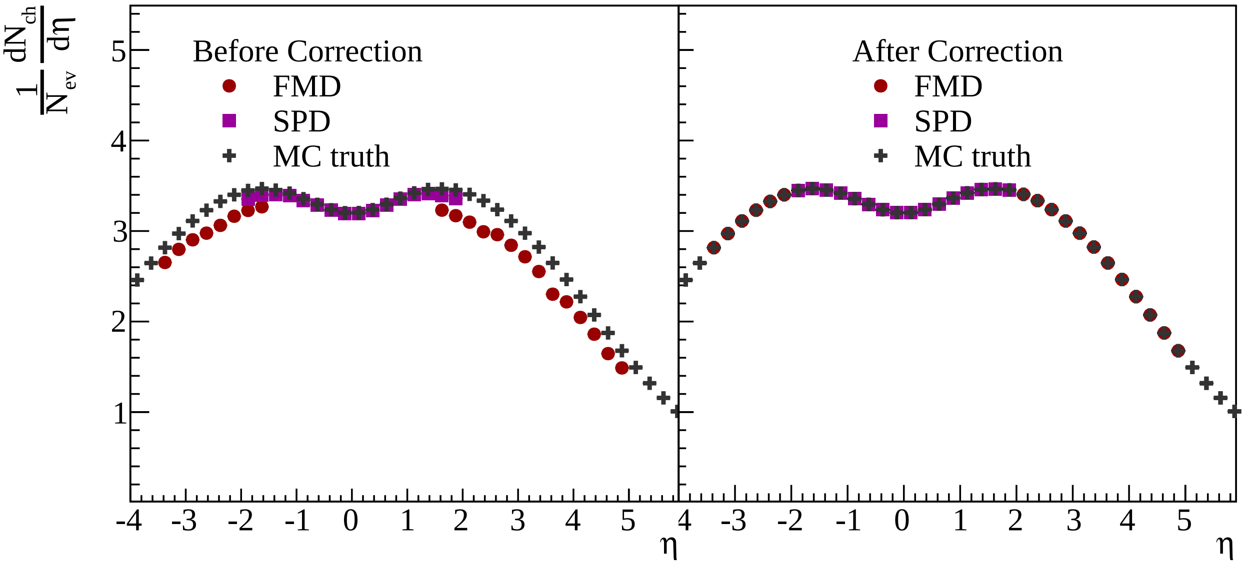

Figure 6.34: $\frac{1}{N}\frac{dN_{\mathrm{ch}}}{d\eta}$ in simulations of p+p collisions at $\sqrt{s} = 900$ GeV before and after the application of the final correction given in (6.23).

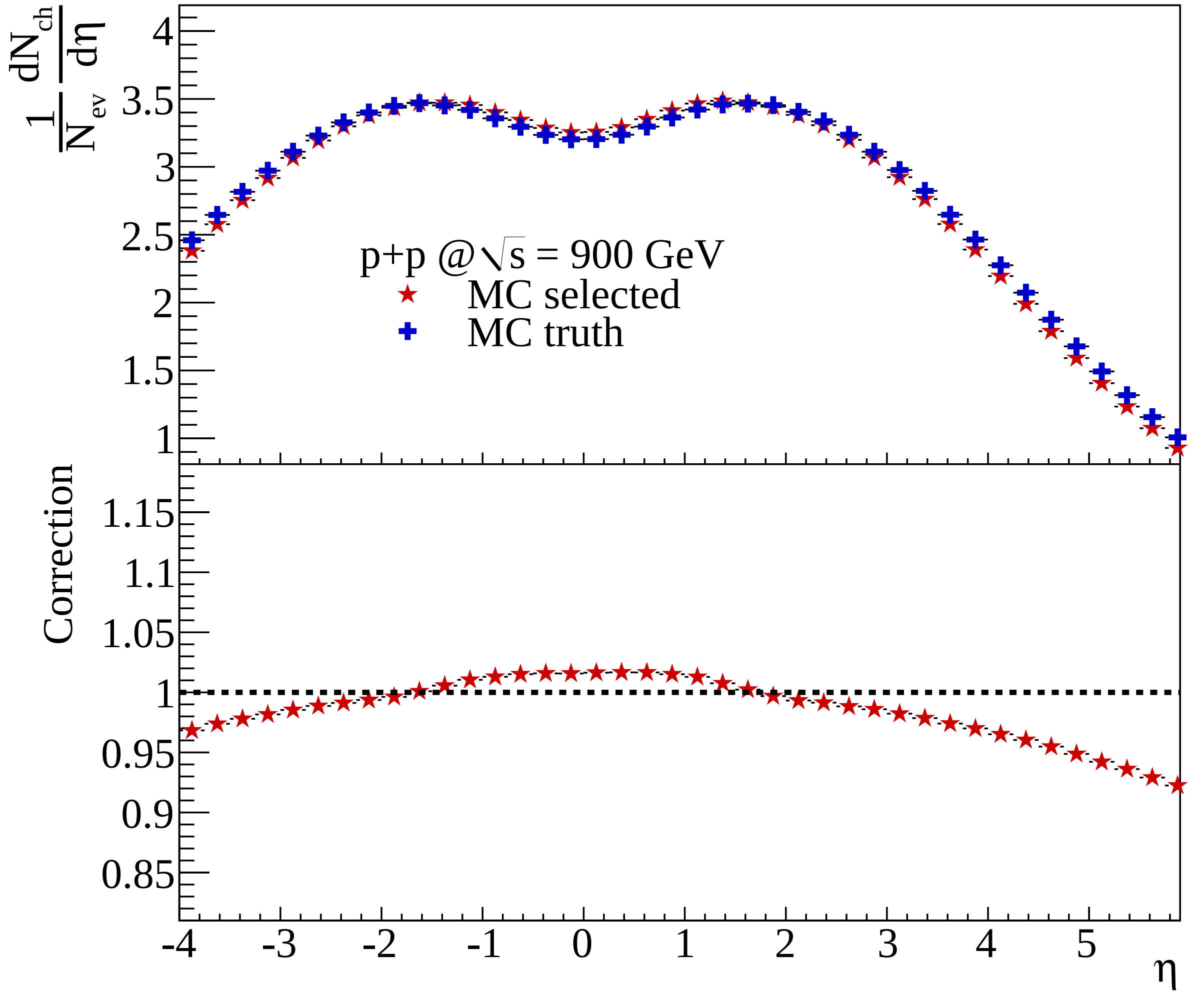

Figure 6.35: Correction for trigger and vertex bias in p+p collisions at $\sqrt{s} = 900$ GeV.

p_T interval	Correction factor
$p_T < 0.17$ GeV/c	1.0
$0.17 < p_T < 0.4$ GeV/c	$1.0 + 0.3 \times (p'_T - 0.17)$
$0.4 < p_T < 0.6$ GeV/c	$1.07 + 0.9 \times (p'_T - 0.4)$
$0.6 < p_T < 1.2$ GeV/c	$1.25 + 0.42 \times (p'_T - 0.6)$
1.2 GeV/c $< p_T$	1.5

Table 6.6: The correction per secondary particle for the enhanced strangeness observed by ALICE. p'_T is p_T in dimensionless units ie. $p_T/(\text{GeV/c})$.

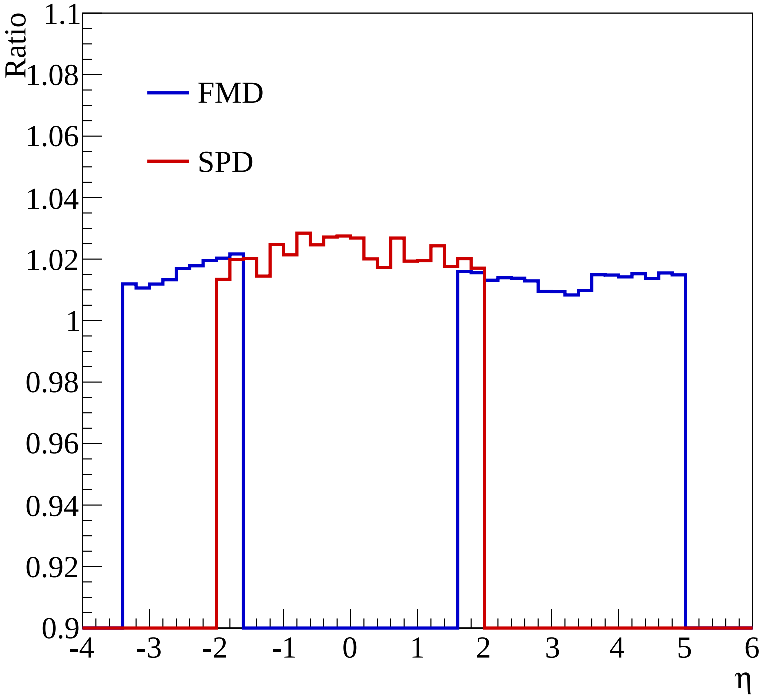

Figure 6.36: Correction for strangeness enhancement calculated as the ratio of secondaries without the weights in Table 6.6 and the unweighted secondaries. The correction is $\sim 2\%$ for the SPD and $1.5-2\%$ in the FMD.

6.6.2 Secondary Strangeness Enhancement in ALICE

In the spring of 2011 it was found that there is a discrepancy in the production of decayed particles containing strange quarks in the simulations compared to data in the central region[6]. The observation has been converted to a p_T correction factor per secondary particle, shown in Table 6.6. Since the FMD and SPD inner layer do not measure p_T this correction has to be calculated from simulations. Lacking more accurate knowledge it is assumed that the effect does not depend on rapidity. Since the effect was not included in any of the simulations used in this analysis it is calculated separately as a function of η and applied to the $\frac{1}{N}\frac{dN_{\text{ch}}}{d\eta}$ directly. Figure 6.36 shows the resulting correction for the FMD and SPD calculated as the ratio of the weighted secondaries to the not–weighted secondaries (the ones used for the secondary correction). The effect is seen to have an effect of up to 2% on this analysis.

6.7 Systematic Errors

For the systematic errors we consider the following contributions for both the FMD and the SPD:

Centrality A study of the effect on N_{ch} of varying the method used to select centrality is found in [114].

---

[6] Andrea Dainese and Jan Fiete Grosse-Oetringhaus, private communication.

Here the error is found to be $< 1\%$ in the most central events $(0 - 5\%)$ rising to $\sim 6\%$ in the most peripheral events $(70 - 80\%)$.

Normalization Only relevant for p+p collisions we assign a systematic error on the calculation of the number of events in (6.18) which propagates into the $dN_{\text{ch}}/d\eta$. The magnitude of these errors are the uncertainties on the trigger efficiencies found in Table 6.2. These errors are seen to range from 1.3% to 3 %.

Trigger– and Vertex–Bias correction To estimate the systematics of the vertex and trigger bias correction in p+p analysis the generator is replaced to see the effect on the correction. In case of the $\sqrt{s} = 900$ GeV and $\sqrt{s} = 7$ TeV analysis the generator is changed to PYTHIA and in the $\sqrt{s} = 2.76$ TeV analysis we replace the generator to PHOJET. The effect is found to be $\sim 3\%$.

Strangeness enhancement Due to the unknown rapidity and energy dependence of the correction a systematic error of $\sim 1\%$ is assigned for this correction.

6.7.1 FMD Systematic Errors

The following contributions are considered for the FMD only:

Variation of E_{hit} and E_{high} The values of E_{hit} and E_{high} are varied from $0.7 \times$ MPV to $0.6 \times$ MPV and $0.8 \times$ MPV. The resulting systematic errors are found to be $< 2\%$ when added in quadrature in Pb+Pb collisions for all centralities. For p+p collisions we find the errors to be $< 3\%$.

Calculation of N_{ch} It was seen in section 6.2.4 that two methods were implemented for the high occupancy correction. It was discussed that the two methods agreed within 3% in Pb+Pb collisions and 4% in p+p collisions. We take these values as the systematic errors from the calculation of N_{ch}.

Dependence of Correction for Secondaries on the choice of generator The stability of the correction for secondaries is tested through variation of the event generator used to produce the simulation. Figure 6.37 shows an example of such a study in FMD3I for $0 < v_z < 2$ cm in p+p collisions at $\sqrt{s} = 7$ TeV. The generators used here are PYTHIA and PHOJET and the variation is seen to be of the order of 2% which is taken as the systematic error. Similar results are obtained for other vertex bins and the other FMD rings.

Material Budget in the Correction for Secondaries The sheer amount of material is the main cause of uncertainty in the correction for secondaries. To estimate this effect special simulations are considered in which the material density of all ALICE materials is raised by 10 % or lowered by 10 %. Comparison to a reference analysis gives an estimate of the systematic error. The left panel of Figure 6.39 shows the results of this study for the FMD. The effect is estimated to be $\sim 7\%$ which makes it the dominant effect in the systematic errors.

6.7.2 SPD Systematic Errors

For the SPD we consider the following contributions:

Dependence of Correction for Secondaries on the choice of generator The stability of the correction for secondaries is tested through variation of the event generator similarly to the FMD. An example of the comparison is shown in Figure 6.38 for $0 < v_z < 2$ cm in p+p collisions at $\sqrt{s} = 7$ TeV. The variation is seen to be $\sim 2\%$ which is taken as the systematic error from the choice of generator. The results do not vary over the vertex bins.

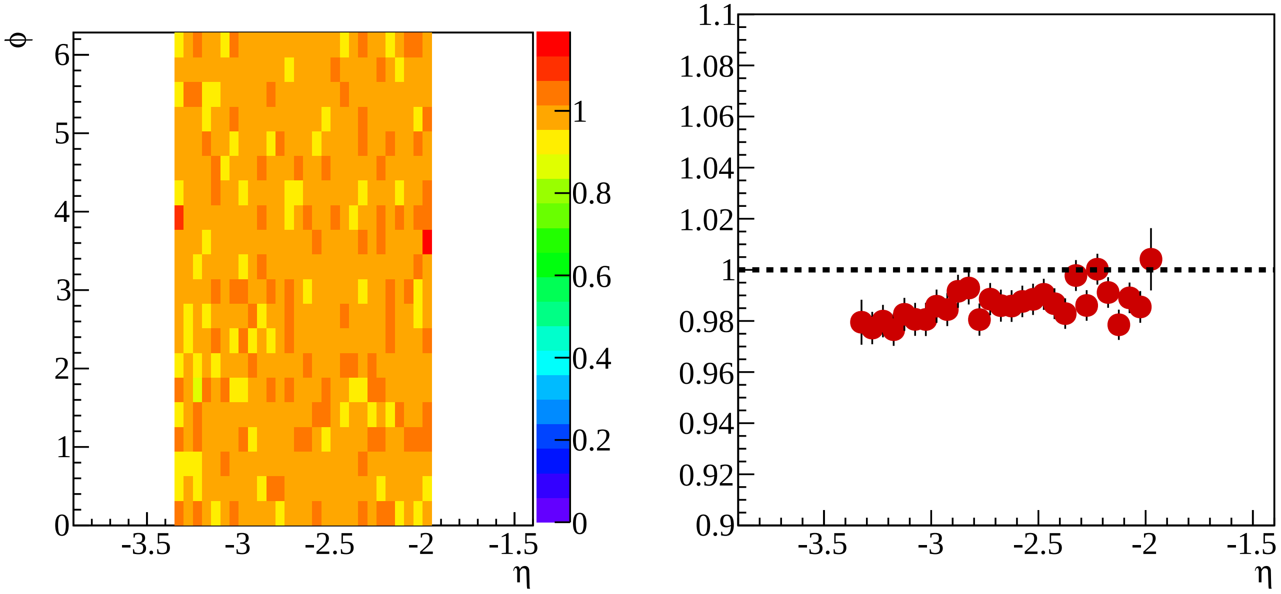

Figure 6.37: Left panel: The ratio of a secondary correction map in FMD3O calculated with PYTHIA and a secondary correction map calculated with PHOJET. Right panel: The projection as a function of η. The effect is estimated to be $\sim 2\%$ which is taken as the systematic error.

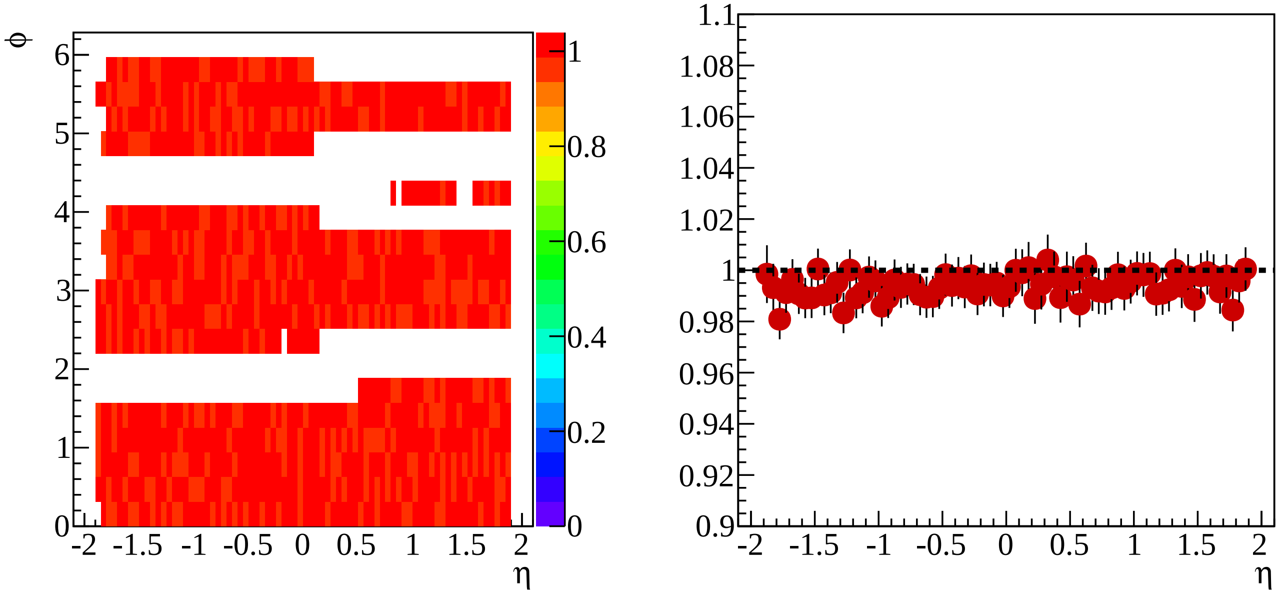

Figure 6.38: Left panel: The ratio of a secondary correction map in the SPD calculated with PYTHIA and a secondary correction map calculated with PHOJET. Right panel: The projection as a function of η. The effect is estimated to be $\sim 2\%$ which is taken as the systematic error.

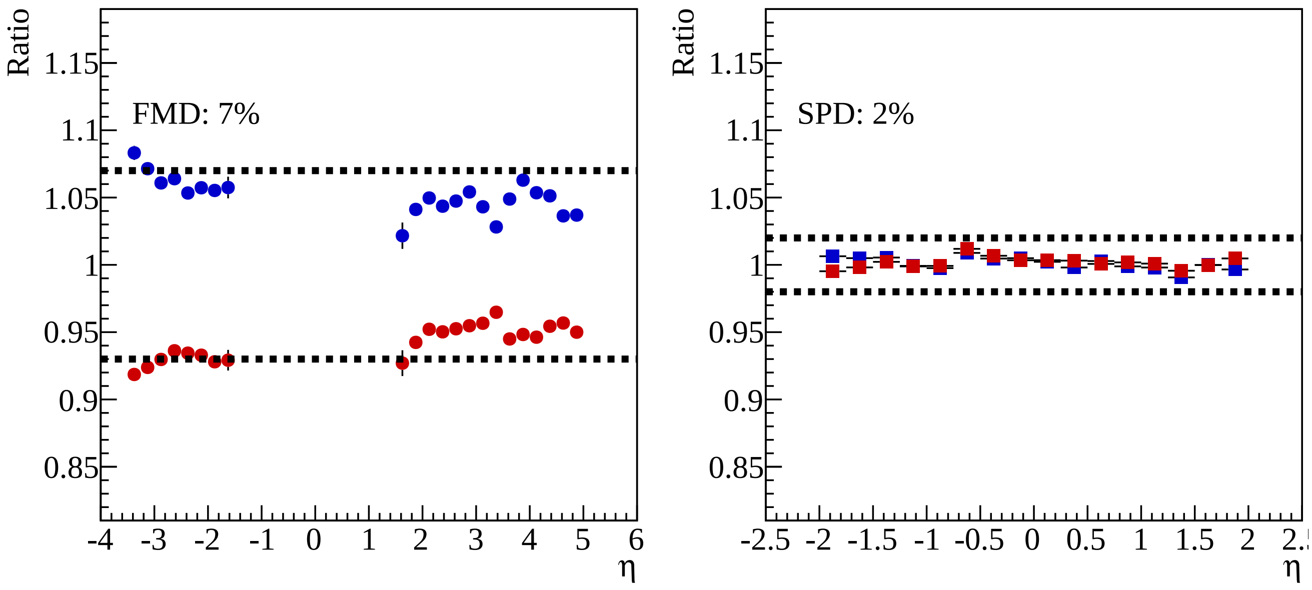

Figure 6.39: Left Panel: The results in the FMD of the variation of the ALICE material budget by ±10%. The effect is significant and for the systematic errors the lines indicate the 7% chosen for this analysis. Right Panel: Same study for the SPD. Due to the lower production of secondaries the effect is smaller in the SPD, taken in the systematic error to be 2%, indicated by the lines.

Material budget in the Correction for Secondaries The right panel of Figure 6.39 shows the results of variations with ±10% of the ALICE material budget. It is seen that the effect is much smaller than for the FMD namely $\sim 2\%$.

For the FMD the systematic errors as well as the total systematic errors are summarized in Table 6.7. For the SPD the errors and the total error are found in Table 6.8.

Effect	Magnitude in Pb+Pb analysis	Magnitude in p+p analysis
Variation of E_{hit} and E_{high}	2%	3%
Calculation of N_{ch}	3%	4%
Material budget	7 %	7 %
Generator	2%	2%
Vertex and trigger bias	N/A	3%
Centrality	1% –6%	N/A
Normalization	N/A	1.3% - 3%
Total in quadrature	8.2% – 10.1%	9.4 % – 9.8%

Table 6.7: The table summarizes the systematic errors in the FMD including the total systematic error obtained by addition in quadrature.

Effect	Magnitude in Pb+Pb analysis	Magnitude in p+p analysis
Material budget	2%	2%
Generator	2%	2%
Vertex and trigger bias	N/A	3%
Centrality	1% –6%	N/A
Normalization	N/A	1.3% - 3%
Total in quadrature	2.2% – 6.6%	4.3%– 5.1%

Table 6.8: Summary of the systematic errors in the SPD as well as the total systematic error obtained by addition in quadrature.

Chapter 7

Results

In this Chapter the results of the data analysis will be presented. While the main results are $\frac{1}{N}\frac{dN_{\mathrm{ch}}}{d\eta}$ in p+p and Pb+Pb collisions model comparisons will also be included. Furthermore some of the results presented in Chapter 2 will also be reviewed in light of the new measurements.

7.1 $dN_{ch}/d\eta$ in Pb+Pb collisions at $\sqrt{s_{NN}} = 2.76$ TeV

Figure 7.1 shows the measured $dN_{ch}/d\eta$ in Pb+Pb collisions at $\sqrt{s_{NN}} = 2.76$ TeV. The data are presented in the centrality classes outlined in Table 6.3. The Figure includes the systematic errors which are shown by the grey boxes.

As a first check of the analysis a comparison to the published ALICE analysis shown in Figure 2.1 has been done. The result is shown in Figure 7.2 and it is clear that there is very good agreement between this analysis and the published results.

The expansion of the initial ALICE measurement to the full rapidity coverage of the experiment makes a qualitative comparison to the RHIC $dN_{ch}/d\eta$ from PHOBOS and BRAHMS presented in section 2.2 possible. The most striking observation is that the midrapidity 'plateau' observed at RHIC is not immidiately recognized in the LHC data since there are clear indications of a two–peak structure with peaks at $|\eta| \sim 2$. This will be elaborated upon and discussed further in section 7.4.1.

7.1.1 Energy Density

As described in section 2.1.1 the total energy available at midrapidity can be estimated from (2.1). From Figure 7.1 $\frac{dN_{ch}}{d\eta}_{|\eta|<1} \sim 1600 \pm 40$ in 0–5 % central Pb+Pb collisions at $\sqrt{s_{NN}} = 2.76$ TeV. Using values: $E_{part} = 600$ MeV, $f_{neutral} = 1.5$, and $f_{4\pi} = 1.3$ we obtain for the total energy:

$$E_{tot} = 2 \times 600\text{MeV} \times 1600 \times 1.5 \times 1.3 \sim 4000 \text{ GeV}$$

This gives $E_{tot}/\sqrt{s_{NN}} = 1.36$ at LHC compared to $E_{tot}/\sqrt{s_{NN}} = 8$ at RHIC. Using the estimate by Bjorken for the longitudinal extent of the fireball, ~ 2 fm and assuming the area of the colliding Pb nuclei to be ~ 150 fm^2 the estimate for the energy density in central Pb+Pb collisions at LHC becomes $\epsilon \approx 13.5$ GeV/fm^3 compared to $\epsilon \approx 5$ GeV/fm^3 at RHIC. This is much higher than the estimated critical density of $\epsilon \approx 1$ GeV/fm^3 discussed in section 1.2.1. Similar to the situation at RHIC the energy density at LHC is extremely high but this in itself is not enough to provide evidence for (s)QGP formation. However, it is clear that the energy density is certainly sufficiently high to form a QGP.

The huge energy densities at RHIC and LHC means that QGP formation would be possible at both RHIC and LHC from a thermodynamical point of view (see section 1.2.1). Considering Figure 1.6 where the energy density over T^4 saturates as a function of temperature we can write for the temperature of

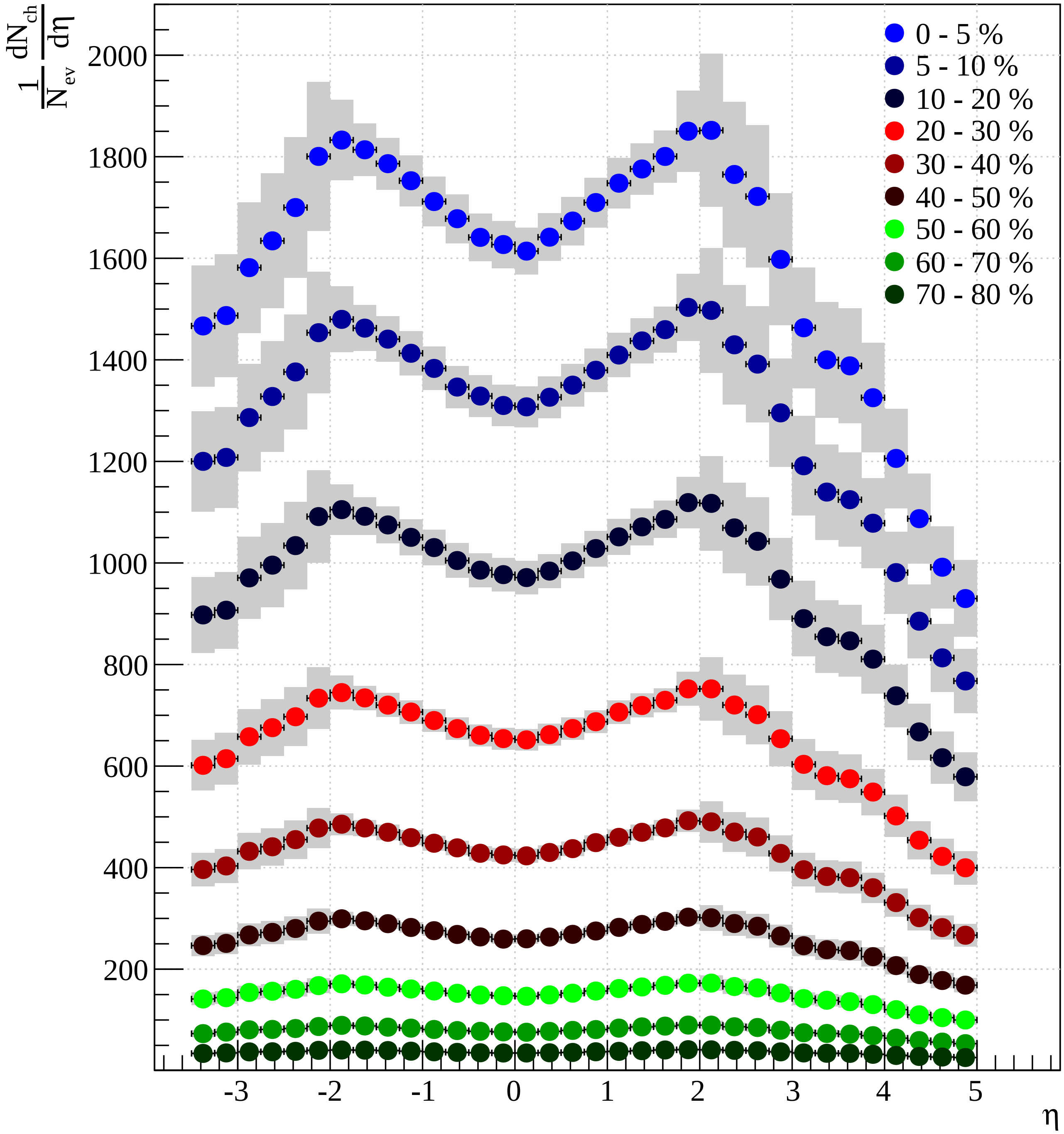

Figure 7.1: The Figure shows the $dN_{ch}/d\eta$ in Pb+Pb collisions at $\sqrt{s_{NN}} = 2.76$ TeV measured with the FMD and SPD. Statistical errors are drawn as vertical bars and the grey boxes indicate the total errors in quadrature.

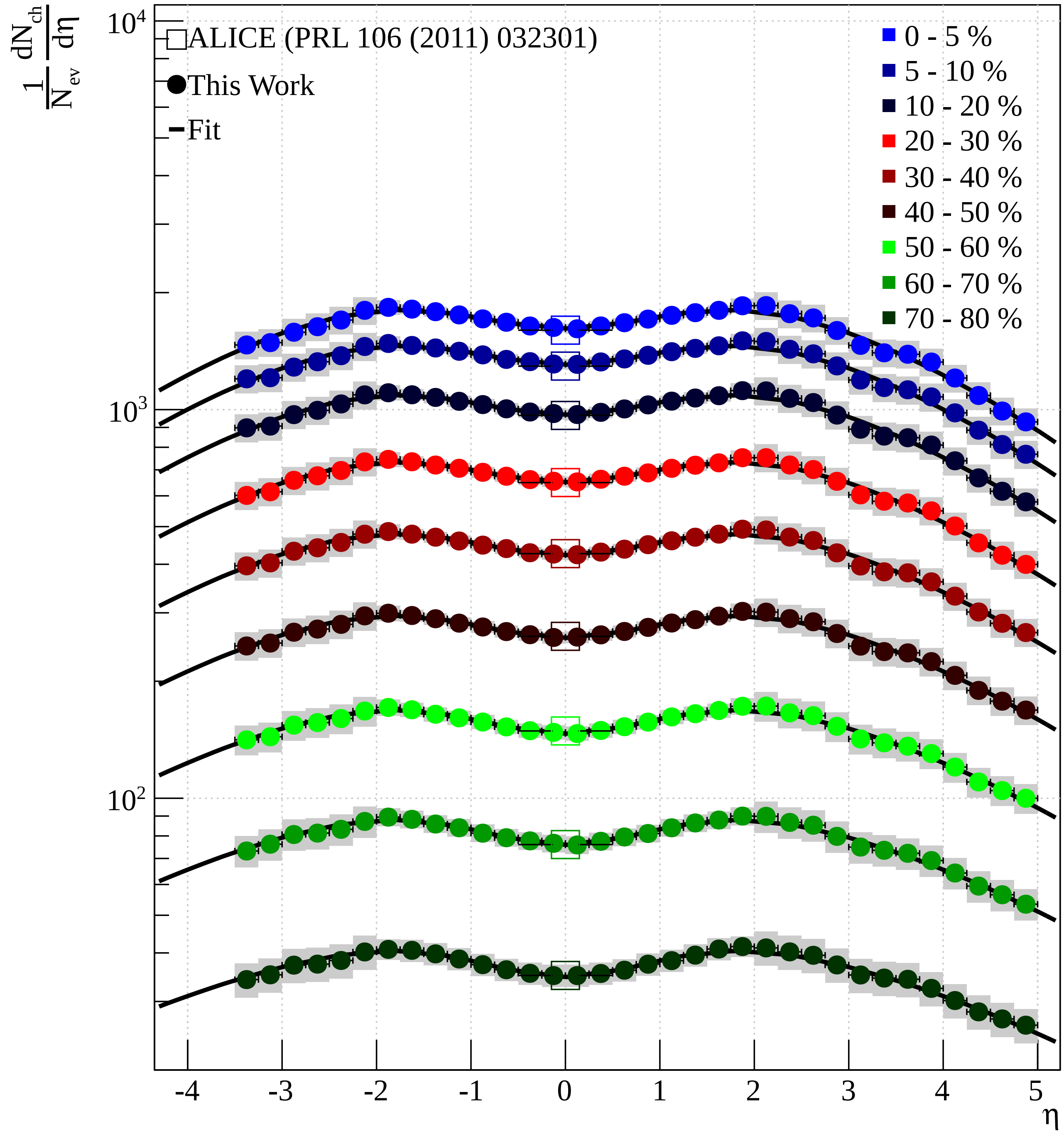

Figure 7.2: The Figure is a comparison between the measurement of $dN_{ch}/d\eta$ in Figure 7.1 and the published ALICE measurement at midrapidity. The vertical bars on the published ALICE values indicate the total errors (statistical and systematical errors). Note the logarithmic scale on the ordinate. It is seen that there is very good agreement between the two measurements. The Figure also includes fits to the $\frac{1}{N}\frac{dN_{\mathrm{ch}}}{d\eta}$ using the function discussed in section 7.3.1.

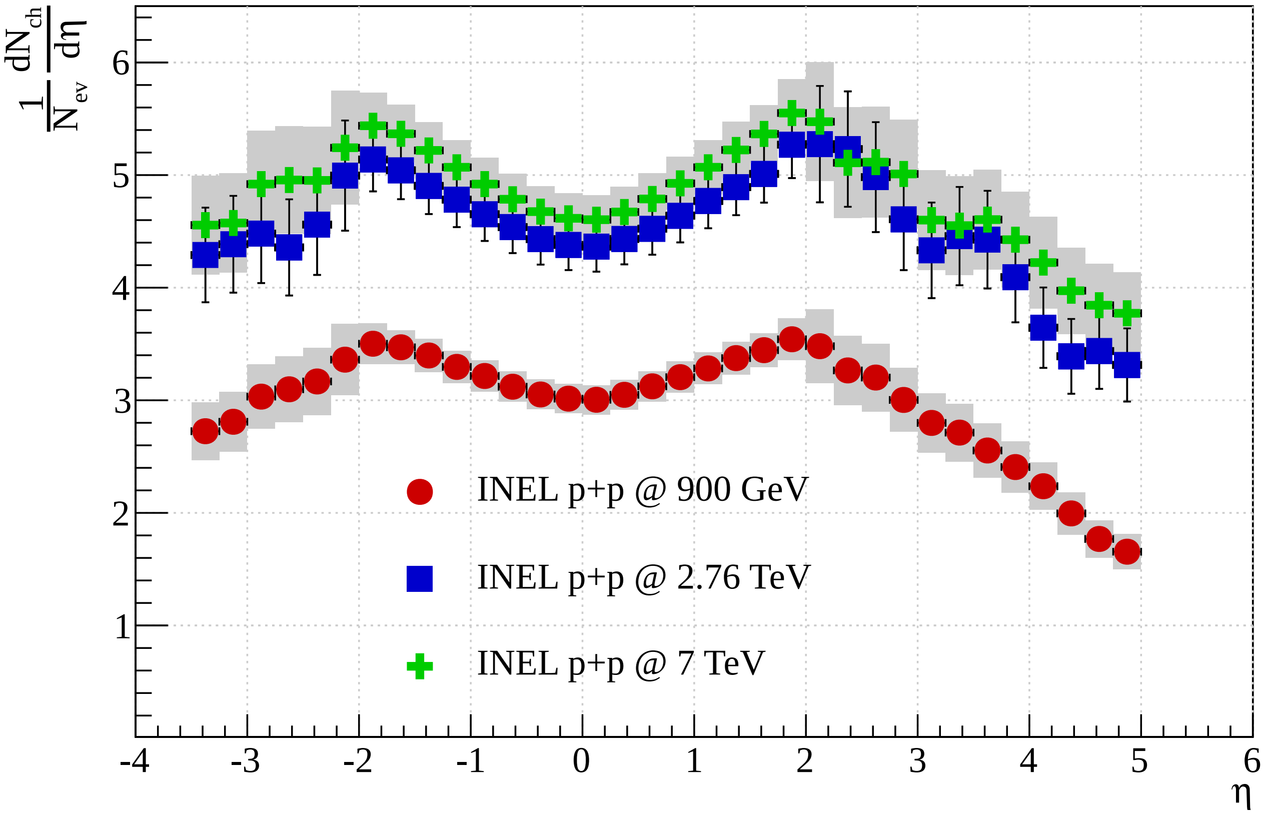

Figure 7.3: The Figure shows the inelastic $dN/d\eta$ in p+p collisions at $\sqrt{s}$ = 900 GeV, $\sqrt{s}$ = 2.76 TeV, and $\sqrt{s}$ = 7 TeV measured with the FMD and SPD. Total errors are shown as grey boxes except for the $\sqrt{s}$ = 2.76 TeV data where they are shown as horizontal bars for clarity.

the LHC fireball:

$$\frac{\epsilon_{RHIC}}{T^4_{RHIC}} = \frac{\epsilon_{LHC}}{T^4_{LHC}} \rightarrow T_{LHC} = \sqrt[4]{\frac{\epsilon_{LHC}}{\epsilon_{RHIC}}}T_{RHIC} \sim 1.3T_{RHIC} \tag{7.1}$$

Thus, we find that if the assumption of saturation of ϵ/T^4 holds the temperature in Pb+Pb collisions at LHC is $\sim$ 30% higher than in Au+Au collisions at RHIC.

7.2 $dN_{ch}/d\eta$ in p+p collisions at LHC energies

Figure 7.3 shows the $dN_{ch}/d\eta$ for inelastic collisions measured with the FMD and SPD in p+p collisions at $\sqrt{s}$ = 900 GeV, $\sqrt{s}$ = 2.76 TeV, and $\sqrt{s}$ = 7 TeV. Total errors are shown as grey boxes for $\sqrt{s}$ = 900 GeV and $\sqrt{s}$ = 7 TeV and vertical bars for $\sqrt{s}$ = 2.76 TeV. To validate the measurement in the full rapidity range a comparison to the UA5 data presented in section 2.2.2 is shown in Figure 7.4. Furthermore the Figure includes the first ALICE measurement which was the $dN/d\eta$ in p+p collisions at $\sqrt{s}$ = 900 GeV measured using SPD tracklets [115]. It is seen that the measurement presented here is in good agreement with the ALICE measurement as well as the UA5 measurement in the full rapidity range. This is a strong indication that the overall method presented in Chapter 6 is sound and that the FMD can perform high–quality measurements despite its large background of secondary particles.

While the comparison to previous measurements is successful Figure 7.3 shows quite some structure in the $\sqrt{s}$ = 2.76 TeV, and, to some extent, the $\sqrt{s}$ = 7 TeV data that is not present in the $\sqrt{s}$ = 900 GeV

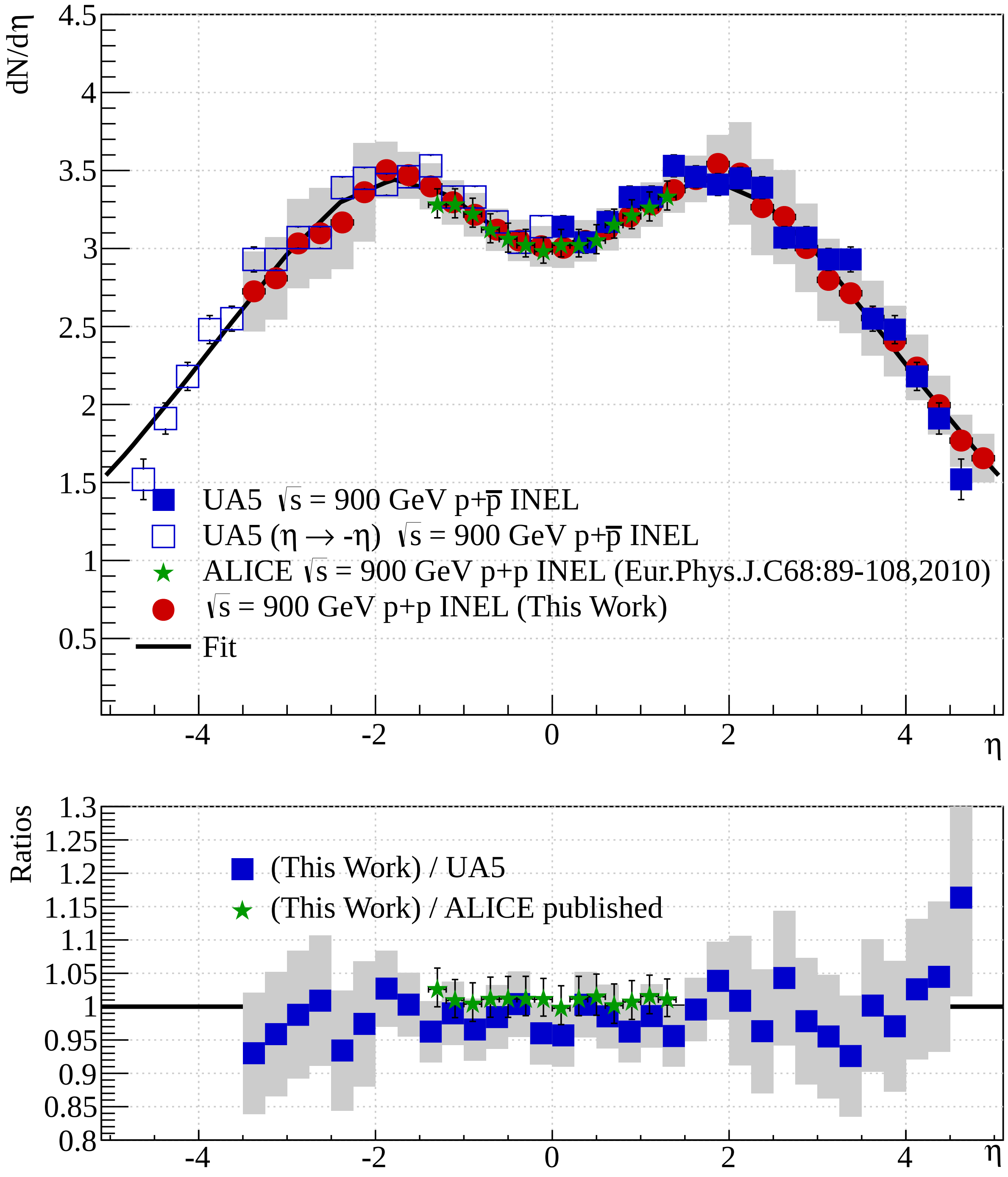

Figure 7.4: Top panel: Comparison between this measurement of $dN/d\eta$ in p+p collisions at $\sqrt{s} = 900$ GeV, the ALICE tracklet measurement [115], and the UA5 measurement in $\sqrt{s} = 900$ GeV $p{+}\bar{p}$ collisions. The UA5 data have been mirrored to allow comparison at negative pseudorapidities. Also shown is a fit to the data using a function discussed in section 7.3.1. Bottom panel: Ratios of this measurement to the UA5 measurement and the published ALICE measurement. The latter is done using the fit function to take into account the different binning.

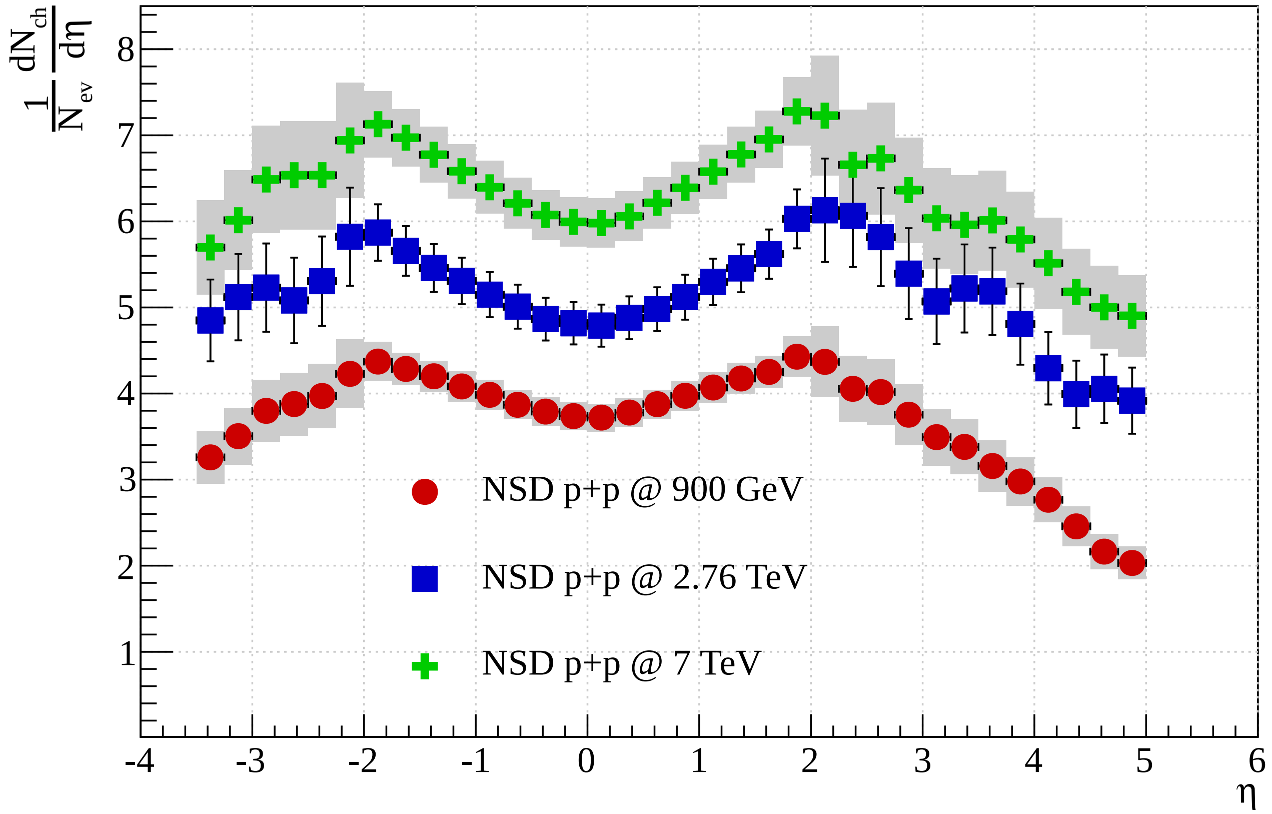

Figure 7.5: The Figure shows the Non–Single Diffractive $dN/d\eta$ in p+p collisions at $\sqrt{s}$ = 900 GeV, $\sqrt{s}$ = 2.76 TeV, and $\sqrt{s}$ = 7 TeV measured with the FMD and SPD. Total errors are shown as grey boxes except for the $\sqrt{s}$ = 2.76 TeV data where they are shown as horizontal bars for clarity.

data which appears smoother. This is currently not understood and should be subject to further studies. It could certainly be connected to the issues in the energy distributions of the p+p data at $\sqrt{s}$ = 2.76 TeV discussed in section 6.2.3.

The issue could be time related as the $\sqrt{s}$ = 900 GeV data were taken first in 2010, followed by the $\sqrt{s}$ = 7 TeV data (the sample used here), and finally the $\sqrt{s}$ = 2.76 TeV data were taken in 2011.

NSD Results

The results for the Non–Single Diffractive p+p analysis are shown in Figure 7.5. These results were found using the efficiencies in Table 6.2. As discussed in section 6.1.1 these NSD efficiencies are calculated directly from the simulations without any additional requirements on the Single–Diffractive events. The results presented here are likely to change when properly calculated trigger efficiencies become available. For published data, Figure 7.6 shows a comparison to UA5, ALICE, and CMS NSD data at $\sqrt{s}$ = 900 GeV and $\sqrt{s}$ = 7 TeV. It is seen that there are substantial discrepancies between the results presented here and the published measurements. The trigger efficiencies can only shift the distributions up or down so if there are issues with the shapes of the distributions there must be another reason for them. The most likely cause of issues with the shape of the NSD distributions is the correction for trigger and vertex bias (section 6.6.1) since they will depend on the description of the diffractive processes at the event generator level.

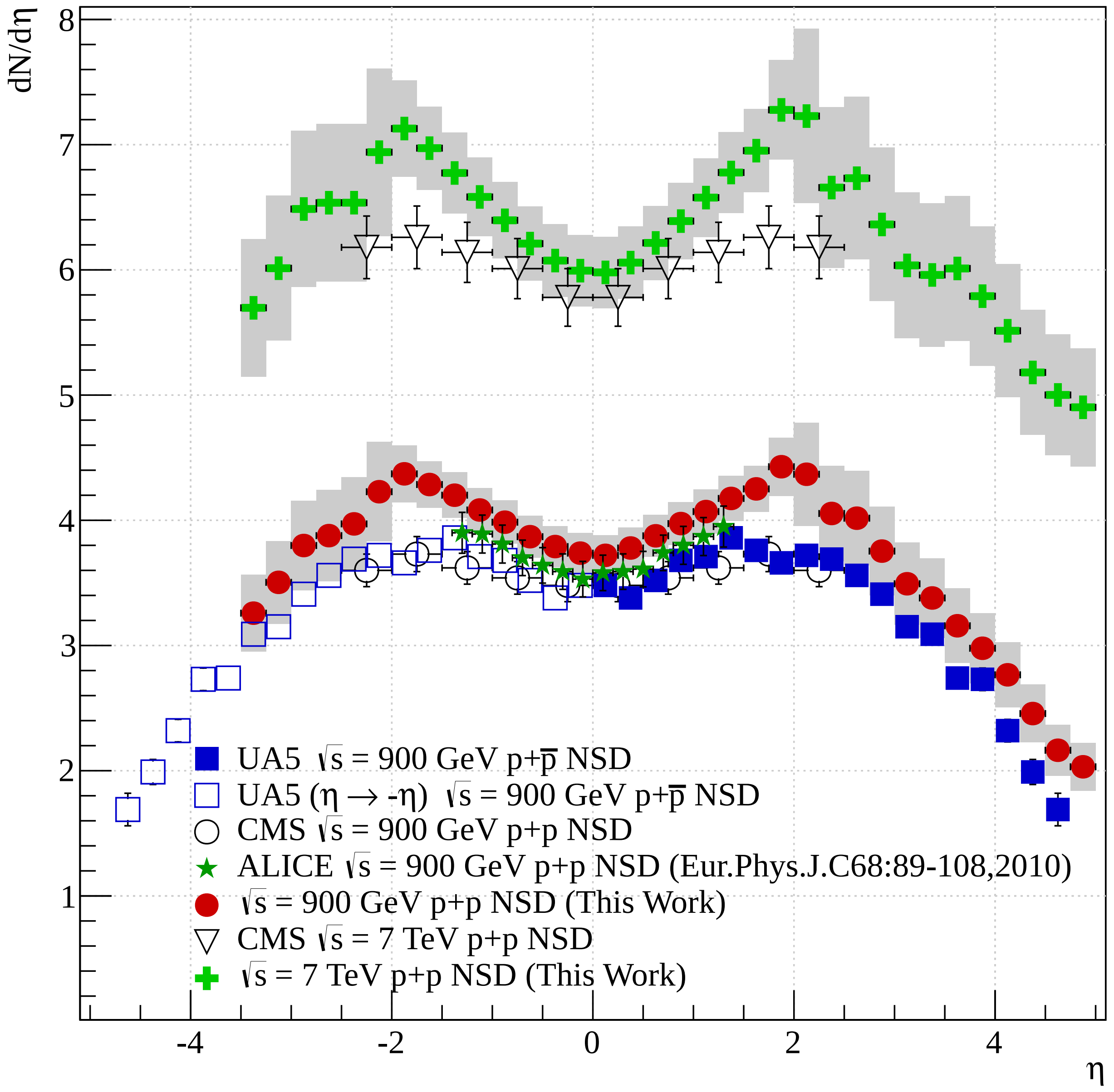

Figure 7.6: The Figure shows the Non–Single Diffractive $dN/d\eta$ in p+p collisions at $\sqrt{s} = 900$ GeV and $\sqrt{s} = 7$ TeV compared to UA5, published ALICE results [115], and CMS [116].

System		A_1	σ_1	A_2	σ_2	χ^2/NDF
Pb+Pb						
	$0-5\%$	2212.9 ± 162.7	3.68 ± 0.25	596.7 ± 155.8	1.10 ± 0.18	0.076
	$5-10\%$	1786.9 ± 132.9	3.72 ± 0.25	482.4 ± 127.9	1.11 ± 0.18	0.073
	$10-20\%$	1331.2 ± 101.1	3.75 ± 0.27	361.4 ± 95.4	1.10 ± 0.19	0.066
	$20-30\%$	892.8 ± 66.4	3.80 ± 0.28	242.5 ± 62.0	1.11 ± 0.19	0.063
	$30-40\%$	578.3 ± 41.9	3.87 ± 0.29	156.1 ± 40.4	1.09 ± 0.18	0.063
	$40-50\%$	353.2 ± 25.1	3.96 ± 0.31	94.7 ± 52.1	1.08 ± 0.19	0.055
	$50-60\%$	198.9 ± 13.7	4.09 ± 0.34	52.4 ± 13.2	1.04 ± 0.20	0.044
	$60-70\%$	102.0 ± 6.8	4.25 ± 0.37	26.2 ± 6.6	1.00 ± 0.21	0.039
	$70-80\%$	46.1 ± 3.1	4.48 ± 0.45	11.5 ± 3.1	0.97 ± 0.23	0.036
INEL p+p						
	900 GeV	4.3 ± 0.4	3.52 ± 0.25	1.3 ± 0.4	1.08 ± 0.19	0.049
	2.76 TeV	5.7 ± 0.4	4.50 ± 0.44	1.4 ± 0.4	0.99 ± 0.21	0.170
	7 TeV	5.8 ± 0.3	5.03 ± 0.51	1.3 ± 0.3	0.89 ± 0.18	0.084

Table 7.1: The parameters of the fits to the data using $F(\eta)$ defined in (7.2).

7.3 Scaling at LHC energies

In this section some of the scaling properties of $dN_{ch}/d\eta$ in Pb+Pb collisions and p+p collisions that were discussed in Chapter 2 will be reviewed.

7.3.1 Fitting the $\frac{1}{N}\frac{dN_{\mathrm{ch}}}{d\eta}$

To be able to extrapolate the data $\frac{1}{N}\frac{dN_{\mathrm{ch}}}{d\eta}$ are fitted to a function given by^1:

$$F(\eta) = A_1 e^{\frac{\eta}{2\sigma_1^2}} - A_2 e^{\frac{\eta}{2\sigma_2^2}} \tag{7.2}$$

That is a Gaussian around $\eta \sim 0$ subtracted from another Gaussian around $\eta \sim 0$. The function is found to describe the $\frac{1}{N}\frac{dN_{\mathrm{ch}}}{d\eta}$ well with χ^2/NDF < 0.5 for p+p and Pb+Pb collisions. Table 7.1 summarizes the fit parameters for this analysis. The fits to the $\frac{1}{N}\frac{dN_{\mathrm{ch}}}{d\eta}$ are used wherever the interpretation of the data require extrapolation. They are used for calculating the total number of charged particles, assess longitudinal scaling, and comparison with other data where the binnings are different. Examples of the fits are shown for Pb+Pb collisions in Figure 7.2 and for p+p collisions in 7.4.

7.3.2 Scaling with the Number of Participants

The scaling with the number of participants, N_{part}, was measured at midrapidity by ALICE as described in section 2.2.5. The measurement presented here allows an expansion of the system size dependence or scaling with N_{part}. Using the N_{part} values from Table 6.3 the results from Figure 7.1 are used to calculate $(dN_{ch}/d\eta)/(N_{part}/2)$ which are shown in Figure 7.7. The original ALICE measurement is included in this Figure as the grey band.

By inspection the $(dN_{ch}/d\eta)/(N_{part}/2)$ of the rapidity intervals in Figure 7.7 look very similar. This is tested directly in Figure 7.8 where the ratios are taken with regard to the midrapidity result. It is clear from the Figure that these ratios are indeed constant for $N_{part} > 100$.

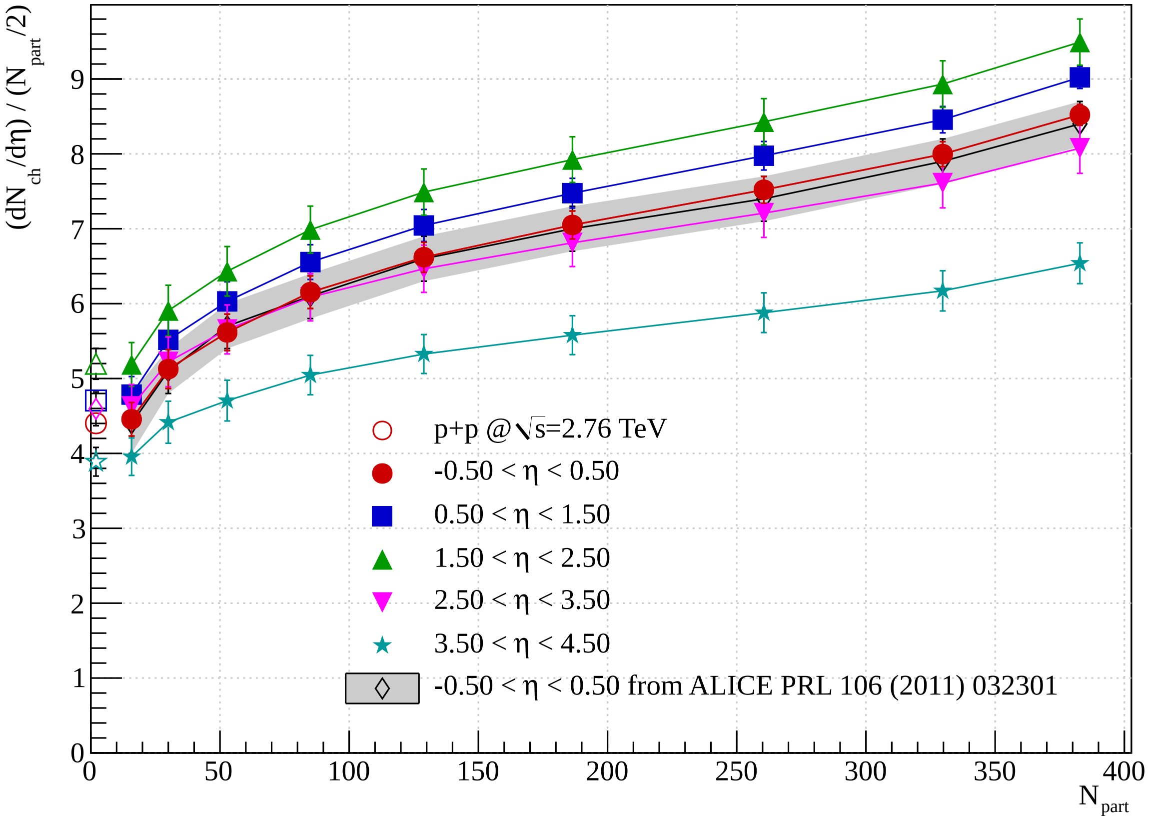

Figure 7.7: $(dN_{ch}/d\eta)/(N_{part}/2)$ in 5 pseudorapidity intervals in Pb+Pb collisions at $\sqrt{s_{NN}} = 2.76$ TeV. The figure includes the ALICE measurement at midrapidity shown as a grey band[48] and the two measurements are seen to be in good agreement. It is seen that the shapes of the $(dN_{ch}/d\eta)/(N_{part}/2)$ are very similar across all the rapidity ratios. Also included in the figure are data from p+p collisions at $\sqrt{s} = 2.76$ TeV which seem to be consistent with the Pb+Pb values.

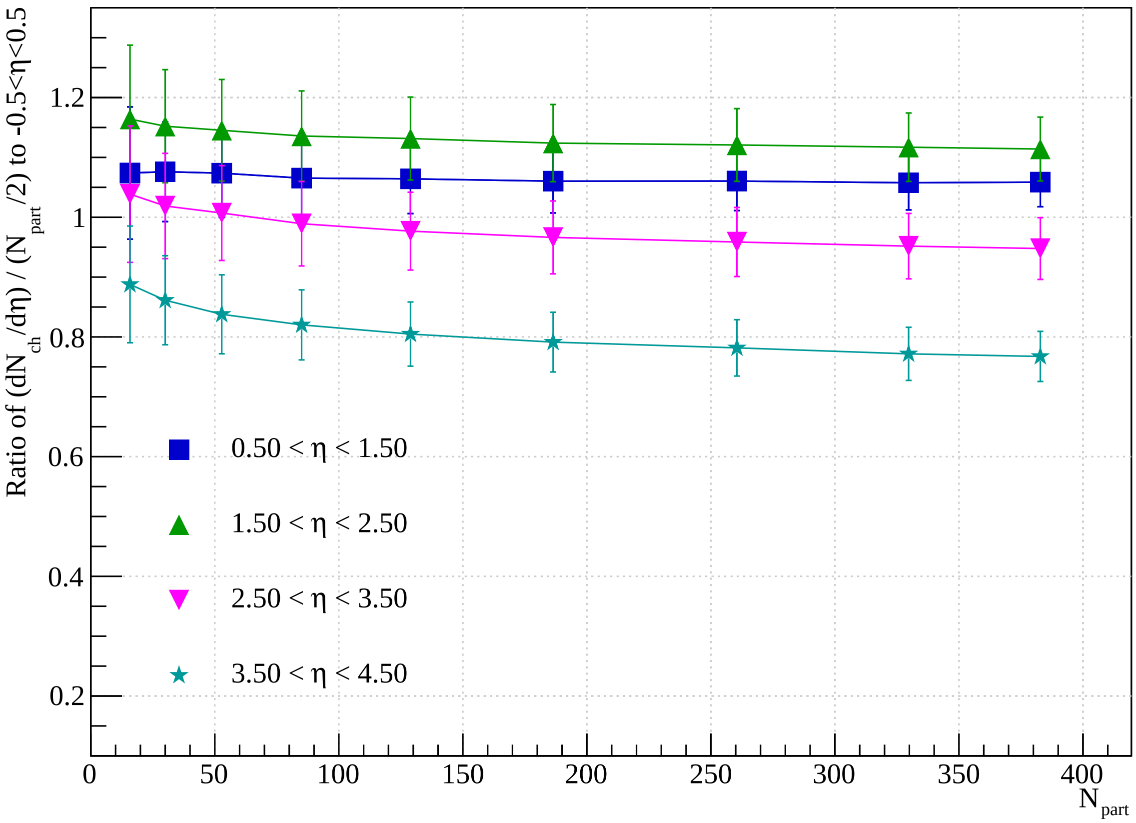

Figure 7.8: Ratios of $(dN_{ch}/d\eta)/(N_{part}/2)$ in Pb+Pb collisions in 4 pseudorapidity intervals compared to $(dN_{ch}/d\eta)/(N_{part}/2)$ for $-0.5 < \eta < 0.5$. It it seen that for $N_{part} > 100$ the ratios are roughly constant.

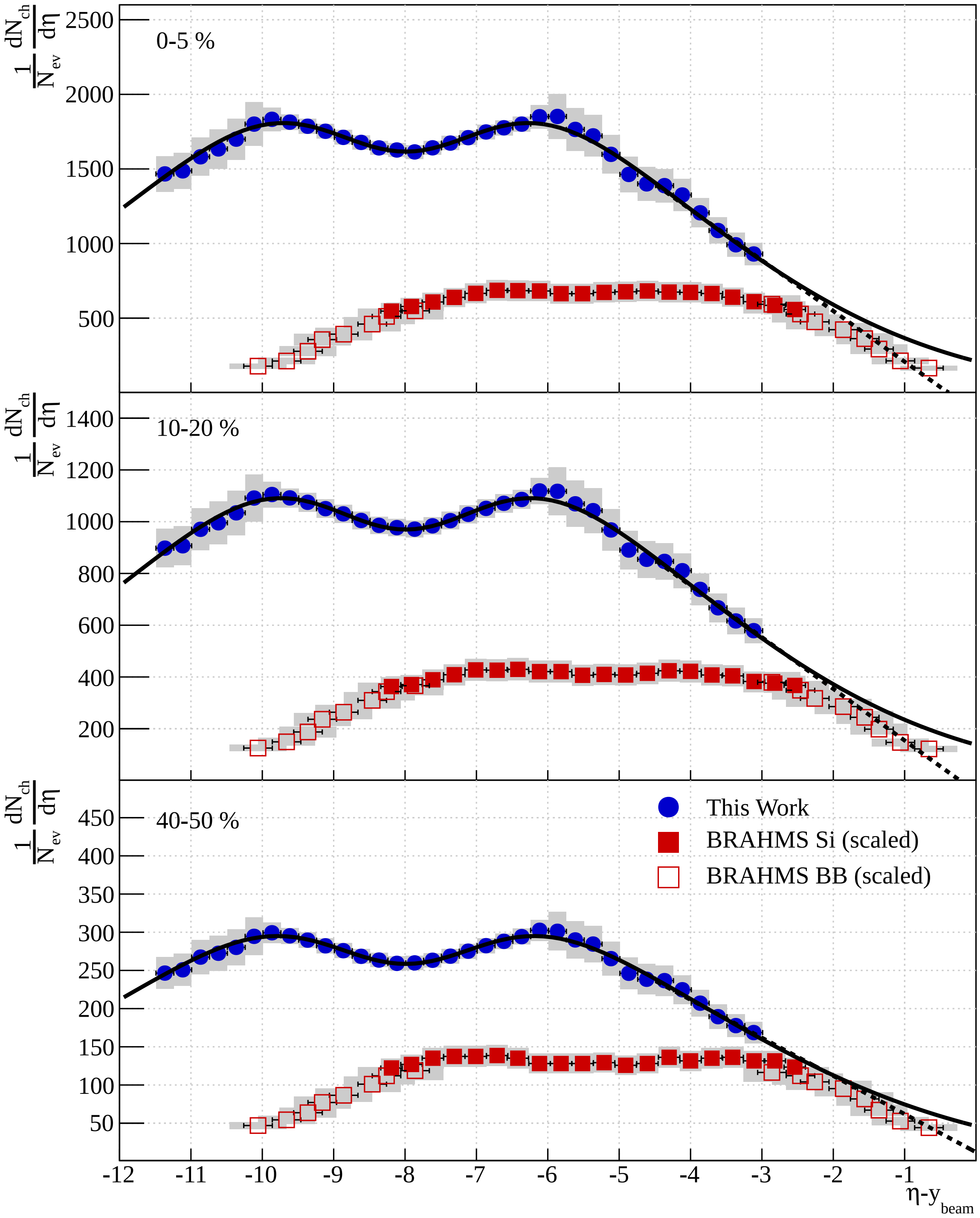

Figure 7.9: $\frac{1}{N}\frac{dN_{\text{ch}}}{d\eta}$ in three centrality intervals as a function of $y' = \eta - y_{beam}$. Also shown are data from BRAHMS (Silicon detector and Beam–Beam counters) scaled as described in section 2.2.1 to take the difference in N_{part} into account. Two fits to this measurement are shown: $F(\eta)$ and a simple linear fit for $y' > -5$. It is seen that it is certainly possible that extended longitudinal scaling is also observed from LHC to RHIC energies especially in the more peripheral collisions.

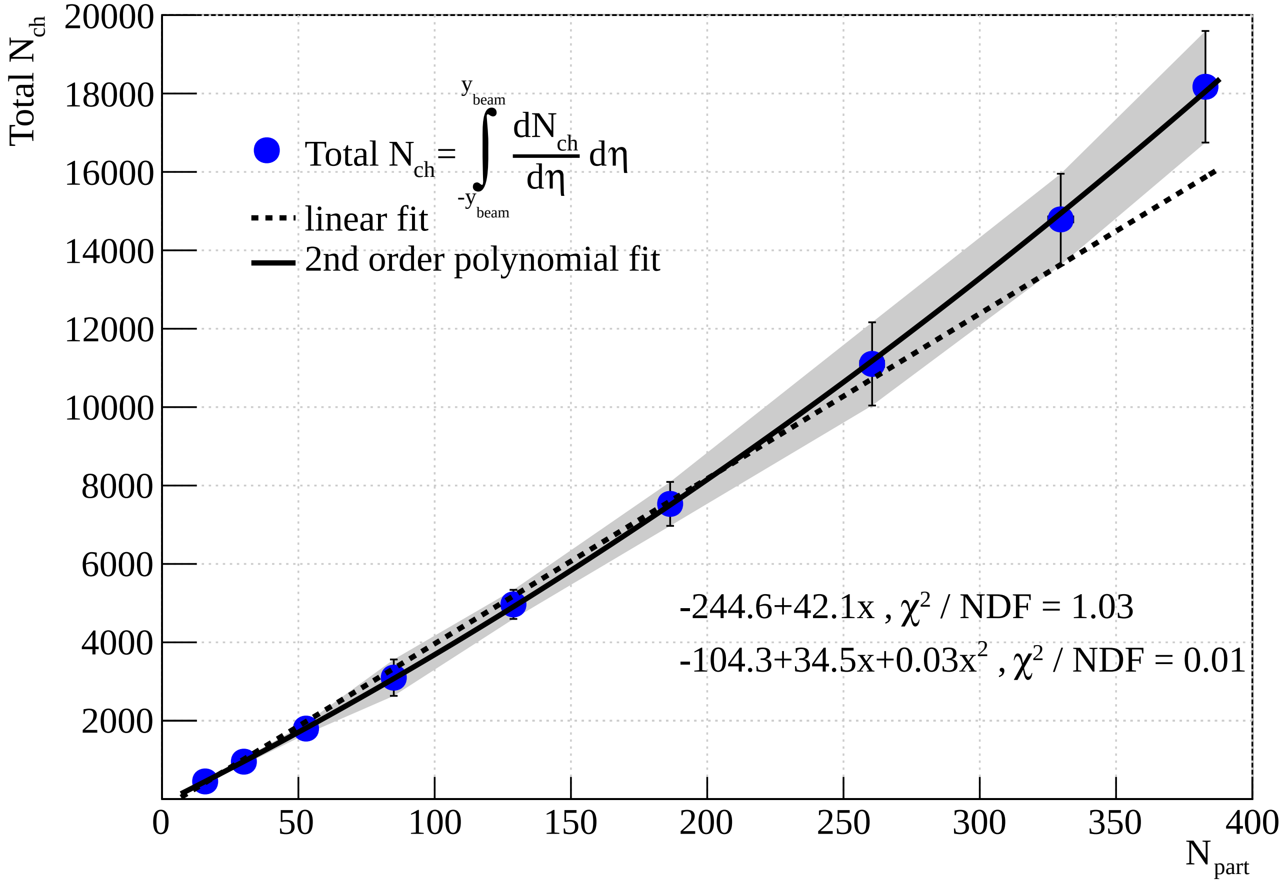

Figure 7.10: The Figure shows the total N_{ch} in Pb+Pb collisions at $\sqrt{s_{NN}} = 2.76$ TeV measured with the FMD and SPD.

7.3.3 Longitudinal Scaling

As discussed in section 2.2.3 extended longitudinal scaling has been observed over a wide range of energies including RHIC energies. This scaling expresses itself as a scaling of $\frac{1}{N}\frac{dN_{\text{ch}}}{d\eta}$ as a function of $y' = \eta - y_{beam}$. To study the possibility that the scaling extends to LHC energies Figure 7.9 shows $\frac{1}{N}\frac{dN_{\text{ch}}}{d\eta}$ in Pb+Pb collisions at $\sqrt{s_{NN}} = 2.76$ TeV versus y' compared to BRAHMS data from Au+Au collisions at $\sqrt{s_{NN}} =$ 200 GeV scaled according to (2.2). Due to the large gap in energy, fits to the data have to be used to assess the possible scaling. These are included in the Figure and it is seen that it is indeed possible that extended longitudinal scaling also applies to LHC energies. Due to the Gaussian nature of the fit function it does not go to zero at $\eta \sim y_{beam}$ so a linear fit has been included in Figure 7.9. This is a simple line: $\frac{1}{N}\frac{dN_{\text{ch}}}{d\eta} \propto (\eta - y_{beam})$ fitted in the range $(\eta - y_{beam}) \in [-5; -3]$. This function is seen to be close to zero at $\eta \sim y_{beam}$ and it suggests a longitudinal scaling behavior from RHIC to LHC.

To fully understand if longitudinal scaling applies from RHIC to LHC, data at an intermediate energy would be helpful e.g., Pb+Pb collisions at $\sqrt{s_{NN}} = 1.38$ TeV. Furthermore the running of LHC at full energy ($\sqrt{s_{NN}} = 5.5$ TeV) will reveal whether extended longitudinal scaling is present between the top and current LHC energies.

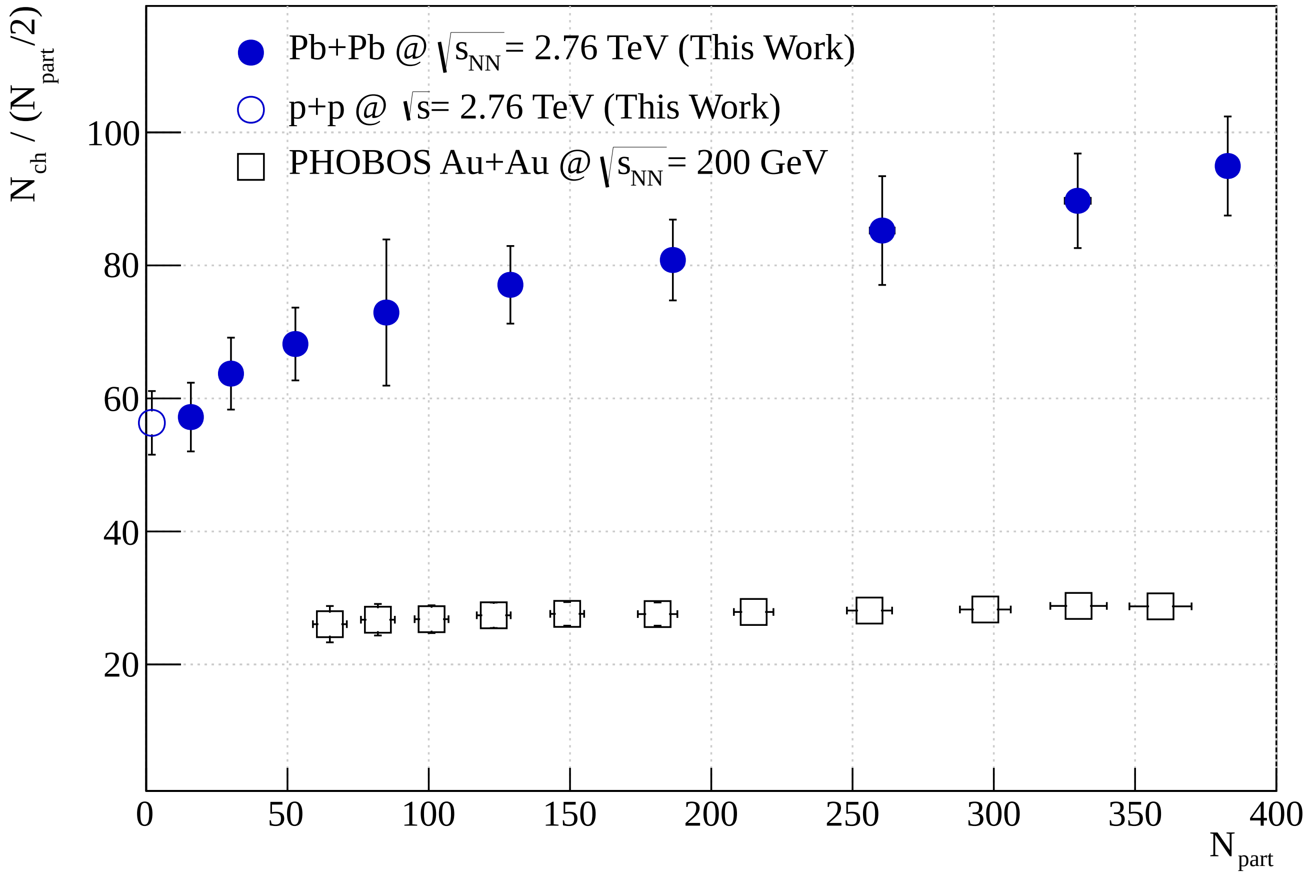

Figure 7.11: The Figure shows the total $N_{ch}/(N_{part}/2)$ in Pb+Pb collisions at $\sqrt{s_{NN}} = 2.76$ TeV measured with the FMD and SPD. The figure includes the $N_{ch}/(N_{part}/2)$ measured by PHOBOS in Au+Au collisions at $\sqrt{s_{NN}} = 200$ GeV at RHIC [117]. There is a clear difference in the shape; the PHOBOS data are only rising slightly (close to constant) while the data presented here data rise faster.

Centrality class	$\int_{-3.5}^{5} \frac{1}{N}\frac{dN_{\rm ch}}{d\eta} d\eta$	$\int_{-3.5}^{5} F(\eta)d\eta$	$\int_{-y_{beam}}^{y_{beam}} F(\eta)d\eta$	$\int_{-\infty}^{\infty} F(\eta)d\eta$
$0-5\%$	13513.6 ± 634.0	13507.4 ± 1132.7	18172.1 ± 1423.6	18787.3 ± 1415.5
$5-10\%$	10945.9 ± 522.0	10943.5 ± 931.3	14789.1 ± 1164.1	15316.1 ± 1153.4
$10-20\%$	8183.0 ± 398.2	8179.6 ± 983.5	11102.4 ± 1061.3	11518.0 ± 1016.7
$20-30\%$	5514.9 ± 265.9	5513.0 ± 272.2	7531.6 ± 560.7	7834.5 ± 626.1
$30-40\%$	3606.9 ± 173.9	3606.6 ± 178.1	4967.9 ± 371.3	5188.1 ± 420.1
$40-50\%$	2227.5 ± 109.8	2227.7 ± 242.6	3098.9 ± 464.4	3252.5 ± 539.5
$50-60\%$	1276.8 ± 66.3	1277.1 ± 100.7	1800.0 ± 140.4	1904.0 ± 149.5
$60-70\%$	667.7 ± 37.8	668.1 ± 38.7	956.0 ± 78.4	1021.4 ± 94.8
$70-80\%$	309.0 ± 19.5	309.2 ± 20.0	451.9 ± 39.9	490.6 ± 50.9

Table 7.2: The total N_{ch} for various centralities in Pb+Pb collisions at $\sqrt{s_{NN}} = 2.76$ TeV obtained by direct integration as well by extrapolation to $(-y_{beam}, y_{beam})$ and $(-\infty, \infty)$.

System	$\int_{-3.5}^{5} \frac{1}{N}\frac{dN_{\rm ch}}{d\eta} d\eta$	$\int_{-3.5}^{5} F(\eta)d\eta$	$\int_{-y_{beam}}^{y_{beam}} F(\eta)d\eta$	$\int_{-\infty}^{\infty} F(\eta)d\eta$
p+p @ $\sqrt{s} = 900$ GeV	25.3 ± 1.4	25.4 ± 1.4	32.5 ± 2.5	34.4 ± 2.9
p+p @ $\sqrt{s} = 2.76$ TeV	38.5 ± 2.3	38.5 ± 2.3	56.3 ± 4.8	61.2 ± 6.2
p+p @ $\sqrt{s} = 7$ TeV	41.0 ± 2.4	41.1 ± 2.4	65.2 ± 5.7	70.8 ± 7.6

Table 7.3: The total N_{ch} for in INEL p+p collisions at $\sqrt{s} = 900$ GeV, $\sqrt{s} = 2.76$ TeV, and $\sqrt{s} = 7$ TeV obtained by direct integration as well by extrapolation to $(-y_{beam}, y_{beam})$ and $(-\infty, \infty)$.

7.3.4 Scaling of total Number of Charged Particles

Using $F(\eta)$ defined in (7.2) the total number of charged particles produced in p+p and Pb+Pb collisions at LHC can be estimated. Integrals are taken in 3 pseudorapidity intervals: The actual ALICE coverage $-3.5 < \eta < 5$, $-y_{beam} < \eta < y_{beam}$, and finally $-\infty < \eta < \infty$. The results are shown in Table 7.2 for Pb+Pb collisions and Table 7.3 for inelastic p+p collisions. The errors include fitting errors and for the extrapolations a contribution from variation of the fit function (using the lines from Figure 7.9). In the following we use the choice $N_{ch} = \int_{-y_{beam}}^{y_{beam}} F(\eta)d\eta$ for the total number of charged particles. The scaling of N_{ch} can be shown in several ways: Figure 7.10 shows N_{ch} versus N_{part} in Pb+Pb collisions. Also shown in the figure are two fits, a straight line and a second order polynomial. From the fits it is seen that the straight line fit underestimates N_{ch} in the most central collisions. This point is expanded in Figure 7.11 that shows $N_{ch}/(N_{part}/2)$ versus N_{part}. Compared to the PHOBOS data included in the figure the trend in the ALICE data is that $N_{ch}/(N_{part}/2)$ rises faster with N_{part}. The Figure includes p+p data at $\sqrt{s} = 2.76$ TeV that extends the trend to the lowest N_{part}. It would be expected that ultra–peripheral Pb+Pb collisions and p+p collisions exhibit similar behaviour so the correspondance observed in Figure 7.11 is not surprising.

7.3.5 Pb+Pb and p+p comparison at $\sqrt{s_{NN}} = 2.76$ TeV

The p+p data at $\sqrt{s} = 2.76$ TeV allows for a direct comparison between $\frac{1}{N}\frac{dN_{\rm ch}}{d\eta}$ in p+p and Pb+Pb collisions. Figure 7.12 shows the ratio of $\frac{1}{N}\frac{dN_{\rm ch}}{d\eta}$ in Pb+Pb and p+p collisions at $\sqrt{s_{NN}} = 2.76$ TeV. Also included in figure are line showing the ratios of N_{part}. In the most peripheral collisions $(70-80\%)$ we find that the ratio of $\frac{1}{N}\frac{dN_{\rm ch}}{d\eta}$ coincides with the ratio of the N_{part}. While the particle production is still higher the peripheral Pb+Pb collisions begin to behave like scaled p+p collisions. This is also supported by the p+p data included in Figures 7.7 and 7.11 which are at the same level as the peripheral Pb+Pb data.

---

[1] Suggested by Jamie Nagle in private communication

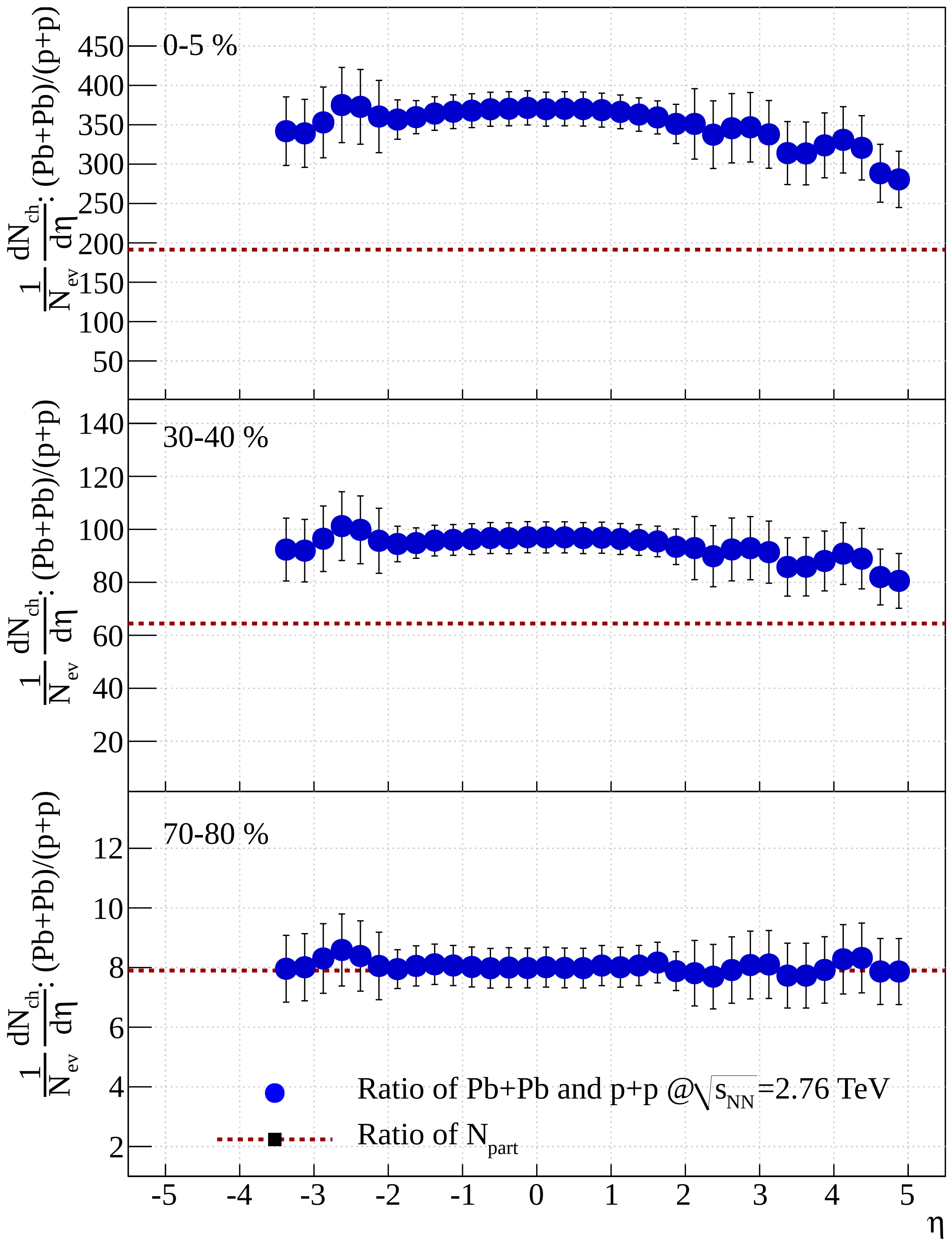

Figure 7.12: The figure shows the ratios between $\frac{1}{N}\frac{dN_{\rm ch}}{d\eta}$ in Pb+Pb collisions at $\sqrt{s_{NN}} = 2.76$ TeV (in three centrality intervals) and p+p collisions at $\sqrt{s} = 2.76$ TeV. The dotted lines indicate the ratios of the N_{part} of the Pb+Pb collisions and $N_{part}(= 2)$ in p+p collisions. It is observed that while the shape does not change with respect to η the level of the ratios approach simple scaling with N_{part} in the most peripheral collisions.

7.3.6 Summary of Scaling

The behaviour of $(dN_{ch}/d\eta)/(N_{part}/2)$ at LHC energies does not indicate a dramatic change to RHIC energies considering Figure 2.9 in section 2.2.5. Furthermore we found that $(dN_{ch}/d\eta)/(N_{part}/2)$ only differed by a scaling factor between various pseudorapidity intervals for $N_{part} > 100$. This seems to indicate a similar behaviour at LHC to that observed at RHIC.

The massive leap in energy makes an interpretation of the extended longitudinal scaling study at LHC difficult since the actual overlap in $y' = \eta - y_{beam}$ becomes small. However using functions fitted to the data a statement can be made that at least for peripheral collisions it seems likely that the data exhibit extended longitudinal scaling from RHIC to LHC energies. The interpretation of this can point in several directions. First, extended longitudinal scaling is expected from the CGC model of the initial state of heavy ion collisions so it could be interpreted as supportive for the existence of the CGC. However, as discussed in section 2.2.3 it can also be interpreted as a consequence of the Landau collision picture.

We found that the total number of charged particles as a function of N_{part} deviates slightly from a linear dependence. A second order polynomial gave a better description. The physical interpretation of this observation is not completely clear. We also studied $N_{ch}/(N_{part}/2)$ as a function of N_{part}. Here we found a slightly rising trend which was not observed to the same extent at RHIC (PHOBOS).

The direct comparison of $\frac{1}{N}\frac{dN_{\mathrm{ch}}}{d\eta}$ in Pb+Pb collisions to p+p collisions at the same energy can give a hint of the nature and magnitude of collective effects in the heavy ion collisions. Despite the non–understood structure in the p+p $\frac{1}{N}\frac{dN_{\mathrm{ch}}}{d\eta}$ at $\sqrt{s} = 2.76$ TeV we observed that the ratio is quite flat at all centralities. This can be interpreted such that the behaviour of the produced particles is similar in p+p and Pb+Pb collisions. We also found that for the most peripheral Pb+Pb collisions the level of the ratio can be described as simple scaling with N_{part}. For the most central collisions, however, the particle production is roughly twice what could be expected from such scaling. This certainly indicates that the most central collisions exhibit collective effects likely due to the effects of the produced hot and dense medium.

7.4 Comparisons to other Data and Models

This section is devoted to comparisons of the data to other measurements and models. These comparisons fall in three categories:

Comparison to RHIC (BRAHMS) data These comparisons are an attempt to study the behaviour of the particle production in A+A collisions from $\sqrt{s_{NN}} = 200$ GeV to $\sqrt{s_{NN}} = 2.76$ TeV. These comparisons may reveal new features at LHC energies or it may reinforce the understanding of particle production and collision dynamics from RHIC.

Comparison to other ALICE and LHC measurements These comparisons are made to check for discrepancies that may point to areas where more work are needed. In contrast to the comparisons in Figures 7.2, 7.4, and 7.6 here we will use data that is preliminary and not published.

Model Comparisons To some extent this could be considered the climax of this work. By comparing to models the models are tested for their ability to describe the fundamental particle production in A+A collisions.

7.4.1 RHIC comparison

The data are compared to the BRAHMS measurement presented in section 2.2.1 in the centrality classes where BRAHMS data are available. The results per centrality class are shown in Figure 7.13. The left column shows the direct comparison and the right panels show the ratios versus η. The BRAHMS data have been scaled according to Equation 2.2 to take into account the difference between the N_{part} in Au+Au and Pb+Pb collisions.

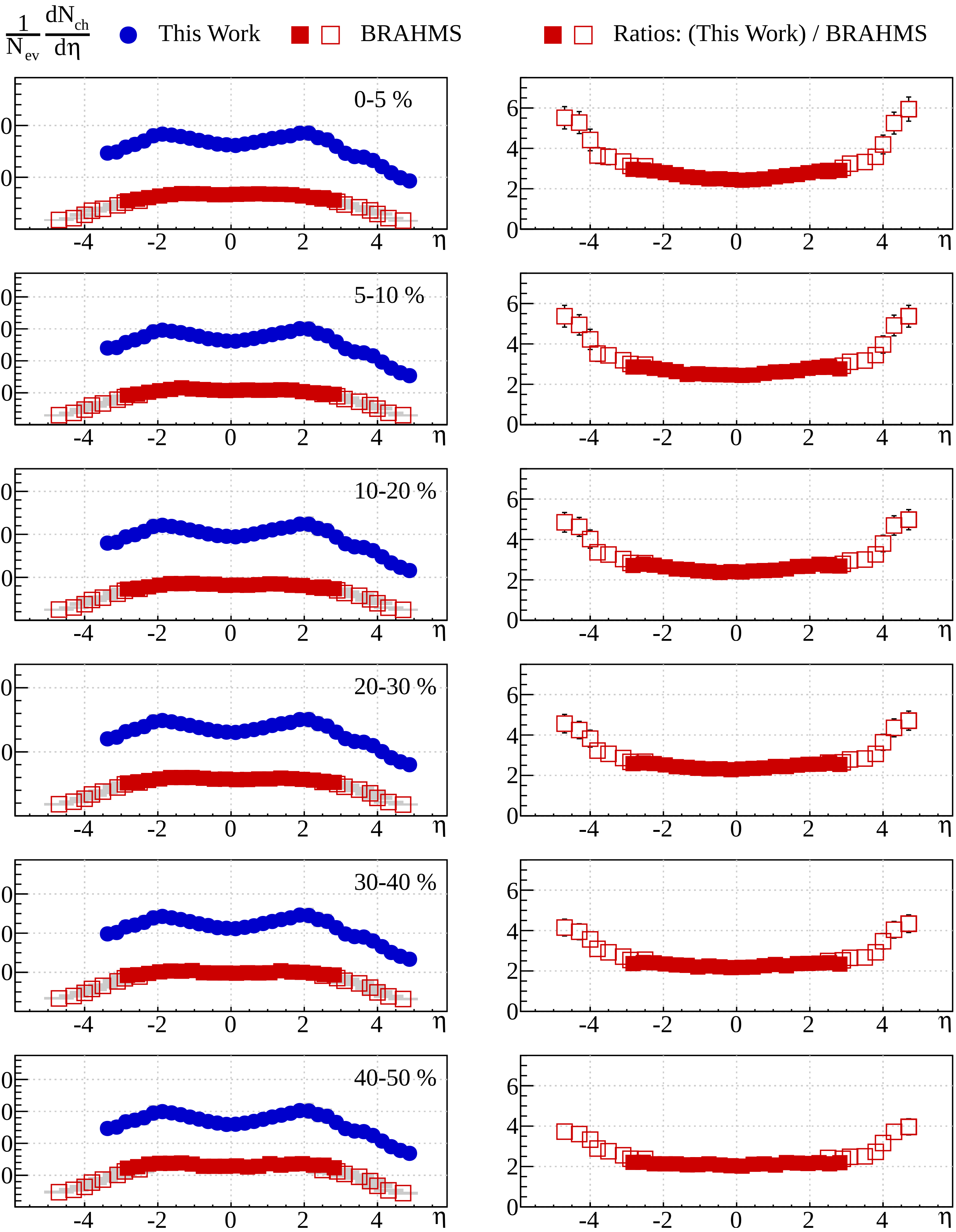

Figure 7.13: The left column of the figure shows $\frac{1}{N}\frac{dN_{ch}}{d\eta}$ from this work and BRAHMS compared in 6 centrality classes. The hollow BRAHMS symbols are from their Beam–Beam Counters while the solid points are from their silicon detector. The Right panels show the ratios of the fits to the FMD and SPD data in Table 7.1 and the BRAHMS points. The same structure is observed for all centralities.

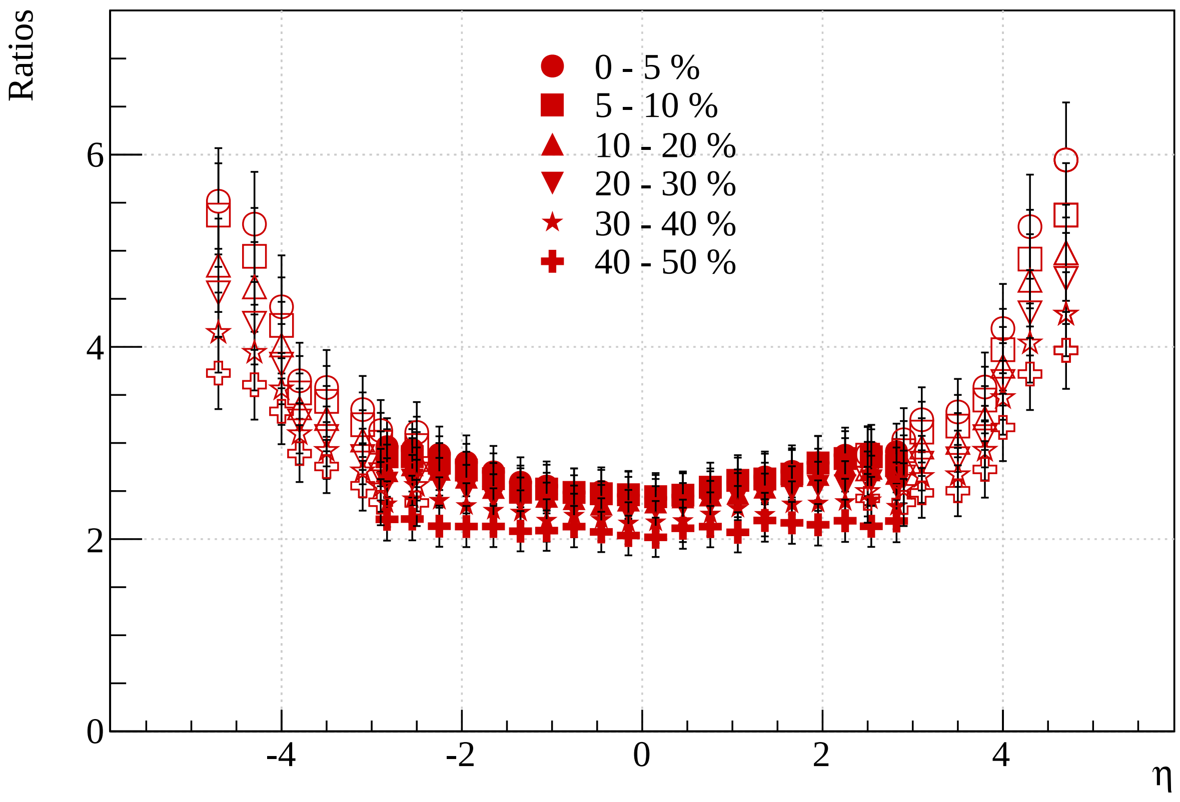

Figure 7.14: The figure shows the ratios of the fits to the $\frac{1}{N}\frac{dN_{\mathrm{ch}}}{d\eta}$ of this work to the BRAHMS $\frac{1}{N}\frac{dN_{\mathrm{ch}}}{d\eta}$ in 6 centrality classes from the right column of Figure 7.13 drawn on top of each other. It is clear that while the particle production is slightly higher in the most central collisions the shapes are similar.

The ratios are seen to vary little with centrality. A close–up look at the ratios is presented in Figure 7.14. It is very significant that the ratios are flat over almost 6 units of pseudorapidity around midrapidity. This seems to indicate that the particle production in this region is somehow governed by the same mechanisms at RHIC and LHC. For $|\eta| > 3$ the particle production is significantly larger at LHC than at RHIC. This is a result of the different y_{beam} ($y_{beam} = 5.36$ at RHIC and $y_{beam} = 7.99$ at LHC). As a result the LHC data must cover ~ 16 units of pseudorapidity while the RHIC data cover ~ 11 units. In the forward regions we have seen that it is very likely that there exists extended longitudinal scaling from RHIC to LHC which means that no direct scaling should be expected in the forward regions.

7.4.2 LHC comparison

The CMS and ATLAS data from Quark Matter 2011 were presented in section 2.3. While no publications are available at the time of this work the data points have been read off the plots[2] and comparisons to the most central data are shown in Figure 7.15. From these comparisons it is seen that the data of this work seems to be higher than both ATLAS and CMS at $|\eta| \sim 2$. While the discrepancy is at the edge of the systematic errors it is clear that the ALICE data are indeed systematically higher in this region. This could be caused by missing components or incorrect descriptions in the ALICE virtual geometry which would cause the correction for secondaries (see section 6.4) to be too low.

This point is strengthened further if a comparison is made to the other measurements under development in ALICE. This comparison is shown in Figure 7.16 where 3 other ALICE measurements are presented:

- SPD tracklet measurement[3]. This uses the official ALICE method of SPD measurements touched upon in Chapter 4.
- Measurement with the V0 detector[4]. The V0 detector is mainly a trigger detector. However it is possible to measure a $\frac{1}{N}\frac{dN_{\mathrm{ch}}}{d\eta}$ distribution with no absolute scale using vertices up to 3 meters away from the nominal IP. This distribution will have a η overlap with the SPD tracklet measurement which can then be taken as reference to fix the scale of the distribution.
- Measurement with the T0 detector[5].

It is seen that the FMD and V0 measurements differ by $\sim 10\%$ which is not understood at the moment. The T0 measurements are seen to be in good agreement with the FMD results. The V0 measurement is done using displaced vertices which means it will 'see' a different material budget than the FMD. This could point to issues in the ALICE geometry description.

The SPD cluster measurement and the SPD tracklet measurement are in good agreement except for $|\eta| > 1.5$ where the clusters seem to count too much. The fact that the FMD and SPD clusters both seem to count too many particles makes it more likely that there are issues with the material budget rather than a detector effect. It could also be that the strangeness enhancement observed in ALICE (see section 6.6.2 had a non–trivial pseudorapidity dependence which could cause the discrepancy. This effect and the material budget need to be studied further in ALICE.

7.4.3 Models

The model comparisons are shown in Figures 7.17 and 7.18. The models were introduced in section 2.3 and include PYTHIA and PHOJET for the p+p data and HIJING, AMPT, and DPMjet II for the Pb+Pb data. It is important to note that there exists an upgraded version of the DPMjet model (DPMjet III)

---

[2] Using a clever utility program known as 'datastealer' developed by C.H. Christensen, Niels Bohr Instiute.

[3] Ruben Shahoyan, private communication.

[4] Maxime Guilbaud, private communication

[5] Maxime Guilbaud, private communication

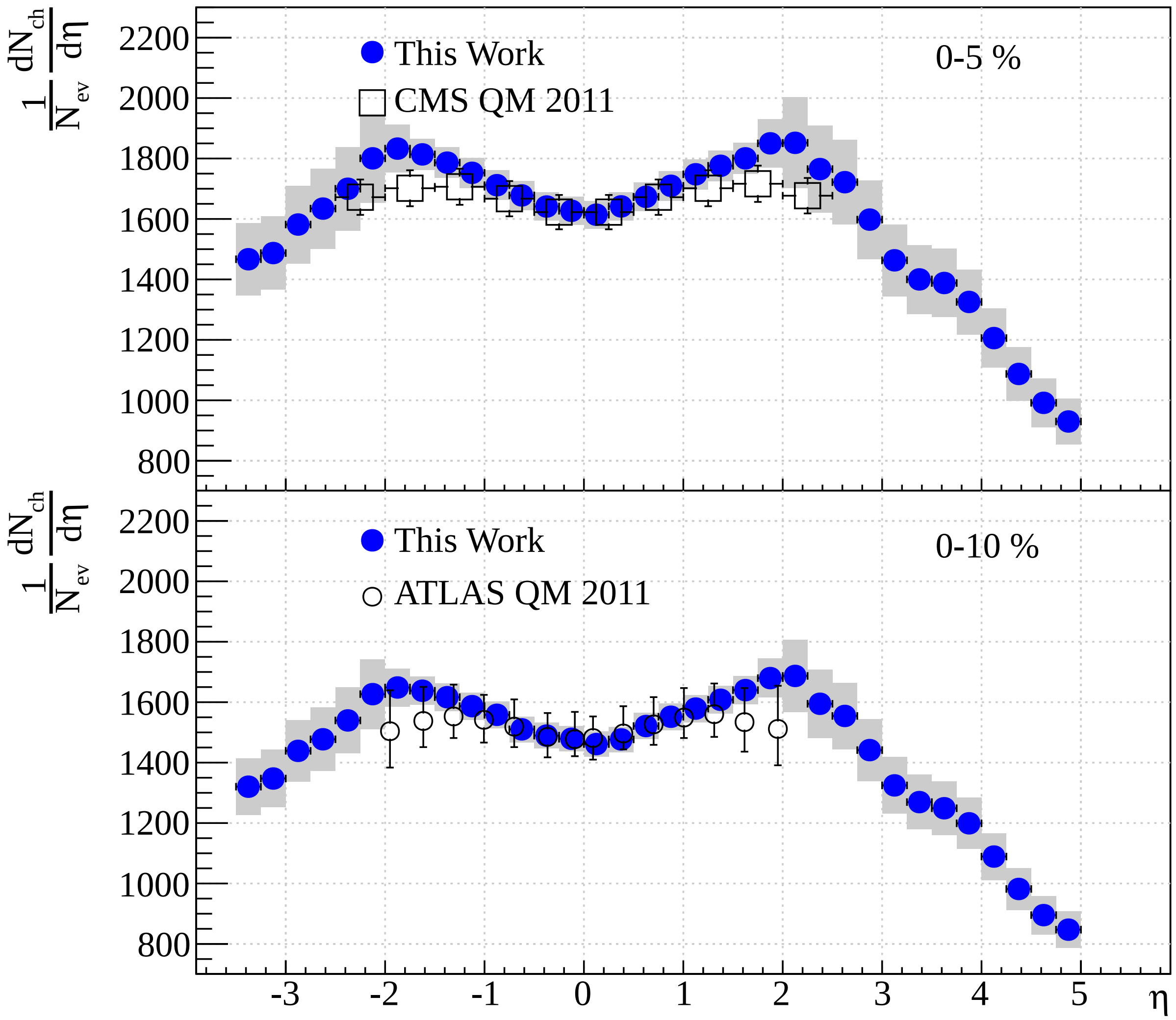

Figure 7.15: Top Panel: Comparison between this work and CMS for $0-5\%$ central Pb+Pb collisions. Bottom Panel: Comparison between this work and ATLAS for $0-10\%$ central Pb+Pb collisions. The CMS and ATLAS data points are read off the preliminary plots presented at Quark Matter 2011 [53, 54]. While the agreement at midrapidity is excellent discrepancies are observed with respect to both CMS and ATLAS data around $|\eta| \sim 2$. These discrepancies are not completely understood.

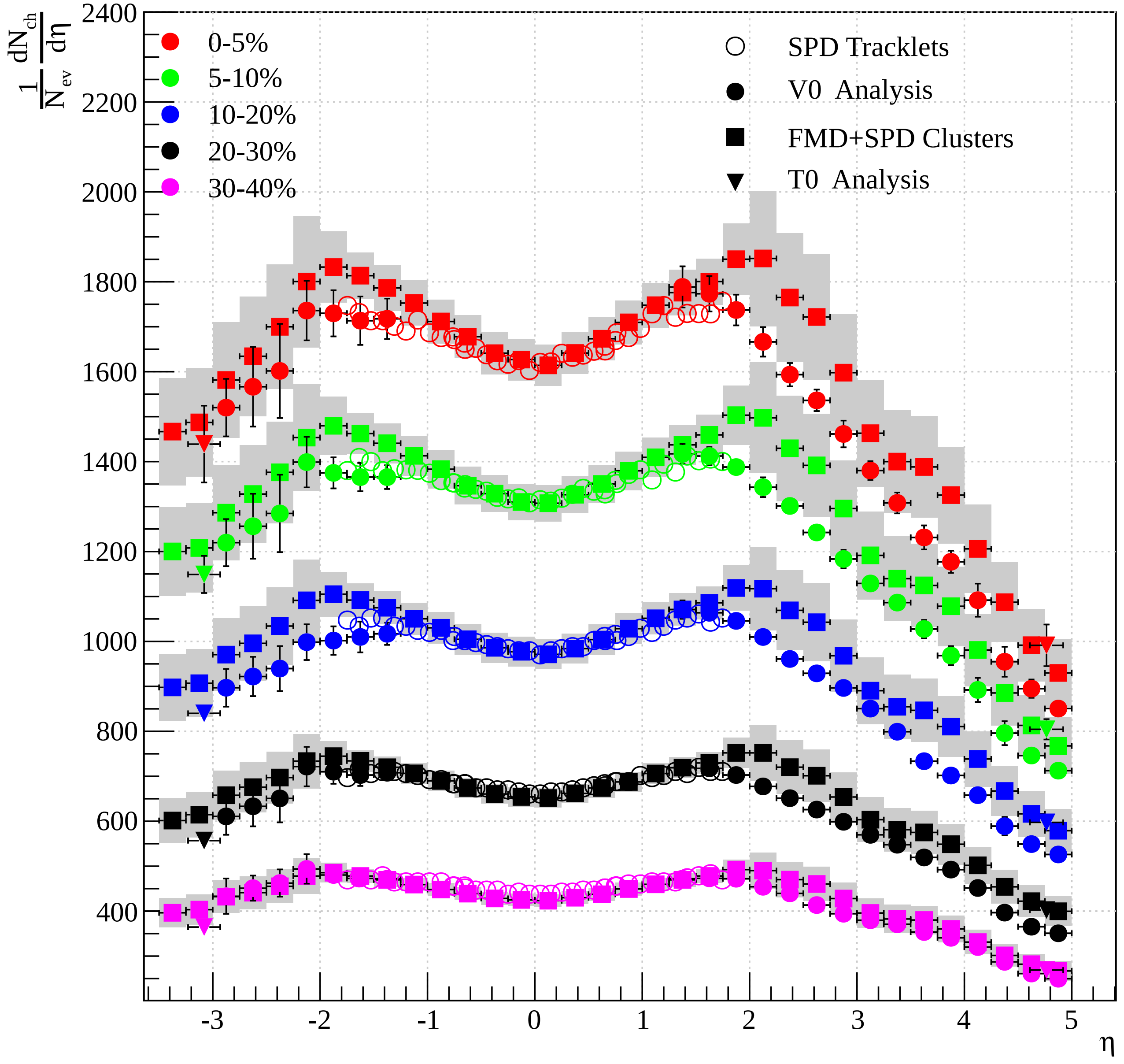

Figure 7.16: Comparison of ALICE analysis in progress in 5 centrality classes. It is seen that there are discrepancies between the V0 based analysis and the FMD analysis presented here. The SPD clusters have discrepancies from the SPD tracklets for $|\eta| > 1.5$. The T0 analysis is in good agreement with the FMD analysis for $\eta > 0$ while it is in reasonable agreement with both the V0 and FMD analysis for $\eta < 0$. The conclusion is that there is a $\sim 10\%$ discrepancy between the measurements that must be resolved.

but the attempt to produce plots with it were unsuccesful. Figure 7.17 includes a version of the DPMjet II points scaled to the ALICE $\frac{1}{N}\frac{dN_{\mathrm{ch}}}{d\eta}$ at midrapidity. Also included in the figure are points from the CGC based model by Albacete discussed in section 2.3. For the Pb+Pb data it is seen from Figure 7.17 that the models have different issues. HIJING gives a good description for the most central collisions while it underestimates $\frac{1}{N}\frac{dN_{\mathrm{ch}}}{d\eta}$ for more peripheral collisions. On the contrary, AMPT seems to do better in peripheral collisions than in the most central. DPMjet II overestimates the overall level of $\frac{1}{N}\frac{dN_{\mathrm{ch}}}{d\eta}$ but the shape looks reasonable.Finally, the CGC based model from Albacete agrees very well with the ALICE data at the 3 centralities in its limited η acceptance.

For p+p the comparison in Figure 7.18 shows that the PYTHIA tune presented here underestimates $\frac{1}{N}\frac{dN_{\mathrm{ch}}}{d\eta}$ at all energies while PHOJET gets the 900 GeV data right. PHOJET slightly underestimates the $\frac{1}{N}\frac{dN_{\mathrm{ch}}}{d\eta}$ at higher energies.

7.4.4 Summary of Comparisons

A direct comparison of the ALICE $\frac{1}{N}\frac{dN_{\mathrm{ch}}}{d\eta}$ and the BRAHMS $\frac{1}{N}\frac{dN_{\mathrm{ch}}}{d\eta}$ from RHIC was carried out. It was observed that for 6 units of pseudorapidity around midrapidity the ratios of $\frac{1}{N}\frac{dN_{\mathrm{ch}}}{d\eta}$ from RHIC and LHC were close to flat. These observations lead to the interpretation that the collisions at LHC seems to be governed by the same dynamics as RHIC despite the leap in energy by a factor of ~ 14.

Comparisons to the published results show good agreement for Pb+Pb collisions at $\sqrt{s_{NN}} = 2.76$ TeV and inelastic p+p at $\sqrt{s} = 900$ GeV. However, comparisons to preliminary Quark Matter 2011 results of ATLAS and CMS reveal discrepancies in the region $|\eta| \sim 2$. Furthermore the comparison to other ALICE measurements show a discrepancy to the V0 based measurement and a discrepancy between the SPD clusters and tracklets at higher η. The present understanding of the experiment is insufficient to explain these discrepancies and therefore the potential causes should be studied further. The issues are most likely related to missing information in the simulations. Some of these issues are discussed in sections 7.5.3 and 7.5.4.

Several model comparisons have been done. For p+p collisions we have seen PHOJET and PYTHIA have difficulties with describing the full $\frac{1}{N}\frac{dN_{\mathrm{ch}}}{d\eta}$. It is clear that other tunes of the models presented here should be compared to the data since the tunes here are limited to the selection in the ALICE simulations. No comparison has been attempted for NSD results due to the fact that the measurements are work–in–progress and likely to change.

For the Pb+Pb the most successful model is a CGC based model. This seems to hint that a CGC could be formed at the LHC. However, predictions from the CGC based model in the most forward region would test this model here as well. The issues observed in HIJING could be an issue with the centrality selection which should be examined further for a better comparison. A proper comparison to DPMjet III should also be carried out. The scaled DPMjet II results shown here did a reasonable job of describing the data.

7.4.5 Other Aspects of Multiplicity

The programs that have been used for data analysis is discussed in appendix C. These programs also support other applications where the fundamental input comes from the SPD and FMD. These include multiplicity distributions [118], rapidity correlations [119], and anisotropic transverse flow [120]. Figures 7.19 and 7.20 show results for unfolded multiplicity distributions for p+p collisions at $\sqrt{s} = 900$ GeV and $\sqrt{s} = 7$ TeV including comparisons to other measurements.

7.5 Discussion

This section is devoted to a discussion of the physics results and the issues that have been identified in this analysis.

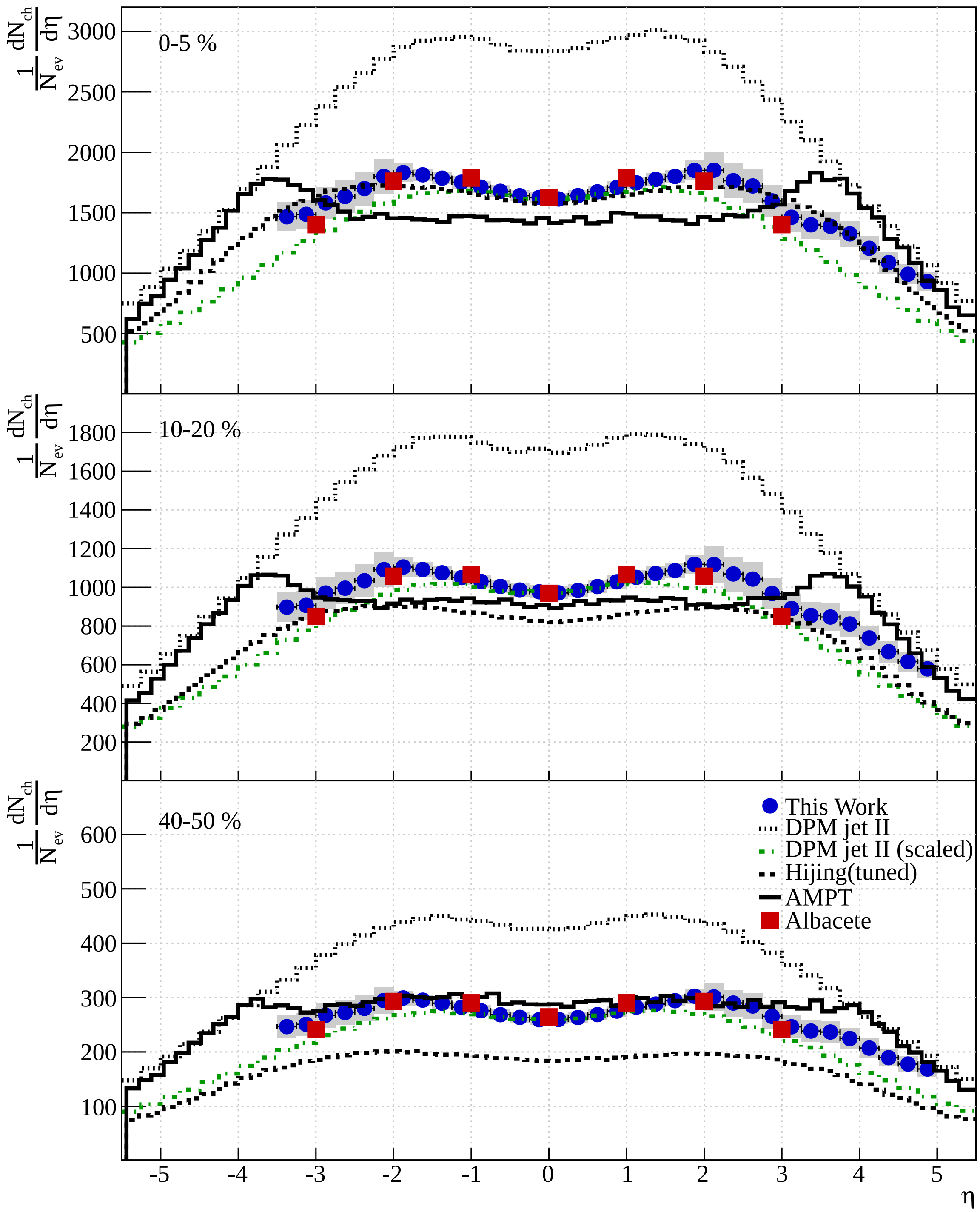

Figure 7.17: Model comparison of $\frac{1}{N}\frac{dN_{\rm ch}}{d\eta}$ in Pb+Pb collisions at $\sqrt{s_{NN}}$ = 2.76 TeV in 3 centrality intervals. Three models are tested: HIJING (tuned to the first ALICE measurement at midrapidity), AMPT, and DPMjet II. Note that there is a more recent version of DPMjet (DPMjet III) available. It is observed that HIJING gives a good description of the most central collisions but seem to underestimate $\frac{1}{N}\frac{dN_{\rm ch}}{d\eta}$ in more peripheral collisions. AMPT does a better job in peripheral collisions while the shape diverges from the data in central collisions. DPMjet II overestimates the $\frac{1}{N}\frac{dN_{\rm ch}}{d\eta}$ for all centralities but the shape appears to be close to the data as indicated by the green curve, scaled to $\frac{1}{N}\frac{dN_{\rm ch}}{d\eta}$ at $\eta = 0$. Finally, the model from Albacete et al [69] does a very good job in its η coverage[7].

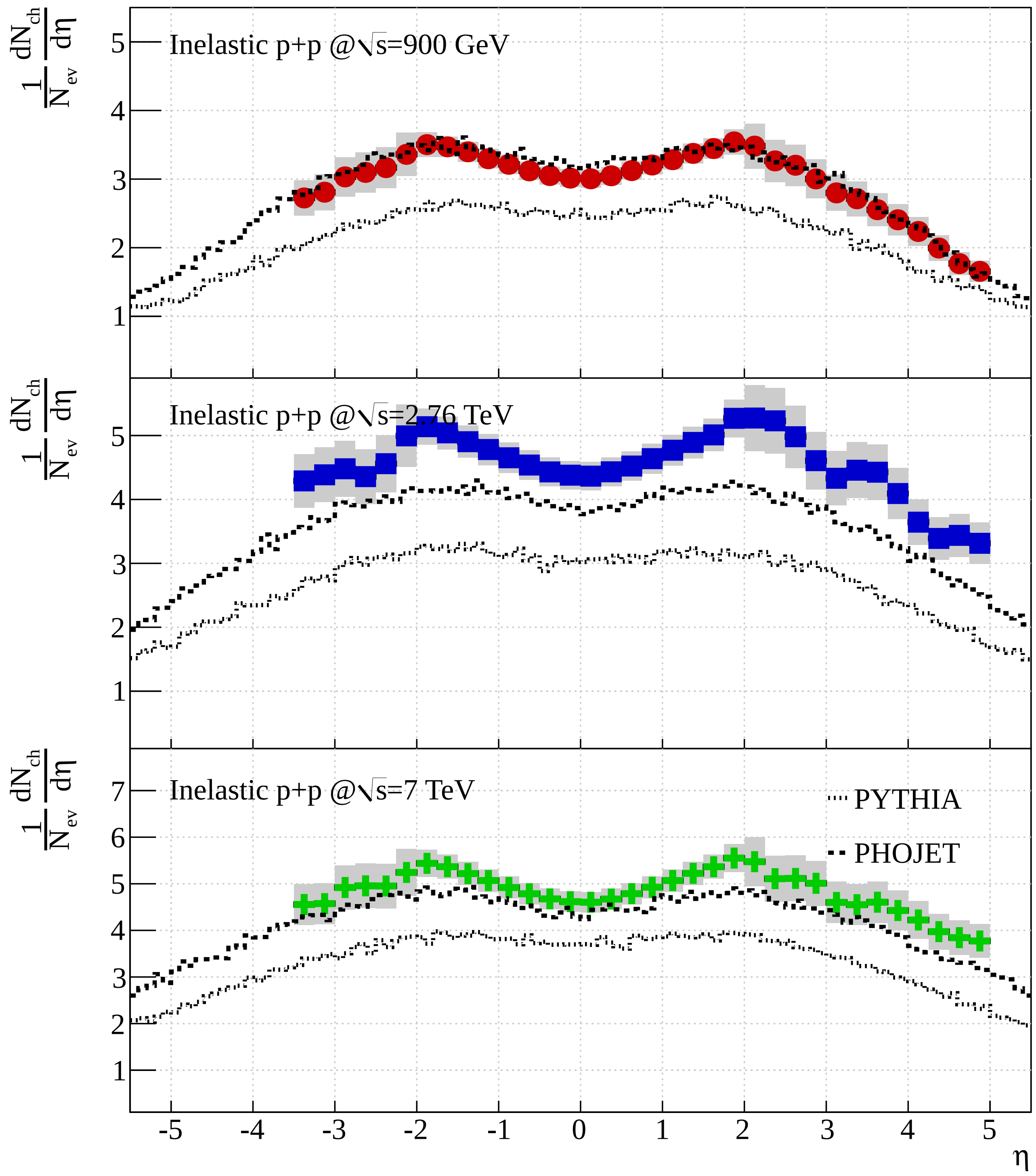

Figure 7.18: The three panels show comparisons of PYTHIA and PHOJET to the Inelastic p+p data at $\sqrt{s}$ = 900 GeV, $\sqrt{s}$ = 2.76 TeV, and $\sqrt{s}$ = 7 TeV from top to bottom, respectively. The comparisons show that PHOJET gives a better description of the data than PYTHIA, in particular at $\sqrt{s}$ = 900 GeV but both models underestimate $\frac{1}{N}\frac{dN_{\rm ch}}{d\eta}$.

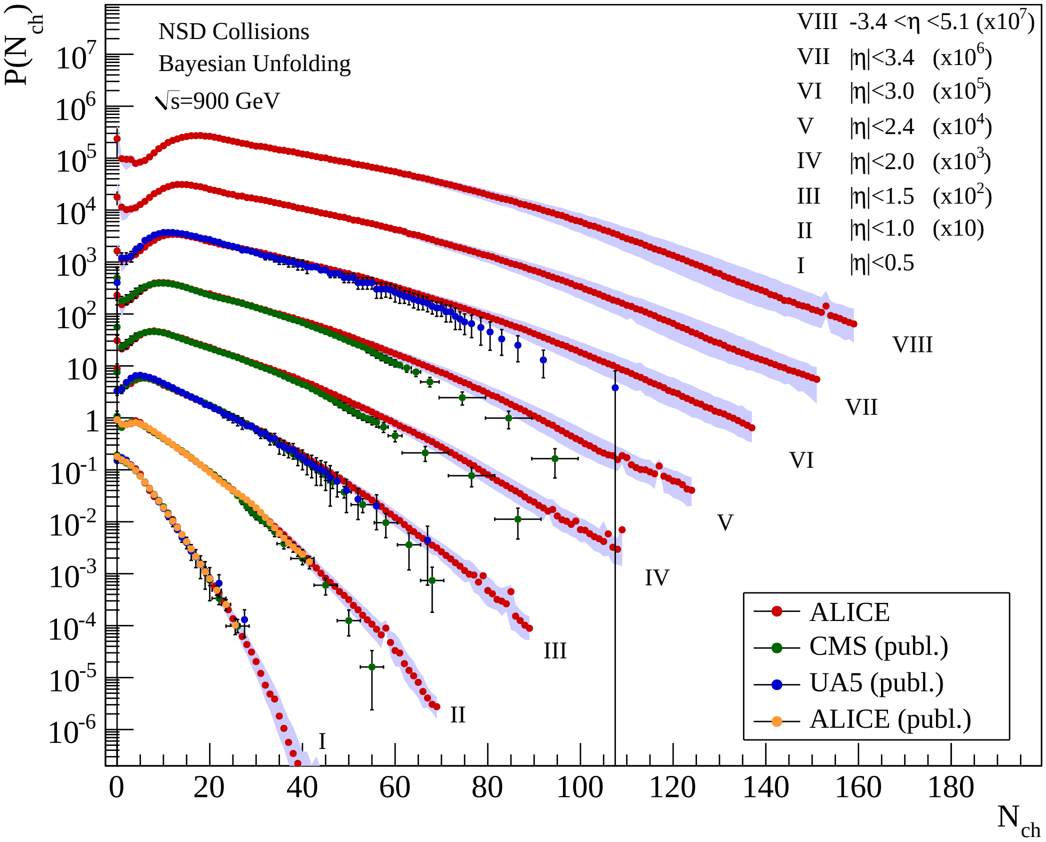

Figure 7.19: Multiplicity distributions, $P(N_{ch}$ measured with the ALICE SPD and FMD in 8 pseudorapidity intervals in p+p collisions at $\sqrt{s} = 900$ GeV [118]. The results are compared to results from UA5, ALICE (published), and CMS.

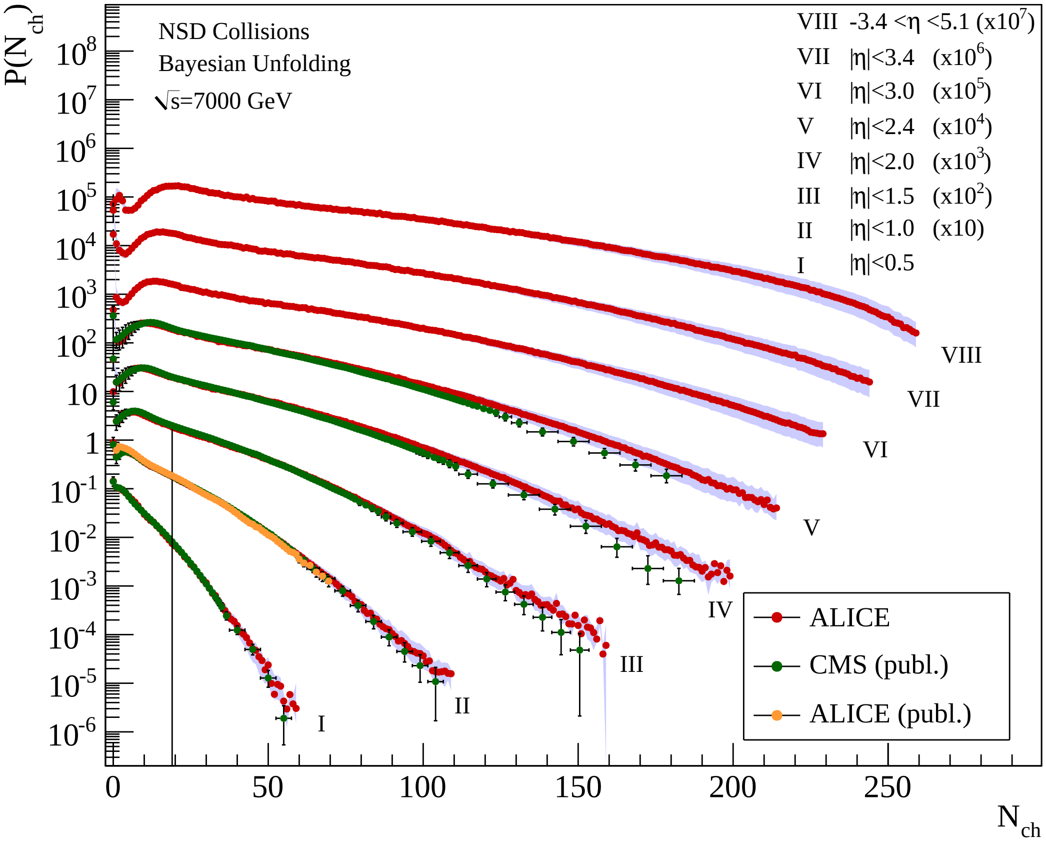

Figure 7.20: Multiplicity distributions, $P(N_{ch}$ measured with the ALICE SPD and FMD in 8 pseudorapidity intervals in p+p collisions at $\sqrt{s} = 7$ GeV [118]. The results are compared to results from ALICE (published) and CMS results.

7.5.1 At the Frontier

The closing remark of Chapter 1 concerned the frontier in heavy ion physics. With the measurements presented here the mapping of the forward region at LHC energies advances. This chapter has seen the presentation of $\frac{1}{N}\frac{dN_{\mathrm{ch}}}{d\eta}$ in 10 centrality classes in Pb+Pb collisions at $\sqrt{s_{NN}} = 2.76$ TeV and $\frac{1}{N}\frac{dN_{\mathrm{ch}}}{d\eta}$ in inelastic p+p collisions at $\sqrt{s} = 900$ GeV, $\sqrt{s} = 2.76$ TeV, and $\sqrt{s} = 7$ TeV. We have also presented work in progress on the $\frac{1}{N}\frac{dN_{\mathrm{ch}}}{d\eta}$ in p+p NSD collisions where the calculations of the trigger efficiencies are incomplete at the time of this work. This means that the level of the NSD $\frac{1}{N}\frac{dN_{\mathrm{ch}}}{d\eta}$ are likely to change when the calculations are done.

For the Pb+Pb data issues were observed when comparing to other measurements in progress, in particular around $|\eta| \sim 2$. These issues should have the highest priority in the future of FMD and SPD analysis.

Despite the issues the data contain many physics messages. We have observed that the scaling of $(dN_{ch}/d\eta)/(N_{part}/2)$ holds from RHIC to LHC and that there is a similar scaling between different pseudorapidity intervals at LHC. We have also observed that is seems probable that longitudinal scaling holds from RHIC to LHC. Furthermore we have seen that $N_{ch}/(N_{part}/2)$ is consistent with p+p collisions but seems to rise faster at LHC than at RHIC. A direct comparison to the RHIC data from BRAHMS showed a consistent behaviour of the data in 6 units of pseudorapidity despite the increase in energy of a factor of 14. The most successful model available appears to be a model based on the existence of the CGC phase in the initial phase of the collisions. From this is would be unreasonable to conclude the existence of the CGC but this observation certainly supports its existence.

7.5.2 FMD detector issues in 2011?

It was found in section 6.2.3 that the hit merging algorithm gives results for the double signals for p+p data at $\sqrt{s} = 2.76$ TeV that differ from the expected structure seen in p+p data at $\sqrt{s} = 900$ GeV and $\sqrt{s} = 7$ TeV. Furthermore it was observed that the pedestal remnant seems to broaden in the energy distributions in p+p data at $\sqrt{s} = 2.76$ TeV. The structure observed in the $\frac{1}{N}\frac{dN_{\mathrm{ch}}}{d\eta}$ (see Figure 7.3) is interpreted as a consequence of these issues. It is clear that these issues should be studied and understood for the FMD data of 2011.

7.5.3 Energy distributions in the FMD - towards better simulations?

In section 6.2 it was discussed that the distributions of energy loss in the FMD differ in physics data compared to simulated data. In this section we will suggest a way to 'tune' the simulations to generate distributions of the energy loss that resemble those observed in the data. The idea is modulate the energy loss in the simulations with a function based on parameters from data distributions.

We assume that the simulations derive from a probability function (most likely a Landau distribution) of a single variable, $\frac{E-E_0}{\sigma}$. However, we want to change simulations to be wider in the probability function because we observe wider energy distributions in the physics data. Let E' be the energy of the new distribution with spread σ'. Thus, we will recalculate the energy as follows:

$$\frac{E-E_0}{\sigma} = \frac{E'-E_0}{\sigma'} \quad \text{, thus} \quad E' = \frac{\sigma'}{\sigma}E + \left(1 - \frac{\sigma'}{\sigma}\right)E_0 \tag{7.3}$$

In the simulations we pick up E from the simulation and recalculate E' using $\frac{\sigma'}{\sigma}$ from the fits to the simulated and physics data. In this way we can 'tune' the simulations to resemble the energy distributions of physics data. The results of such tuning for 2 values of $\frac{\sigma'}{\sigma}$ are shown in Figure 7.21. It is clear that the tuning successfully changes the energy distributions to resemble the physics data. It should noted that analysis of the tuned simulations shows no change to the fractions of single, double, and triple signals shown in Tables 6.4 and 6.5. Neither can it explain the observed low energy tail in physics data (see Figure 6.15) since the levels at low energies are the same for the 3 cases in Figure 7.21.

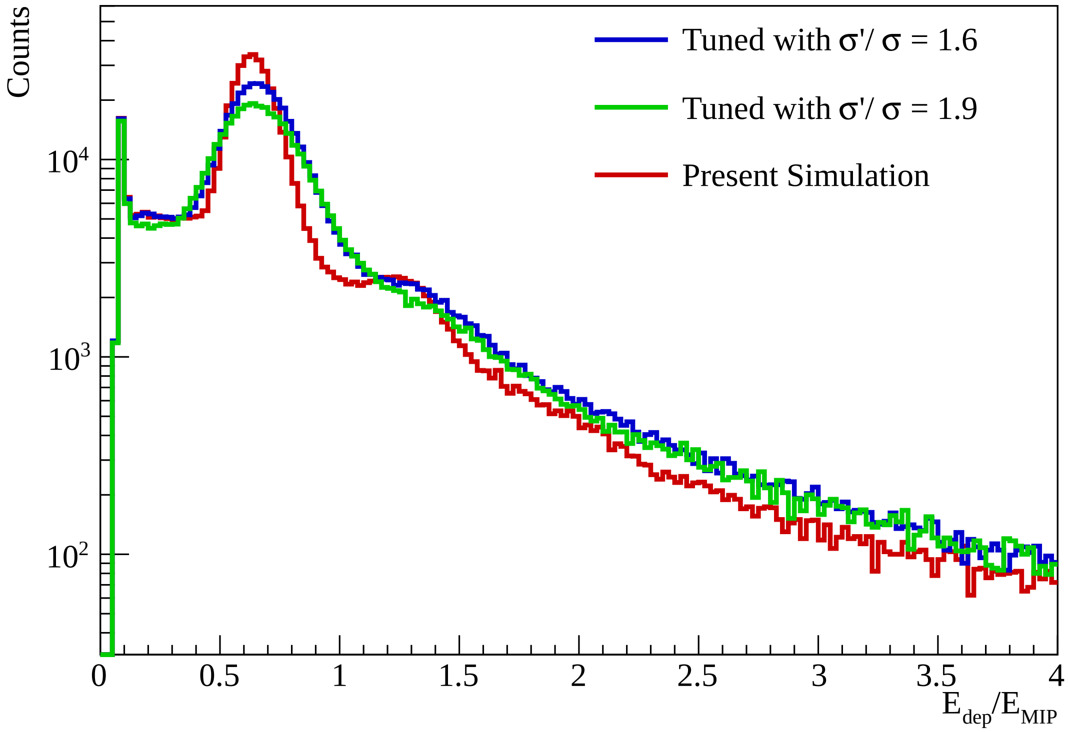

Figure 7.21: The resulting energy distributions in FMD2O for two tuned values of σ'/σ compared to the present simulations. It is clear that the simulations can be tuned to approach the behaviour seen in the data.

While this study is not complete it shows that it would be possible to tune the simulations of the FMD signals to resemble the physics data better. However, a better understanding of the issues in the detector concerning the low energy tail and the distributions of single, double, and triple signals could still improve the foundation of this analysis.

7.5.4 Material Budget and Secondaries in ALICE

Due to its large impact on the $\frac{1}{N}\frac{dN_{\mathrm{ch}}}{d\eta}$ analysis, the precision of the description of the material budget in the ALICE geometry is crucial. It is also found to be the largest single contribution to the systematic error. For these reasons ALICE will perform a scan of the detector with the TPC where vertices outside the range of the normal vertices $|v_z| \sim 70$ cm are used to compare the detected secondary particles with the secondaries predicted by the simulations. Unfortunately this study is not available at the time of this thesis.

The TPC study can also address the issue of the enhanced secondary strangeness production observed in ALICE. This was discussed in section 6.6.2. A better understanding of this effect and in particular its pseudorapidity dependence is desirable for this analysis since every secondary particle counts in the correction for secondaries.

Appendix E gives a more thorough discussion of the issues that have been found and fixed in the ALICE material budget. Furthermore studies from simulations of the production of secondary particles are presented.

Conclusion

When I completed my masters studies in 2007 the FMD installation was not complete. Only FMD3 was installed and the installation activity in the ALICE cavern was intense, sometimes hectic. The coming years saw the final installation of FMD1 and FMD2 as well as all the service and support required to run the FMD. In the beginning of the FMD running several problems were detected and fixed so the FMD was in good shape for the first LHC collisions.

November 23, 2009 is a milestone date in physics. On this day the first collisions of protons took place inside the LHC followed by celebration at the LHC experimental sites. The fields of particle and heavy ion physics had waited 25 years for the LHC to become operational. 25 years of planning, hard work, and waiting for new realms to open up in modern physics. But finally physicists can reap the long–awaited new physics that come out of the LHC experiments.

Some of the new physics reaped at LHC has been presented in this thesis. Using the Silicon Pixel Detector and Forward Multiplicity Detector of ALICE the $\frac{1}{N}\frac{dN_{\mathrm{ch}}}{d\eta}$ in Pb+Pb and p+p collisions have been measured at unprecedented energies. Results on $\frac{1}{N}\frac{dN_{\mathrm{ch}}}{d\eta}$ have been presented for Minimum Bias Pb+Pb collisions at $\sqrt{s_{NN}} = 2.76$ TeV in 10 centrality classes and for inelastic p+p collisions at three energies. Furthermore we have presented work–in–progress on $\frac{1}{N}\frac{dN_{\mathrm{ch}}}{d\eta}$ in Non–Single Diffractive p+p collisions at three energies.

The interpretation of the results have only begun in this thesis. Measurements at forward pseudorapidities allow estimates of the total number of charged particles produced with small errors as well as the ability to compare different pseudorapidity intervals. The total number of produced charged particles in central Pb+Pb collisions at LHC was found to be ~ 18000 compared to the 2×202 nucleons entering the collisions. It was found that there are similarities in the observations made at LHC and at RHIC. Longitudinal scaling of the fragmentation regions appears to hold also from RHIC to LHC. Furthermore it was found that the ratio of $\frac{1}{N}\frac{dN_{\mathrm{ch}}}{d\eta}$ from RHIC and LHC was almost flat over 6 units of pseudorapidity, perhaps hinting common dynamics. Furthermore it was found that the shapes of $\frac{1}{N}\frac{dN_{\mathrm{ch}}}{d\eta}$ scaled with $N_{part}/2$ in different pseudorapidity intervals were constant as a function of N_{part} for $N_{part} > 100$.

Comparisons to models show a good agreement to models working from the Color Glass Condensate initial state (using the McLerran–Venugopalan assumption of $\gamma = 1$). This supports the present conception in heavy ion physics that a Color Glass Condensate is formed in the heavy ion collisions at RHIC and LHC energies followed by formation of a strongly interacting Quark–Gluon Plasma. However, even with the coming of LHC the ‘smoking gun’ of Quark–Gluon Plasma has yet to be observed. So far the chiral symmetry restoration has not been measured which would immidiately confirm the first observations of a Quark–Gluon Plasma since the dawn of time.

Concerning the future of this analysis, there is still work to do. The FMD and SPD systems have been run succesfully in almost two years but there are still issues with the detectors that are not understood. The full understanding of these issues would put the measurements presented here on much more solid ground and allow publication of the data. The comparisons to other ALICE results on $\frac{1}{N}\frac{dN_{\mathrm{ch}}}{d\eta}$ and the preliminary ATLAS and CMS results show that there are issues in the forward regions that must be taken into account. To give a summary, 4 key issues are identified the understanding of which would complete the picture in this thesis:

- **Material Budget** It must be studied whether the description of the ALICE material budget in the virtual ALICE geometry is accurate enough, especially in the forward regions. Hopefully this can be studied by the TPC using displaced vertices.

- **Low Energy signals in the FMD** A 'low energy tail' was observed in the energy distributions in the FMD following hit merging. The origin of this tail should be studied and understood. Furthermore the fractions of single, double, and triple signals after hit merging were found to be different in data and simulations which require attention.

- **FMD 2011 Data Quality** It was seen from the hit merging as well as the final result for $\frac{1}{N}\frac{dN_{\mathrm{ch}}}{d\eta}$ in p+p collisions at $\sqrt{s} = 2.76$ TeV that there seem to be issues that are not present in p+p data at $\sqrt{s} = 900$ GeV and $\sqrt{s} = 7$ TeV. These issues should be understood fast considering the upcoming of the next Pb+Pb run at LHC.

- **Improvement of the Simulations** It was seen that the energy distributions from the simulations had different shapes than the physics data. This should be fixed by tuning the simulations so they reflect reality better. Furthermore the simulations should be upgraded to take into account the two above issues.

While these issues are in some sense annoying since the results would rest on more firm ground in their absence the quest of solving them is one of the things that make it exciting to be a physicist. I hope to be able to help in solving these issues and improving the foundation of my results on $\frac{1}{N}\frac{dN_{\mathrm{ch}}}{d\eta}$. The LHC era in high energy particle and nuclear physics has begun.

Hans Hjersing Dalsgaard,
Copenhagen, October 2011

Bibliography

[1] I. Arsene *et al.*, “Nuclear stopping and rapidity loss in Au+Au collisions at s(NN)**(1/2) = 62.4-GeV,” *Phys.Lett.*, vol. B677, pp. 267–271, 2009.

[2] N. Ishii, S. Aoki, and T. Hatsuda, “The nuclear force from lattice QCD,” *arXiv.org*, 2006.

[3] G. S. Bali, “QCD forces and heavy quark bound states,” *Phys. Rept.*, vol. 343, pp. 1–136, 2001.

[4] M. Kliemant, R. Sahoo, T. Schuster, and R. Stock, “Global Properties of Nucleus-Nucleus Collisions,” *Lect.Notes Phys.*, vol. 785, pp. 23–103, 2010. * Temporary entry *.

[5] J. M. Maldacena, “The Large N limit of superconformal field theories and supergravity,” *Adv.Theor.Math.Phys.*, vol. 2, pp. 231–252, 1998.

[6] J. C. Collins and M. J. Perry, “Superdense Matter: Neutrons Or Asymptotically Free Quarks?,” *Phys. Rev. Lett.*, vol. 34, p. 1353, 1975.

[7] G. Baym, “RHIC: From dreams to beams in two decades,” *Nucl. Phys.*, vol. A698, pp. XXIII–XXXII, 2002.

[8] J. Letessier and J. Rafelski, “Hadrons and quark - gluon plasma,” *Camb. Monogr. Part. Phys. Nucl. Phys. Cosmol.*, vol. 18, pp. 1–397, 2002.

[9] M. Gyulassy and L. McLerran, “New forms of QCD matter discovered at RHIC,” *Nucl. Phys.*, vol. A750, pp. 30–63, 2005.

[10] J. Breitweg *et al.*, “ZEUS results on the measurement and phenomenology of F(2) at low x and low Q**2,” *Eur.Phys.J.*, vol. C7, pp. 609–630, 1999.

[11] K. J. Eskola, “On predictions of the first results from RHIC,” *Nucl. Phys.*, vol. A698, pp. 78–87, 2002.

[12] H. Satz, “Colour deconfinement in nuclear collisions,” *Rept. Prog. Phys.*, vol. 63, p. 1511, 2000.

[13] I. Y. Pomeranchuk, “On the theory of multiple particle production in a single collision,” *Dokl. Akad. Nauk Ser. Fiz.*, vol. 78, pp. 889–891, 1951.

[14] A. Andronic and P. Braun-Munzinger, “Ultrarelativistic nucleus nucleus collisions and the quark-gluon plasma,” *Lect. Notes Phys.*, vol. 652, pp. 35–68, 2004.

[15] F. Karsch, “Lattice QCD at high temperature and density,” *Lect. Notes Phys.*, vol. 583, pp. 209–249, 2002.

[16] H. Satz, “The Thermodynamics of Quarks and Gluons,” *Lect.Notes Phys.*, vol. 785, pp. 1–21, 2010.

[17] M. Gazdzicki and M. I. Gorenstein, “On the early stage of nucleus nucleus collisions,” *Acta Phys. Polon.*, vol. B30, p. 2705, 1999.

[18] R. Stock, “Hadron production in relativistic nuclear collisions,” *arXiv.org*, 2002.

[19] K. Rajagopal, “Theory overview.” Quark Matter 2011 plenary talk.

[20] L. D. Landau, “On the multiparticle production in high-energy collisions,” *Izv. Akad. Nauk SSSR Ser. Fiz.*, vol. 17, pp. 51–64, 1953.

[21] I. G. Bearden *et al.*, “Charged meson rapidity distributions in central Au + Au collisions at $\sqrt{s_{NN}} = 200 - gev$,” *Phys. Rev. Lett.*, vol. 94, p. 162301, 2005.

[22] J. D. Bjorken, “Highly relativistic nucleus-nucleus collisions: The central rapidity region,” *Phys. Rev.*, vol. D27, pp. 140–151, 1983.

[23] M. L. Miller, K. Reygers, S. J. Sanders, and P. Steinberg, “Glauber modeling in high energy nuclear collisions,” *Ann.Rev.Nucl.Part.Sci.*, vol. 57, pp. 205–243, 2007.

[24] B. Back *et al.*, “Baryon rapidity loss in relativistic Au+Au collisions,” *Phys.Rev.Lett.*, vol. 86, pp. 1970–1973, 2001.

[25] L. Ahle *et al.*, “Proton and deuteron production in Au + Au reactions at 11.6/A-GeV/c,” *Phys.Rev.*, vol. C60, p. 064901, 1999.

[26] J. Barrette *et al.*, “Proton and pion production in Au + Au collisions at 10.8A-GeV/c,” *Phys.Rev.*, vol. C62, p. 024901, 2000.

[27] H. Appelshauser *et al.*, “Baryon stopping and charged particle distributions in central Pb + Pb collisions at 158-GeV per nucleon,” *Phys.Rev.Lett.*, vol. 82, pp. 2471–2475, 1999.

[28] I. G. Bearden *et al.*, “Nuclear stopping in Au + Au collisions at $\sqrt{s_{NN}} = 200$ GeV,” *Phys. Rev. Lett.*, vol. 93, p. 102301, 2004.

[29] F. Videbaek and O. Hansen, “Baryon rapidity loss and mid-rapidity stacking in high- energy nucleus-nucleus collisions,” *Phys. Rev.*, vol. C52, pp. 2684–2693, 1995.

[30] J. Adams *et al.*, “Experimental and theoretical challenges in the search for the quark gluon plasma: The STAR collaboration’s critical assessment of the evidence from RHIC collisions,” *Nucl. Phys.*, vol. A757, pp. 102–183, 2005.

[31] B. Schenke, “Flow - theory perspective.” Quark Matter 2011 plenary talk.

[32] S. S. Adler *et al.*, “Common suppression pattern of eta and pi0 mesons at high transverse momentum in Au + Au collisions at $\sqrt{s_{NN}} = 200gev$,” *Phys. Rev. Lett.*, vol. 96, p. 202301, 2006.

[33] H. Appelhauser, “Particle production at large transverse momentum with alice.” Quark Matter 2011 plenary talk.

[34] Y.-J. Lee, “Nuclear modification factors from the cms experiment.” Quark Matter 2011 plenary talk.

[35] C. Roland, “Jet measurements by the cms experiment in pp and pbpb collisions.” Quark Matter 2011 plenary talk.

[36] A. M. Poskanzer and S. A. Voloshin, “Methods for analyzing anisotropic flow in relativistic nuclear collisions,” *Phys. Rev.*, vol. C58, pp. 1671–1678, 1998.

[37] S. Voloshin and Y. Zhang, “Flow study in relativistic nuclear collisions by Fourier expansion of Azimuthal particle distributions,” *Z. Phys.*, vol. C70, pp. 665–672, 1996.

[38] J. Hamblen, "Pseudorapidity Dependence of Elliptic Flow in Au+Au Collisions at 19.6, 62.4, 130, and 200 GeV using the PHOBOS Experiment at RHIC." Talk given at DNP 2004, 2004.

[39] B. B. Back *et al.*, "Centrality and pseudorapidity dependence of elliptic flow for charged hadrons in Au + Au collisions at $\sqrt{s_{NN}} = 200gev$," *Phys. Rev.*, vol. C72, p. 051901, 2005.

[40] G.-Y. Qin, H. Petersen, S. A. Bass, and B. Muller, "Translation of collision geometry fluctuations into momentum anisotropies in relativistic heavy-ion collisions," *Phys.Rev.*, vol. C82, p. 064903, 2010.

[41] J. Jia, "Atlas v_n results." Quark Matter 2011 plenary talk.

[42] S. Esumi, "Collective flow measurements from the phenix experiment." Quark Matter 2011 plenary talk.

[43] R. Snellings, "Anisotropic flow measurements from alice." Quark Matter 2011 plenary talk.

[44] G. Watt, "Overview: Diffraction in ep and pp collisions." Talk from Workshop on Future Prospects in QCD at High Energy, BNL 2006.

[45] M. Good and W. Walker, "Diffraction disssociation of beam particles," *Phys.Rev.*, vol. 120, pp. 1857–1860, 1960.

[46] J. F. Grosse-Oetringhaus, *Measurement of the charged particle multiplicity in Proton-Proton collisions measured with the ALICE detector*. PhD thesis, University of Munster, 2009.

[47] F. Antinori, "The high energy frontier of aa." Quark Matter 2011 plenary summary talk.

[48] K. Aamodt *et al.*, "Centrality dependence of the charged-particle multiplicity density at mid-rapidity in Pb-Pb collisions at sqrt(sNN) = 2.76 TeV," *Phys.Rev.Lett.*, vol. 106, p. 032301, 2011. Long author list - awaiting processing.

[49] e. . Carminati, F. *et al.*, "ALICE: Physics performance report, volume i," *J. Phys.*, vol. G30, pp. 1517–1763, 2004.

[50] B. B. Back *et al.*, "The PHOBOS perspective on discoveries at RHIC," *Nucl. Phys.*, vol. A757, pp. 28–101, 2005.

[51] I. Arsene *et al.*, "Quark Gluon Plasma an Color Glass Condensate at RHIC? The perspective from the BRAHMS experiment," *Nucl. Phys.*, vol. A757, pp. 1–27, 2005.

[52] I. Bearden *et al.*, "Pseudorapidity distributions of charged particles from Au+Au collisions at the maximum RHIC energy," *Phys.Rev.Lett.*, vol. 88, p. 202301, 2002.

[53] K. Krajczar, "Charged hadron multiplicity and transverse energy densities in pbpb collisions from cms." Quark Matter 2011 parallel talk.

[54] Y. Chen, "Measurement of charged particle pseudorapidity density in pb+pb collisions at $\sqrt{s_{NN}} =$ 2.76 tev with the atlas detector." Quark Matter 2011 parallel talk.

[55] W. Thome *et al.*, "Charged Particle Multiplicity Distributions in p p Collisions at ISR Energies," *Nucl.Phys.*, vol. B129, p. 365, 1977.

[56] G. Alner *et al.*, "An Investigation of Multiplicity Distributions in Different Pseudorapidity Intervals in anti-p p Reactions at a CMS Energy of 540-GeV," *Phys.Lett.*, vol. B160, p. 193, 1985.

[57] R. Ansorge *et al.*, “Charged Particle Multiplicity Distributions at 200-GeV and 900-GeV Center-Of-Mass Energy,” *Z.Phys.*, vol. C43, p. 357, 1989.

[58] G. Arnison *et al.*, “CHARGED PARTICLE MULTIPLICITY DISTRIBUTIONS IN PROTON ANTI-PROTON COLLISIONS AT 540-GeV CENTER-OF-MASS ENERGY,” *Phys.Lett.*, vol. B123, p. 108, 1983. Revised version.

[59] R. Harr, C. Liapis, P. Karchin, C. Biino, S. Erhan, *et al.*, “Pseudorapidity distribution of charged particles in $\bar{p}p$ collisions at $\sqrt{s}$ = 630-GeV,” *Phys.Lett.*, vol. B401, pp. 176–180, 1997.

[60] F. Abe *et al.*, “Pseudorapidity distributions of charged particles produced in $\bar{p}p$ interactions at $\sqrt{s}$ = 630 GeV and 1800 GeV,” *Phys.Rev.*, vol. D41, p. 2330, 1990.

[61] J. Benecke, T. T. Chou, C. N. Yang, and E. Yen, “Hypothesis of limiting fragmentation in high-energy collisions,” *Phys. Rev.*, vol. 188, pp. 2159–2169, Dec 1969.

[62] P. Steinberg, “Landau hydrodynamics and RHIC phenomena,” *Acta Phys.Hung.*, vol. A24, pp. 51–57, 2005.

[63] K. Aamodt *et al.*, “Charged-particle multiplicity density at mid-rapidity in central Pb-Pb collisions at sqrt(sNN) = 2.76 TeV,” *Phys.Rev.Lett.*, vol. 105, p. 252301, 2010. Long author list - awaiting processing.

[64] K. J. Eskola, K. Kajantie, P. V. Ruuskanen, and K. Tuominen, “Scaling of transverse energies and multiplicities with atomic number and energy in ultrarelativistic nuclear collisions,” *Nucl. Phys.*, vol. B570, pp. 379–389, 2000.

[65] S. Roesler, R. Engel, and J. Ranft, “The Monte Carlo event generator DPMJET-III,” pp. 1033–1038, 2000.

[66] W.-t. Deng, X.-N. Wang, and R. Xu, “Gluon shadowing and hadron production in heavy-ion collisions at LHC,” 2010. * Temporary entry *.

[67] N. Armesto, C. A. Salgado, and U. A. Wiedemann, “Relating high-energy lepton-hadron, proton-nucleus and nucleus-nucleus collisions through geometric scaling,” *Phys.Rev.Lett.*, vol. 94, p. 022002, 2005.

[68] D. Kharzeev, E. Levin, and M. Nardi, “Color glass condensate at the LHC: Hadron multiplicities in pp, pA and AA collisions,” *Nucl.Phys.*, vol. A747, pp. 609–629, 2005.

[69] J. L. ALbacete and A. Dumitru, “A model for gluon production in heavy-ion collisions at the LHC with rcBK unintegrated gluon densities,” 2010.

[70] X.-N. Wang and M. Gyulassy, “HIJING: A Monte Carlo model for multiple jet production in p p, p A and A A collisions,” *Phys. Rev.*, vol. D44, pp. 3501–3516, 1991.

[71] Z.-W. Lin, C. M. Ko, B.-A. Li, B. Zhang, and S. Pal, “A Multi-phase transport model for relativistic heavy ion collisions,” *Phys.Rev.*, vol. C72, p. 064901, 2005.

[72] T. Sjostrand *et al.*, “High-energy-physics event generation with PYTHIA 6.1,” *Comput. Phys. Commun.*, vol. 135, pp. 238–259, 2001.

[73] P. Z. Skands, “The Perugia Tunes,” 2009.

[74] F. W. Bopp, R. Engel, and J. Ranft, “Rapidity gaps and the PHOJET Monte Carlo,” pp. 729–741, 1998.

[75] L. Evans and P. Bryant, "LHC machine," *Journal of Instrumentation*, vol. 3, no. 08, p. S08001, 2008.

[76] C. Vanoli, "Cern accelerator complex." CERN document server, 2006.

[77] C. H. Christensen, *The ALICE Forward Multiplicity Detector - From design to installation.* PhD thesis, Niels Bohr Insitute, University of Copenhagen, 2007.

[78] The ALICE Collaboration, "Alice Technical Design Report, of the Inner Tracking System (ITS)."

[79] K. Aamodt *et al.*, "The ALICE experiment at the CERN LHC," *JINST*, vol. 3, p. S08002, 2008.

[80] The ALICE Collaboration, "Alice Technical Design Report, of the Time Projection Chamber."

[81] J. Alme, Y. Andres, H. Appelshauser, S. Bablok, N. Bialas, *et al.*, "The ALICE TPC, a large 3-dimensional tracking device with fast readout for ultra-high multiplicity events," *Nucl.Instrum.Meth.*, vol. A622, pp. 316–367, 2010.

[82] The ALICE Collaboration, "Alice Technical Design Report, of the Time of Flight System."

[83] The ALICE Collaboration, "Alice Technical Design Report, of the Transition Radiation Detector."

[84] W.R.Leo, *Techniques for Nuclear and Particle Physics Experiments.* Springer-Verlag, 1994.

[85] The ALICE Collaboration, "Alice Technical Design Report, of the High Momentum Particle Identification Detector."

[86] The ALICE Collaboration, "Alice Technical Design Report, of the Photon Spectrometer."

[87] The ALICE Collaboration, "Alice Technical Design Report, the Electromagnetic Calorimeter."

[88] M. C. Abreu *et al.*, "Anomalous J / psi suppression in Pb - Pb interactions at 158 GeV/c per nucleon," *Phys. Lett.*, vol. B410, pp. 337–343, 1997.

[89] The ALICE Collaboration, "Alice Technical Design Report, of the Dimuon Forward Spectrometer."

[90] A. Adare *et al.*, "J/psi production vs centrality, transverse momentum, and rapidity in Au + Au collisions at s(NN)**(1/2) = 200- GeV," *Phys. Rev. Lett.*, vol. 98, p. 232301, 2007.

[91] The ALICE Collaboration, "Alice Technical Design Report, Forward Detectors: Fmd, T0, V0."

[92] The ALICE Collaboration, "Alice Technical Design Report, of the Forward Multiplicity Detector."

[93] The ALICE Collaboration, "Alice Technical Design Report, of the Zero Degree Calorimeter."

[94] K. Aamodt *et al.*, "First proton-proton collisions at the LHC as observed with the ALICE detector: Measurement of the charged particle pseudorapidity density at s**(1/2) = 900-GeV," *Eur.Phys.J.*, vol. C65, pp. 111–125, 2010.

[95] Kittel, *Introduction to Solid State Physics.* Wiley, 1995.

[96] D. Vasileska, "Theory of pn diodes," Jun 2009.

[97] W. M. Yao *et al.*, "Review of particle physics," *J. Phys.*, vol. G33, pp. 1–1232, 2006.

[98] L. Landau, "On the energy loss of fast particles by ionization," *J. Phys. (USSR)*, vol. 8, pp. 201–205, 1944.

[99] K.S.KÃ¶lbig and B.Schorr, *A program package for the Landau distribution*, 1983.

[100] S. Hancock, F. James, J. Movchet, P. Rancoita, and L. Van Rossum, "ENERGY LOSS DISTRIBUTIONS FOR SINGLE PARTICLES AND SEVERAL PARTICLES IN A THIN SILICON ABSORBER," *Nucl.Instrum.Meth.*, vol. B1, p. 16, 1984.

[101] S. Hancock, F. James, J. Movchet, P. Rancoita, and L. Van Rossum, "ENERGY LOSS AND ENERGY STRAGGLING OF PROTONS AND PIONS IN THE MOMENTUM RANGE 0.7-GeV/c TO 115-GeV/c," *Phys.Rev.*, vol. A28, p. 615, 1983.

[102] P. Sarin, *Measurement of charged particle multiplicity distributions in Au+Au collisions up to 200 GeV*. PhD thesis, Massachusetts Institute of Technology, 2003.

[103] The ROOT project, "Homepage of the Root project: http://root.cern.ch." World Wide Web.

[104] R. Santoro, "Status of the ALICE silicon pixel detector," *Nucl.Instrum.Meth.*, vol. A581, pp. 330–334, 2007.

[105] A. collaboration, "http://aliweb.cern.ch/offline/activities/analysis/analysisframework/index.html." World Wide Web.

[106] CERN, "Geant 3.2.1." CERN program library.

[107] M. Liendl, "Experiment simulation." Talk given at CERN School of Computing, Helsinki 2006, 2005.

[108] A. collaboration, "http://alimonitor.cern.ch/map.jsp." World Wide Web.

[109] P. Buncic, A. Peters, P. Saiz, and J. Grosse-Oetringhaus, "The architecture of the AliEn system," pp. 951–954, 2005.

[110] M. Poghosyan, "Diffraction dissociation in proton-proton collisions at $\sqrt{s} = 0.9$ tev, 2.76 tev and 7 tev, with alice at the lhc." Quark Matter 2011 parallel talk.

[111] A. Toia, "Bulk properties of pb-pb collisions at LHC measured by ALICE." Quark Matter 2011 plenary talk.

[112] B. Alver, M. Baker, C. Loizides, and P. Steinberg, "The PHOBOS Glauber Monte Carlo," 2008.

[113] C. Soegaard, "The alice forward multiplicity detector – test beam results," Master's thesis, Niels Bohr Insitute, University of Copenhagen, 2007.

[114] A. Collaboration, "Analysis note for pb+pb multiplicity papers." Internal note, 2011.

[115] K. Aamodt *et al.*, "Charged-particle multiplicity measurement in proton-proton collisions at sqrt(s) = 0.9 and 2.36 TeV with ALICE at LHC," *Eur.Phys.J.*, vol. C68, pp. 89–108, 2010.

[116] V. Khachatryan *et al.*, "Transverse-momentum and pseudorapidity distributions of charged hadrons in pp collisions at sqrt(s) = 7 TeV," *Phys.Rev.Lett.*, vol. 105, p. 022002, 2010.

[117] B. Alver and B. B. e. a. Back, "Charged-particle multiplicity and pseudorapidity distributions measured with the phobos detector in Au+Au, Cu+Cu, $\mathbf{d}+$Au, and $\mathbf{p}+\mathbf{p}$ collisions at ultrarelativistic energies," *Phys. Rev. C*, vol. 83, p. 024913, Feb 2011.

[118] C. Nygaard, *Charged particle multiplicity distributions into forward pseudorapidities in pp and PbPb collisions at the LHC*. PhD thesis, University of Copenhagen, 2011.

[119] C. Sø gaard, *Pseudorapidity Correlations in p+p collisions at LHC energies*. PhD thesis, University of Copenhagen, 2011.

[120] A. Hansen, "Pseudorapidity dependence of elliptic flow in pb+pb collisions at $\sqrt{s_{NN}} = 2.76$ TeV with alice," Master's thesis, University of Copenhagen, 2011.

[121] D. Ourdane, *Charged Pion and Kaon Production in Central Au+Au Collisions at* $\sqrt{s_{NN}} = 200$ *GeV*. PhD thesis, University of Copenhagen, 2003.

[122] A. Collaboration, "http://aliweb.cern.ch/offline/." World Wide Web.

Appendices

Appendix A

The ALICE collaboration

The ALICE collaboration consists of 33 countries, 116 institutes, > 1000 members. The map in Figure A.1 shows the geographical distribution of member nations. Present spokesperson is Paolo Giubellino, CERN.

Figure A.1: The ALICE collaboration June 2011.

Copenhagen Group

The Copenhagen ALICE group is the High Energy Heavy Ion (HEHI) group with the following members:

- Bearden, Ian
- Bøggild, Hans

- Christensen, Christian Holm
- Dalsgaard, Hans Hjersing
- Gulbrandsen, Kristjan
- Gaardhøje, Jens Jørgen
- Hansen, Alexander
- Nielsen, Børge Svane
- Nygaard, Casper
- Søgaard, Carsten

Appendix B

Relevant Variables and Concepts

This appendixintroduces the necessary variables and concepts to describe the kinematics of heavy ion collisions.

Kinematics

Figure B.1 shows a schematic view of a heavy ion collision in the CM frame. The nuclei approach each other as Lorentz compressed 'pancakes' because of the relativistic velocities. They interpenetrate and interact forming the socalled *fireball* and are then (to some extent) slowed down by the collision and continue along their original directions of motion. Section 1.2 discusses several scenarios for this. The nucleons directly involved in the collisions are labeled participants and the nucleons not interacting are called spectators. These terms are important to keep in mind because only the participants contribute to the fireball and thus to the production of particles that takes place there. The point in space where the collision occurs is known as the *Interaction Point* (IP). The measured IP is known as the (primary) collision *vertex*. Figure B.2 introduces a global coordinate system[1]. The particles move along the z axis (the beam axis) which is the standard convention. In an accelerator ring the y axis usually points upward

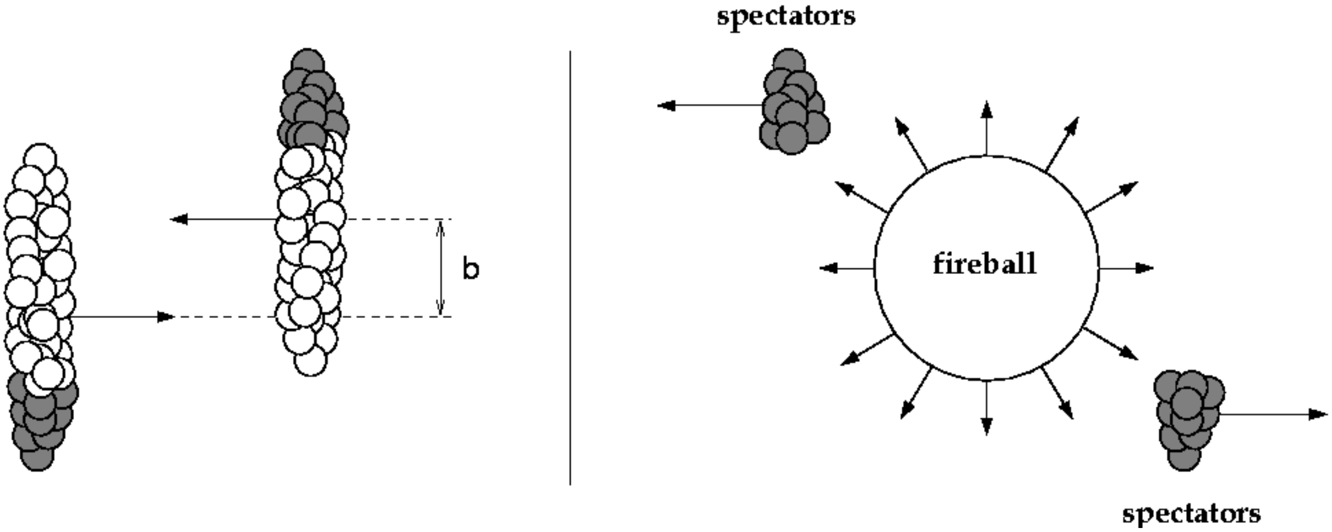

Figure B.1: A heavy ion collision in the CM frame.

---

[1] in the sense that the coordinate system used in a particular subdetector may be different.

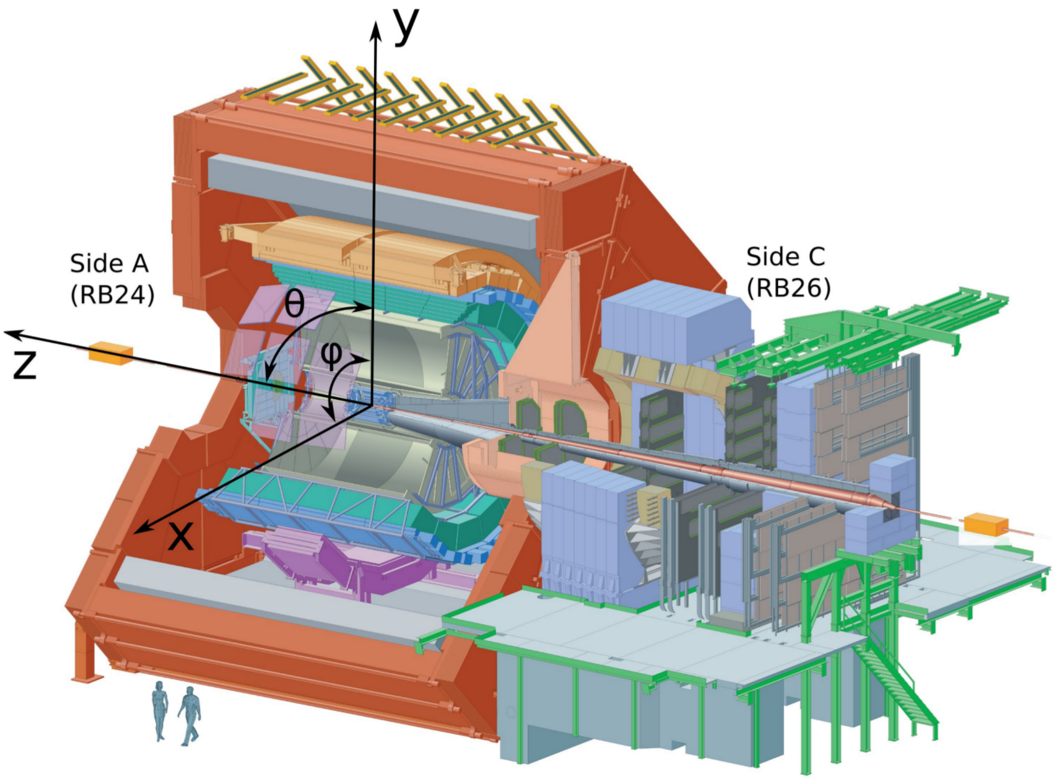

Figure B.2: The global ALICE coordinate system. The z axis is the beam axis and the x axis points to the center of the LHC. θ is the polar angle, and φ is the azimuthal angle.

so the x axis points in the radial direction. The 4-vectors of the incoming nuclei in the CM frame are then $(E, 0, 0, p_z)$ and $(E, 0, 0, -p_z)$.

Rapidity

The rapidity of a particle is defined as :

$$y = \frac{1}{2} \ln \left(\frac{E + p_z}{E - p_z} \right) \tag{B.1}$$

Rapidity is an important variable in heavy ion physics as it plays the same role in the Lorentz transformation as velocity plays in the Gallilei transformation. It is shown below that the rapidity is additively invariant under the Lorentz transformation. This means that the differential of y, dy, is Lorentz invariant.

Rapidity under the Lorentz Transformation

The Lorentz transformation of E and p_z is [97]:

$$E' = \gamma E - \gamma\beta p_z \tag{B.2}$$

$$p'_z = -\gamma\beta E + \gamma p_z \tag{B.3}$$

Here β is defined as the velocity of the frame from which the collision is seen and γ is defined as $\gamma = \frac{1}{\sqrt{(1-\beta^2)}}$.

The transformation is done by inserting the transformations of E and p_z into the definition of the rapidity:

$$\begin{aligned} y' &= \tfrac{1}{2}\ln\tfrac{E'+p'_z}{E'-p'_z} = \tfrac{1}{2}\ln\tfrac{\gamma E-\gamma\beta p_z-\gamma\beta E+\gamma p_z}{\gamma E-\gamma\beta p_z+\gamma\beta E-\gamma p_z} \\ &= \tfrac{1}{2}\ln\tfrac{E+p_z}{E-p_z} + \tfrac{1}{2}\ln\tfrac{\gamma-\gamma\beta}{\gamma+\gamma\beta} = y + \tfrac{1}{2}\ln\tfrac{\gamma-\gamma\beta}{\gamma+\gamma\beta} \\ &\Rightarrow dy' = dy \end{aligned} \tag{B.4}$$

Thus, the result is that dy is Lorentz invariant which means that eg. $\frac{dN}{dy}$ is also Lorentz invariant.

Pseudorapidity

The calculation of the rapidity requires knowledge of the mass of the particle so it can only be calculated for identified particles. For non-identified particles with $m \ll p$ (that is $E = \sqrt{m^2+p^2} \to p$), the pseudorapidity can be used instead of the rapidity. It is defined as :

$$\eta = -\ln(\tan\frac{\theta}{2}) \tag{B.5}$$

where θ is the angle between the direction of emission of the particle and the z axis (see Figure B.2). For $m \ll p$, $y \approx \eta$ because for $E = p$ (B.1) yields:

$$y = \frac{1}{2}\ln\left(\frac{E+p_z}{E-p_z}\right) \approx \frac{1}{2}\ln\left(\frac{p+p_z}{p-p_z}\right) = \frac{1}{2}\ln\left(\frac{1+\cos(\theta)}{1-\cos(\theta)}\right) = -\ln(\tan\frac{\theta}{2})$$

Accelerators and Colliders

Here the calculation of $\sqrt{s_{NN}}$ for accelerators and colliders is reviewed. The center of mass system is labelled 'CM' and the laboratory frame is labelled 'lab'. In the following $c = 1$. Consider a system of two colliding particles with energies E_1 and E_2 and momenta p_1 and p_2 in the lab frame. For simplicity only one dimensional collisions are considered. It is known from the formalism of 4-vectors that the 4-momentum is conserved and that the square of the 4-momentum is invariant. Furthermore:

$$P_{lab} = (E_{lab}, \vec{p}_{lab}) = (E_{lab}, 0, 0, p_{lab})$$

$$P_{CM} = (E_{CM}, 0, 0, 0)$$

Thus by evaluating the total 4-momentum of the system in the CM frame and the lab frame we get:

$$P^2_{CM} = P^2_{lab} \Leftrightarrow E^2_{CM} = E^2_{lab} - p^2_{lab} \tag{B.6}$$

By defining $s_{NN} \equiv E^2_{CM}$ and inserting the total energy and momentum of the system we get:

$$\sqrt{s_{NN}} = \sqrt{E^2_{lab} - p^2_{lab}} = \sqrt{(E_1+E_2)^2 - (p_1+p_2)^2} \tag{B.7}$$

In an accelerator system where an incoming beam of particles hits a stationary target this reduces to (assuming the mass of the particles in the beam is equal to the mass of the particles in the target):

$$\sqrt{s_{NN}} = \sqrt{2m(E_{beam}+m)} = \sqrt{\frac{2m}{\sqrt{1-(tanh(y_p))^2}}} \tag{B.8}$$

Here y_p is the beam rapidity. For the collider system, where $p_1 = -p_2$, we obtain the simple expression:

$$\sqrt{s_{NN}} = 2E_{beam} = 2m(\frac{1}{\sqrt{1-(tanh(y_p))^2}} - 1) \tag{B.9}$$

From this it is obvious why a collider is a far more powerful tool than an accelerator. The SPS, a fixed target accelerator, uses a beam with energy 158 GeV but it reaches only $\sqrt{s_{NN}} = 17$ GeV. RHIC uses two 100 GeV beams and is able to reach $\sqrt{s_{NN}} = 200$ GeV. The LHC will reach $\sqrt{s_{NN}} = 5.5$ TeV. Table B.1 summarises the energies and beam rapidities of AGS, SPS, RHIC and LHC.

	$\sqrt{s_{NN}}$	y_{beam}
AGS	5 GeV	1.61
SPS	17 GeV	2.91
RHIC	200 GeV	5.36
LHC	900 GeV	6.87
LHC	2.76 TeV	7.99
LHC	5.5 TeV	8.67
LHC	7 TeV	8.92

Table B.1: Summary of AGS, SPS, RHIC and LHC energies.

Transverse Momentum and Spectra

It was shown that dy is Lorentz invariant. Another Lorentz invariant variable, the transverse momentum is defined as:

$$p_T = \sqrt{p_x^2 + p_y^2} = |p \sin\theta| \tag{B.10}$$

This quantity is Lorentz invariant as the transverse components of the 4-momentum transforms as $p_x = p'_x$ and $p_y = p'_y$.

Often p_T is replaced by the transverse mass defined as $m_T \equiv \sqrt{p_T^2 + m^2}$ which is also Lorentz invariant. The identity $p_T dp_T = m_T dm_T$ holds because

$$m_T dm_T = \sqrt{p_T^2 + m^2} d(\sqrt{p_T^2 + m^2}) = p_T dp_T$$

To describe the particle production the spectrum or invariant differential yield of the particles is introduced [121]:

$$E\frac{d^3\sigma}{\sigma dp^3} = \frac{d^2N}{2\pi p_T dp_T dy} \qquad \left(= \frac{d^2N}{2\pi m_T dm_T dy}\right) \tag{B.11}$$

The invariant yield describes the number of particles produced per rapidity and transverse momentum. Note that the equation above assumes azimuthal isotropy as the factor of 2π comes from the integration of ϕ (basically the equation expresses a change of coordinates from 3–momentum to (p_T, y, ϕ)). For non-central collisions, this is only approximately true.

Momentum transfer and the Feynmann x

In inclusive reactions the total cross–section can be parametrized in a transverse component and a longitudinal component [4]. The transverse momentum has been discussed above. It was found by Feynmann that it was convenient to define a variable that was a fraction of the maximum longitudinal momentum (which is beam–dependent). This variable, x_F, is defined in the CMS frame as:

$$x_F = \frac{p_L}{p_L(max)} = \frac{2p_L}{\sqrt{s}} \tag{B.12}$$

The momentum transfer in a reaction is labelled Q^2. Parton Distribution Functions are probability functions in (x, Q^2) space that give the probability of finding a particle with a particular (x, Q^2).

Centrality

Figure B.1 introduces the impact parameter (b). It is the component perpendicular to the beam axis of the vector between the centres of the colliding nuclei. Since it is impossible to measure b directly another technique must be used to distinguish between central collisions (small values of b) and peripheral collisions (larger values of b). This distinction is important because the physics involved in a collision might depend on how centrally the nuclei collide. For example the particle production is larger in central events than in peripheral events as more particles interact in the central collisions. Due to the geometry of the colliding heavy ions the zone of central collisions is azimuthally isotropic.

In experiments, the centrality is used instead of the impact parameter to distinguish between central and peripheral collisions. The idea is that the most central collisions have the largest overlap and thus will produce the most particles. From measurements of the particle production centrality 'classes' can be defined. The definition of the centrality class corresponding to impact parameters $0 < b < b_c$ is:

$$c = \frac{\int_0^{b_c} \frac{d\sigma_{in}(b')}{db'} db'}{\sigma_{in}} \tag{B.13}$$

Here σ_{in}, $\frac{d\sigma_{in}(b')}{db'}$ and b_c are the total inelastic nuclear reaction cross section, the differential cross section at $b = b_c$ and a cut-off in the impact parameter, respectively. Equation (B.13) can be understood as an integral over the overlap region so that the most central collisions will be those with the largest overlap.

It is seen that the centrality classes are classes of the differential cross section for different impact parameters. For practical purposes the experimental definition of centrality classes is based on particle production instead of cross-section. This means that a centrality class will contain collisions having produced a certain fraction of the total particle production. For example collisions in the 0-5% centrality class will be the collisions with the highest particle production for which 5% of the total particle production was produced.

If the colliding particles are identical (as in e.g. Pb+Pb collisions) and assumed spherical the differential cross section is given as $\frac{d\sigma_{in}(b)}{db} = 2\pi b db$ [121] and $b_{max} = 2R$ where R is the radius of the nuclei. From Equation (B.13) $c = \frac{b_c^2}{4R^2}$ is obtained. This means that for lead where $R = 1.2 \cdot 208^{1/3}$ fm, 0-5% centrality corresponds to $0 < b < 3.5$ fm.

Appendix C

Overview of the code

In this appendix an overview of the AliROOT classes and macros used for the analysis is given. The overview is not comprehensive; for a full overview of the AliROOT project see [122].

The AliROOT code is kept in a software repository[1] at CERN where it is available to all ALICE users. Each week a so–called *tag* is produced which is a snapshot of the repository containing a up–to–date working version of AliROOT. These tags are installed in AliEn and can be accessed using the appropriate software. The tag used for the analysis presented here is **v5-02-03-AN**.

The following tasks are used to generate the AOD objects from the ESD files. They implement all the analysis presented in Chapter 6:

AliPhysicsSelectionTask The trigger selection is handled automatically by this task that selects the relevant trigger classes and manages varying settings of the trigger detectors run by run.

AliCentralitySelectionTask The determination of the centrality in the ANALYSIS framework is handled by this task. From here the user can pick the method to use.

AliForwardMultiplicityTask This task contains all the FMD analysis including all corrections.

AliForwardMCMultiplicityTask A special version of the FMD analysis task for simulated data.

AliCentralMultiplicityTask This task runs all of the SPD analysis including all corrections

AliCentralMCMultiplicityTask The version of the SPD analysis supposed to run with simulated data.

For $\frac{1}{N}\frac{dN_{\mathrm{ch}}}{d\eta}$ specific analysis the AOD files must be processed and the relevant information extracted. This is handled by two tasks:

AliForwarddNdetaTask This task calculates $\frac{1}{N}\frac{dN_{\mathrm{ch}}}{d\eta}$ for the FMD.

AliCentraldNdetaTask This task calculates $\frac{1}{N}\frac{dN_{\mathrm{ch}}}{d\eta}$ for the SPD.

Apart from the tasks themselves which are compiled into AliROOT, a number of macros are required to run the analysis. These macros take care of adding the tasks to framework with the correct settings, arguments etc. They are:

- AddTaskPhysicsSelection.C
- AddTaskCentralitySelection.C
- AddTaskForwardMult.C

---

[1] Powered by subversion, a repository management project

- AddTaskForwarddNdeta.C
- AddTaskCentralMult.C
- AddTaskCentraldNdeta.C

Appendix D

Quark Matter 2011 Results

The Figures shown in this appendix were shown at Quark Matter 2011. Figure D.6 is indeed the poster.

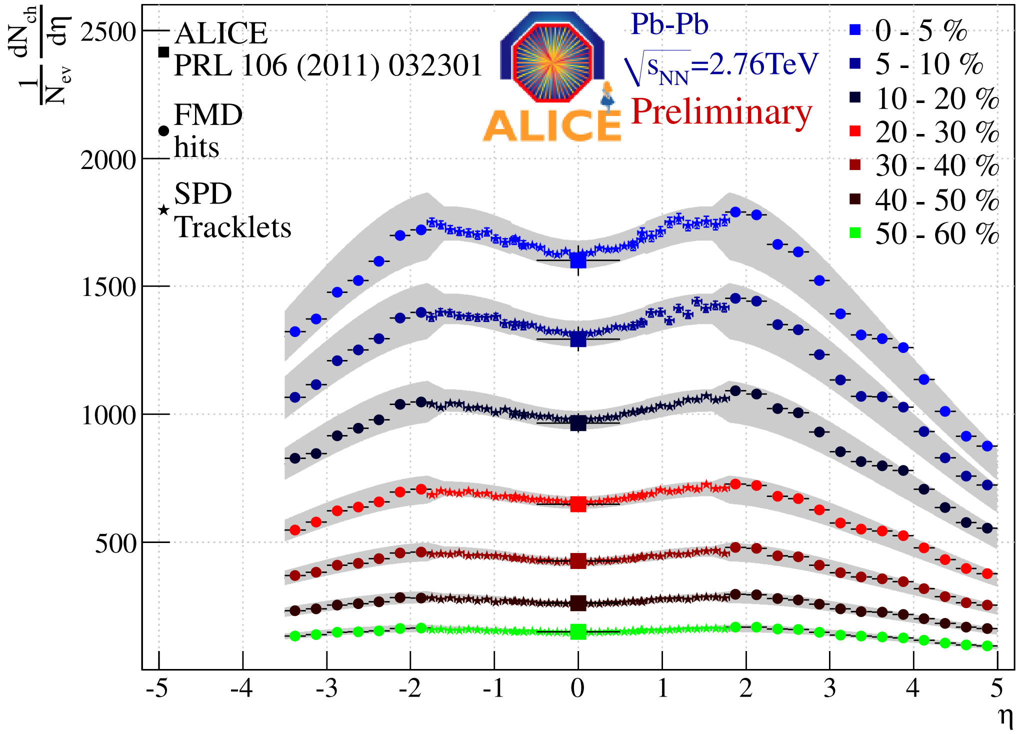

Figure D.1: QM2011 Pseudorapidity Density. $\frac{1}{N}\frac{dN_{\rm ch}}{d\eta}$ in 10 centrality classes.

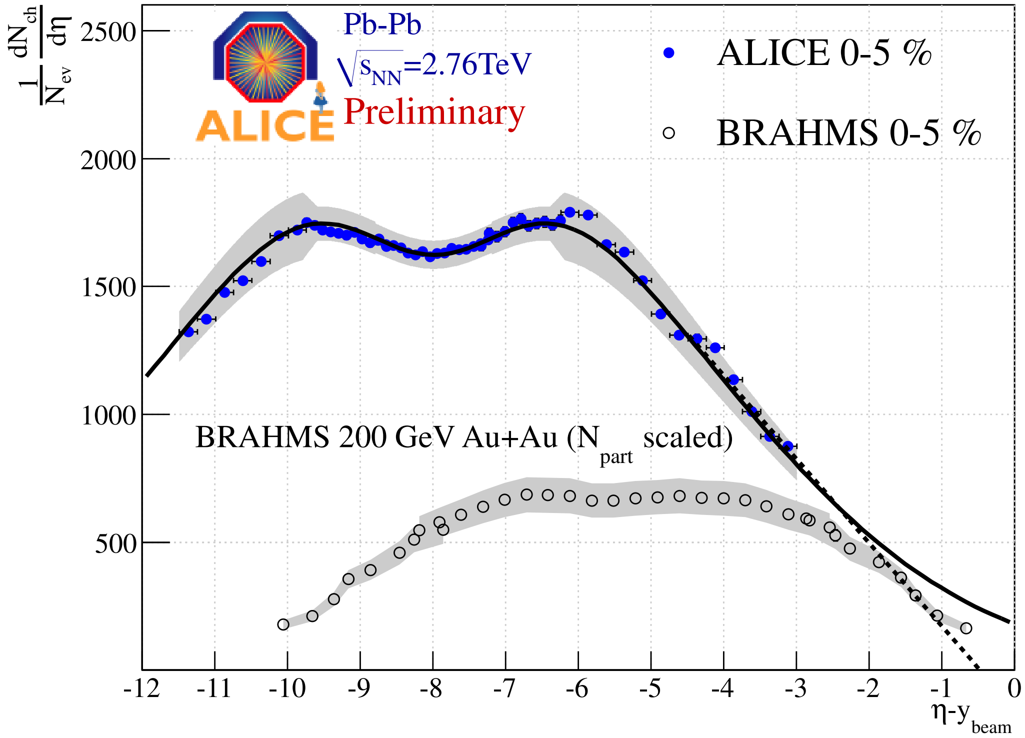

Figure D.2: QM2011 sketch of longitudinal scaling for $0-5\%$ central collisions from ALICE to BRAHMS.

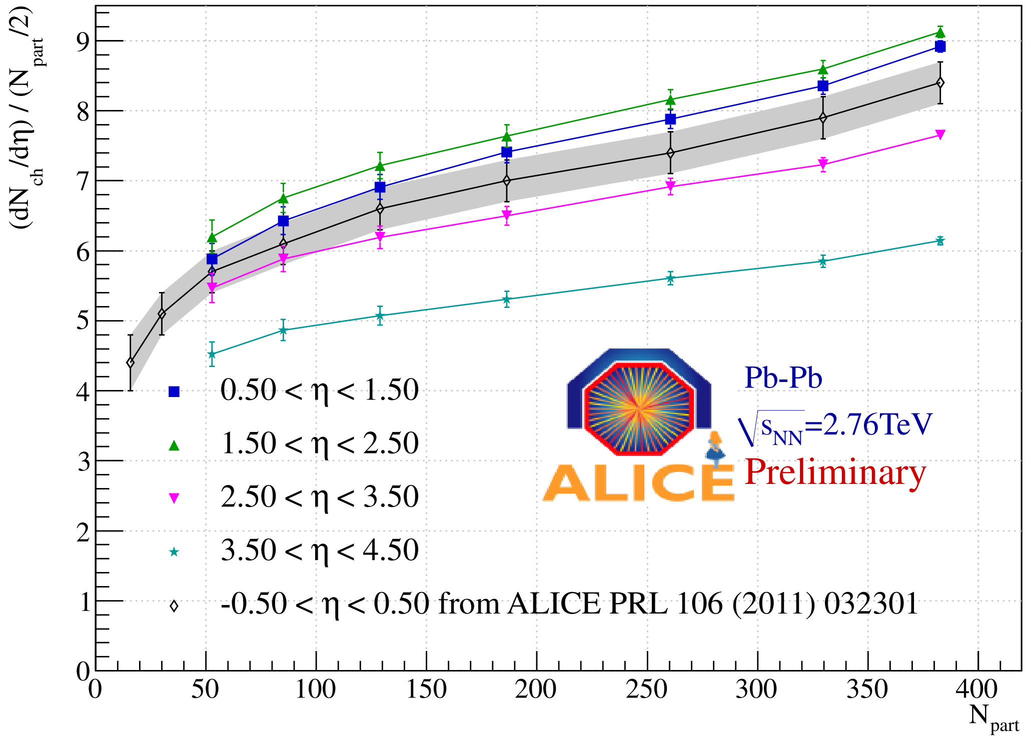

Figure D.3: QM2011 Scaling with N_{part}.

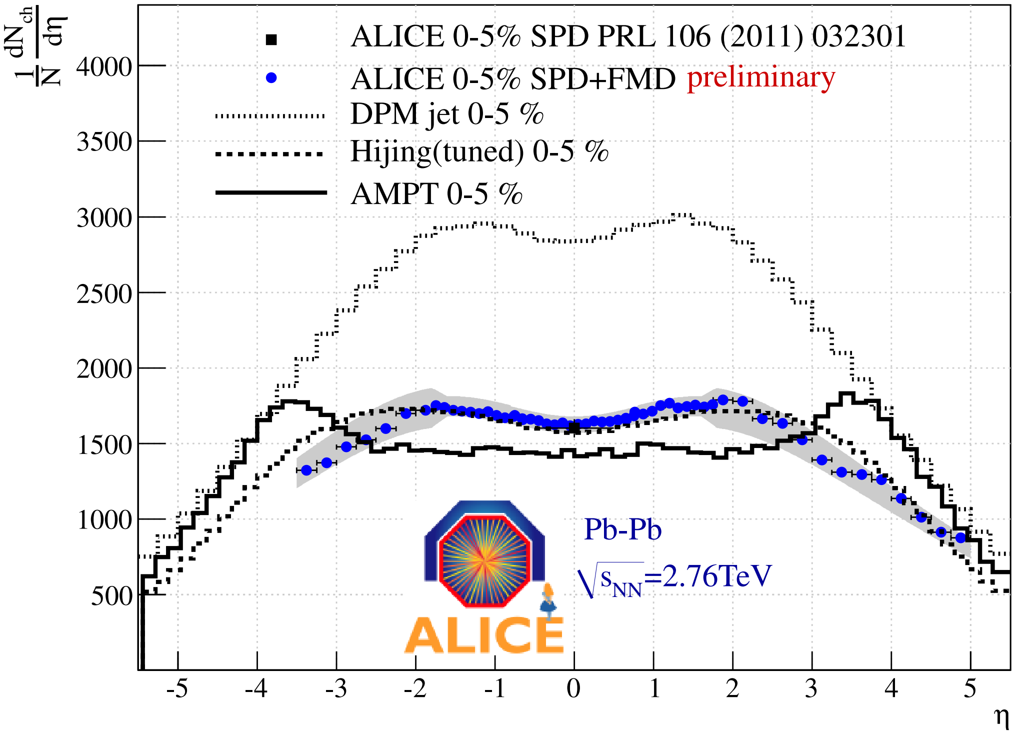

Figure D.4: QM2011 Model Comparison.

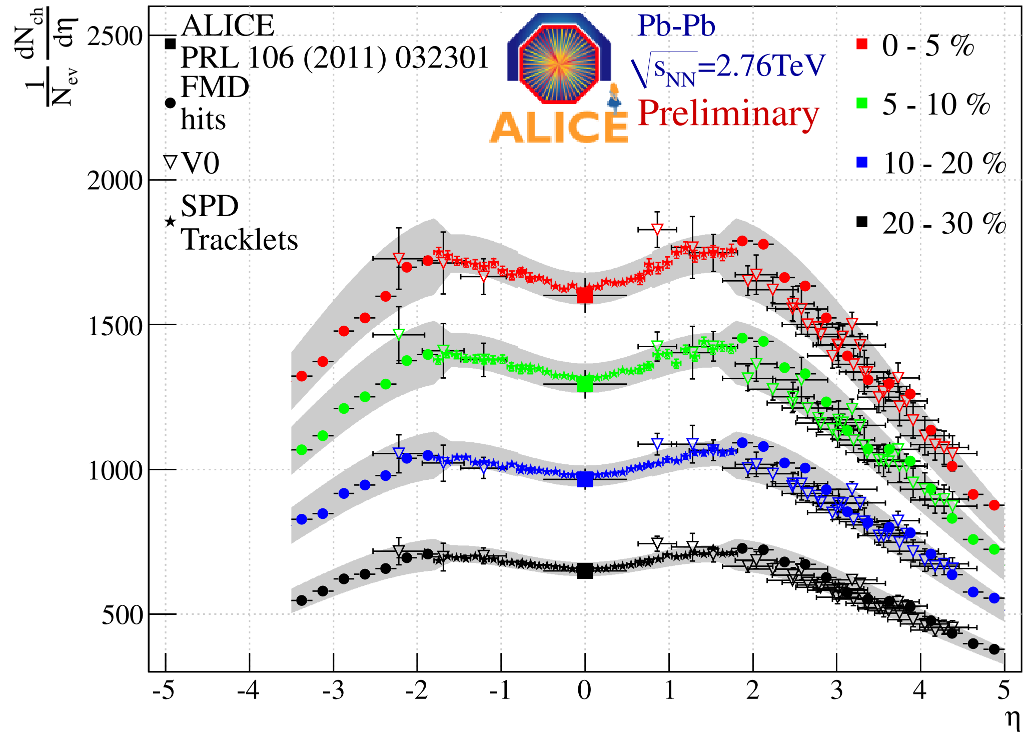

Figure D.5: QM2011 V0 Comparison. Comparison between the FMD measurement and the V0 measurement of $\frac{1}{N}\frac{dN_{\rm ch}}{d\eta}$.

Pseudorapidity density of charged particles and its centrality dependence in Pb-Pb collisions at $\sqrt{s_{NN}} = 2.76$ TeV

Hans Hjersing Dalsgaard, for the ALICE collaboration
Niels Bohr Institute, University of Copenhagen

Pseudorapidity density

The $dN_{ch}/d\eta$ measured by ALICE in centrality bins of $0-5\%$, $5-10\%$, $10-20\%$, $20-30\%$, $30-40\%$, $40-50\%$, and $50-60\%$. The systematic errors of 7.6% are drawn around a fitted function: $A_1 e^{\frac{\eta^2}{2\sigma_1^2}} - A_2 e^{\frac{\eta^2}{2\sigma_2^2}}$. Statistical errors are negligible. Previously published points in $|\eta| < 0.5$ also shown [1].

Longitudinal scaling?

Comparison between the $0-5\%$ $dN_{ch}/d\eta$ from ALICE and data from RHIC 200 GeV Au+Au data from BRAHMS [2] scaled to $\frac{N_{part,ALICE}}{N_{part,BRAHMS}}$. Two extrapolations from $\eta - y_b > -3$: Double-Gaussian (see box to the left) fit to data extended to infinity and a linear extrapolation from data.

Model comparisons and scaling with number of participants

$(dN_{ch}/d\eta)/(N_{part}/2)$ as a function of the number of participants, N_{part} for seven centrality classes as measured by the ALICE experiment.

Total number of charged particles, $N_{ch} = \int_{-y_b}^{y_b} \frac{dN_{ch}}{d\eta} d\eta$ as a function of the number of participants, N_{part} for seven centrality classes measured by the ALICE experiment.

Comparison of the $dN_{ch}/d\eta$ for $0-5\%$ central collision with DPMjet [3], AMPT [4] and HIJING [5]. HIJING has been tuned to 2000 particles for $\eta = 0$ and $b = 0$.

Measuring with ALICE

A sketch of the ALICE detectors used in this analysis. The Silicon Pixel Detector SPD and the Forward Multiplicity Detector (FMD) were used for measuring the $dN_{ch}/d\eta$. The V0, T0 and SPD were used for triggering, while the V0 was used for the centrality determination.The V0 in addition provides a measurement of the $dN_{ch}/d\eta$ (see lower right panel).

Complementarity between ALICE detectors

The $dN_{ch}/d\eta$ can also be measured using the ALICE V0 detector (using the SPD tracklets to set the level of the distribution) instead of the FMD. This figure shows a comparison where it is clear that these two measurements are complementary with the SPD measurements to give the full ALICE $dN_{ch}/d\eta$. The errors band and bars show total errors. For more details see the ALICE poster by *M. Guilbaud*.

References

[1] K. Aamodt *et al.*, ALICE Collaboration, Phys.Rev.Lett. **106**, 032301 (2011)
[2] Bearden, I. G. *et al.*, BRAHMS Collaboration, Phys.Rev.Lett. **88**, 202301 (2002)
[3] J. Ranft, SI-99-6, hep-ph/9911232 (1999)
[4] Zi-Wei Lin *et al.*, Phys.Rev. C72 064901 (2005)
[5] X.-N. Wang and M. Gyulassy, Phys.Rev. vol. D44, pp. 3501–3516 (1991)

Hans Hjersing Dalsgaard hans.dalsgaard@cern.ch

Figure D.6: The QM2011 Poster.

Appendix E

Discussion of possible issues in the ALICE material budget

This appendix takes a look on the possible issues that could remain in the description of the ALICE geometry in AliROOT. During 2010 two major issues were detected in the setup of the simulations:

Missing δ electrons in FMD Due to a software issue δ electrons were not produced in the FMD volumes in the ALICE geometry. This turned out to be a $15 - 20\%$ effect. Luckily, the fix for this was extremely simple.

Cooling connectors missing in SPD support geometry A review of the ITS geometry was carried out in the spring and summer 2010. The main finding was that the aluminum cooling connectors that distributes the cooling water from the cooling plant into the ITS were missing in the geometry description. This is rather serious since they are made of a metal and they sit directly in the FMD acceptance (see Figure E.1). Other issues were also found but none as grave as this. In total, this was a $\sim 10\%$ effect which required a non–significant effort from the ITS groups. The cooling connectors are visible in the SPD picture in Figure 4.1 as the metal chunks around the edge of the SPD thermal screen.

There could still be issues at play in the description of the ALICE geometry. The ALICE TPC team has developed a technique to scan the experiment using $e^{+} - e^{-}$ decays coming from interactions with material. This technique can reveal differences in the produced (primary + secondary) particles in the experiment compared to the simulated data. In this way the simulations can be tested directly and the material budget can be assessed. So far this has been limited to the central region but a data have been taken with the IP shifted up to a meter up and down. These data can be used to assess the material in front of the FMD and this can tell if something is missing. The results of this 'parasitic vertex' scan are not ready as this thesis goes to print but are eagerly awaited. If material is missing in the ALICE description in front of the FMD it can have a big impact on the analysis presented in this thesis.

Figure E.1 shows the simulated distribution of the origin of all secondary particles in ALICE. As indicated in the Figure all the detectors are visible by the 'footprint' they leave as secondaries.

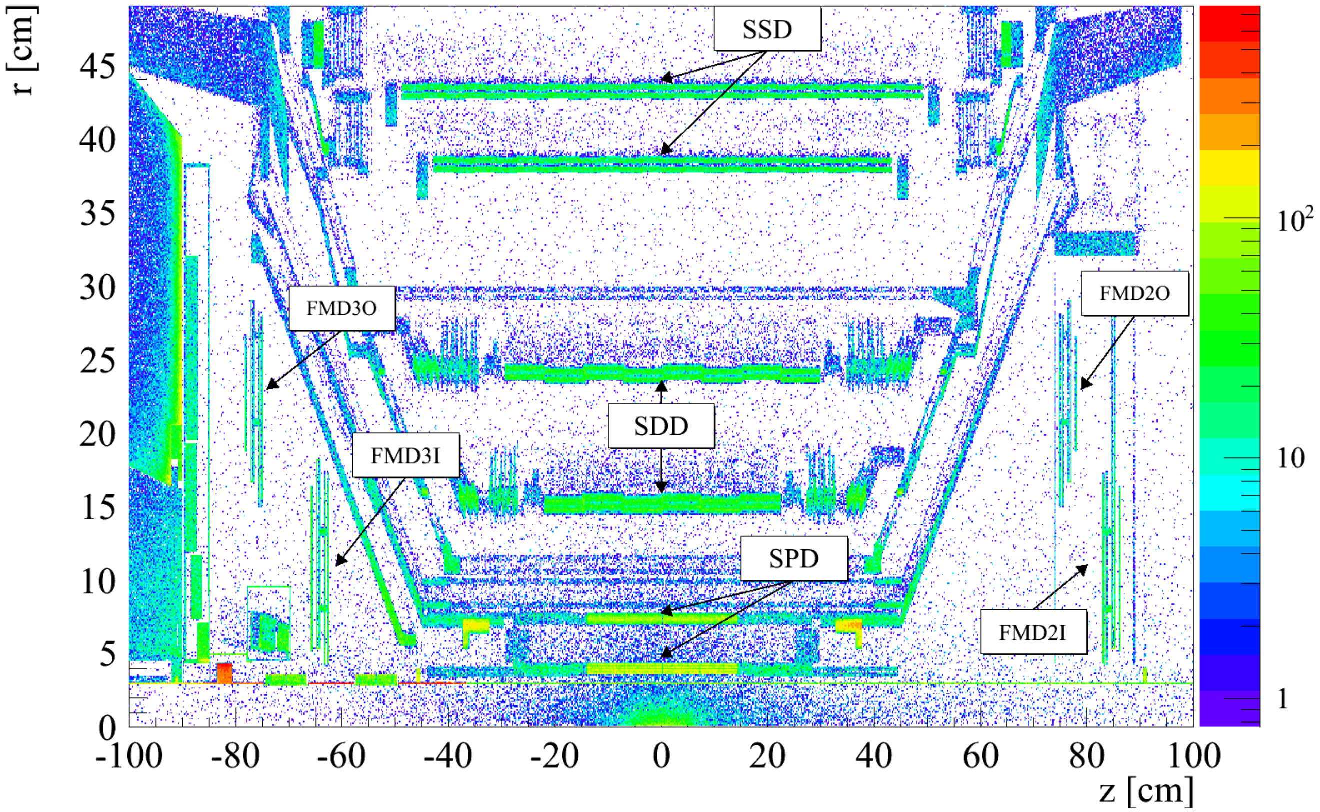

Figure E.1: The origin of all secondary particles in ALICE from simulated data [118]. The cooling connectors in the SPD are visible around $(z, r) = (\pm 35\ \text{cm}, 5\ \text{cm})$.

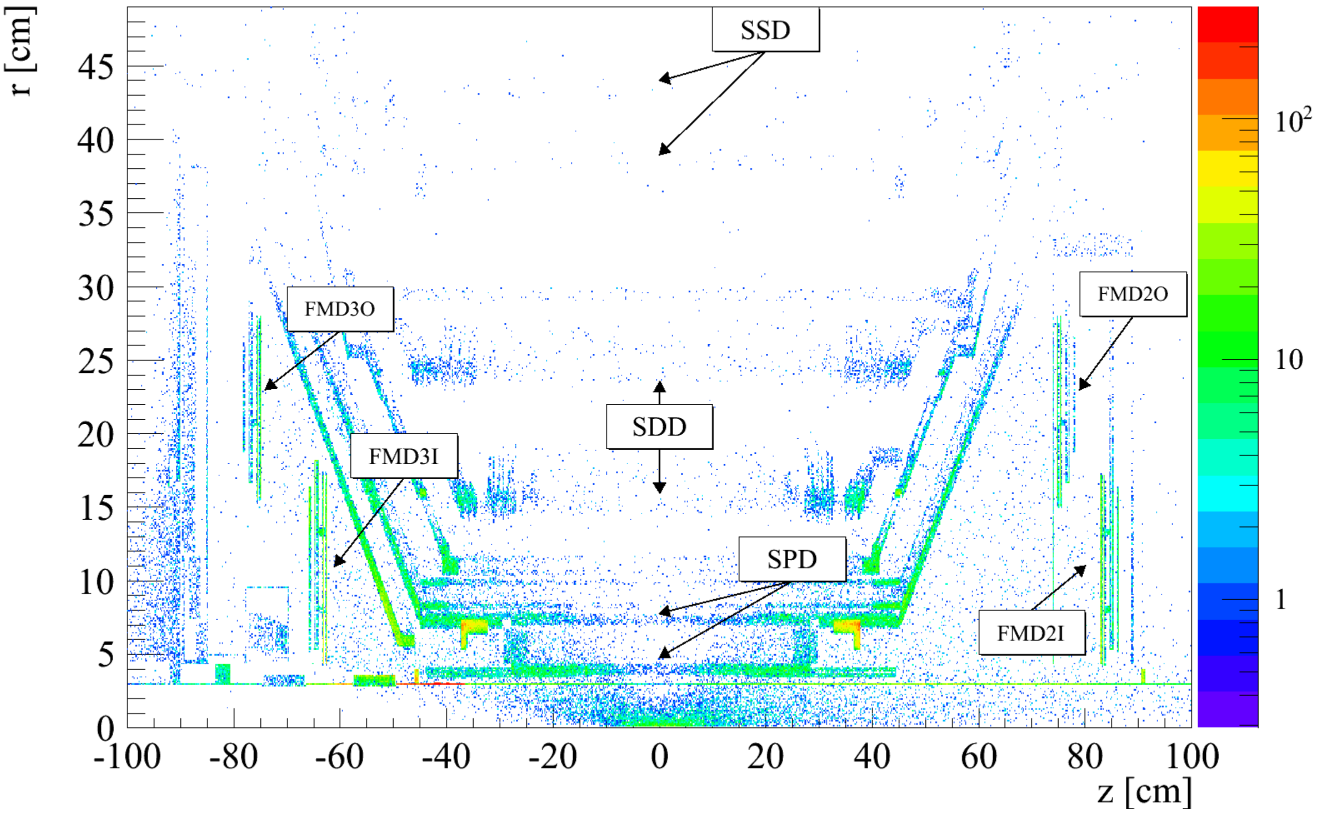

Figure E.2: The origin of all secondary particles that hit the FMD from simulated data. This is in principle a 2D representation of Figures 6.28 and 6.29.

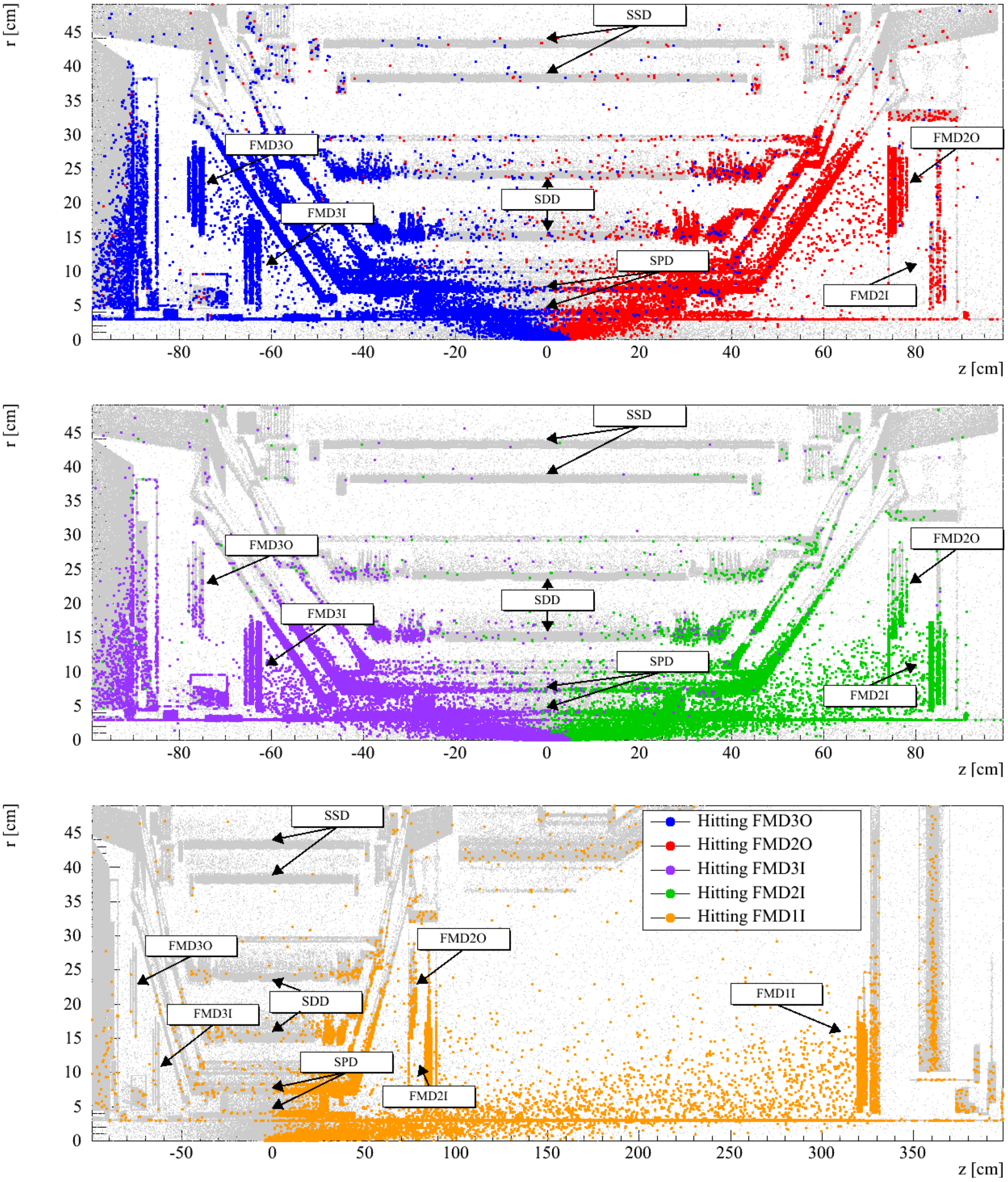

Figure E.3: Top Panel: The origin of all secondaries hitting FMD2O and FMD3O. It is interesting to note that the simulations predict particles travelling through the whole experiment during the transport of particles. Middle Panel: The origin of all secondaries hitting FMD2I and FMD3I. Bottom Panel: The origin of all secondaries hitting FMD1I.

Appendix F

Additional Analysis Figures

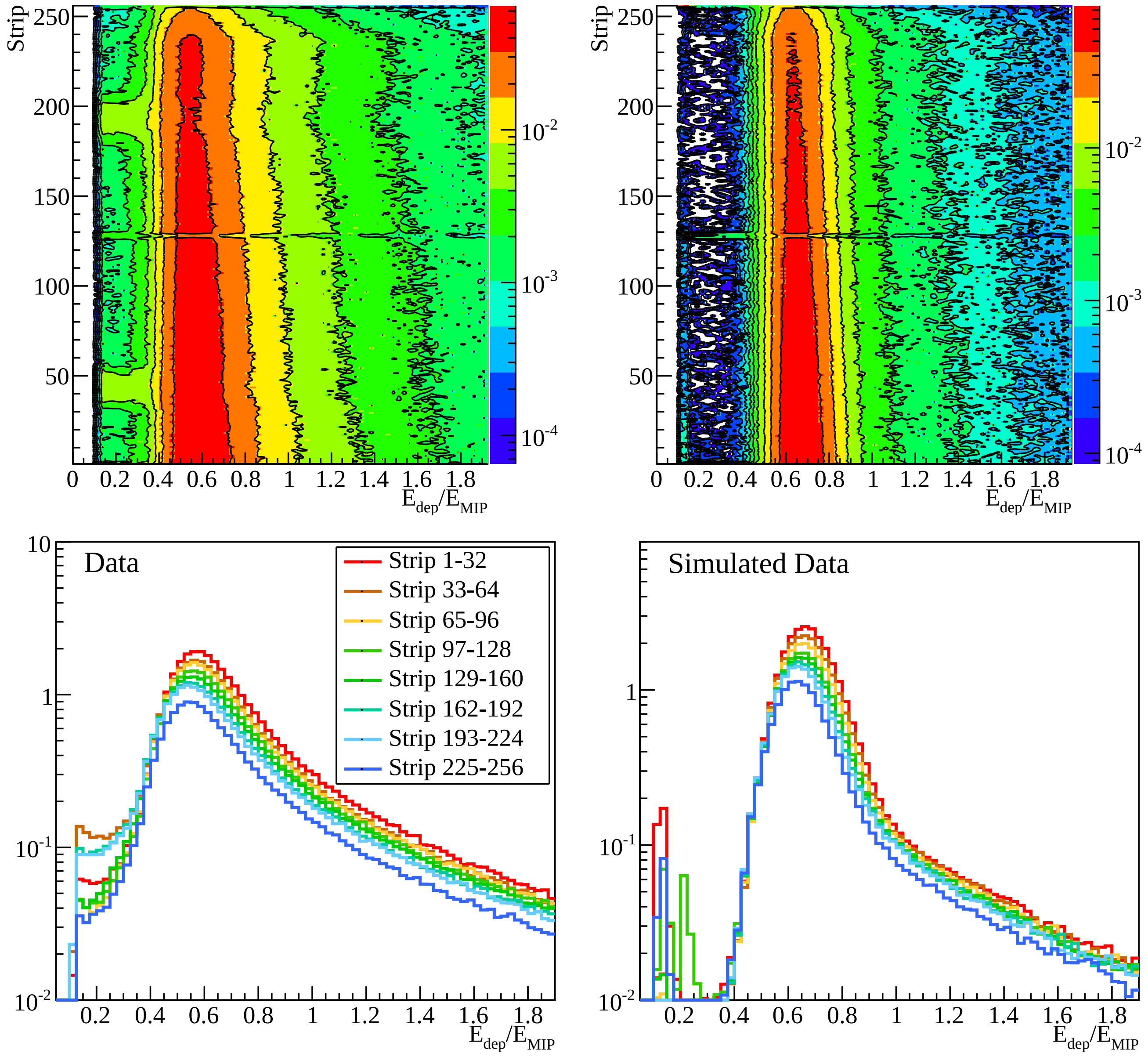

Figure F.1: The top panels show the single strip energy signal versus strip in FMD2O in $\sqrt{s} = 900$ GeV p+p physics data (left) and simulated data (right). While the general features are similar a structure at low energies ($E_{dep}/E_{MIP} \sim 0.2$) is observed in physics data which is not present in the simulated data. This is also evident from the lower panels which show the projections of groups of 32 strips. Apart from the observed structure it is clearly seen that the low energy tail is much more pronounced in physics data than in simulated data. The band structure at strip ~ 128 is understood as a consequence of dead channels.

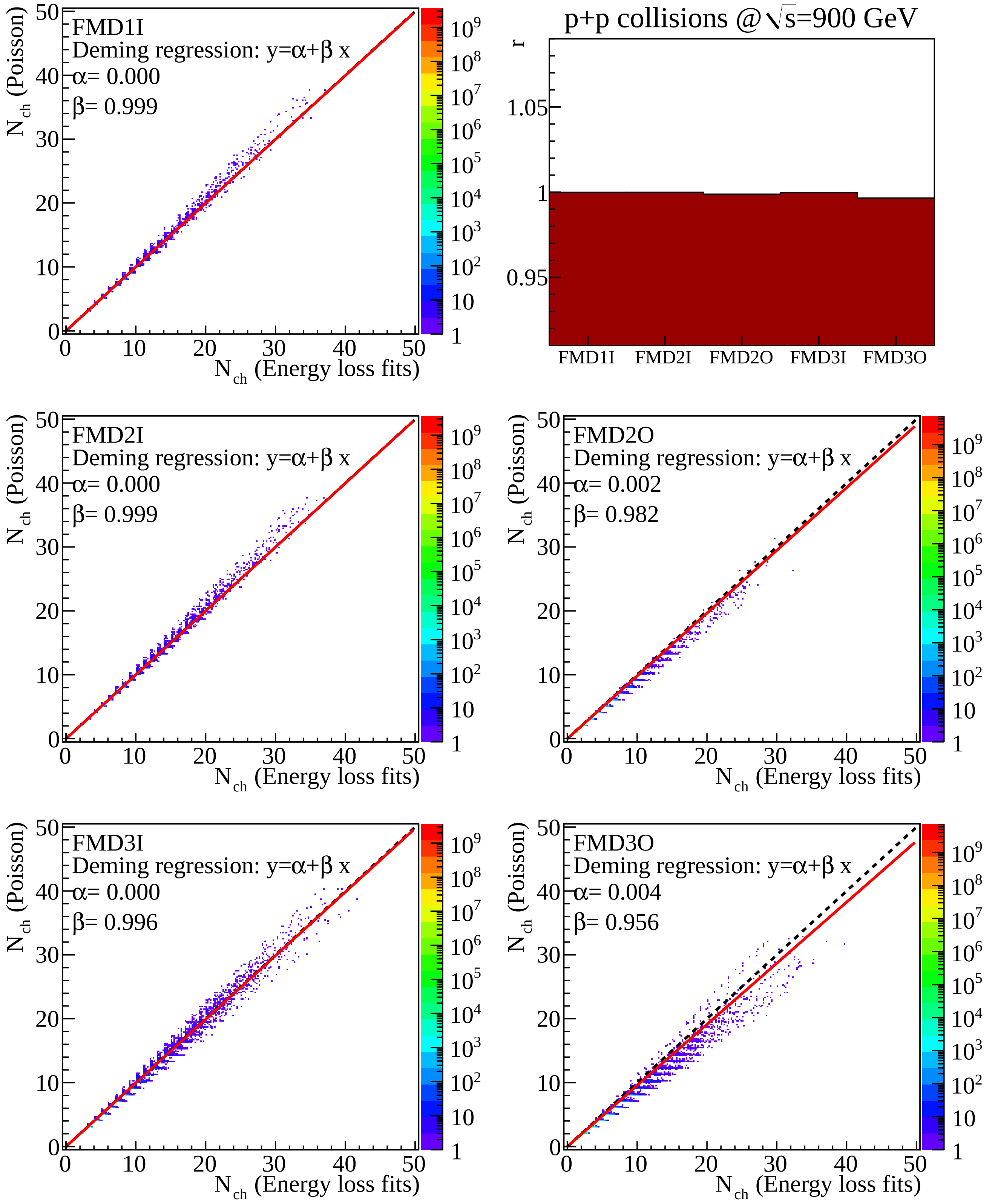

Figure F.2: Poisson and Energy fit high occupancy correction comparison in p+p collisions at $\sqrt{s} = 900$ GeV. It is seen that there is reasonable correspondance between the two methods as the red line is a fit to the data and the black line is N_{ch}(Poisson) $= N_{ch}$(Energy Loss Fits). The upper right corner shows the correlation coefficients of the fits to the data.

List of Figures

List of Tables